HZDR-113

ANNUAL REPORT 2020

Institute of Resource Ecology

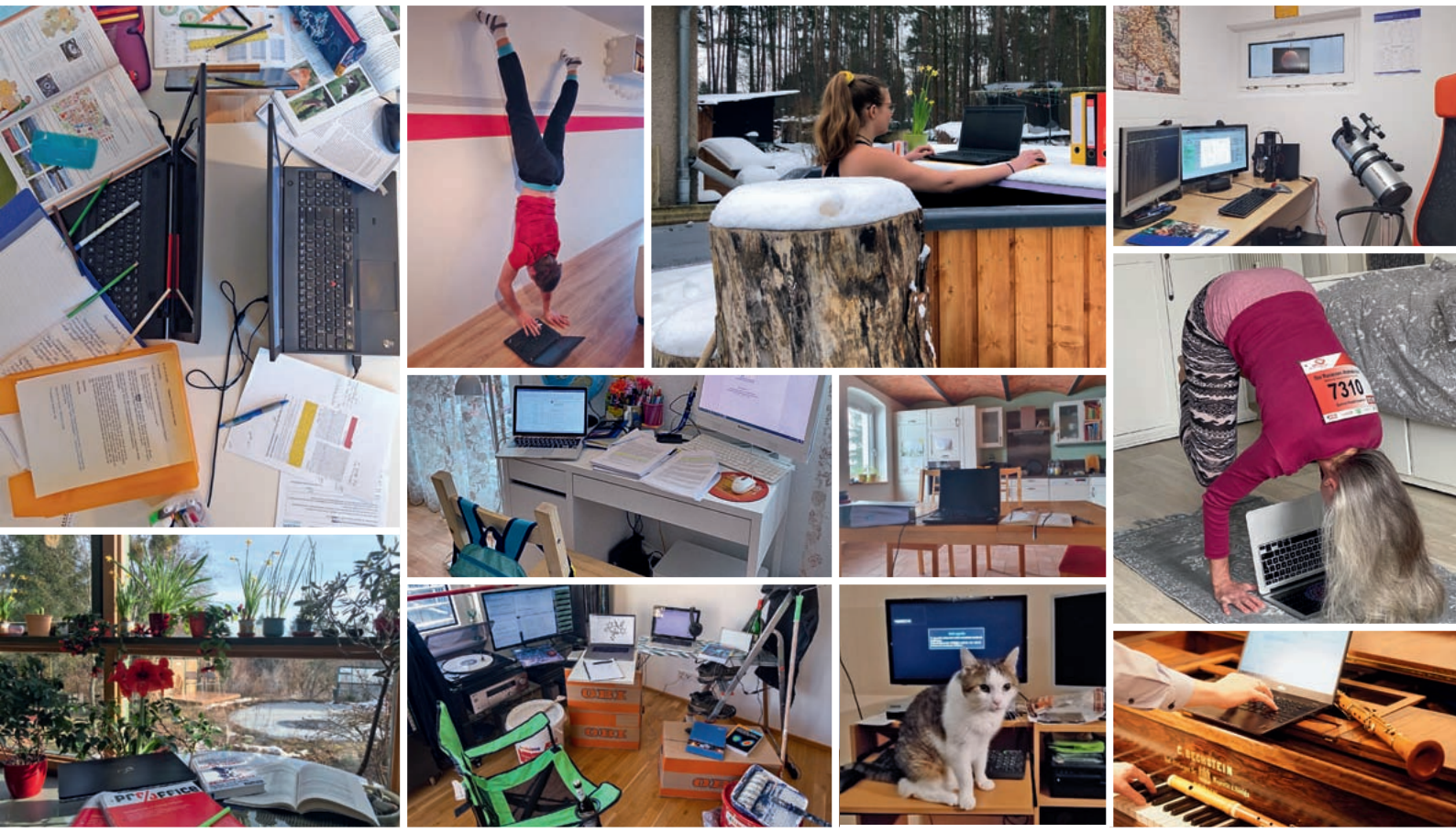

Wissenschaftlich-Technische Berichte
HZDR-113 2021 . ISSN 2191-8708

HELMHOLTZ ZENTRUM
DRESDEN ROSSENDORF

Wissenschaftlich-Technische Berichte
HZDR-113

Annual Report 2020

Institute of Resource Ecology

HELMHOLTZ ZENTRUM
DRESDEN ROSSENDORF

Impressum

Print edition: ISSN 2191-8708
Electronic edition: ISSN 2191-8716

https://www.hzdr.de/publications/Publ-32278
https://nbn-resolving.org/urn:nbn:de:bsz:d120-qucosa2-741305

Published by Helmholtz-Zentrum Dresden–Rossendorf e.V.

Contact

Helmholtz-Zentrum Dresden–Rossendorf e.V.
Institute of Resource Ecology
Bautzner Landstraße 400
D-01328 Dresden
Germany

Phone: +49 (0) 351 260 3210
Fax: +49 (0) 351 260 3553
e-mail: contact.resourceecology@hzdr.de
https://www.hzdr.de/fwo

This report is also available at https://www.hzdr.de/fwo

Cover pictures

How the Institute of Resource Ecology was kept running from home in 2020 due to pandemic restrictions — Impressions

Photos provided by: D. Abbasova, S. Bachmann, R. Berndt, S. Beutner, F. Bok, M. Demnitz, E. Dräger, B. Drobot, C. Fischer, C. Franzen, R. Gericke, S. Gürtler, E. Krawczyk-Bärsch, K. Kurde, H. Moll, K. Müller, K. Nebe, J. Raff, A. Richter, Q. Roode-Gutzmer, R. Steudtner, M. Stockmann, T. Stumpf, W. Webersinke.

Preface

The Institute of Resource Ecology (IRE) is one of the eight institutes of the Helmholtz-Zentrum Dresden–Rossendorf (HZDR). Our research activities are mainly integrated into the program "Nuclear Waste Management, Safety and Radiation Research (NUSAFE)" of the Helmholtz Association (HGF) and focused on the topics "Safety of Nuclear Waste Disposal" and "Safety Research for Nuclear Reactors". The program NUSAFE, and therefore all work which is done at IRE, belong to the research field "Energy" of the HGF.

Our research objective is the protection of humans and the environment from the effects of radioactive radiation. To this end, we create a molecular process understanding using the most modern methods of spectroscopy, microscopy, diffraction, numerical simulation and theoretical chemistry. This takes place in a unique research environment at the HZDR. Our interdisciplinary approach combines radiochemistry, geosciences, and biosciences as well as materials science and reactor physics. This generates knowledge with application in particular for reactor and repository safety as well as in radioecology.

In 2020, the Corona pandemic made our work much more difficult. The laboratories were closed for several weeks and nearly no direct scientific exchange with collaborators, partners, and friends was possible. To my surprise, this had no influence on our scientific outcome. In 2020, 108 original papers were published in peer-reviewed international scientific journals with an average impact factor of 5.77. The extraordinary broadness of research topics and activities is illustrated below by some selected highlights.

Data of a start-up experiment at the Chinese Experimental Fast Reactor (CEFR) provided within an IAEA coordinated research project have been used for post-test calculations by means of the continuous energy Monte Carlo code SERPENT2. Beside the excellent agreement between calculation and measurement data, this activity demonstrates the feasibility to routinely conduct time-dependent simulations, an area which until recently was limited to deterministic methods. In general, due to the more accurate interaction physics combined with practically unlimited geometric complexity, Monte Carlo codes have a strong potential to produce high-fidelity reference solutions for the verification of deterministic codes, not just in static neutronic calculations as they are widely used so far, but also in time-dependent analyses (→ p. 81).

We investigated relations between calculated primary displacement damage, the irradiated nanostructure, and the nanoindentation response of ion-irridiated Fe-Cr alloys. Cross-sectional scanning transmission electron microscopy indicated the appearance of irradiation-induced dislocation loops and revealed their number density as a function of the distance from the irradiated surface. A model aimed at integrating the calculated local hardening contributions over the indentation plastic zone was calibrated using the measured nanoindentation response. The model allowed the effect of the implanted interstitials to be separated from the total hardening. The result is an important step towards improved transferability of ion irradiations to the case of much more expensive neutron irradiations, where implanted interstitials do not appear (→ p. 73).

Within the framework of both the GRaZ joint project (BMWi) and the EURAD CORI project (EURATOM) investigations on the U(VI)-Citrate system were performed. Remaining unnoticed for over 70 years of intensive research until recently, complexes of a so-called sandwich structure were characterized combining NMR spectroscopy, especially of rarely applied ^{17}O, ^{23}Na, and ^{139}La nuclei, and DFT calculation. As these species remain soluble in pH neutral media even at high U concentrations, the results are vital for understanding uranium's versatile coordination chemistry as well as environmental migration behavior (→ p. 16).

Molecular diffusion is the prevailing mechanism for radionuclide transport within clay-rich rocks. Current reactive transport modeling (RTM) applies a simplified parametrization of the effective diffusivity for simulating migration in host rocks such as the Opalinus clay. This prevents to model the heterogeneous diffusion behavior currently identified by using positron emission tomography (GeoPET) measurements, based on Na-22 as a conservative tracer for long-term transport experiments (→ p. 43). To improve the predictive capabilities of RTM, we developed an upscaling workflow that integrates nm- and μm-scale simulations based on synthetic multiscale digital rocks for the prediction of the effective diffusivity of radionuclides (→ p. 40). Both the spatial variability of the pore network and the compositional heterogeneities at the pore scale are now available for studying heterogeneous diffusion patterns, in contrast to commonly assumed homogeneous behavior.

The mechanism of isotope-dependent hydrogen permeability of graphene membranes has been controversially discussed during the past few years. We confirm in a theoretical study (→ p. 46) that ideal graphene is quasi-impermeable to protons, yet the most common defect in sp2 carbons, the topological Stone–Wales defect, has an H^+-over-D^+ selectivity explaining all experimental results on graphene membranes that are available to date, thus challenging local hydrogenation as the competing explanation.

The investigations of basic properties of actinides were expanded to include a series of ligands with soft N-donor functions. (→ p. 21). Particularly noteworthy is a work that combines theory and experiment in order to elucidate the binding relationships in actinide complexes with the PEBA ligand. As expected, the proportion of covalent bonds increases significantly with the occurrence of f-electrons in Pa(IV). Almost identical covalencies are found for U(IV), Np(IV), and Pu(IV), but the origin of this covalency shifts from a strong d-character for uranium to a stronger f-character for plutonium (→ p. 22).

Proteomics studies were conducted this year to investigate the interaction of uranium with *Nicotiana tabacum* (tobacco) cells to understand how radionuclides migrate in the biosphere and through the food chain on a molecular level. First results elucidated an increase in the glutathione (GSH) metabolism of these cells in the presence of uranium. This confirmed the initiation of GSH-mediated sequestration upon uranium exposure to plant cells as part of the cellular response to the heavy metal stress (→ p. 55).

The European Synchrotron Radiation Facility opened its new 4th generation electron storage ring for user operation in 2020, and with it our newly constructed Rossendorf Beamline (ROBL). Three experimental stations, the 5-crystal spec-

trometer for high-energy-resolution X-ray absorption and emission spectroscopy, the Pilatus 2M diffractometer for single-crystal and *in situ* diffraction, and the EXAFS station with the world's first multielement Ge detector with CUBE amplifiers and unprecedented detection limit, have accomplished the first successful user experiments; the 6-circle Huber diffractometer for surface and high-resolution powder diffraction has been delivered and is currently under commissioning. The combination of different synchrotron-based X-ray techniques, which are now available at ROBL, has proven vital to elucidate the plutonium oxidation state and structure of PuO_2 nanoparticles, which was hitherto heavily debated in the scientific literature (→ p. 13).

Beside these highlights, we obtained many other new scientific results in the past year, which are presented in this annual report.

In the last year, more than 170 scientists, technicians, and students working on their Ph.D., diploma, master, or bachelor theses, were employed at the Institute of Resource Ecology. Thereof, 39 Ph.D. students worked at the institute in 2020.

As an important event in 2020, the international workshop entitled "How to integrate geochemistry at affordable costs into reactive transport for large-scale systems" was organized by the institute on February 5–7. Besides many interesting scientific talks and poster presentations, four excellent keynote talks were presented. In total, 40 scientists from 28 research institutes and eight countries extensively discussed advanced numerical concepts in geochemistry (→ p. 103).

Furthermore, the annual meeting of HGF and BMBF funded interdisciplinary project iCross (Integrity of nuclear waste repository systems - Cross-scale system understanding and analysis) was organized fully virtual from November 25–26. More than 70 participants from HZDR, KIT, FZJ, UFZ and GFZ and invited guests from ministries, federal agencies and universities discussed in detail studies performed on laboratory scale and in the underground research laboratory Mont Terri (CH) as well as modern modeling approaches.

In 2020, funding to implement "Hover" – a decentralized research infrastructure was finally approved. Located at KIT, FZJ, and HZDR, it is dedicated to enable new and to support existing advanced scientific investigations and technical developments in the context of the phase out of nuclear energy within the German 'Energiewende' project. At HZDR, a radiotechnicum will permit comprehensive, host rock-independent investigations as necessary due to the long-time scales expected until a final decision on the siting of a nuclear waste repository in Germany will be made. The radiotechnicum will offer the facilities for experimental investigations of bio/geo/radiochemical processes on larger scales up to the mesoscale. Furthermore, Hover will be the seed crystal for a new controlled area building, which will replace the old radiochemical laboratories.

In 2020, the scientific director as well as the administrative director at HZDR changed. Prof. Dr. Sebastian M. Schmidt took over the position of the scientific director from Prof. Sauerbrey, who retired. We thank Prof. Sauerbrey for his strong support and wish him all the best for the new phase of life. Furthermore, at the end of the year, Dr. Diana Stiller took on the position of the administrative director. We are looking forward to a successful and trustful collaboration in the future.

In retrospect of a challenging but at the end successful year, I would like to thank the (unfortunately only a few) visitors, German and international ones, for their interest in our research and for their participation in the institute seminars. Although it was very limited in 2020, we will continue to strongly encourage the collaborations and visits by scientists in the future. Special thanks are due to the executive board of the HZDR, the Ministry of Science and Arts of the Free State Saxony (SMWK), the Federal Ministry of Education and Research (BMBF), the Federal Ministry of Economic Affairs and Energy (BMWi), the Deutsche Forschungsgemeinschaft (DFG), the European Commission, and other organizations for their support.

Prof. Dr. Thorsten Stumpf
Director of the
Institute of Resource Ecology

Contents

SCIENTIFIC CONTRIBUTIONS

Part I: The Chemistry of Long-Lived Radionuclides

All roads lead to PuO_2 nanoparticles 13
E. Gerber, A. Y. Romanchuk, I. Pidchenko, L. Amidani, A. Rossberg, C. Hennig, G. B. M. Vaughan, A. Trigub, T. Egorova, S. Bauters, T. V. Plakhova, M. O. J. Y. Hunault, S. Weiss, S. M. Butorin, A. C. Scheinost, S. N. Kalmykov, K. O. Kvashnina

Accurate structural characterization of ThO_2 nanoparticles with HEXS and HERFD-XANES 14
L. Amidani, G. B. M. Vaughan, T. V. Plakhova, A. Y. Romanchuk, E. Gerber, S. Weiss, S. N. Kalmykov, K. O. Kvashnina

Single-step, high pressure, and two-step spark plasma sintering of UO_2 nanopowders 15
E. De Bona, L. Balice, L. Cognini, M. Holzhäuser, K. Popa, O. Walter, M. Cologna, D. Prieur, T. Wiss, G. Baldinozzi

Trimeric uranyl(VI)–citrate sandwiches Na^+, Ca^{2+}, and La^{3+} in aqueous solution 16
J. Kretzschmar, S. Tsushima, B. Drobot, R. Steudtner, K. Schmeide, T. Stumpf

Pu(III)-malate complexation study using isothermal micro-titration calorimetry 17
M. Acker, F. Taube, S. Taut, S. Shams Aldin Azzam, S. Weiss, N. Huittinen, H. Foerstendorf

Low-valent plutonium precursor compounds for metal-organic complexes 18
S. Fichter, J. März

Covalency in actinide bonding: trends in Th−Pu monosalen complexes 19
T. Radoske, M. Patzschke, M. Schmidt, T. Stumpf, J. März

Mononuclear actinide (UO_2^{2+}, U^{4+}, Th^{4+}, Np^{4+}) complexes with a new Schiff base ligand 20
D. Bansal, M. Patzschke, P. Kaden, M. Schmidt

Ion size-driven change of coordination environments in *bis*-pyrophen complexes 21
L. Köhler, T. Stumpf, J. März

Understanding covalency in tetravalent actinide amidinates 22
R. Kloditz, S. Fichter, J. März, M. Patzschke, M. Schmidt

Following up on $ThSiO_4$ synthesis by *in situ* SWAXS measurements 23
P. Estevenon, J. Causse, S. Szenknect, E. Welcomme, A. Mesbah, P. Moisy, C. Poinssot, N. Dacheux

High-energy-resolution X-ray spectroscopy studies on Th compounds at the Th L_3 and L_1 edges 24
J. Galanzew, S. Weiss, L. Amidani, A. Ikeda-Ohno, J. März, A. Beck, D. Schild, S. M. Butorin, T. Vitova, K. O. Kvashnina

Combining *ab-initio* multiple scattering (FEFF) calculations with Fourier filtering: eased derivation and validation of EXAFS structural models 25
A. Rossberg

Signatures of technetium oxidation states: a new approach 26
S. Bauters, A. C. Scheinost, K. Schmeide, S. Weiss, K. Dardenne, J. Rothe, N. Mayordomo, R. Steudtner, T. Stumpf, U. Abram, S. M. Butorin, K. O. Kvashnina

Implementation of a 'Rolling Ball' algorithm for spectroscopy 27
B. Drobot, M. Vogel, R. Steudtner, A. Rossberg, H. Foerstendorf

Electrochemical synthesis of aqueous Pu stock solutions in chloride media 28
N. Huittinen, S. Shams Aldin Azzam, S. Weiss, H. Foerstendorf

Part II: Long-Lived Radionuclides & Transport Phenomena in Geological Systems

Sorption of curium(III) on crystalline rock material 31
M. Demnitz, K. Molodtsov, S. Schymura, A. Schierz, K. Müller, M. Schmidt

Development of a generic surface complexation model for the sorption of trivalent actinides and lanthanides on orthoclase 32
H. Brinkmann, J. Neumann, S. Britz, J. Lützenkirchen, F. Bok, M. Stockmann, V. Brendler, T. Stumpf, M. Schmidt

First sorption results of Np(V) on ZrO_2 33
I. Jessat, H. Foerstendorf, N. Jordan

Effect of background electrolyte composition on the formation of Th(IV) nanoparticles on the muscovite (001) basal plane 34
J. Neumann, C. Qiu, P. Eng, S. Skanthakumar, L. Soderholm, T. Stumpf, M. Schmidt

Tc removal by Sn and Mn pre-sorbed on alumina 35
N. Mayordomo, T. Füssel, D. M. Rodríguez, K. Müller

New insights on the reductive immobilization of ^{99}Tc(VII) by iron sulfide 36
D. M. Rodríguez, N. Mayordomo, D. Schild, V. Brendler, K. Müller, T. Stumpf

Heterogeneous sorption of radionuclides predicted by crystal surface nanoroughness 37
T. Yuan, S. Schymura, T. Bollermann, K. Molodtsov, P. Chekhonin, M. Schmidt, T. Stumpf, C. Fischer

PET imaging of actinide analogue transport and retention through fractured crystalline rock 38
S. Schymura, F. Jankovsky, M. Zuna, T. Frühwirt, A. Mansel, K. Franke, J. Kulenkampff

Site-specific crystal surface reactivity 39
T. Bollermann, C. Fischer

Effective diffusivity prediction of radionuclides in clay formations using an integrated upscaling workflow 40
T. Yuan, C. Fischer

Combined μCT and MIP porosity measurements for identification of transport pathway distributions in salt rocks 41
J. Kulenkampff, T. Wilsnack

PET transport experiments under confining pressure 42
J. Kulenkampff, S. Gruhne, D. Lösel

Production of ^{22}Na by the non-common nuclear reaction ^{nat}Mg(d,α) and purification of ^{22}Na for investigations with GeoPET 43
A. Mansel, T. Bollermann, J. Kulenkampff, K. Franke

First-time production of Nb-92m/95 at the cyclotron Cyclone 18/9 in Leipzig 44
K. Franke

Metal dissociation from humic colloids: kinetics with time-dependent rate constants 45
H. Lippold, L. Zedek

Stone–Wales defects cause high proton permeability and isotope selectivity of single-layer graphene 46
Y. An, A. F. Oliveira, T. Brumme, A. Kuc, T. Heine

Size dependence of lattice parameter and electronic structure in CeO_2 47
D. Prieur, W. Bonani, K. Popa, O. Walter, K. W. Kriegsman, M. H. Engelhard, X. Guo, R. Eloirdi, T. Gouder, A. Beck, T. Vitova, A. C. Scheinost, K. O. Kvashnina, P. Martin

Isotopic dual-radiolabeling of CeO_2 nanoparticles for uptake and dissolution studies 48
S. Schymura, I. Rybkin, T. Rijavec, A. Mansel, A. Lapanje, K. Franke, M. Strok

Uncertainty explorations in the context of nuclear waste management 49
S. Pospiech, V. Brendler

Implementation of the smart K_d-concept in the reactive transport code OpenGeoSys (OGS-6) 50
M. Stockmann, R. Lu, V. Brendler

Thermodynamic reference database THEREDA: 10. The cumulative 2020 data release and major developments 51
F. Bok, A. Richter, J. Sohr, W. Voigt

Part III: Long-Lived Radionuclides in Biological Systems

Proteomics confirms initiation of glutathione-mediated sequestration upon uranium exposure to tobacco (*Nicotiana tabacum*) BY-2 cells 55
W. A. John, N. Matschiavelli, D. Thieme, W. Hoehenwarter, S. Sachs

Do carotenoids quench uranium(VI) luminescence in TRLFS spectra of plant cells? 56
J. Jessat, M.-L. Bilke, S. Sachs

Interactions of *Desulfosporosinus hippei* DSM8344 with Eu(III) 57
M. Puhlmann, S. Hilpmann, H. Moll, T. Stumpf, A. Cherkouk

Influence of fetal bovine serum and citrate on Eu speciation in cell culture medium 58
A. Heller, F. Bok, A. Barkleit

Lanthanide–dependent methanol dehydrogenase studied by computational chemistry 59
S. Tsushima

Interactions of *Brassica napus* callus cells with Eu(III) and U(VI) 60
H. Moll, W. A. John, S. Sachs

Evidence of uranium immobilization by *Magnetospirillum magneticum* AMB-1 under ambient conditions 61
J. Ramtke, R. Hübner, S. Kluge, E. Krawczyk-Bärsch

Microbially influenced corrosion of cast iron in different types of bentonite: microscopic investigation 62
V. Sushko, M. Dressler, N. Matschiavelli, A. Schierz, T. Stumpf, A. Cherkouk

Corrosion at the bentonite-cast iron interface under high-salt conditions with H_2 63
V. Sushko, T. Neubert, M. Löffler, B. Rellinghaus, A. Schierz, A. Cherkouk, N. Matschiavelli

When the biofilm on materials is needed: biofilm formation after electrostatically attachment of films of living bacterial cells 64
D. Deev, I. Rybkin, T. Rijavec, A. Lapanje

The lab lysimeter – an application for biogeochemical research with radionuclides 65
A. Günther, J. Raff

Liquid light guide technology augments use of small economical detectors in liquid scintillation counting 66
S. Stalke, R. Steudtner, K. Grossmann

Part IV: Nuclear Reactor Safety Research

The dominant mechanisms for the formation of solute clusters in steels exposed to irradiation 69
F. Bergner

Use of the small punch test for the estimation of ductile-to-brittle transition temperature shift of irradiated steels 70
E. Altstadt, F. Bergner, M. Houska

Microstructural characterization of inhomogeneity in 9Cr ODS EUROFER steel 71
P. Chekhonin, A. Das, E. Altstadt, F. Bergner, C. Kaden

Microstructure and fracture toughness characterization of three 9Cr ODS EUROFER steels with different thermo-mechanical treatments 72
A. Das, P. Chekhonin, E. Altstadt, D. McClintock, F. Bergner, C. Kaden, R. Lindau

Relationships between primary radiation damage, irradiation-induced microstructure and hardening of ion-irradiated Fe-Cr and ODS Fe-Cr alloys 73
K. Vogel, C. Kaden, P. Chekhonin, F. Bergner

Vacancy-solute clustering in Fe-Cr alloys after neutron irradiation 74
A. Ulbricht, M. J. Konstantinovic

Characterization of the porous network structure of concrete 75
Q. I. Roode-Gutzmer, J. Kulenkampff

Volume expansion of quartz aggregate in ion-irradiated concrete 76
Q. I. Roode-Gutzmer, S. Schymura, H. Lippold

Microscopic characterization of un-irradiated and irradiated steel shielding material of a nuclear power plant 77
G. Yassin, A. Barkleit, V. Brendler

Neutron fluence calculations and validation based on metal foils placed inside a German PWR 78
R. Rachamin, J. Konheiser, A. Barkleit

Coupled thermal hydraulic and neutronic simulations of the ESFR-SMART core 79
E. Nikitin, E. Fridman

Validation of a CFD simulation against a ROCOM mixing experiment 80
A. Grahn, E. Diaz Pescador, S. Kliem, F. Schäfer, T. Höhne

Validation of McSAFE simulation tools 81
Y. Bilodid, S. Kliem, A. Gommlich

Assessment of ATHLET heat transfer models by comparison to steam condensation experiments performed at the COSMEA test rig 82
M. Jobst

Investigations on the multiscale and multi-physics dynamic behavior of German PWRs during reactivity accidents 83
E. Diaz Pescador, F. Schäfer, Y. Bilodid, S. Kliem

Extension of ATHLET/DYN3D to SFRs: Verification against DYN3D on the Phénix reactor core 84
V. A. Di Nora

New developments of the Monte Carlo code TRAMO and their validations on experiments of Russian VVER-1000 reactor equipment 85
S. Baier, J. Konheiser, P. Borodkin

Development of a generally usable weight window generator using the TRAWEI code 86
P. Yadav, R. Rachamin, J. Konheiser, S. Baier

PUBLICATIONS

- Articles (peer-reviewed) 89
- Editorial Work 95
- Further Contributions 96
- Patent 96
- Oral Presentations 96
- Theses 98

SCIENTIFIC ACTIVITIES

- International Workshop on "How to integrate geochemistry at affordable costs into reactive transport for large-scale systems" 103
- Seminars (Talks of Visitors) 104
- Teaching Activities 104

PERSONNEL 107

ACKNOWLEDGEMENTS 113

INDEX OF AUTHORS 118

The Chemistry of

LONG-LIVED RADIONUCLIDES

All roads lead to PuO_2 nanoparticles

E. Gerber, A. Y. Romanchuk,[1] I. Pidchenko, L. Amidani, A. Rossberg, C. Hennig, G. B. M. Vaughan,[2] A. Trigub,[3] T. Egorova,[1] S. Bauters, T. V. Plakhova,[3] M. O. J. Y. Hunault,[4] S. Weiss, S. M. Butorin,[5] A. C. Scheinost, S. N. Kalmykov,[1,3] K. O. Kvashnina

[1]Lomonosov Moscow State University, Department of Chemistry, Moscow, Russia; [2]ESRF – The European Synchrotron, Grenoble, France; [3]National Research Centre "Kurchatov Institute", Moscow, Russia; [4]Synchrotron SOLEIL, France; [5]Molecular and Condensed Matter Physics, Uppsala University, Uppsala, Sweden

Here, we report a full characterization of PuO_2 nanoparticles (NPs) at the atomic level and probe their local and electronic structure by a variety of synchrotron methods. Well dispersed, crystalline NPs with a size of ~2.5 nm in diameter are always formed in spite of varying synthesis conditions. Identical crystal structures and the presence of only the Pu(IV) oxidation state in all NPs were confirmed.[1]

Plutonium can migrate in colloidal form in the subsurface environment across several kilometers.[2,3] Recent spectroscopic and microscopic investigations showed that so called "colloidal Pu(IV) polymers" are in fact aggregates of PuO_2 nanoparticles,[4,5] however, the exact stoichiometry and structure of such nanoparticles remain still questionable as well as the purity of the tetravalent oxidation state. In this study, the synthesized PuO_2 NPs are characterized by a variety of experimental methods: High-Resolution Transmission Electron Microscopy (HRTEM), Selected-Area Electron Diffraction (SAED), Extended X-Ray Absorption Fine Structure (EXAFS), X-ray Absorption Near Edge Structure (XANES) in High Energy Resolution Fluorescence Detection (HERFD) mode, High Energy X-ray Scattering (HEXS) and X-ray Diffraction (XRD).

EXPERIMENTAL. The nanoparticles were synthesized from precursors with different oxidation states of plutonium (III, IV, and V) under various environmentally and waste storage relevant conditions (pH 8 and pH>10). The Pu L_3 HERFD and EXAFS experiments as well as XRD measurements were performed at The Rossendorf Beamline at ESRF.[6] The HERFD spectra (except one) at the Pu M_4 edge were collected at Beamline ID26 of ESRF. High energy X-ray scattering data were collected at room temperature at the ID15A beamline of the ESRF.

RESULTS. It was found that similar non-amorphous NPs are formed, regardless of different precursors and pH conditions. The crystalline structure of the NPs is similar to that of bulk PuO_2. The particle size varies in the range of 2.3–3.2 nm. Pu oxidation state in the PuO_2 NPs turns out to be exclusively Pu(IV), as proven here by HERFD methods at L_3 and M_4 edges in Fig. 1. The EXAFS spectra (Fig. 2) show effects of increased static disorder and reduced coordination numbers, which are clear influences of the nanometer-size of the particles, without the need to invoke different Pu oxidation states or a substantially different structure. Finally, the agreement among the results from the EXAFS shell fit, MC EXAFS simulations (Fig. 2), and from HEXS all unequivocally indicate that only one Pu(IV)-O interaction with a rather symmetric distance distribution (similar to the PuO_2 reference) is present for all six PuO_2 NPs samples.

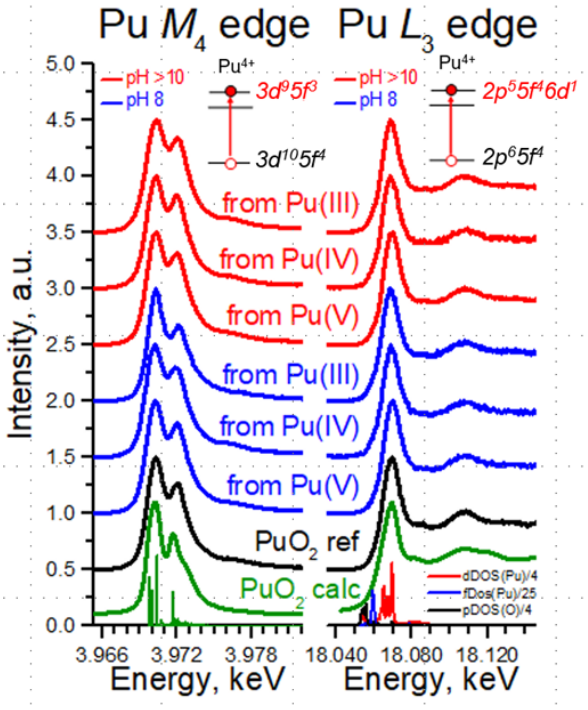

Fig. 1: Pu M_4 and L_3 HERFD experimental data. Data recorded for six PuO_2 NPs samples and compared with a PuO_2 reference and theoretical calculations, using AIM approximation (left) and FEFF code (right). The density of states is plotted at the bottom for clarity.

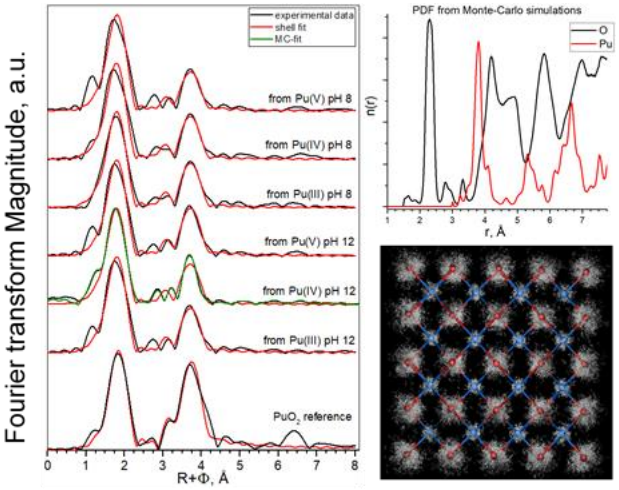

Fig. 2: Pu L_3-EXAFS spectra χ(R) fit results, Fourier transform (FT) magnitude of experimental EXAFS data (black) and a one Pu-O, one Pu-Pu shell fit (red), Monte-Carlo simulations fit (green). The area of the shell fit in R-space is marked with two dashed lines, MC simulation output: radial particle distribution function (n(r)) for Pu-O and Pu-Pu and 3D structural refinement based on bulk PuO_2 starting structure.

[1] Gerber, E. *et al.* (2020) *Nanoscale* **12**, 18039–18048.
[2] Kersting, A. *et al.* (1999) *Nature* **397**, 56–59.
[3] Novikov, A. *et al.* (206) *Science* **314**, 638–642.
[4] Powell, B. *et al.* (2011) *Environ. Sci. Technol.* **45**, 2698–2703.
[5] Romanchuk, A. *et al.* (2018) *Dalton Trans.* **47**, 11239–11244.
[6] Kvashnina, K. *et al.* (2016) *J. Synchrotron Radiat.* **23**, 836–841.

Accurate structural characterization of ThO_2 nanoparticles with HEXS and HERFD-XANES

L. Amidani, G. B. M. Vaughan,[1] T. V. Plakhova,[2] A. Y. Romanchuk,[2] E. Gerber, S. Weiss, S. N. Kalmykov,[2] K. O. Kvashnina

[1]ESRF – The European Synchrotron Radiation Facility, Grenoble, France; [2]Lomonosov Moscow State University, Department of Chemistry, Moscow, Russia

An accurate characterization of the structure of nanoparticles (NPs) is often very hard to achieve, especially for non-homogeneous samples and NPs < 3 nm in diameter. By combining High-Energy X-ray Scattering (HEXS) and High-Energy-Resolution Fluorescence-Detected X-ray Absorption Near-Edge Structure (HERFD-XANES) spectroscopy, we characterized both the short- and medium-range structure of ThO_2 NPs obtained by chemical precipitation. The initial stage of NPs formation shows a high concentration of Th units similar to Th hexamer clusters. With annealing, the average size of NPs grows and the Th clusters disappear.

The formation mechanism, reactivity, and environmental interaction of actinide nanoparticles is of substantial concern, but still poorly understood. Especially the accurate structural characterization of NPs is fundamental and not trivial, especially when NP size is < 3 nm and samples are not homogeneous. The case of ThO_2 NP formation by chemical precipitation shows the importance of accurate structural characterization: many reports found that NP formation proceeds *via* an intermediate amorphous phase,[1] while other reported the direct formation of crystalline ThO_2 NPs of size < 5 nm.[2] The key to correctly address the problem is to measure both short- and medium-range structural order to characterize the relevant length scales of the system. To this purpose, we measured HEXS and HERFD XANES at Th M_4 edge.[3] The pair distribution function (PDF) extracted from HEXS probes both medium- and long-range order, while HERFD XANES probes the local environment of Th atoms.

EXPERIMENTAL. ThO_2 NPs of different sizes were synthesized by sequential heat treatment of freshly precipitated Th^{IV} samples. Characterization with XRD and HRTEM shows the presence of NPs <3 nm in freshly precipitated samples and of NPs of increasing size with annealing at increasing temperature. HEXS and Th M_4 HERFD XANES were measured on ID15A and ID26 beamlines at the ESRF.

RESULTS. The PDF of bulk ThO_2, 150 °C annealed and 40 °C dried Th^{IV} samples shows a progressive decrease of size (Fig. 1a). A fit based on NPs of different size allowed determination of the NP distribution in each sample. The 40 °C dried sample contains a large amount of Th clusters similar to reported Th hexamers (60 %), while mild annealing at 150 °C promotes recrystallization to bigger NPs and the disappearance of Th hexamers (see fit component legend in Fig. 1a). Th M_4 edge HERFD XANES of the 1200 °C sample (Fig. 1b) shows four characteristic peaks, labelled A–D. The 40 °C samples only show A and B and this change can be correlated to reduced size. Because M_4 edge XANES probes the Th f-orbitals, the spectrum can be interpreted based on the Th f-density of states (DOS), as shown in the inset of Fig. 1b, where simulated f-DOS of bulk ThO_2 and of Th hexamer from literature are shown below experimental data. The disappearance of feature C is well reproduced by the simulations, confirming that changes in the spectral shape are correlated to the presence of Th hexamers, for which Th local structure differs from that in bulk ThO_2.

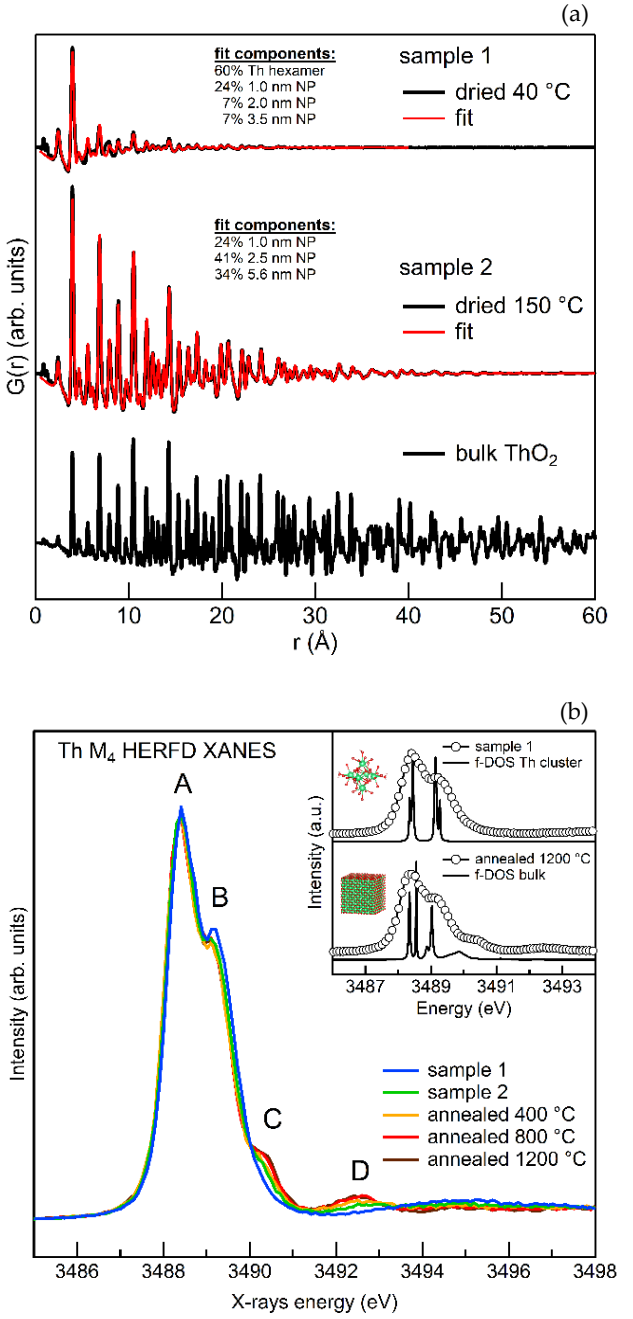

Fig. 1: PDFs of bulk ThO_2, on 150 °C annealed and 40 °C dried Th^{IV} precipitates. Fit results are shown in red on top of data and the resulting size distribution indicated in the text box (a). Experimental Th M_4 HERFD XANES in the main panel. Inset reports the comparison of spectra on 1200 °C annealed and 40 °C dried samples with simulated f-DOS of bulk ThO_2 and Th hexamer (b).

[1] Rothe, J. *et al.* (2002) *Inorg. Chem.* **41**, 249–258.
[2] Plakhova, T. *et al.* (2019) *J. Phys. Chem. C* **123**, 23167–23176.
[3] Amidani, L. *et al.* (2021) *Chem. Eur. J.* **27**, 252–263.

Single-step, high pressure, and two-step spark plasma sintering of UO_2 nanopowders

E. De Bona,[1,2] L. Balice,[2,3] L. Cognini,[2,4] M. Holzhäuser,[2] K. Popa,[2] O. Walter,[2] M. Cologna,[2] D. Prieur, T. Wiss,[2] G. Baldinozzi[1]

[1]Laboratoire Structures, Propriétés et Modélisation des Solides, CNRS, CentraleSupélec, Université Paris-Saclay, Gif-sur-Yvette, France; [2]Joint Research Centre, European Commission, Karlsruhe, Germany; [3]Université Grenoble Alpes, Saint-Martin-d'Hères, France; [4]Politecnico di Milano, Department of Energy, Nuclear Engineering Division, Milano, Italy

Highly sinter-active UO_{2+x} nanopowders were densified using three different Spark Plasma Sintering (SPS) treatments. For the first time, a two-step method was adopted in SPS (2S-SPS), and its outcome was compared with the more established single-step (SPS) and high-pressure SPS (HP-SPS). The 2S-SPS and HP-SPS treatments were optimized to limit coarsening while reaching the same density as in SPS. Such samples can be extremely helpful to study the effect of grain size on nuclear fuel properties (such as its oxidation behavior).

SPS is a field assisted sintering technique (FAST) that enables powder densification at relatively low sintering temperatures and hold times with respect to conventional sintering.[1] The powder is loaded into a graphite assembly (die and pistons), through which pulsed direct current is passed, quickly heating up the sample due to the Joule effect.[2] The graphite environment results in a reductive atmosphere above 600 °C that is beneficial for the processing of UO_{2+x} powders.[3] HP-SPS and 2S-SPS are two approaches that can be adopted to try to reduce the final grain size, in order to synthesize surrogate materials reproducing the spent nuclear fuel (SNF) high-burnup structure (HBS), which are characterized, among other features, by 100–300 nm grains.[4]
In HP-SPS, SiC inserts are added to the assembly, allowing the application of higher pressures through the pistons (500 MPa instead of 100 MPa), and thus providing extra driving force for densification (*i.e.* lowering the sintering temperature).[5,6]
Two-step sintering instead involves the quick firing of the sample to a relatively high temperature (T_1), and then a long hold time at a lower temperature (T_2) where densification is completed. Taking advantage of the different activation energies for grain boundary diffusion and grain boundary migration, with the correct choice of T_1 and T_2 densification can take place in the second step while grain growth is inhibited. For this to happen, the sample has to reach sufficient density in the first step (about 75 % TD).[7]

EXPERIMENTAL. Batches of roughly 1 g of UO_{2+x} powder were produced by loading 2 g of oxalate powder in an autoclave together with 5 mL of water and 0.5 mL of hydrazine, and heating up at 170 °C for 5 h under autogenic pressure.
The sintering treatments are summarized in Tab. 1. All samples were densified to 95 % of the theoretical density (95 % TD). The parameters reported for 2S-SPS and HP-SPS are already optimized to limit coarsening during densification.

Tab. 1: Processing parameters (sintering temperature, applied pressure, hold time, and heating rate) used in the SPS, 2S-SPS, and HP-SPS treatments.

SPS	2S-SPS	HP-SPS
1600 °C	650–550 °C	660 °C
70 MPa	70 MPa	500 MPa
10 min	3 s–100 min	30 s
200 °C/min	200 °C/min	100 °C/min

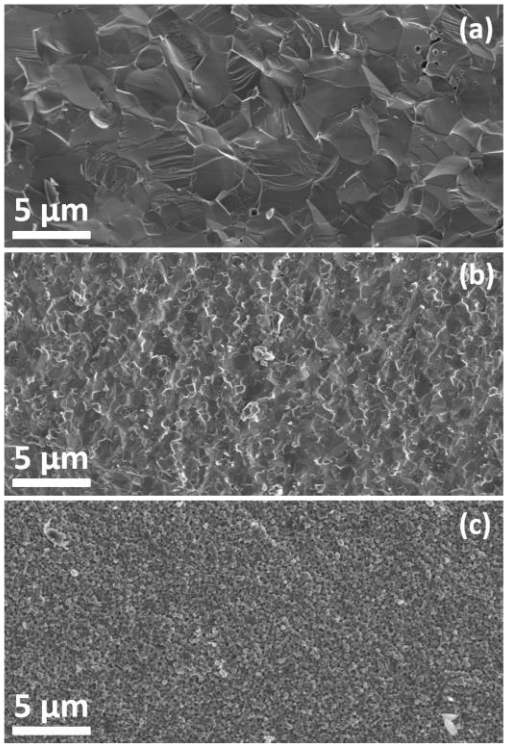

Fig. 1: SEM SE images of the microstructures obtained by applying SPS (a), 2S-SPS (b), and HP-SPS (c) treatments to the UO_{2+x} nanopowders. All samples have the same density (95 % TD) but differ significantly in grain size.

RESULTS. XRD characterization of the as-produced powder showed a lattice parameter of 5.464 ± 0.001 Å, indicating a stoichiometry of $UO_{2.04}$, and Williamson-Hall analysis returned a crystallite size of 5 ± 1 nm.
The microstructures obtained by applying the treatments summarized in Tab. 1 are shown in Fig. 1. The grain sizes calculated with the ASTM E112-12 intercept method[8] were: 3.08 ± 0.06 µm for the single-step SPS, 478 ± 17 nm for the 2S-SPS, and 163 ± 9 nm for the HP-SPS. Due to the presence of SiC components, the sample produced by HP-SPS was slightly hyperstoichiometric, and therefore required a supplementary annealing step at 600 °C under Ar-4 %H_2 for 2 h to be reduced to $UO_{2.00}$.
The microstructure obtained by HP-SPS is of extreme interest for the study of SNF properties, as it settles in the range of grain size of the HBS. On the other hand, the much simpler 2S-SPS setup (not involving additional SiC components) also proved to be a suitable route to produce UO_2 with relatively small final grain size. Such samples will be used for a study on the effect of grain size on the oxidation behavior of UO_2.

[1] Ge, L. *et al.* (2013) *J. Nucl. Mater.* **435**, 1–9.
[2] Cologna, M. (2020) in: *Comprehensive Nuclear Material*, p. 811–839, Elsevier, Amsterdam.
[3] Ge, L. *et al.* (2014) *J. Eur. Ceram. Soc.* **34**, 1791–1801.
[4] Noirot, J. *et al.* (2008) *J. Nucl. Mater.* **372**, 318–339.
[5] Tyrpekl, V. *et al.* (2017) *J. Am. Ceram. Soc.* **100**, 1269–1274.
[6] De Bona, E. *et al.* (2019) *J. Am. Ceram. Soc.* **102**, 3814–3818.
[7] Chen, I.-W. *et al.* (2000) *Nature* **404**, 168–171.
[8] ASTM E112–12 (2012) *Standard Test Methods for Determining Averaging Grain Size*, p. 1–27, ASTM International, West Conshohocken PA, U.S.A.

Trimeric uranyl(VI)–citrate sandwiches Na^+, Ca^{2+}, and La^{3+} in aqueous solution

J. Kretzschmar, S. Tsushima, B. Drobot, R. Steudtner, K. Schmeide, T. Stumpf

The uranyl(VI) oxygen atoms (O_{yl}) of two 3:3 uranyl(VI)–citrate complex molecules sandwich a sodium ion in single-crystals.[1] Nuclear magnetic resonance (NMR) spectroscopy supported by density functional (DFT) calculations provided unambiguous evidence for this U(VI)–O_{yl}–Na^+ Lewis acid–base adduct, persisting in aqueous solution above a critical concentration of 3 mM uranyl(VI) citrate. Coordination to O_{yl} is not limited to Na^+ only, but applies also to di- and even trivalent cations of comparable ionic *radii*. That is, Na^+, Ca^{2+}, and La^{3+} are sandwiched, while Li^+, K^+, and Rb^+ are not, with uranyl(VI)-oxo Lewis base coordination to aqueous Ca^{2+} and La^{3+} being unprecedented.

EXPERIMENTAL. Details of both sample preparation and quantum chemical calculation can be found in our recent paper.[2] Briefly, D_2O solutions of uranyl(VI) citrate, U(VI)-Cit, were prepared from stock solutions of uranyl(VI) nitrate and sodium citrate or citric acid. NaOD (for sodium containing samples, pD 6.9 ± 0.1) and LiOD were used for pD adjustment. The latter was used for sodium-free samples prepared in the presence of the following metal ions: $Li^+/K^+/Rb^+$ (pD 6.9 ± 0.1), Ca^{2+} (pD 5.4) or La^{3+} (pD 4.8). NMR spectra were obtained at 298 K on a 14.1 T Agilent DD2-600 NMR system using 5 mm quartz NMR tubes.

RESULTS. Formation of the 6:6 U(VI)-Cit Na^+ sandwich complex is evidenced by the observation of three distinct ^{23}Na NMR signals (Fig. 1A). The narrow signal at about 0 ppm corresponds to free Na^+ aquo ions (*aq*). As can be seen, two further distinct Na^+ sites are present, whose signals show remarkable upfield shifts. Upon coordination by six O_{yl} the sandwiched Na^+ (*s*) senses the strongest shielding, hence resonating at −25 ppm. The third signal shows a chemical shift (−9 ppm) with magnitude between those of the free and sandwiched Na^+. It is thus assigned to peripheral Na^+ (*p*) strongly localized at the highly negatively charged complex $[Na\{\eta^3\text{-}((UO_2)_3(\mu_3\text{-}O)(Cit)_3)\}_2]^{15-}$.

The well-resolved ^1H NMR resonances (Fig. 1B and D) are likewise characteristic for the sandwich complex as its conformation is fixed. That is, the particular arrangement prevents intramolecular site exchange of U(VI)-bound and free $-CH_2COO$ moieties whereupon the latter are kept in an all-*cis* conformation, *i.e.*, for either 3:3 sub-unit being on the same side of the molecular plane (Fig. 1E and F).

Based on dilution series (Fig. 1C and D) we found that above a critical concentration of 3 mM uranyl(VI) citrate at neutral pD conditions two units of the 3:3 complex form the sandwich superstructure. The spectral features associated with the Na^+ sandwich complex – ^{23}Na signals *p* and *s* as well as ^1H signals *a* through *d* – remain detectable until the sample concentration falls below 3 mM. As of this point, the sandwich complex falls apart in two 3:3 U(VI)-Cit units. Since the latter species reveals no steric demands on conformation, intramolecular dynamics facilitate easily, and the ^1H signals of the different $-CH_2COO$ moieties average to the unresolved feature *e* in Fig. 1D.

Based on both NMR spectroscopy and DFT calculations, a corresponding aqueous solution molecular model was derived respecting these three types of Na^+ (Fig. 1E).

Surprisingly, the sandwich superstructure forms also in the presence of other important Lewis acids such as Ca^{2+} and La^{3+} as inferred from the sharp ^1H signals obtained from sodium-free samples containing the nitrate salts of calcium or lanthanum (Fig. 1B). Interestingly, varying the nature of the present metal ions, only Na^+, Ca^{2+}, and La^{3+} with ionic radii of 1.02, 1.00, and 1.03 Å, respectively, match the sandwich cavity, while Li^+ (0.76 Å) is too small, and K^+ (1.38 Å) and Rb^+ (1.52 Å) are too large.

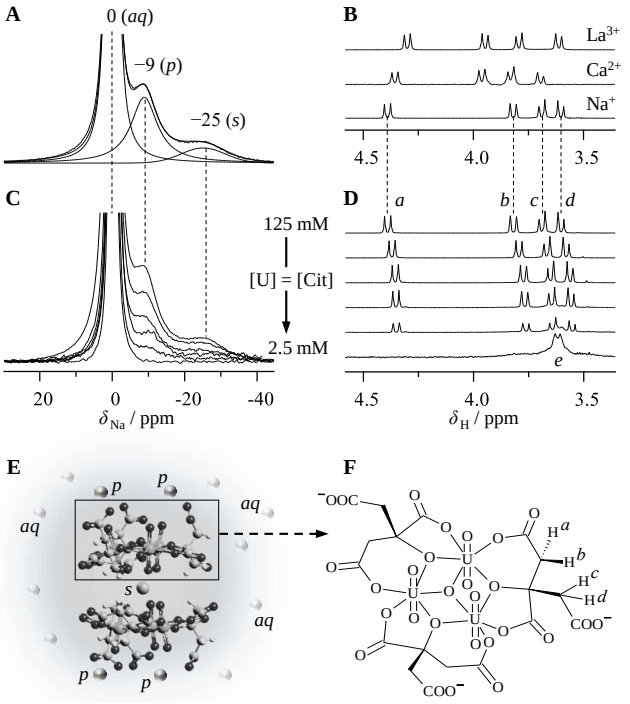

Fig. 1: Spectral deconvolution of the experimental ^{23}Na NMR spectrum obtained from the sample containing the 6:6 U(VI)-Cit Na^+ sandwich complex (A). ^1H NMR spectra associated with the 6:6 U(VI)-Cit sandwich complexes of Na^+, Ca^{2+}, and La^{3+}, respectively (B). ^{23}Na (C) and ^1H (D) NMR spectra of a dilution series; from top to bottom: [U] = [Cit] = 125, 25, 12.5, 6.2, 3.1, and 2.5 mM. Correspondingly derived aqueous solution molecular model of the Na^+ sandwich complex, respecting three types of sodium: aquo ion (*aq*), peripheral ions (*p*), and the sandwiched ion (*s*) (E). Generic structure of one of the sandwich complex' two constituting trimeric U(VI)-Cit species together with proton labelling used for ^1H NMR signal assignment (F).

ACKNOWLEDGEMENTS. This work was funded by the European Union's Horizon 2020 research and innovation programme (CORI project, no. 847593) as well as by the German Federal Ministry for Economic Affairs and Energy (BMWi) (GRaZ project, no. 02E11415B). The authors thank D. Goldbach for his support in the lab and S. Beutner for ICP-MS measurements.

[1] Basile, M. *et al.* (2015) *Chem. Commun.* **51**, 5306–5309.
[2] Kretzschmar, J. *et al.* (2020) *Chem. Commun.* **56**, 13133–13136.

Pu(III)-malate complexation study using isothermal micro-titration calorimetry

M. Acker,[1] F. Taube,[1,2] S. Taut,[1] S. Shams Aldin Azzam, S. Weiss, N. Huittinen, H. Foerstendorf

[1]Central Radionuclide Laboratory, TU Dresden; [2]Chair of Radiochemistry and Radioecology, TU Dresden, Germany

Isothermal micro-titration calorimetric (ITC) experiments of the complexation reaction between Pu(III) and malate were performed. Preliminary values of the complexation constant (β) and reaction enthalpy (ΔH) were determined.

Up to now, there is a lack of thermodynamic data for the interaction of trivalent plutonium with organic ligands, which are relevant for the long-term assessment of a potential high-level nuclear waste disposal. Malic acid (Mal), an α-hydroxycarboxylic acid, is a model ligand for complex organic matter like humic substances or concrete admixtures, that contains both hydroxyl and carboxyl groups. ITC permits the simultaneous determination of reaction enthalpies and stability constants in a single experiment at a given temperature and ionic strength. Micro-ITC is the method of choice for calorimetric experiments with actinides, as the radioactivity can be minimized owing to the very low required sample volume of ~200 µL.

EXPERIMENTAL. An aqueous Pu(III) solution (~3.6 mM , pH ~0.7) in chloride medium was adjusted to pH 3.95 by stepwise addition of aliquots of aq. NaOH (0.1, 1, and 5 M) under continuous electrolysis in an inert gas glove box. Ionic strength was adjusted to 0.6 m by addition of 67 µL of 6 m NaCl solution (pH 3.95) to 1 mL of the Pu(III) solution. Thus, the final Pu(III) concentration was 3.2 mM. For the ITC experiments (iTC_{200}, GE Healthcare), three aliquots (~300 µL) of the Pu(III) sample were titrated in 1 µL steps with solutions containing 73.1, 187.3, or 387.5 mM Mal and 6 m NaCl until pH 3.95 was reached. The ITC method and the data analysis are described elsewhere.[1] The oxidation state of Pu was controlled by UV-vis (Cary300, Agilent) after the sample preparation, and before and after the ITC experiments.

RESULTS. The Pu absorption spectra show pure Pu(III), described by the two characteristic bands between 575 and 625 nm and the weak band at 665 nm (Fig. 1).[2] Neither dissolved Pu(IV), which is mainly characterized by a strong absorption band at 470 nm,[2] nor Pu(IV) colloids were detected in the samples and no oxidation of Pu(III) to Pu(IV) occurred during the ITC experiments (Fig. 1).

The calorimetric heat curves of the Pu(III)-Mal titration (Fig. 2) are very similar to those of analogous experiments with Nd^{3+} and to the Am^{3+}/Nd^{3+}-ITC measurements in Taube *et al.* 2019.[1] All curves show two features with different slopes indicating more than one reaction. Based on the 1:1 and 1:2 complexation model, the heat curves were fitted using the program NITPIC-SEDPHAT.[1,3] Different parameter sets were evaluated. The best fits and most plausible results were obtained when fixing the value for ΔH_2. For this, we used the Nd(III) and Am(III) literature values (Tab. 1). The ΔH_1 of Nd(III)-Mal agrees with previous results,[1] ΔH_1 of Pu(III)-Mal is lower than the Am(III) and Nd(III) values. This could be explained by small differences of the inert salt concentration of the Mal titrant in comparison to the Pu(III) sample. At pH 3.95, the values of $\log\beta_1$ and $\log\beta_2$ are one and two orders of magnitude smaller than at pH 5.5, respectively, for both, Pu(III) and Nd(III) (Tab. 1). In analogy to previous ITC experiments of Am(III) complexation reactions, respective Pu(III) experiments are now feasible.

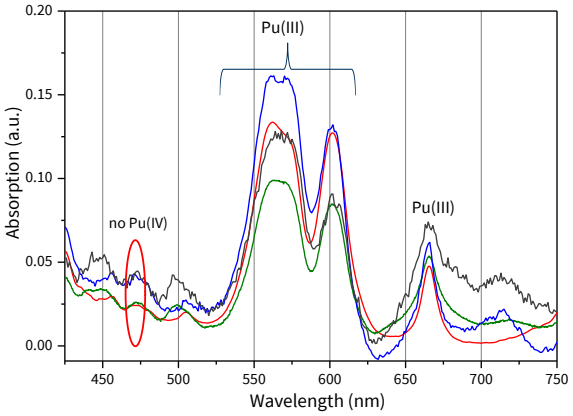

Fig. 1: Absorption spectra of Pu(III) samples at different times after sample preparation: 0 h (red), 4 h (after ITC-Exp. 1, green), 16 h (before ITC-Exp. 2, blue), and 19 h (after ITC-Exp. 2, black).

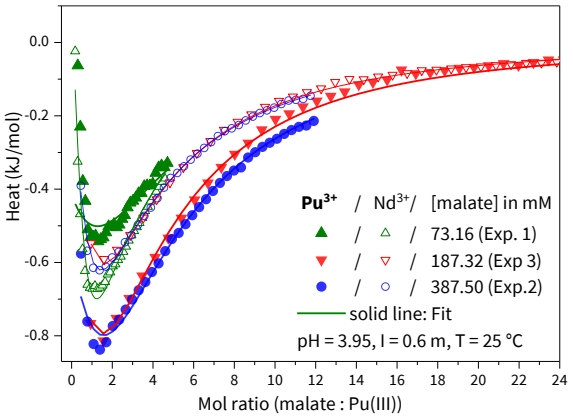

Fig. 2: Integrated calorimetric heat curves of the Pu(III)-Mal and analogue Nd(III)-Mal titration, $[Pu^{3+}]$ = 3.2 mM $[Nd^{3+}]$ = 3.1 mM; heat curves were corrected for the dilution heat of the Mal.

Tab. 1: Conditional thermodynamic data of $[Pu(Mal)_n]^{3-2n}$ (n = 1, 2) complexes at I = 0.6 m, compared with $[Am(Mal)_n]^{3-2n}$ and $[Nd(Mal)_n]^{3-2n}$.

Metal ion	$\log\beta_1$	ΔH_1 (kJ/mol)	$\log\beta_2$	ΔH_2 (kJ/mol)
Pu^{3+}	2.8±0.6	−1.3±0.6	4.5±0.9	−4 or −6 #
Nd^{3+}	3.0±0.4	−0.3±0.4	4.7±0.2	−4 #
Am^{3+} *[1]	3.9±0.1	−0.4±0.2	6.6±0.1	−6±1
Nd^{3+} *[1]	3.8±0.8	0.1±0.2	6.3±1.4	−4±2

error: 2σ value, #: fixed value, *: I = 0.65 m, pH 5.5.

ACKNOWLEDGEMENTS. This work was funded by the German Ministry of Economic Affairs and Energy under the grants 02E11451G within the GRaZ project.

[1] Taube, F. *et al.* (2019) *Inorg. Chem.* **58**, 368–381.
[2] Clark, D. L. *et al.* (2006) in: *Chemistry of the Actinide and Transactinide Elements*, Vol. 2, p. 813–1265, Springer, Dordrecht.
[3] Zhao, H. *et al.* (2015) *Methods* **76**, 137–148.

Low-valent plutonium precursor compounds for metal-organic complexes

S. Fichter, J. März

The synthesis of a stabilized tetravalent plutonium chloride (*i. e.* $[PuCl_4(dme)_2]$, dme = 1,2-dimethoxyethane) starting from PuO_2 under ambient conditions is reported. Spontaneous reduction of the desired product yielded an unprecedented trivalent plutonium chloride $[PuCl_3(dme)]_n$ which holds potential for the synthesis of molecular trivalent plutonium complexes.

The availability of suitable anhydrous actinide starting materials is crucial for the synthesis of actinide complexes with organic or inorganic ligands. Based on previous work investigating the synthesis of tetravalent starting materials for thorium, uranium, and neptunium,[1] we herein report a synthetic procedure to yield the tetravalent plutonium chloride $[Pu^{IV}Cl_4(dme)_2]$ (**1**). The synthesis of this compound has been described previously starting from a solution of $^{239}Pu^{IV}$ in hydrochloric acid.[2] We have expanded this procedure to enable the usage of $^{242}PuO_2$. The group of Scott *et al.* already investigated the limited redox stability of **1** in tetrahydrofuran solution yielding a mixed Pu^{III}/Pu^{IV} complex.[3] We have observed similar reactivity of **1** in dme yielding the trivalent plutonium complex $[Pu^{III}Cl_3(dme)]_n$ (**2**).

EXPERIMENTAL. All preparations have been performed in dedicated glove boxes to handle milligram amounts of ^{242}Pu. All manipulations have been performed under inert conditions to prevent oxidation or hydrolysis reactions. The used solvents have been dried over molecular sieve 3 Å prior to use.

RESULTS. PuO_2 has been dissolved in a mixture of 14 M nitric acid and 0.1 M hydrofluoric acid in 10:1 v/v ratio by stirring at 80 °C over two days to yield a dark green solution. The solvents have been subsequently evaporated in a stream of argon at elevated temperatures. The residue, a Pu^{IV} nitrate, is dissolved in concentrated hydrochloric acid generating a dark red solution accompanied by the evolution of nitrous gases. The solvent is again removed by evaporation. The procedure of dissolving in concentrated hydrochloric acid and evaporation of the solution is repeated three times to finally yield a dark red residue. This residue is dissolved in dimethoxyethane yielding a gold-colored solution. Residual moisture is removed by adding a few drops of trimethylsilylchloride. The supernatant is separated from a small amount of insoluble compounds and the volume is reduced by slow evaporation. The dark reddish brown residue is washed with diethylether to finally yield $[Pu^{IV}Cl_4(dme)_2]$ (**1**). The oxidation state of **1** has been verified by UV/vis spectroscopy (see Fig. 1).[2, 4]

Over time, the formation of dark blue crystals was observed in a concentrated solution of **1** in dme. Analysis of these crystals by single-crystal X-ray diffraction revealed the formation of an unprecedented trivalent plutonium chloride which is stabilized by dimethoxyethane $[Pu(\mu_2\text{-}Cl)_3(dme)]_n$ (see Fig. 2). Each plutonium is coordinated by six chlorides and two oxygen atoms of dme forming a square antiprismatic coordination sphere. Three chlorides each are μ_2-bridging to the next plutonium ion forming infinite chains along the [010] direction.

Such a polymeric structure is similar to $[AmCl(\mu_2\text{-}Cl)_2(thf)_2]_n$ as previously reported,[5] although the same all-μ_2-bridging chloride constitution has only been observed for a trivalent lanthanum chloride (*i. e.* $[La(\mu_2\text{-}Cl)_3(thf)_2]_n$).[6]

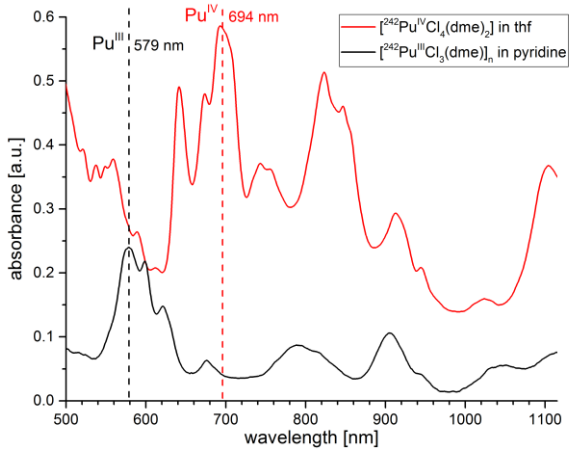

Fig. 1: UV/visible spectra of $[Pu^{IV}Cl_4(dme)_2]$ (**1**, red) and of $[Pu^{III}Cl_3(dme)]_n$ (**2**, black). The concentrations are approximately 10 mM.

The Pu^{III} compound **2** is soluble in pyridine yielding a blue-colored solution. UV/visible spectroscopy revealed a significant change of the absorption bands which is in accordance with the complete reduction of the tetravalent plutonium complex **1** to the trivalent compound **2** (see Fig. 1). As no additional reducing agent has been used, these results underline the redox sensitivity of tetravalent plutonium in organic solvents, even under inert atmosphere.[3] Thus, the choice of the ligand system is crucial for the synthesis of oxidation state pure plutonium complexes. Both low-valent plutonium precursor compounds **1** and **2** will be used for the synthesis of metal-organic plutonium complexes in the near future.

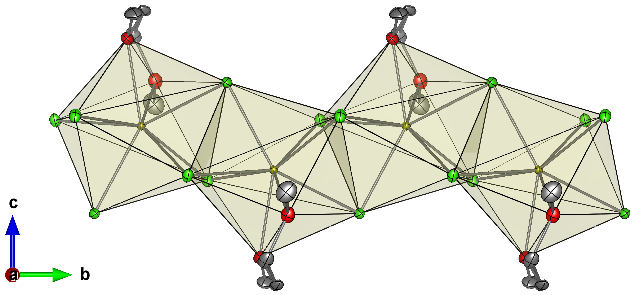

Fig. 2: Molecular structure of $[PuCl_3(dme)]_n$ (**2**). View along [100]. Hydrogen atoms have been omitted for clarity. Color code: plutonium (Pu, ochre), chlorine (Cl, green), oxygen (O, red), carbon (C, gray).

ACKNOWLEDGEMENTS. This work was supported by the German Federal Ministry of Education and Research (BMBF) under the project number 02NUK046B (FENABIUM).

[1] März, J. (2015) *Report HZDR-067*, p. 16.
[2] Reilly, S. D. *et al.* (2014) *Dalton Trans.* **43**, 1498–1501.
[3] Pattenaude, S. A. *et al.* (2018) *Chem. Commun.* **54**, 6113–6116.
[4] Morss, L. R. *et al.* (2010) *The Chemistry of the Actinide and Transactinide Elements*, Springer, Dordrecht.
[5] Galley, S. S. *et al.* (2019) *Organometallics* **38**, 606–609.
[6] Deacon, G. B. *et al.* (1998) *Aust. J. Chem.* **51**, 75–89.

Covalency in actinide bonding: trends in Th–Pu monosalen complexes

T. Radoske, M. Patzschke, M. Schmidt, T. Stumpf, J. März

Three series of tetravalent actinide (*An* = Th, U, Np, Pu) monosalen complexes [*An*Cl$_2$(salen)(*pyx*)$_2$] (H$_2$salen = N,N′-bis(salicylidene)ethylenediamine; *pyx* = pyridine, 4-methylpyridine, 3,5-dimethylpyridine) were synthesized and studied regarding their affinity for neutral *N*-donor molecules. Single-crystal (SC) XRD as well as IR spectroscopy revealed isostructural series with conformational stability. Experimentally determined bond lengths *An*–Cl and *An*–N$_{salen}$/*An*–N$_{pyx}$ point to an ionic binding behavior, whereas the trend of *An*–O distances clearly indicates covalent interactions for U, Np, and Pu. Quantum chemical (QC) calculations confirm these findings including that *An*–O bonds have the highest degree of covalency.[1]

The question of covalency in early actinide binding can be approached by studying isostructural series in which the actinide (*An*) has one specific oxidation state, the longest such series being *An*(IV). Besides the actinide, the electronic and geometric properties of the ligand influence the complex properties. Schiff bases are known to be versatile ligands for almost every metal ion and oxidation state. They also allow partially saturated coordination spheres with labile complex positions and thus potentially reactive sites at transition metals or *An*, *e. g.* for biomolecules or as a basis for catalysis.[2] Here, we investigate the solvent exchange on labile monosalen *An*(IV) complex positions using pyridine (py), 4-picoline (pic) and 3,5-lutidine (lut) using SC-XRD and quantum chemical calculations in order to analyze bonding trends with a focus on covalent contributions.

EXPERIMENTAL. All syntheses were carried out in nitrogen-filled glove boxes or using Schlenk technique for a strict exclusion of oxygen and moisture. The actinide chloride starting materials were synthesized according to literature procedures. Solvents were distilled and stored over 3 Å molecular sieve prior to use. The synthesis of [*An*Cl$_2$(salen)(*pyx*)$_2$] (*An* = Th, U, Np, Pu; *pyx* = py (**1**–**4**), pic (**5**–**8**), lut (**9**–**12**)) was performed *via* [*An*(salen)$_2$] and [*An*Cl$_2$salen(MeOH)$_2$].[1] A general synthesis route of **1**–**12** is as follows: The respective monosalen complex with methanol (*i. e.* [*An*Cl$_2$salen(MeOH)$_2$]) is dissolved in py, pic, or lut. Layering of these solutions with pentane yields single crystals.

RESULTS. Each *An*(IV) monosalen complex series with py (**1**–**4**), pic (**5**–**8**), and lut (**9**–**12**) isomorphously crystallizes in *P*–1, *A*ea2 or *P*2$_1$/c, respectively. Figure 1 exemplarily shows [*An*Cl$_2$(salen)(pic)$_2$] (**5**–**8**).
In all complexes, the actinide is eightfold coordinated by a tetradentately binding salen molecule, two chloro ligands, and two pyridine-based molecules (*pyx*).
Among the *pyx* series, almost identical distances *An*–O, *An*–N$_{salen}$/*An*–N$_{pyx}$ or *An*–Cl were found demonstrating a minor effect of the coordinating solvent *pyx* on the coordination environment. *An*–O bonds are the shortest with approx. 2.18 Å, compared to *An*–N$_{salen}$ (≈ 2.59 Å) or *An*–Cl (≈ 2.72 Å). Interestingly, the *pyx* molecules occupy identical geometrical positions in **1**–**12** showing *An*–N$_{pyx}$ distances (≈ 2.65 Å) that are about 7 pm longer than *An*–N$_{salen}$ indicating weaker interactions. This explains the facile ligand exchange of *e. g.* MeOH and *pyx* at those positions.

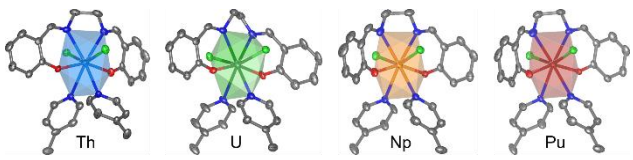

Fig. 1: Molecular structures of [*An*Cl$_2$(salen)(pic)$_2$] (*An* = Th, U, Np, Pu (from left to right)) with ellipsoids drawn at 50 % probability level and hydrogen atoms emitted for clarity. (C: dark grey, O: red, N: dark blue, Cl: light green, Th: light blue, U: dark green, Np: orange, Pu: red).

For a detailed analysis of the bonding trends, structure optimizations and bonding were performed using Turbomole 7.3.1 and Orca 4.2.1.[3, 4] All optimized structures show only minor deviations (about 2 pm) from the SC-XRD structures. The trend of coordinating bond lengths is displayed in Fig. 2, showing a general decrease from Th^{IV} to Pu^{IV} with decreasing cation size. *An*–Cl and *An*–N$_{pyx/salen}$ almost linearly follow the ionic radii of *An*(IV) with a coordination number (CN) of 8, indicating a purely ionic interaction.[5] However, the *An*–O bond length suddenly decreases from Th to U followed by a plateau until Pu. This rather reflects the trend of covalent radii and suggests a significant contribution of covalent bonding. Calculated delocalization indices (DI) of 0.6 for *An*–O *vs.* 0.28 for *An*–N proof this hypothesis. Interestingly, the DI for the *An*–Cl bond of 0.56 is close to the DI for *An*–O. This points to strong interactions and a substantial degree of covalency in this bond which is usually assumed to be purely ionic.

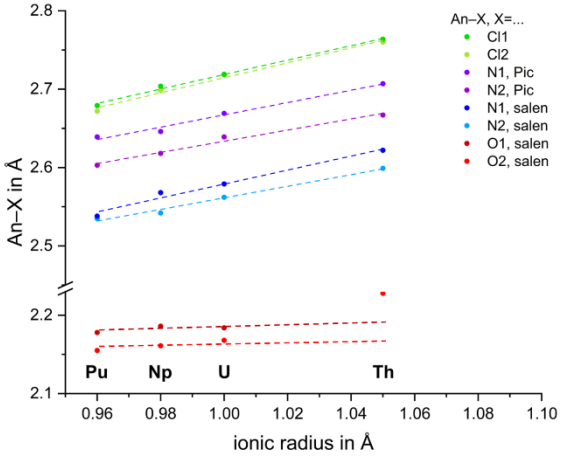

Fig. 2: Coordinating bond lengths from SC-XRD in [*An*Cl$_2$(salen)(pic)$_2$] *vs.* the ionic radii (Shannon) for CN 8 with linear fits for *An*–N and *An*–Cl.[5]

We conclude that the complexes [*An*Cl$_2$(salen)(*pyx*)$_2$] possess two labile positions suitable for solvent exchange. The bonding analysis revealed major differences within the coordinating bonds, being mostly ionic for *An*–N but surprisingly covalent for both *An*–O and *An*–Cl.

ACKNOWLEDGEMENTS. T. Radoske thanks the BMBF for funding (project number 02NUK046B, FENABIUM).

[1] Radoske, T. *et al.* (2020) *Chem. Eur. J.* **26**, 16853–16859.
[2] Dame, A. N. *et al.* (2015) *J. Coord. Chem.* **68**, 3718–3726.
[3] TURBOMOLE V7.3.1 2018, a development of University of Karlsruhe and Forschungszentrum Karlsruhe GmbH.
[4] Neese, F. (2012) *Wiley Interdiscip. Rev.-Comput. Mol. Sci.* **2**, 73–78.
[5] Shannon, D. R. D. (1976) *Acta Cryst. A* **32**, 751–767.

Mononuclear actinide (UO_2^{2+}, U^{4+}, Th^{4+}, Np^{4+}) complexes with a new Schiff base ligand

D. Bansal, M. Patzschke, P. Kaden, M. Schmidt

The reaction of a new Schiff base ligand 2-methoxy-6-(((2-methyl-1-(pyridin-2-yl)propyl)imino)methyl)phenol (HL^{pr}) with actinide elements (UO_2^{2+}, U^{4+}, Th^{4+}, and Np^{4+}) results in the isolation of [UO_2Cl-L^{pr}·THF] (1), [$ThCl_3$-L^{pr}·2THF] (2), [UCl_3-L^{pr}·THF] (3), and [$NpCl_3$-L^{pr}·THF] (4). All crystal structures exhibit formation of mononuclear complexes. Binding studies confirm 1:1 stoichiometries and binding constants in the order $Th^{4+} \approx U^{4+} > Np^{4+} > UO_2^{2+}$.

Coordination chemistry of actinide elements has gained widespread attention due to the actinides' underexplored coordinating properties as well as interesting redox and catalytic properties.[1] Hence, efforts have been made to synthesize and isolate highly reactive, low-valent actinide compounds.[2] Up to now, complexes with low valent actinides are largely dominated by cyclopentadienyl and related ligands.[3] But also other organic ligands, such as di- and monoanionic Schiff base ligands are explored due to the presence of strongly coordinating aryl-oxide donors along with a chelating motif as well as their non-innocent redox behavior.[4,5] Here, we report the synthesis and isolation of mononuclear actinide complexes [UO_2Cl-L^{pr}·THF] (**1**), [$ThCl_3$-L^{pr}·2THF] (**2**), [UCl_3-L^{pr}·THF] (**3**), and [$NpCl_3$-L^{pr}·THF] (**4**).

EXPERIMENTAL. Condensation of o-vanillin with 2-methyl-1-(pyridine-2-yl)propane-1-amine hydrochloride results in the isolation of yellow oily product $\mathbf{HL^{pr}}$ in high yield. Complexes **1**–**4** were synthesized by treating $\mathbf{HL^{pr}}$ in its deprotonated form $(\mathbf{L^{pr}})^-$ with UO_2^{2+} (**1**) or M^{4+} (M = Th (**2**), U (**3**), Np (**4**)) in THF to afford mononuclear complexes.

RESULTS. Crystal structures of complexes **1**, **3**, and **4** exhibit seven-coordinated actinide complexes whereas Th^{4+} in **2** is eight coordinated. In all complexes, the metal center is present inside the ligand cavity comprising deprotonated phenoxide oxygen (O_{Ph}), imine nitrogen ($N_{C=N}$) and pyridyl nitrogen (N_{py}) while chloride atom(s) and THF molecule(s) complete the coordination sphere (Fig. 1).

The uranyl center in complex **1** is coordinated in a pentagonal bipyramidal geometry, whereas the geometry around U^{4+} and Np^{4+} center in **3** and **4** was found to be monocapped trigonal prismatic. Coordination from an additional THF molecule in **2**, results in the formation of an eight-coordinated trigonal dodecahedron geometry around Th^{4+}.

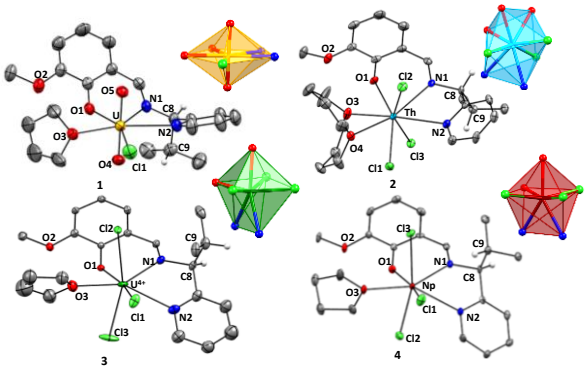

Fig. 1: Ellipsoidal representation of complexes **1**–**4**. The Hydrogen atoms are omitted for clarity. Insets: polyhedral representation of coordination environment around central metal ion.

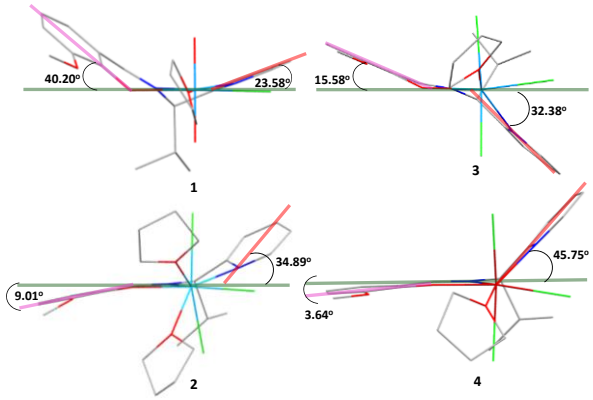

Fig. 2: Capped stick representation of complexes **1**–**4**, displaying the angle formed by phenoxide ring (pink line), pyridyl ring (red line) with the horizontal plane (green line) **1**–**4**.

Importantly, coordination of metal ions to the ligand exhibits differently aligned aromatic rings around the horizontal plane containing An^{n+}, O_{ph} and (H)C = N (Fig. 2). In complex **1**, both phenoxide and pyridyl rings are inclined on the same side of the horizontal plane by 40.2° and 23.6°, respectively. Whereas, in complexes **2**–**4**, aromatic rings are present in a pseudo-trans manner to the horizontal plane. The phenoxide rings make angles of 9.0° in **2**, 15.6° in **3**, and 3.6° in **4** with the horizontal plane, whereas the pyridyl ring is inclined by 34.9°, 32.4° and 45.7° in **2**, **3**, and **4**, respectively. In contrasting observation, angle for phenoxide ring decreases and for pyridyl ring increases w.r.t horizontal plane, in the order **1** → **3** → **2** → **4**.

Binding studies were performed by UV/vis spectroscopy by titrating $(\mathbf{L^{pr}})^-$ with actinide ions. The changes in the absorbance reached maxima on addition of 1.0 equiv. metal ion indicating 1:1 stoichiometry. The binding coefficients were calculated (at 490 nm for **1** and 450 nm for **2**–**4**) using the Benesi–Hildebrand equation (1).[6]

$$\frac{1}{(A - A_0)} = \frac{1}{K(A_{max} - A_0)[An^{n+}]^x} + \frac{1}{(A_{max} - A_0)} \qquad (1)$$

The linear regression plot between absorption intensity, $1/[A-A_o]$ *vs.* $1/[An^{n+}]^x$ varied linearly as a function of $1/[An^{n+}]$ (x = 1), confirming a 1:1 stoichiometry. The calculated binding constants (K) were found to be $2.3(\pm 0.2) \times 10^{-1}\,M^{-1}$ (**1**), $2.3(\pm 0.4) \times 10^{3}\,M^{-1}$ (**2**), $1.54(\pm 0.3) \times 10^{3}\,M^{-1}$ (**3**), and $2.01(\pm 0.4) \times 10^{2}\,M^{-1}$ (**4**). These numbers suggest that UO_2^{2+} binds weakly to $(\mathbf{L^{pr}})^-$ compared to An^{4+} ions. Moreover, among An^{4+}, Th^{4+} and U^{4+} have similar binding affinities, whereas Np^{4+} has comparatively weaker binding affinity than Th^{4+} and U^{4+}. These findings are in coalescence with ongoing quantum-chemical calculations to estimate binding and coordination properties of actinide elements with the new Schiff base ligand.

ACKNOWLEDGEMENTS. D.B. thanks Dr. S. Fichter for his help in the SC-XRD measurement.

[1] Camp, C. *et al.* (2010) *J. Am. Chem. Soc.* **132**, 17374–17377.
[2] Jori, N. *et al.* (2020) *Organometallics* **39**, 1590–1601.
[3] Arnold, P. L. *et al.* (2017) *Chem. Rev.* **117**, 11460–11475.
[4] Camp, C. *et al.* (2013) *Inorg. Chem.* **52**, 7078–7086.
[5] Radoske, T. *et al.* (2020) *Chem. Eur. J.* **26**, 1–8.
[6] Benesi, H. A. *et al.* (1949) *J. Am. Chem. Soc.* **71**, 2703–2707.

Ion size-driven change of coordination environments in *bis*-pyrophen complexes

L. Köhler, T. Stumpf, J. März

The tetravalent thorium and neptunium complexes of the Schiff base ligand 1,2-benzenediamine-*N,N′*-bis(1*H*-pyrrol-2-yl)methylene (pyrophenH_2) were synthesized via salt metathesis reactions using lithium diisopropylamine (LDA) as a base. Molecular structures were determined using SC-XRD and revealed distinct coordination environments for Th^{IV} and Np^{IV}, which presumably can be attributed to different ionic radii. Moreover, varying An–N bond lengths indicate different bonding situations to the pyrrol and imine N donor functionalities.

Understanding the complex chemistry of the early actinides is a huge challenge, going on for several decades now. For this purpose quite a lot of research work has been put into complex formation with salen-type ligands (salen = Bis(salicyliden)ethylendiamine), because of their capability to stabilize metal ions in different oxidation states and their easily changeable electronic and steric properties.[1,2] Contrary to the extensively studied *N,O* donor ligand salen, analogous pure *N* donor systems have lagged behind. In order to characterize subtle differences in the actinide-nitrogen bonding, we have used the less studied salen relative 1,2-benzenediamine-*N,N′*-bis(1*H*-pyrrol-2-yl)methylene (pyrophenH_2) for complex formation with the tetravalent actinides Th and Np.

EXPERIMENTAL. Complexes were synthesized by adding the respective actinide chloride in thf to a stirring solution of the ligand with LDA base in thf. Color change occurred immediately from orange to dark red. After stirring for one day, volatiles were removed in vacuum and the red product was washed with pentane. Crystals were grown by diffusion experiments with pentane.

RESULTS. The synthesis route for the pyrophen complexes is displayed in Fig. 1. As the educts are used in a 1:2 metal to ligand ratio, the formation of a 1:2 complex is expected.

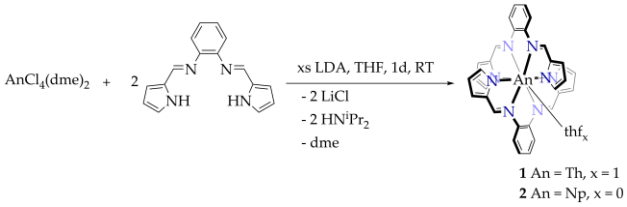

Fig. 1: Reaction scheme for the synthesis of **1** and **2**.

SC-XRD measurements of **1** and **2** revealed the desired stoichiometry with pincer type coordination of both ligands (Fig. 2). The metal center is bound to eight nitrogen atoms of the two surrounding ligands, respectively. For **1** an additional thf molecule is coordinated to the metal, which is absent in the structure of **2**. This results in different coordination numbers (CN) for **1** and **2**, namely 9- and 8-fold**.** The resulting polyhedra can be termed as spherical capped square antiprism (in **1**) or triangular dodecahedron (in **2**). An explanation for the different coordination spheres could be the different ionic radii of the metal centers. Tetravalent Th with CN 9 exhibits a radius of 1.09 Å and Np with CN 8 has a radius of 0.98 Å.[3] Since Np is 0.11 Å smaller, there is not enough space for an additional solvent molecule to coordinate to the metal.

A look at the mean bond lengths between the metal center and the donor atoms reveals remarkable differences. The actinide bonds to the pyrrol nitrogen (An–N_{py}) are 2 or even 9 pm shorter in complexes **1** and **2** than those to the imine nitrogen (An–N_{im}). This indicates a stronger bond to the deprotonated nitrogen atoms, which has to be confirmed by theoretical bonding analysis. Furthermore, the metal ions are not located symmetrically within the cavity, the asymmetry being much more pronounced in **1** due to the additionally coordinating thf molecule. In **1**, the ligand that is perpendicular to the thf molecule exhibits nearly identical distances between Th and the two different nitrogens, that is N_{py} (Th–N5: 2.534 Å, Th–N8: 2.533 Å) and N_{im} (Th–N6: 2.560 Å, Th–N7: 2.561 Å). In contrast, there are quite large differences in the Th–N_{py} (Th–N1: 2.524 Å, Th–N4: 2.555 Å) and Th-N_{im} (Th–N2: 2.552 Å, Th–N3: 2.572 Å) distances of the second ligand. Th is pushed towards N1, meaning the thf molecule is influencing the binding of the metal center to the pyrophen ligands. The asymmetrical coordination environment in **2** may also be attributed to the small ionic radius of Np^{IV}, making a symmetrical coordination energetically unfavored.

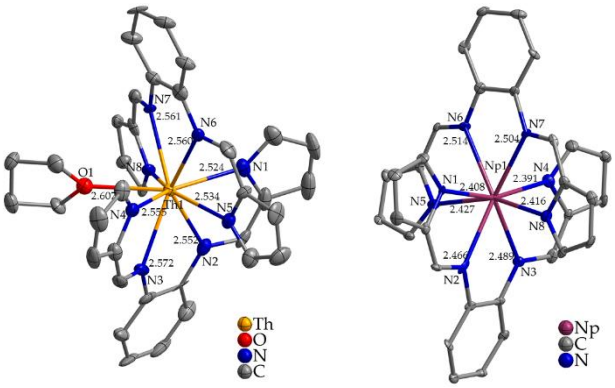

Fig. 2: Molecular structures for [Th(pyrophen)$_2$(thf)] (**1**, left, CN = 9) and [Np(pyrophen)$_2$] (**2**, right, CN = 8). Protons and co-crystallized solvent molecules are omitted for clarity.

Future work will focus on crystal growth and measurement of the U analogue to investigate whether there is an additional coordinating solvent molecule in its complex structure. On the one hand, the ionic radius for an 8-fold coordinated U center is 1.00 Å, which would point to a **2**-like structure. On the other hand, a 9-fold coordinated U exhibits a radius of 1.05 Å, suggesting that coordination of an additional solvent molecule may be possible. Furthermore, the synthesis of the Pu complex (r(Pu^{IV}) = 0.96 Å) shall aim to see if a 1:2 stoichiometry is still possible, when going to even smaller metal centers, and how Pu's bonding situation compares to the earlier actinides.[3]

[1] Dame, A. N. *et al.* (2015) *Eur. J. Inorg. Chem.* **2015**, 2996–3005.
[2] Cozzi, P. G. (2004) *Chem. Soc. Rev.* **33**, 410–421.
[3] Shannon, R. D. (1976) *Acta Crystallogr. A* **32**, 751–767.

Understanding covalency in tetravalent actinide amidinates

R. Kloditz, S. Fichter, J. März, M. Patzschke, M. Schmidt

The emergence of covalency within the actinide-nitrogen bond has been investigated in two series of isostructural tetravalent *f*-element amidinate complexes [MX((*S*)-PEBA)$_3$] (M = Th, Pa, U, Np, Pu, Ce; X = Cl, N$_3$; (*S*)-PEBA: (*S*,*S*)-*N*,*N*′-bis(1-phenylethyl)benzamidinate). The combination of thorough characterization in solid state, in solution, and by quantum chemical bonding analysis reveals an increasing covalent character within the actinide series but a changing origin from mainly 6*d* to 5*f* participation.

The evaluation of the covalent character of actinide heteroatomic bonds is an ongoing hot topic in actinide science. Especially ligands containing soft donor atoms like nitrogen are well suited for these studies. Thus, we have synthesized and characterized two series of tetravalent actinide amidinate complexes with the chiral benzamidinate ligand (*S*,*S*)-*N*,*N*′-bis(1-phenylethyl)benzamidinate ((*S*)-PEBA). This constitutes a rare study of series of pure nitrogen donor complexes of tetravalent actinides including a transuranium element (*i.e.* Np).

EXPERIMENTAL. The synthesis of the tetravalent *f*-element amidinates [MX((*S*)-PEBA)$_3$] (M = Th, U, Np, Ce; X = Cl, N$_3$) has been reported recently.[1,2]

RESULTS. The reported tetravalent actinide amidinate complexes are isostructurally crystallizing in the chiral space group type $P2_12_12_1$ with similar cell parameters. In all reported complexes, the actinide is 7-fold coordinated by three chelating amidinate ligands and one (pseudo)halide forming a monocapped octahedral coordination geometry. The amidinates are coordinating asymmetrically towards the metal center (see Fig. 1) with a shorter and a longer M–N distance as indicated in Tab. 1.
The comparison of the intramolecular bond lengths of the different tetravalent actinide complexes reveals a decreasing trend with decreasing ionic radius of the tetravalent actinide cation. This applies to all intramolecular actinide-donor distances in a similar manner and implies a mainly ionic bonding interaction. However, a clear deviation from this trend is observed for the tetravalent cerium complex as the intramolecular M–Cl and M–N$_a$ distances are significantly longer than expected by the decreasing ionic radius.

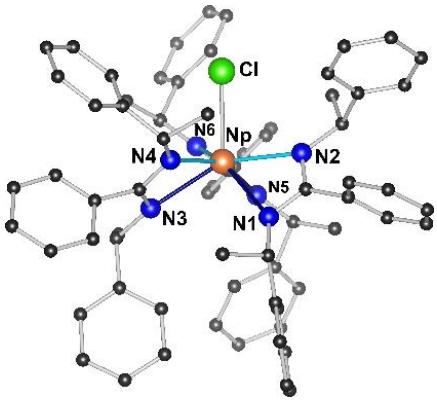

Fig. 1: Molecular structure of [NpCl((*S*)-PEBA)$_3$] as representative of the whole series of tetravalent metal amidinates. Hydrogen atoms have been omitted for clarity.

Tab. 1: Averaged bond lengths in [MCl(L)$_3$] (M = Th, U, Np, Ce; L = (*S*)-PEBA) complexes. Intramolecular distances M–N1, N3, and N5 are averaged to M–N$_a$ and M–N2, N4, and N6 to M–N$_b$.

d (Å)	IR (CN = 7)[3]	M–Cl	M–N$_a$	M–N$_b$
[ThCl(L)$_3$]	1.00	2.701(1)	2.560(12)	2.439(13)
[UCl(L)$_3$]	0.95	2.641(1)	2.499(4)	2.379(19)
[NpCl(L)$_3$]	0.93	2.630(1)	2.497(4)	2.368(15)
[CeCl(L)$_3$]	0.92	2.644(2)	2.512(6)	2.365(20)

To gain a more detailed picture, a quantum chemical bonding analysis using Quantum Theory of Atoms in Molecules (QTAIM) and Natural Population Analysis (NPA) was performed (see Fig. 2). The delocalization index, which is a measure for the number of shared electrons between two atoms is constantly increasing within the actinides series from Th to Pu which indicates an increasing covalent character. This is supported by NPA which indicates an increasing population of the actinides' 6*d* orbitals from Th to U but a decrease to Pu, while the 5*f* excess population is constantly increasing from Pa to Pu. The combination of both methods led us to conclude that the covalent character of the actinide-nitrogen bond is increasing within the actinide series from Th to U and then remains on a similar level until Pu. The reason for this is a change of the origin of this covalent character from mainly 6*d* to stronger 5*f* participation.
Furthermore, the delocalization index shows a similar covalent character of the tetravalent cerium to tetravalent uranium which for Ce is driven by occupancy of 5*d* orbitals.

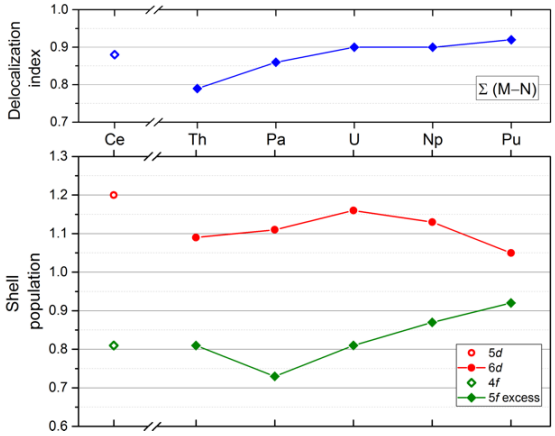

Fig. 2: Quantum chemical bonding analysis of [MCl((*S*)-PEBA)$_3$] (M = Ce, Th, Pa, U, Np, and Pu) complexes. Top: Sum of delocalization indices of M–N bonds within one amidinate ligand. Bottom: Natural Population Analysis (NPA) of metal cations. The *f* excess is defined as the number of electrons in addition to the expected value for M(IV).

ACKNOWLEDGEMENTS. This work was supported by the German Federal Ministry of Education and Research (BMBF) under the project number 02NUK046B (FENABIUM). We thank Prof. Dr. P. Roesky (Karlsruhe Institute of Technology) for providing the benzamidinate ligand.

[1] Fichter, S. *et al.* (2020) *Chem. Eur. J.* **26**, 8867–8870.
[2] Kloditz, R. *et al.* (2020) *Inorg. Chem.* **59**, 15670–15680.
[3] Shannon, R. D. (1976) *Acta Crystallogr., Sect. A* **32**, 751–767.

Following up on $ThSiO_4$ synthesis by *in situ* SWAXS measurements

P. Estevenon, J. Causse,[1] S. Szenknect,[1] E. Welcomme,[2] A. Mesbah,[1] P. Moisy,[2] C. Poinssot,[2] N. Dacheux[1]

[1]ICSM, Université Montpellier, CEA, CNRS, ENSCM, Bagnols-sur-Cèze, France; [2]CEA, DES, ISEC, DMRC, Université Montpellier, Marcoule, France

Thorite, $ThSiO_4$, is one of the most abundant natural sources of thorium on earth. While actinides are known to form nanoparticles in silicate medium, no direct link between those colloids and the crystalline form of thorite has been evidenced until now. We observed that thorite can be produced with experimental conditions close to environmental pH and temperature. Thanks to *in situ* Small and Wide-Angle X-rays Scattering (SWAXS) measurements, colloids of a few nanometers have been first evidenced for low reaction times. These colloids exhibit elongated shapes and ultimately tend to aggregate after the size has reached 10 nm. Once aggregated, the system goes through a maturation step culminating in the emergence of nanocrystallites exhibiting thorite zircon structure. This maturation step is longer when the reaction temperature is decreased highlighting kinetic considerations. These results have potential implications in the paragenesis of Th minerals deposits, but also in the behavior of Th and, by analogy, tetravalent actinides in the environment.[1]

Thorium chemistry may be considered as indicative of the reactivity of the actinide elements at the oxidation state +IV. Due to the abundance of silicate species in the environment, identifying the actinide-silicate interactions is a key point to evaluate the actinide behavior in the environment. On the one hand, thorium, uranium and neptunium are known to form nanometric particles in silicate reactive media.[2–7] The prevailing size of these colloids is less than 20 nm, they appear as virtually amorphous or poorly structured and exhibit low isoelectric point ($pH_{IEP} \leq 4.6$), corresponding to a negative surface charge.[4,6] Thus, An^{IV} oxyhydroxy-silicate colloids may be able to stabilize significant amounts of An^{IV} in a waterborne form and may enhance their mobility in soils and aquifers. On the other hand, the zircon-type structure minerals thorite ($ThSiO_4$) and coffinite ($USiO_4$) are among the most abundant natural sources of thorium and uranium in ore deposits and their syntheses have been studied using high temperature dry chemistry and hydrothermal methods. However, although they could play an important role in the formation of ore deposits, to the best of our knowledge, no specific link between the colloidal species and the corresponding crystalline phases (*i.e.* thorite and coffinite) has been highlighted until now.

EXPERIMENTAL. Thorium nitrate and sodium metasilicate were mixed in aqueous nitric acid solution, the pH of the reactive media was then adjusted to a pH ranging between 3 and 6 with a concentrated NaOH solution.
Small volumes of these solution were taken and placed in sealed glass capillaries in order to perform *in situ* SWAXS measurements at fixed temperature, ranging between room temperature and 60 °C, in a specific oven. Complementary ex-situ experiments were performed by keeping the mother solution at the same temperature in order to confirm the formation of $ThSiO_4$.

RESULTS. This experiment allowed us to follow the formation of $ThSiO_4$ from the aggregation of colloidal particles, characterized by the SWAXS curves at low q values at the beginning of the experiment and the crystallization of thorite

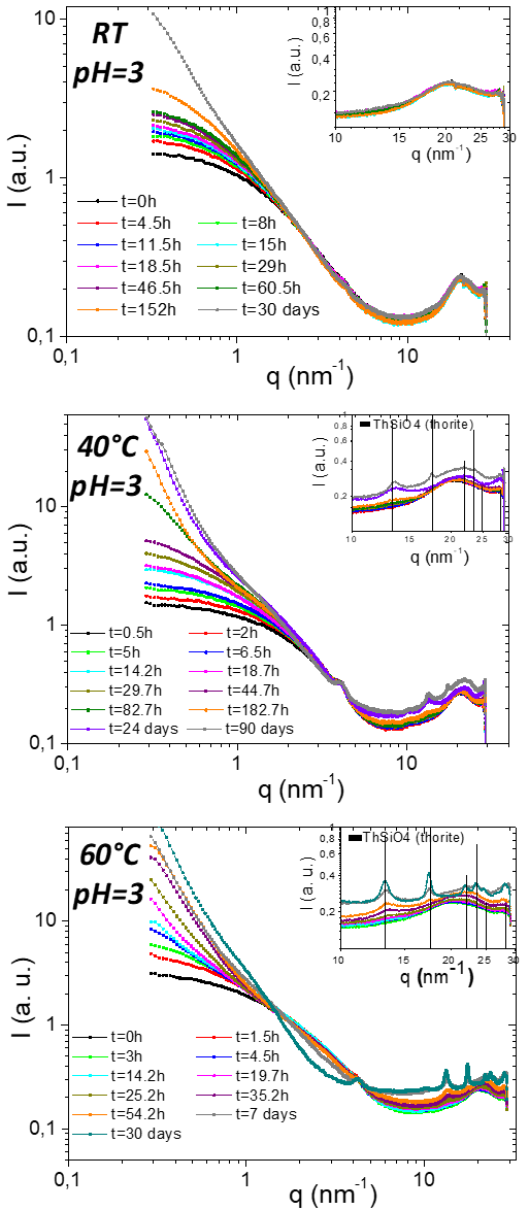

Fig. 1: *In situ* SWAXS measurements kinetics at room temperature (RT), 40 °C and 60 °C for pH = 3. The inset graphics refer to a focus in the q range from 10 nm^{-1} to 30 nm^{-1}.

for longer holding time characterized by thorite diffraction peaks at high q values (Fig. 1). It has been evidenced for the first time that the formation of thorite is possible at environmentally representative temperatures. Moreover, the results proved that the temperature has a strong impact on the kinetic of aggregation of thorium silicate particles and their crystallization.

[1] Estevenon, P. *et al.* (2020) *Dalton Trans.* **49**, 11512–11521.
[2] Neill, T. S. *et al.* (2018) *Environ. Sci. Technol.* **52**, 9118–9127.
[3] Peretroukhine, V. *et al.* (2002) *J. Nucl. Sci. Technol.* **Supplement**, 516–519.
[4] Hennig, C. *et al.* (2013) *Geochim. Cosmochim. Acta* **103**, 197–212.
[5] Zänker, H. *et al.* (2016) *Chemistry Open* **5**, 174–182.
[6] Dreissig, I. *et al.* (2011) *Geochim. Cosmochim. Acta* **75**, 352–367.
[7] Husar, R. *et al.* (2015) *Environ. Sci. Technol.* **49**, 665–671.

High-energy-resolution X-ray spectroscopy studies on Th compounds at the Th L_3 and L_1 edges

J. Galanzew, S. Weiss, L. Amidani, A. Ikeda-Ohno,[1] J. März, A. Beck,[2] D. Schild,[2] S. M. Butorin,[3] T. Vitova,[2] K. O. Kvashnina

[1]Collaborative Laboratories for Advanced Decommissioning Science (CLADS) Japan Atomic Energy Agency (JAEA), Muramatsu, Japan; [2]Karlsruhe Institute of Technology (KIT), Institute for Nuclear Waste Disposal, Karlsruhe, Germany; [3]Department of Physics and Astronomy, Uppsala, Sweden

We report here the X-ray Absorption Near Edge Structure (XANES) at the Th L_3 and Th L_1 edges, re-corded in high-energy-resolution fluorescence-detection (HERFD) mode of Th-based compounds. The capacity of this method to overcome limitations of conventional XANES and to push the limits for obtaining new information about the electronic and geometric structures of several Th compounds is discussed in detail.[1–3] Experimental results are supported by ab-initio computational studies within the FDMNES code. Moreover, all investigations are corroborated by X-ray photoelectron spectroscopy (XPS) and Anderson impurity model calculations. We show that Th L_3 edge is much more sensitive to the electronic structural changes compared to the Th L_1 edge. However, despite the large life-time broadening of the Th L_1 edge, the HERFD at the L_1 edge still shows the sensitivity towards changes in the electronic structure of the Th 7p states, while the crystal field splitting effects of the Th 6d states are studied at the Th L_3 edge.

EXPERIMENTAL. $Th(NO_3)_4 \cdot 4.7H_2O$ was purchased from Merck. ThO_2 was synthesized at HZDR from $Th(NO_3)_4 \cdot 4.7H_2O$ by sintering in an oven at 1,000 °C for several hours. The structure was characterized as crystalline ThO_2 by X-ray powder diffraction. For the Th_2-(μ_2-OH)$_2$(H_2O)$_{12}Cl_2$]$Cl_4 \cdot 2H_2O$ synthesis, first, NH_4OH was added to 1 mL of a 0.7 M $Th(NO_3)_4$ solution to form ThO_2 (am., hyd.) precipitate. This precipitate was washed with distilled water until a neutral pH was reached. 1 mL of 1 M HCl was added to the precipitate. The formation of crystals was observed after a few days.

Th L_3 edge (ROBL): The incident energy was selected using the (1 1 1) reflection from a Si DCM. Rejection of higher harmonics was achieved by two Rh mirrors at an angle of 2.5 mrad relative to the incident beam. The Th L_3 HERFD spectra were recorded by X-ray emission spectrometer set to the maximum of the Th $L_{\alpha 1}$ emission line. The emission energy was selected using the (8 8 0) reflection of one spherically bent striped Si crystal analyzer with 0.5 m bending radius aligned at 84.4° Bragg angle.[4]

RESULTS. The computed spectra agree well with the experimental data (Fig 1). The inspection of DOS reveals an overlap of Th d- and f- states and O p-states for ThO_2. Previously reported DFT calculations on ThO_2 also showed a mixing of Th f- and d-states.[5] [Th_2-(μ_2-OH)$_2$(H_2O)$_{12}Cl_2$]$Cl_4 \cdot 2H_2O$ also shows Th d- and f-states at the same energy as Cl p- and O p-states. However, in the white line the O states show very little overlap with Th d-states in contrast to the Cl p-states which seem to overlap with Th d-states. The pre-edge seems to arise from a mixture of Th d- and f-states with Cl and O p-states. Cl p-states appear to have a better overlap with Th states, observable by the same energy position and shape of the DOS distribution. Also, Cl p-states are less localized than O p-states. The localization of O p-states suggest that the O-ligands behave more ionic than in ThO_2. DOS overlap between Th and Cl offer an interesting starting point for future investigations either with a water free compound or substitution of Cl with other halogens. The

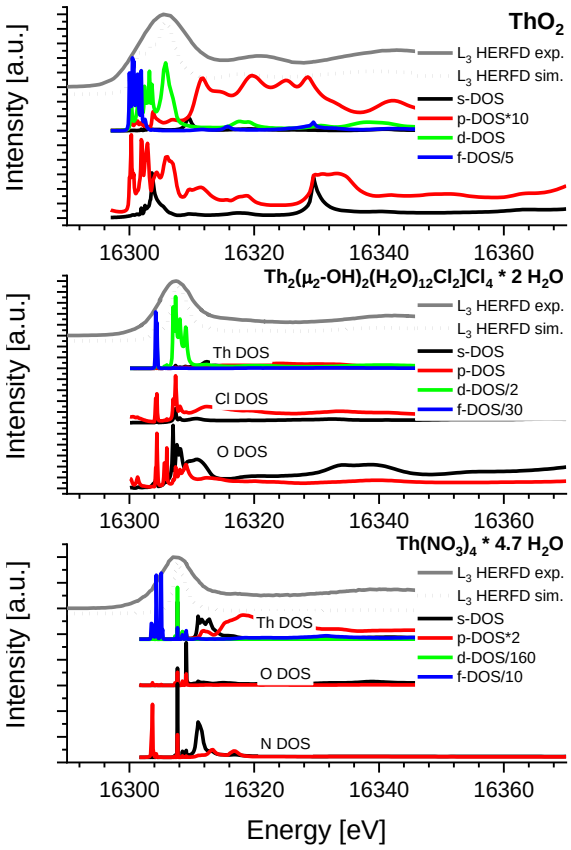

Fig. 1: Simulated L_3 HERFD spectra (grey) and correspondeing local density of states. Only DOS above the Fermi level are shown.

$Th(NO_3)_4 \cdot 4.7H_2O$ is described in the literature as an ionic compound with no covalent bond formation. Our DOS illustrates a strong superposition of Th d states and N p-states in correspondence of the WL. A slight ad-mixture of O p-states is also found for the same spectral feature. The d-DOS of Th is particularly sharp for this compound, confirming its ionic character. Simulated and experimental spectra are found in good agreement and show a different broadening of the absorption edge on various Th systems. Calculated DOS for the three Th-based compounds show clear evidence of the broader distribution of the Th 6d states of ThO_2 compared to $Th(NO_3)_4 \cdot 4.7H_2O$ and [Th_2-(μ_2-OH)$_2$(H_2O)$_{12}Cl_2$]$Cl_4 \cdot 2H_2O$.

ACKNOWLEDGEMENTS. S.M.B. acknowledges support from the Swedish Research Council (Grant 2017-06465).

[1] Butorin, S. M. *et al.* (2016) *Chem. Comm.* **53**, 115–118.
[2] Butorin, S. M. *et al.* (2016) *Chemistry* **22**, 9693–9698.
[3] Butorin, S. M. *et al.* (2016) *Proc. Natl. Acad. Sci. U.S.A.* **113**, 8093–8097.
[4] Kvashnina, K. O. *et al.* (2016) *J. Syn. Rad.* **23**, 836–841.
[5] Wen, X.-D. *et al.* (2012) *J. Chem. Phys.* **137**, 154707.

Combining *ab-initio* multiple scattering (FEFF) calculations with Fourier filtering: eased derivation and validation of EXAFS structural models

A. Rossberg

The *ab-initio* multiple scattering code FEFF allows the calculation of theoretical scattering phase and amplitudes functions based on structural models stemming from XRD structural data bases, quantum chemical calculations or from intuitive chemical information. Since FEFF is able to predict the experimental scattering functions with high accuracy, one may think about a direct comparison between theory and experiment. However, the Debye-Waller damping terms, which are also needed for the calculation of the theoretical EXAFS spectrum (χ_t), cannot be predicted precisely by the theory or are unknown at all, thus spoiling a direct validation of a structural model. Here we propose a Fourier filtering algorithm (FFA) enabling a direct comparison of χ_t with an experimental EXAFS spectrum (χ_e) without least square fitting.

EXPERIMENTAL. The Debye-Waller factor (σ^2) cannot be predicted in a considerable precision by FEFF calculations, hence making a direct comparison between $\chi_t(k)$ and $\chi_e(k)$ (k – photoelectron wave vector) impossible. Thus, the idea behind the FFA is to remove or at least to reduce the influence of the σ^2 on $\chi_t(k)$ by Fourier filtering, which will be described in the following. The Fourier transform (F) of a signal $\chi(k)$ in the k-interval $k_{min} \le k \le k_{max}$ is:

$$F\big(\chi(k)\big) = \frac{1}{\sqrt{2\pi}} \int_{k_{\min}}^{k_{\max}} \chi(k) e^{i(2kr)}\, dk, \qquad (1)$$

and the inverse F^{-1}, *i.e.* the backtransform of F, is given by:

$$z(k) = F^{-1}\left(F\big(\chi(k)\big)\right) = \frac{1}{\sqrt{2\pi}} \int_{r_{\min}}^{r_{\max}} F\big(\chi(k)\big) e^{-i(2kr)}\, dr, \qquad (2)$$

with r_{min} and r_{max} being the lower and upper limits of the filtered range in the r-space.[1] Note that due to the complex nature of F F^{-1} contains an imaginary and a real part, *i.e.* $\Im[z(k)]$ and $\Re[z(k)]$, respectively, which allows the calculation of the amplitude $A(k)$ and the phase $\phi(k)$ of $\chi(k)$,

$$A(k) = \{\Im[z(k)]^2 + \Re[z(k)]^2\}^{1/2} \qquad (3)$$

$$\phi(k) = \arctan\left\{\frac{\Im[z(k)]}{\Re[z(k)]}\right\}, \qquad (4)$$

so that the filtered $\chi(k)$ can be formulated as:

$$\chi(k) = A(k)\sin(\phi(k)).^{[1]} \qquad (5)$$

This holds for any spectrum $\chi(k)$, while for instance for two backscattering atoms:

$$\chi(k) = A(k)\sin\big(\phi(k)\big) = N_h e^{-2\sigma_h^2 k^2} B_h(k,r) \sin\big(2kr_h + \varphi_h(k,r) + \xi(k)\big) + N_j e^{-2\sigma_j^2 k^2} B_j(k,r) \sin\big(2kr_j + \varphi_j(k,r) + \xi(k)\big), \qquad (6)$$

where N, B and φ is the coordination number, the backscattering amplitude function and the backscatter phase shift of the atom type h and j, respectively, and ξ is the phase shift of the central atom. In the case of a FEFF calculation eq. 6 yields $\chi_t(k)$ with $\sigma_h^2 = \sigma_j^2 = 0$, where $F^{-1}\left(F\big(\chi(k)\big)\right) = A_t(k)\sin\big(\phi_t(k)\big)$. If we assume for an experimental spectrum the same underlying structural arrangement as used for $\chi_t(k)$ and a global σ^2 for each atom, $\sigma_h^2 = \sigma_j^2 = \sigma^2$, then:

$$\chi_e(k) = e^{-2\sigma^2 k^2} A_t(k)\sin(\phi_t(k)), \qquad (7)$$

and with the theorem of convolution (*):

$$F\big(e^{-2\sigma^2 k^2} A_t(k)\sin\big(\phi_t(k)\big)\big) = F\big(U(k)\big) * F\big(\sin\big(\phi_t(k)\big)\big) \qquad (8)$$

$$U(k)\sin\big(\phi_t(k)\big) = F^{-1}\big(F\big(U(k)\big) * F(\sin(\phi_t(k)))\big).^{[1]} \qquad (9)$$

In consequence and only if $\chi_e(k) = U(k)\sin(\phi_t(k))$, the assumed structural model used for the FEFF calculation will fit the structural arrangement measured by the experiment. $U(k)$ is gained by the Fourier backtransform of $F(\chi_e(k))$ (eq. 2) and applying eq. 3, while $\phi_t(k)$ is calculated from $F(\chi_t(k))$ (eq. 2) and eq. 4.

For the test of the FFA, a Tc K-edge $\chi_e(k)$ is calculated with eq. 6, where $N_h = 6$ (oxygen atoms), $N_j = 2$ (iron atoms), $\sigma_h^2 = 0.005$ Å² and $\sigma_j^2 = 0.009$ Å² (Fig. 1a)). With the same values and with $\sigma_h^2 = \sigma_j^2 = 0$, $\chi_t(k)$ is calculated (Fig. 1a)). Due to the influence of the σ^2, $\chi_t(k)$ is not comparable with $\chi_e(k)$, hence, the structural model cannot be validated. With FFA and the correct FEFF model the best match is observed (Fig. 1b), while for just small deviations from the correct FEFF model much larger deviations occur (Fig. 1c and d). Notably and even by violating in our test the FFA condition $\sigma_h^2 = \sigma_j^2$, FFA minimizes the influence of the unknown σ^2, hence enables a validation of FEFF structural models for real-world cases.[2,3] Moreover, FFA allows also for the derivation of structural models, simply by adjusting FEFF structural models with for instance any molecular drawing software.

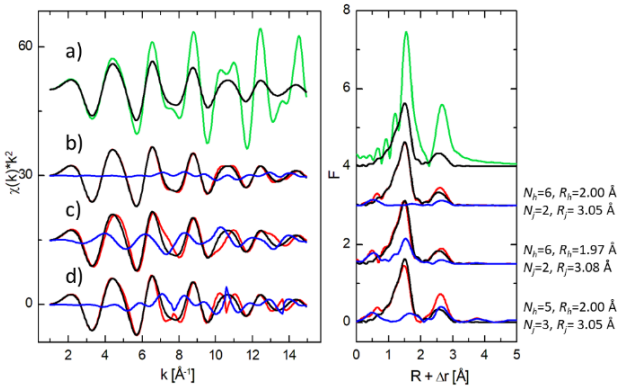

Fig. 1: Tc K-edge EXAFS spectra (left) and corresponding F (right). $\chi_t(k)$ – green, $\chi_e(k)$ – black, $U(k)\sin\big(\phi_t(k)\big)$ calculated by FFA for different structural models (red, values on the right). Residuals – blue.

[1] Smith, S. W. (1997) *The scientist and engineer's guide to digital signal processing*, California Technical Pub., San Diego, U.S.A.
[2] Taube, F. *et al.* (2019) *Inorg. Chem.* **58**, 368–381.
[3] Mayordomo, N. *et al.* (2021) *Chem. Eng. J.* **408**, 127265.

Signatures of technetium oxidation states: a new approach

S. Bauters, A. C. Scheinost, K. Schmeide, S. Weiss, K. Dardenne,[1] J. Rothe,[1] N. Mayordomo, R. Steudtner, T. Stumpf, U. Abram,[2] S. M. Butorin,[3] K. O. Kvashnina

[1]Karlsruhe Institute of Technology (KIT), Institute for Nuclear Waste Disposal, Karlsruhe, Germany; [2]Freie Universität Berlin, Institute of Chemistry and Biochemistry, Berlin, Germany; [3]Molecular and Condensed Matter Physics, Uppsala University, Uppsala, Sweden

A general strategy for the determination of the Tc oxidation state involving X-ray Absorption Near Edge Spectroscopy (XANES) at the Tc L_3 edge is shown. A comprehensive series of ^{99}Tc compounds, ranging from oxidation states I to VII, was measured and subsequently simulated within the framework of crystal-field multiplet theory. This approach could be extended to numerous studies of Tc systems as this method is one of the most sensitive methods for Tc oxidation state and ligand characterization.[1]

^{99}Tc is primarily produced in bulk quantities in nuclear reactors and is considered as unwanted radioactive waste. The short-lived metastable nuclide ^{99m}Tc (γ-emitter, $t_{1/2}$ = 6.01 h) is the dominating isotope in routine diagnostic nuclear medicine with about 40 million administrations annually.
Nine known oxidation states exist, from −I to +VII, with +IV, +V, and +VII being the most common. Lower Tc oxidation states are commonly supported by π-acceptor ligands such as isocyanides, CO or NO^+. It has been shown that Tc^V, Tc^{III} and Tc^I compounds exhibit a diverse chemistry and are frequently used in nuclear medicine. Investigating these types of compounds and their specific coordination chemistry is crucial to determine and improve both their stability and their biological activity.

EXPERIMENTAL. The syntheses of $(NBu_4)[TcNCl_4]$,[2] $(NBu_4)[TcNBr_4]$,[2] $(NBu_4)[TcOCl_4]$[3], $(NBu_4)[TcOBr_4]$,[4] $[TcCl_4(PPh_3)_2]$,[5] $[TcCl_3(PPh_3)_2(CH_3CN)]$,[6] $[TcCl_3(PMe_2Ph)_3]$,[7] $[Tc(thiourea)_6]Cl_3$,[8] $(NBu_4)[Tc(NO)Br_4]$,[9] $(NBu_4)[Tc(NO)Cl_4(MeOH)]$,[10] $[Tc(NO)Cl_2(PPh_3)_2(CH_3CN)]$,[11] and $(NBu_4)[Tc_2(CO)_6Cl_3]$[12] followed published procedures. For the syntheses of $(NH_4)_2[TcCl_6]$ and $(NH_4)_2[TcBr_6]$, solutions of $(NH_4)TcO_4$ in HCl (37 %) or HBr (48 %) were heated under reflux for 10 min. $(NH_4)Cl$ or $(NH_4)Br$ were added and the products precipitated upon cooling as yellow or red crystals. The Tc L_3 edge XANES spectra were recorded at the INE-Beamline of the KARA (Karlsruhe research accelerator) facility in Karlsruhe, Germany. The entire sample environment was encased in a He box to allow for the detection of the low energy Tc fluorescence without any modifications to the sample.

RESULTS. The spectral shape of the Tc L_3 edge white line arises from transitions from the $2p_{3/2}$ to the 4d level. The Tc ground state electron configuration is $[Kr]4d^55s^2$. When Tc ionizes, it loses its valence 5s electrons before losing 4d electrons. Tc has seven valence electrons that can be lost, but the number of 4d electrons will be different only for Tc with oxidation states higher than +II. Therefore, the expected rising trend in the L_3 edge shift might be visible only for compounds starting from oxidation states +III to +VII (see Fig. 1). The simulated spectra reproduce the main edge features well, demonstrating the strong influence of crystal-field interactions in the Tc 4d shell. As expected, the Tc L_3 edge is much more sensitive to the oxidation state than Tc K edge XANES because the L_3 white line position depends directly on the number of 4d electrons. Additionally, Tc L_3 XANES is found to be more sensitive to the Tc speciation in various

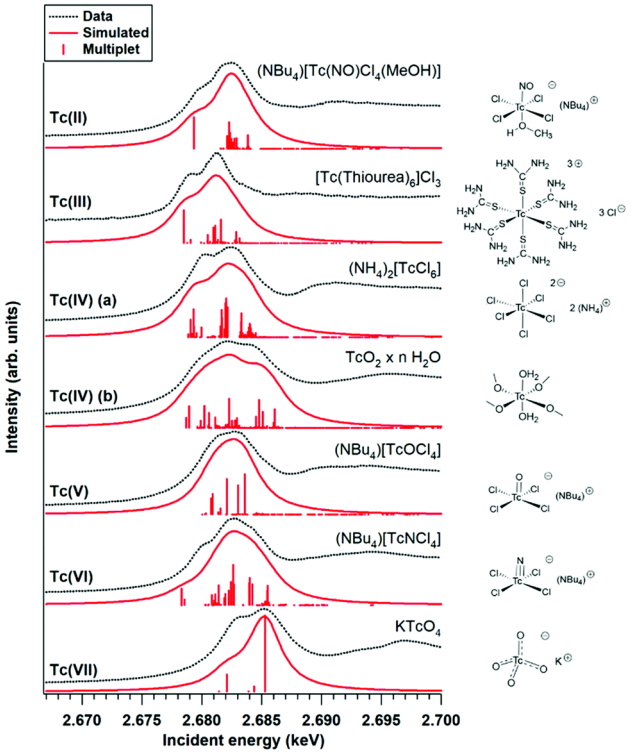

Fig. 1: Representative increasing oxidation state series of Tc L_3 edge XANES and the simulated spectra based on crystal-field multiplet theory. A representation of the local geometry is provided for each compound on the right hand side.

compounds. It can be explained by the fact that 4d orbitals have a rather large radius and thus overlap strongly with orbitals of neighboring atoms. We expect that this approach can be extended to numerous studies of Tc systems and can stimulate further Tc coordination chemistry research relevant to various fields of applications.

[1] Bauters, S. *et al.* (2020) *Chem. Commun.* **56**, 9608–9611
[2] Baldas, J. *et al.* (1984) *Dalton Trans.*, 2395.
[3] Davison, A. (1982) *Inorg. Synth.*, 160–162.
[4] Preetz, W. *et al.* (1980) *Zeitschrift für Naturforsch. B* **35**, 1355–1358.
[5] Mazzi, U. *et al.* (1976) *J. Inorg. Nucl. Chem.* **38**, 721–725.
[6] Pearlstein, R. M. *et al.* (1989) *Inorg. Chem.* **28**, 3332–3334.
[7] Bandoli, G. *et al.* (1976) *Dalton Trans.*, 125.
[8] Abrams, M. J. *et al.* (1984) *Inorg. Chem.* **23**, 3284–3288.
[9] Orvig, C. *et al.* (1981) *J. Labelled Comp. Radiopharm.* **18**, 148.
[10] Ackermann, J. *et al.* (2019) *J. Inorg. Gen. Chem.* **645**, 8–13.
[11] Blanchard, S. S. *et al.* (1996) *Inorg. Chim. Acta* **244**, 121–130.
[12] Hildebrandt, S. (2018) PhD Thesis, FU Berlin.

Implementation of a 'Rolling Ball' algorithm for spectroscopy

B. Drobot, M. Vogel,[1] R. Steudtner, A. Rossberg, H. Foerstendorf

[1]HZDR Innovation GmbH, Dresden, Germany

The 'Rolling ball' algorithm was applied to spectroscopic and spectrometric data for background subtraction obviating the restrictions of polynomial and spline functions.

The adequate subtraction of background contributions in optical spectra containing a high noise level is often challenging, in particular for quantitative analysis. This is mainly due to the impossibility to isolate the intrinsic background from the signal. Polynomial and spline functions are usually applied to simulate native background. As the degree of the polynomials as well as the number and position of interpolation points could not be determined automatically, the selection of these parameters might be significantly biased by the user. The 'Rolling Ball' algorithm inspired by Stanley Sternberg is applied to reduce subjective assessment during data evaluation processes. This algorithm is implemented for images in the ImageJ software package.[1]

METHODOLOGY. The algorithm was originally developed to remove gradient of images, *e. g.* of protein gels. Its name based on the idea, that the contact points of a ball rolling over (or under) an image is representing the background. For dimensional reduced data sets, the dimension of the ball is reduced to a circle (ellipsoid). A graphical illustration of the algorithm is presented in Fig. 1.

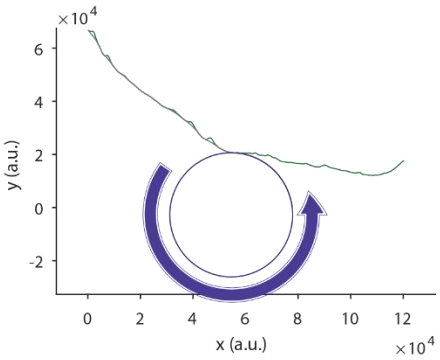

Fig. 1: Illustration of the Rolling Ball algorithm for data vectors. A circle (blue) is rolling along the data (green) and the maximum of its trace is used as background (gray).

Thus, the only user defined parameter is the radius of the ball. Once the radius is chosen, it could be applied for entire datasets, even with backgrounds of different shapes. This makes the background subtraction routine less user biased.

RESULTS. The 'Rolling Ball' algorithm has been applied for infrared (IR) absorption, Raman and luminescence emission spectra, and HPLC chromatograms. The ball radius was set to the length of the datasets and thus big enough to prevent the ball from dipping into signal. As shown in Fig. 2, an appropriate background is found for all data sets. For luminescence spectra, the shapes of the backgrounds is dramatically different. An accurate background subtraction is not feasible with spline or polynomial functions without an adjustment of the parameters during processing.
The algorithm is compatible with noisy data after smoothing procedure. It had to be mentioned, that kinked or discontinuous backgrounds cannot be estimated by the rolling ball, since those effects are too similar to the signal.

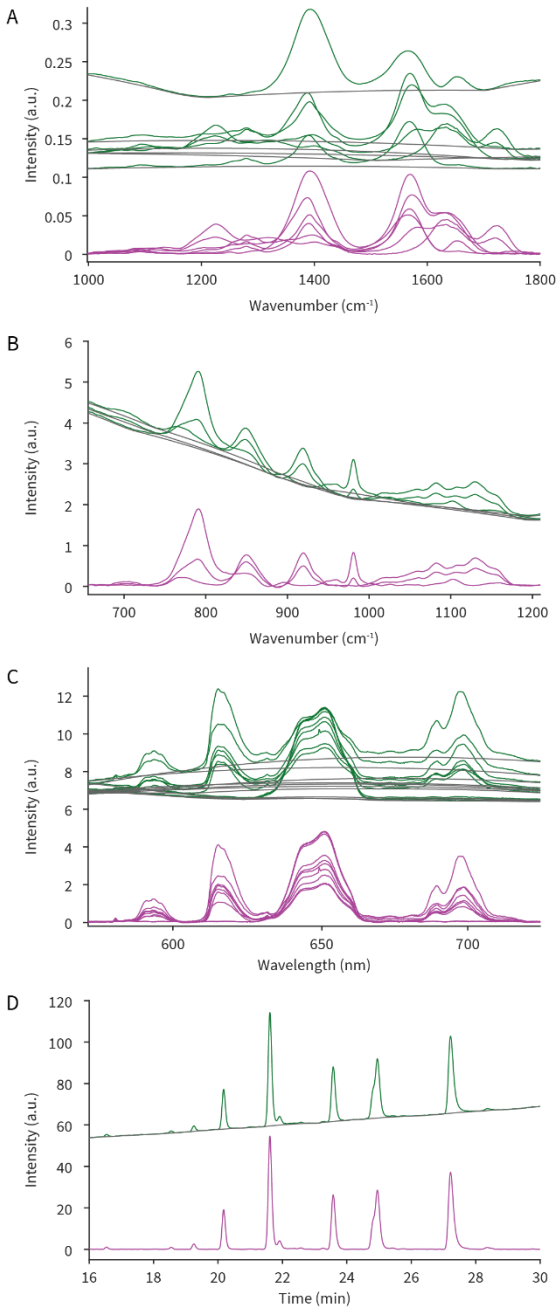

Fig. 2: Examples for the application of the 'Rolling Ball' algorithm. Shown are experimental data (green), background generated by the 'Rolling Ball' algorithm (gray) and final data after background correction (magenta) for IR (A), Raman (B), fluorescence spectra (C), and an HPLC chromatogram(D).

[1] Sternberg, S. (1983) IEEE Computer **16**, 22–34.

Electrochemical synthesis of aqueous Pu stock solutions in chloride media

N. Huittinen, S. Shams Aldin Azzam, S. Weiss, H. Foerstendorf

Aqueous Pu solutions of oxidation states +III, +IV, and +VI were electrochemically synthesized in chloride media. The purity grade obtained was about 100 and 85 % for Pu(III/IV) and Pu(VI), respectively, as monitored by *in situ* photometry. The long-term stability of the Pu(III) solution and the harsh conditions necessary for the oxidation of Pu(IV) to obtain Pu(VI) suggests a strongly stabilizing effect of Pu(III/IV) chloro complexes.

According to demands at the IRE from biological tasks and certain analytical techniques, a preparation of Pu stock solutions containing selective oxidation states at high purity grade in chloride matrix was mandatory. Therefore, we set up an electrochemical experiment providing an *in situ* monitoring of the prevailing oxidation states by photometry.[1]

EXPERIMENTAL. All electrochemical experiments (potentiostat Autolab PGSTAT302, Metrohm) were performed with a cell consisting of a quartz glass vessel (~20 mL) and a home-built Teflon lid providing drillings for the fixation of the electrodes. The vessel is mounted on a special rack equipped with apertures for mounted fiber optics (Fig. 1).

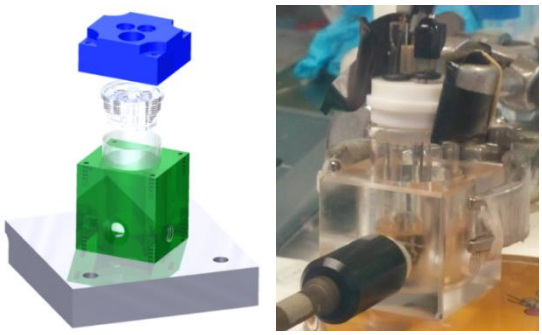

Fig. 1: Technical drawing of the electrochemical cell (left) and set up of the experiment (right) with mounted electrodes and fiber optics for *in situ* photometric measurements.

Photometric monitoring was performed with a spectrometer setup from Avantes (AvaSpec-2048x14). All experiments were performed under continuous stirring in a glove box under inert gas atmosphere except where noted.
The initial ^{242}Pu(IV) solution was purified from ^{241}Am(III) by extraction chromatography (TEVA Resin) to reduce the overall dose.[2] After filtration through a 0.45 µm polypropylene filter to remove potential column residues, an Am-free Pu-stock solution was obtained (~12.5 mM Pu/ ~0.1 M HCl) as verified by γ- and α-spectrometry.

RESULTS. The initial solution (9 mL of ~3 mM Pu(IV) in 4 M HCl) contained nearly 100 % Pu(IV) as verified by photometry.
Synthesis of aqueous Pu(III). Preliminary electrochemical experiments showed that Pu(III) could be successfully obtained in 4 M HCl. Further experiments were performed at lower ionic strength (~0.1 M) which lowers the reduction rate, but a pure Pu(III) solution was eventually obtained after several hours of reduction at a voltage of −0.6 or −0.4 V. For further sorption and complexation experiments, the Pu(III) solution was adjusted to pH 4 as described in [3]. This solution was stored in a sealed quartz glass vessel in the dark at ambient conditions for about six months showing almost no formation of oxidation products after this period of storage.

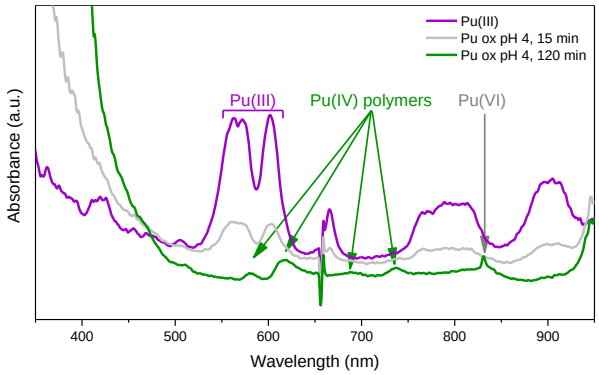

Fig. 2: Photometric spectra of the Pu solution recorded before and after 15 and 120 min of electrolysis at pH 4 demonstrating the formation of colloidal Pu(IV) and a very small fraction of Pu(VI).

Colloidal Pu(IV). The formation of colloidal Pu(IV) at pH 4 was observed by complete oxidation of Pu(III) at +1.7 V for 2 h (Fig. 2). The green-colored solution obtained remained suspended even without any applied stirring. After lowering the pH with 40 µL 4 M HCl and prolonged reduction overnight, interconvertible reduction to Pu(III) was completely achieved.
Oxidation to Pu(VI). As oxidation to Pu(VI) was observed neither at high ionic strengths (4 M HCl) nor in carbonate media in the alkaline pH range, the setup was placed in a fume hood where an influx of ozone into the reaction vessel was feasible. The evolution of Pu(VI) preferentially occurred at slightly acidic pH, reduced ionic strength, highly oxidizing conditions provided by O_3 and during prolonged electrolysis (Fig. 3). After 40 h of electrolysis, a Pu(VI) solution containing 85 % Pu(VI) and 15 % Pu(IV) was obtained.[1]

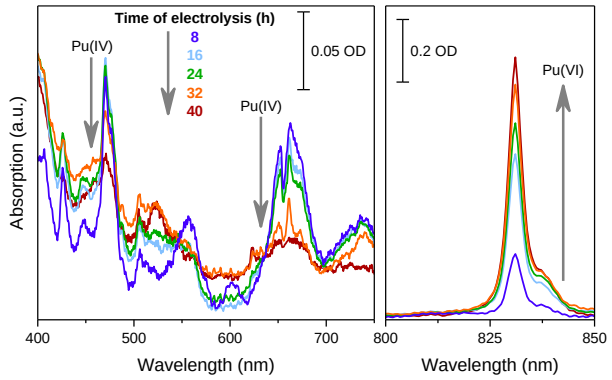

Fig. 3: Photometric spectra of a Pu solution recorded at different times of electrolytic oxidation with influx of ozone. The arrows indicate the decreasing and increasing intensities of the predominant spectral characteristics of Pu(IV) (left panel) and Pu(VI) (right panel), respectively.

This technical paper demonstrates the feasibility of electrochemical preparation of aqueous Pu solutions showing a high selectivity of oxidation states in a chloride matrix. The harsh conditions necessary to generate Pu(VI) and the long-term stability of the Pu(III) solution generally suggests a high thermodynamic stability of the Pu-chloro-species.

[1] Clark, D. L. *et al.* (2010) in: *The Chemistry of the Actinide and Transactinide Elements*, p. 813–1264, Springer, Dordrecht.
[2] Horwitz, E. P. *et al.* (1995) *Anal. Chim. Acta.* **310**, 63–78.
[3] Acker, M. *et al.* (2021) this report, p. 17.

Long-Lived *Radionuclides* & Transport Phenomena in

GEOLOGICAL SYSTEMS

Sorption of curium(III) on crystalline rock material

M. Demnitz, K. Molodtsov, S. Schymura, A. Schierz, K. Müller, M. Schmidt

Cm(III) sorption on heterogeneous crystalline rocks was correlatively investigated using spatially-resolved techniques. Sorption uptake and speciation of Cm(III) between different and on the same mineral grains depends on mineralogy and surface roughness.

EXPERIMENTAL. Two thin sections were prepared from two crystalline rocks, a granite from Eibenstock, Germany, and a migmatised gneiss from Bukov, Czech Republic. Sorption experiments were performed over the course of a week using a 1 µM solution of Cm(III) (pH 8, 0.1 M NaCl). Using interferometry, the surface topography of the thin sections was characterized from which the surface roughness was calculated. The entire thin sections were further analyzed using calibrated autoradiography to quantify sorption uptake.

To evaluate the retention potential of the rocks, the speciation of Cm(III) on the mineral surface must be determined on the molecular level. To this end, smaller regions of interests (ROIs) in the range of 1×1 mm were investigated by µTRLFS (micro-focus time-resolved laser-induced fluorescence spectroscopy).[1] Each luminescence map obtained consisted of 2,601 pixels with one pixel corresponding to one Cm(III) luminescence spectrum. Sorption uptake was then derived from each pixel's integral luminescence intensity (Fig. 1c). To obtain speciation information, all Cm(III) spectra were fitted using Gaussian functions. This provided the wavelength of the Cm(III) peak maxima (Fig. 1d), where stronger red-shifts correlate to stronger bonds to the mineral grain's surface. To further analyze the speciation, the luminescence decay was measured for selected spots. From the determined luminescence lifetimes the number of species present at the surface and the number of water molecules in the first hydration shell of Cm(III) were derived. In addition, Raman microscopy revealed the underlying mineralogy (Fig. 1a).

RESULTS. Generally, the sorption uptake of Cm(III) was highest on mica-like minerals, intermediate to high on feldspars, and smallest on quartz, which fits well with previous studies of Eu(III) sorption on the same crystalline rocks.[1,2] A new finding is that this observation only reflects areas exhibiting a low surface roughness. With increasing surface roughness sorption uptake on quartz and feldspar increases by one to two orders of magnitude. Such an increased sorption uptake was also seen at surface features such as mineral grain boundaries, defects and cracks (Fig. 1b).

Highest luminescence intensities (LI) were measured on feldspar and epidote, while LIs on quartz were lower (Fig. 1c). Mica and amphibole did not show any luminescence since they are Fe-bearing minerals, therefore quenching the luminescence of Cm(III).

Speciation was investigated by examining the Cm(III) peak position. On quartz mainly strong inner-sphere sorption takes place (602–605 nm), generally showing a homogeneous speciation of Cm(III) on the quartz surface (Fig. 1d).

On feldspar the speciation was found to be less homogeneous on both crystalline rocks (600–605 nm). On both, quartz and feldspar, the Cm(III) peak maximum was more red-shifted (603 – 605 nm) for regions with a higher surface roughness than for lower surface roughness areas (602–603 nm). This clearly shows that the surface roughness has a measurable effect on the speciation of Cm(III) on the mineral surface, and not just the sorption quantity.

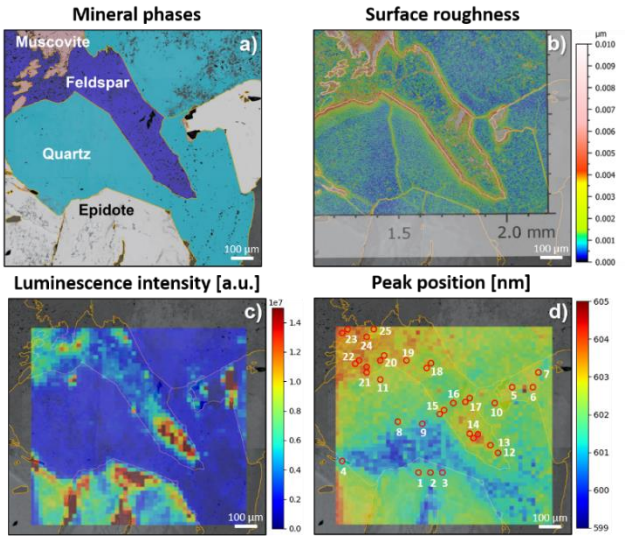

Fig. 1: ROI analysis to determine mineralogy using Raman-microscopy (a), surface roughness using interferometry (b), sorption uptake using µTRLFS (c), and peak maximum positions by Gaussian peak fitting and in red measured luminescence lifetime spots (d).

To better characterize the speciation, lifetime analysis was performed, which showed that on quartz and feldspar with increasing surface roughness the number of water molecules surrounding Cm(III) decreases, meaning that Cm(III) surface complexation becomes stronger. This can be explained by areas of high surface roughness possessing a larger number of kink and defect sites.[3] Sorption at these sites allows Cm(III) to form more bonds to the mineral surface, replacing water molecules from the hydration shell, while also inducing the previously described red-shift of the peak maxima. A similar explanation was hypothesized previously, regarding the inhomogeneous distribution of Eu(III) sorbed on quartz in Eibenstock granite.[1]

In our studies we could show that sorption of Cm(III) and its speciation on the millimeter and centimeter scale is dependent on the mineralogy and the topography of the available surfaces on the nanometer scale. Surface roughness has an impact on the amount of Cm(III) sorbed on the surface as well as the speciation of Cm(III) on the mineral surface.

ACKNOWLEDGEMENTS. We gratefully acknowledge the funding provided by the German Federal Ministry of Education and Research (BMBF) (Grant 02NUK053E) and The Helmholtz Association (Grant SO-093). UJV Řež is acknowledged for providing the Bukov migmatised gneiss drill core.

[1] Molodtsov, K. *et al.* (2018) *Sci. Rep.* **9** (1).
[2] Molodtsov, K. *et al.* (2021) *Environ. Sci. Technol.*, submitted.
[3] Fischer, C. *et al.* (2014) *Appl. Geochem.* **43**, 132–157.

Development of a generic surface complexation model for the sorption of trivalent actinides and lanthanides on orthoclase

H. Brinkmann, J. Neumann, S. Britz,[1] J. Lützenkirchen,[2] F. Bok, M. Stockmann, V. Brendler, T. Stumpf, M. Schmidt

[1]Gesellschaft für Anlagen- und Reaktorsicherheit gGmbH, Braunschweig, Germany; [2]Karlsruhe Institute of Technology (KIT), Institute for Nuclear Waste Disposal, Karlsruhe, Germany

In this study a surface complexation model (SCM) for the sorption of various trivalent rare earth elements and actinides (unified to M^{3+}) on orthoclase was developed. A generic approach was used to keep the model as simple as possible and simultaneously to cover many similar elements. Four surface complexes are responsible for the retention of M^{3+} on orthoclase, for which reliable formation constants were determined.

EXPERIMENTAL. The sorption of different trivalent lanthanides (Y, La, Nd, Eu, Lu) and Am on orthoclase was investigated under different experimental conditions ([M^{3+}], ionic strength, grain size, solid-liquid ratio). The experimental procedure is described elsewhere.[1] In total, 201 observations from 13 experimental series were used to develop an SCM. As the different trivalent metals showed a comparable behavior under the same experimental conditions (Fig. 1), only one generic trivalent metal, M^{3+}, was considered. The thermodynamic data of Eu^{3+} in the ThermoChimie-TDB (10a, Version of Sept. 26, 2018) was used to calculate the aqueous speciation of M^{3+}. The SCM development was a stepwise process and the model was evaluated after each addition of a surface complex (SC). To fit formation constants of considered SCs, the parameter estimation code UCODE 2014 (version 1.004)[2] was coupled with the geochemical speciation code PhreeqC (version 3.5.2),[3] while the diffuse layer model was applied.[4] All observations were simultaneously used to fit surface complexation parameters (SCP). A bidentate coordination of M^{3+} to surface functional groups (≡S-OH) was assumed. A log K of −2.5 for the deprotonation of these groups was separately determined by column titration experiments.[1]

RESULTS. Four SCs are necessary to adequately reproduce experimental batch data under the various experimental conditions. All formation reactions as well as their optimized formation constants are listed in Tab. 1.

Tab. 1: Formation constants of the considered surface complexes with their nonlinear confidence intervals.

Species	Equation	Log *K*	Nonlinear conf. int.
SC-1	$2\ \equiv S\text{-}OH + M^{3+} \leftrightarrow (=S\text{-}OH)_2M^{3+}$	−3.4	−3.1 / −3.8
SC-2	$2\ \equiv S\text{-}OH + M^{3+} \leftrightarrow (=S\text{-}O)_2M^{+} + 2H^{+}$	−8.0	−7.7 / −8.6
SC-3	$2\ \equiv S\text{-}OH + M^{3+} + 2H_2O \leftrightarrow (=S\text{-}OH)_2M(OH) + 3H^{+}$	−11.6	−11.3/−12.1
SC-4	$2\ \equiv S\text{-}OH + M^{3+} + 2H_2O \leftrightarrow (=S\text{-}OH)_2M(OH)_2^{-} + 4H^{+}$	−16.6	−16.1/−17.4

The species SC-1, in which M^{3+} is coordinated to two protonated surface groups, improves the fit for low M^{3+} concentrations at low pH values. Deprotonation of the surface groups leads to the formation of SC-2. Its two hydrolysis forms SC-3 and SC-4 are necessary to reproduce the immobilization at higher pH values. The existence of SC-2 to SC-4, which can be seen as inner sphere complexes, was supported by time-resolved laser-induced fluorescence spectroscopy (TRLFS) measurements, using Cm^{3+} as luminophore.[1]

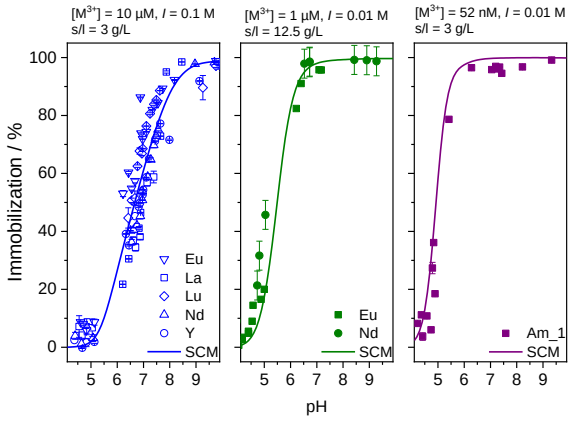

Fig. 1: Experimentally observed sorption of M^{3+} to orthoclase (symbols) and simulations for different selected experimental conditions (adapted and modified from [1]).

Figure 1 shows experimentally determined values (symbols) for different experimental conditions and different M^{3+} in comparison with simulations (lines), using SC-1 to SC-4. The agreement between experimental and simulated values is very good for all conditions and all different M^{3+}, which verifies the generic approach.

High robustness of the model is provided by the huge experimental data on which this model was built. Furthermore, the spectroscopic identification of the inner sphere complexes increases the reliability of the proposed SCM. The consideration of spectroscopic data during the fitting procedure, which is described in [1], leads to similar log K values. Furthermore, the proposed model yields reliable simulations, which were successfully validated for two individual and independent experimental literature data sets (detailed information is given in [1]).

The derived SCP values close an important gap in the thermodynamic database for the interaction of trivalent metals, relevant for nuclear waste disposal, and their interaction with mineral phases. Furthermore, they will be used to extend the database of the Smart K_d-concept,[5] which is a modern approach for the simulation of radionuclide transport, which in turn contributes to a better safety assessment of repositories for radioactive waste.

ACKNOWLEDGEMENTS. This work was supported by the Federal Ministry for Economic Affairs and Energy (BMWi) through the SMILE project with grants 02E 11668A and 02E 11668B.

[1] Neumann, J. *et al.* (2021) *J. Colloid Interface Sci.*, in press.
[2] Poeter, E. P. et al (2014) *UCODE_2014, with new capabilities to define parameters unique to predictions, calculate weights using simulated values, estimate parameters with SVD, evaluate uncertainty with MCMC, and more.* Integrated Groundwater Modeling Center Report Number GWMI 2014–02.
[3] Parkhurst, D. L. & Appelo, C. A. J. (2013) https://doi.org/10.3133/tm6A43.
[4] Dzombak, D. A. & Morel, F. M. M. (1990) *Surface Complexation Modeling: Hydrous Ferric Oxide*, John Wiley & Sons, Inc.
[5] Stockmann, M. *et al.* (2017) *Chemosphere* **187**, 277–285.

First sorption results of Np(V) on ZrO_2

I. Jessat, H. Foerstendorf, N. Jordan

Batch sorption experiments of Np(V) onto zirconia (ZrO_2) revealed a fast, pH-dependent sorption process. The isoelectric point (pH_{IEP}) of the ZrO_2 was found at pH 8.3 by zeta potential measurements. Np(V) concentrations in the lower micromolar range do not significantly impact the pH_{IEP}, whereas a shift to higher pH values was found with increasing Np(V) concentrations.

For the safety assessment of a nuclear waste repository, the interactions of long-lived radionuclides, such as neptunium, with corroded phases in the near field of the repository have to be considered. Zirconia is the corrosion product of the zircaloy cladding material of spent nuclear fuel rods and thus may represent one of the first barriers for radionuclides.

EXPERIMENTAL. All batch experiments (Tab. 1) were performed under inert gas (N_2) conditions with a ZrO_2 solid-to-liquid ratio of 0.5 g L^{-1}. Except for the time dependent investigations, samples were equilibrated for three days and subsequently centrifuged (1 h; 4,020 × g). Concentrations of Np-237 in the supernatants were derived from liquid scintillation counting. For experiments conducted at 0.01 M NaCl, zeta potential measurements were performed before centrifugation under exclusion of CO_2.

Tab. 1: Experimental conditions of the Np(V) batch sorption experiments. Concentrations and ionic strengths are given in mol L^{-1}.

Variable	pH	Time	[Np(V)]	*I* (NaCl)
Time	8	1 h–7 d	10^{-6}	0.1
pH/*I*	3–10	3 d	10^{-6}	0.01 or 0.1
[Np(V)]	9	3 d	10^{-6}–5×10^{-5}	0.01

The zeta potentials of the pure ZrO_2 suspension (0.5 g L^{-1}) were measured to determine the pH_{IEP} of the mineral. The samples were prepared with background electrolyte concentrations of 0.005 or 0.01 M NaCl and shaken for three days.

RESULTS. Time-dependent batch experiments revealed that complete sorption occurred after a few hours (data not shown). The pH series at 0.01 M NaCl showed a broad sorption edge reaching a maximum at pH ≥ 7 (Fig. 1).
Under inert conditions, the predominant aqueous species is expected to be the fully hydrated neptunyl ion (NpO_2^+) in the investigated pH range.[1, 2] The presence of chloro species, such as NpO_2Cl (aq), can be neglected.[3] Thus, the increased sorption at higher pH is due to interactions of the NpO_2^+ species with a more negatively charged ZrO_2 surface. Two batch samples with a higher ionic strength (0.1 M NaCl) showed no impact on the Np(V) sorption suggesting the predominant formation of inner-sphere complexes (Fig. 1).
The pH_{IEP} of the solid phase was found at pH 8.3 (Fig. 2) and is in agreement with literature values.[4, 5] Thus, complete sorption of Np(V) was already observed below the pH_{IEP} of the zirconia.
The zeta potential curves at 0.01 M NaCl obtained in the presence and absence of 10^{-6} M Np(V) are shown in Fig. 2. All curves are in very good agreement, indicating no significant impact on the zeta potential by the sorption of Np(V). Further experiments were conducted at 0.01 M NaCl and pH 9 but with higher Np(V) concentrations of up to 5×10^{-5} M. The sorption curves and zeta potential plots are shown in Figs. 1 and 3, respectively.

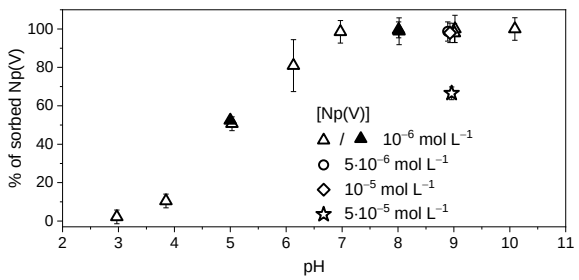

Fig. 1: Sorption edges of Np(V) on ZrO_2 at different Np concentrations at (filled symbols) 0.1 M NaCl and (open symbols) 0.01 M NaCl (solid/liquid ratio: 0.5 g L^{-1}).

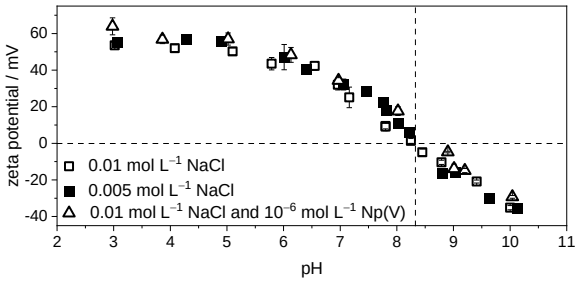

Fig. 2: Zeta potential curves of ZrO_2 suspensions at different NaCl concentrations and in presence of 10^{-6} M Np(V) (solid/liquid ratio: 0.5 g L^{-1}).

Only the highest Np(V) concentration of 5×10^{-5} M showed that sorption is significantly reduced at alkaline pH values (Fig. 1). However, an increase of the zeta potential to nearly same extent could be observed for Np(V) concentrations higher than 10^{-6} M at pH 9 (Fig. 3). These findings suggest a possible saturation effect occurring at higher Np(V) concentrations. Spectroscopic investigations (IR, XAS) will be conducted to gain a better understanding of the Np(V) sorption processes on the molecular scale.

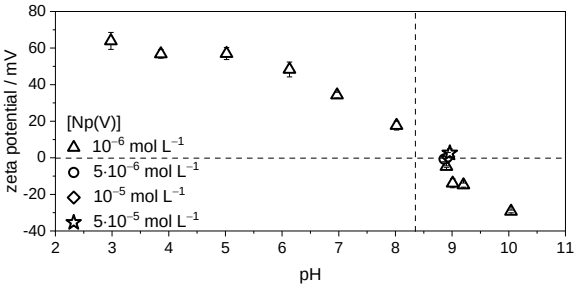

Fig. 3: Zeta potential curves of ZrO_2 suspensions in presence of Np(V) at different concentrations (solid/liquid ratio: 0.5 g L^{-1}; I = 0.01 mol L^{-1} NaCl).

[1] Neck, V. *et al.* (1992) *Radiochim. Acta* **56**, 25–30.
[2] Lierse, C. *et al.* (1985) *Radiochimica* **38**, 27–28.
[3] Müller, K. *et al.* (2015) *Environ. Sci. Technol*. **49**, 2560–2567.
[4] Kosmulski, M. (2003) *Colloids Surfaces A Physicochem. Eng. Asp.* **222**, 113–118.
[5] Kosmulski, M. (2016) *Adv. Colloid Interface Sci.*, **238** 1–61.

Effect of background electrolyte composition on the formation of Th(IV) nanoparticles on the muscovite (001) basal plane

J. Neumann, C. Qiu, P. Eng,[1] S. Skanthakumar,[2] L. Soderholm,[2] T. Stumpf, M. Schmidt

[1]University of Chicago, Chicago, IL, U.S.A.; [2]Argonne National Laboratory, Lemont, IL, U.S.A.

We study the impact of background electrolyte composition on the sorption of Th(IV) on mica (001). Surface X-ray diffraction and *in situ* AFM show the formation of Th nanoparticles. Two main retention mechanisms are identified: At low [Th] = 0.1 mM, oligomerization occurs at the mineral-water interface (heterogeneous nucleation) and is strongly influenced by the electrolyte. A strong decrease in Th uptake is observed from Li to Cs in the alkali series, with Na as a clear outlier in this series, showing much lower uptake than expected according to the trend. At high [Th] = 3 mM, retention occurs by the formation of Th oligomers in solution (homogeneous nucleation) and their subsequent sorption onto the mineral surface. This second process appears to be largely independent of the electrolyte.

Actinide nanoparticle (NP) formation is known to have an influence on radionuclide mobility in the environment. For a reliable safety assessment of nuclear waste repositories, a fundamental understanding of the formation of actinide NPs as well as their interactions with charged mineral surfaces is thus important.

Previous studies investigated the retention of Th(IV) on muscovite using surface X-ray diffraction (SXD) and reported an unusual trend of Th(IV) uptake on muscovite (001), depending on the electrolyte composition ($LiClO_4$ > $KClO_4$ > $NaClO_4$).[1,2] In case of $LiClO_4$, Th uptake (4.9 Th/A_{UC}, A_{UC}: area of mica (001) unit cell) was observed to be higher than required for compensation of the mica basal plane's surface charge (1 e^-/A_{UC}), indicating particle formation. However, the reaction mechanisms remained unclear. Therefore, we applied SXD and *in situ* AFM to shed light onto the reactions causing the electrolyte effect on the retention of Th(IV) on muscovite (001).

EXPERIMENTAL. For SXD and *in situ* AFM measurements solutions of 0.1 and 3 mM $Th(NO_3)_4$ and 0.1 M ACl (A = Li, K, NH_4, Cs) at pH 3.2 were prepared. The reaction occurred over night by dropping a freshly cleaved muscovite crystal into the sample solution.

SXD was performed at beamline 13-ID-C at the Advanced Photon Source. Experimental details can be found elsewhere.[1] *In situ* AFM was performed using an Asylum Research Cypher ES instrument with Bruker MSNL-10 silicon tips in tapping mode with a resonance frequency of ~9 kHz. SPIP software was used for image processing. For grain size analysis, particles were automatically detected by a height threshold of 1 nm.

RESULTS. At low [Th] = 0.1 mM, a rather broad Th electron density (ED) is observed for all investigated electrolytes ACl (A = Li, K, NH_4, Cs), reaching up to ~50 Å in case of LiCl (exemplarily shown in Fig. 1, top) and KCl. The observed Th uptakes decrease strongly within the alkali ion series and a linear correlation (R^2 = 0.9962) to the ionic radius of the electrolyte cation is observed (Fig. 2, left), suggesting competitive sorption of Th^{4+} and A^+. With increasing ionic radius, the hydration energy of the electrolyte cation decreases, leading to an increased tendency to adsorb as inner-sphere sorption complexes,[3] which seem to be preferable over the sorption

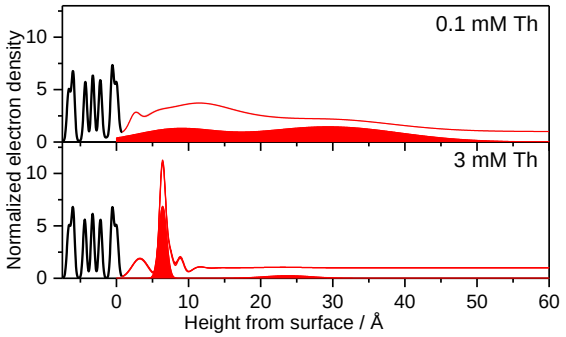

Fig. 1: Total electron density (lines) and Th contribution (filled area) of samples reacted with 0.1 and 3 mM $Th(NO_3)_4$ and 0.1 M LiCl at pH 3.2 ± 0.1.

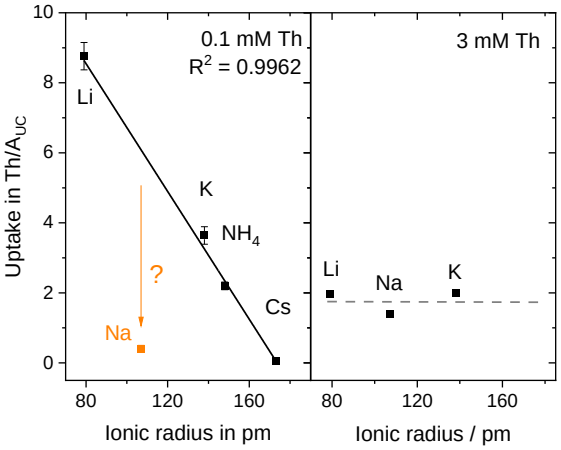

Fig. 2: Th coverage for samples reacted with 0.1 mM (left) or 3 mM (right) $Th(NO_3)_4$ and 0.1 M ACl (A = Li, Na, K, NH_4, Cs) at pH = 3.2 ± 0.1.

of Th^{4+} and inhibits the subsequent particle formation. However, the reported value for NaCl is a clear outlier in this series, showing lower Th uptake than expected according to the trend.[2] The occupancies from SXD are in perfect agreement with the number of particles per area, obtained from grain size analysis of *in situ* AFM images. The particles have a median height of ~1–2 nm and lateral size of ~10–20 nm, typical for particles formed at mineral surfaces (heterogeneous nucleation), which is known to be influenced by the aqueous chemistry of the solution.

At high [Th] = 3 mM oligomerization of Th(IV) is known to occur in solution. The interfacial structures of all samples are dominated by a large amount of Th ED at a distinct height from the surface (~6.5 Å, see Fig. 1, bottom). Here, LiCl (2.0 Th/A_{UC}), KCl (1.7 Th/A_{UC}), and NaCl (1.4 Th/A_{UC}) show comparable Th uptakes (Fig. 2, right). Based on the results, it is suggested that Th oligomers form in solution (electrolyte-independent) by homogeneous nucleation, which sorb onto the surface.[4]

[1] Schmidt, M. *et al.* (2015) *Geochim. Cosmochim. Acta* **165**, 280–293.
[2] Schmidt, M. *et al.* (2012) *Geochim. Cosmochim. Acta* **88**, 66–76.
[3] Lee, S. S. *et al.* (2012) *Langmuir* **28**, 8637–8650.
[4] Neumann, J. *et al.* (2021) in preparation.

Tc removal by Sn and Mn pre-sorbed on alumina

N. Mayordomo, T. Füssel, D. M. Rodríguez, K. Müller

A well-known methodology to immobilize Tc consists of reducing the highly mobile $Tc^{VII}O_4^-$ to Tc^{IV} since its most stable species is a low soluble oxide. We have studied the aqueous scavenging of Tc by redox-active Mn^{II} and Sn^{II} pre-sorbed on alumina as a function of pH. It was shown that Tc was quantitatively removed ($K_d \approx 10^5$ L/g) from solution when using Sn pre-sorbed on alumina. K_d ranges from 50 L/g to 600 L/g when Tc is immobilized by Mn pre-sorbed on alumina.

Soluble Sn^{II} has been used for years as Tc reductant in solution (homoreduction),[1] whereas the reductant behavior of Mn^{II} has not been analyzed up to date. Previous works reported that Tc reduction is highly enhanced when Fe is sorbed on a mineral phase (heteroreduction).[2]

EXPERIMENTAL. All the experiments were performed in a N_2 glove box (O_2 < 0.5 ppm). The alumina used in the experiments has been previously characterized.[3] For the batch sorption experiments, suspensions of alumina containing XCl_2 (60 μM, where X = Mn or Sn) at different pH values have been in contact for seven days. Consecutively, the samples were centrifuged, the pH was measured and the supernatant sampled to determine the remaining X concentration in solution by ICP-MS. Then, the supernatant was discarded and the solid was dried inside the glove box. Once dried, the solid was re-suspended using a solution containing 5 μM Tc^{VII}. After seven days in contact, the samples were centrifuged, the pH and redox potential (Eh) were measured and the supernatant was sampled for quantification of Tc concentration in solution by liquid scintillation counter.
The sorption yield of Y (where Y = Tc, Mn or Sn) was calculated as a distribution coefficient (K_d) using the equation:

$$K_{d_Y} = \left(\frac{[[Y]_0 - [Y]_t]}{[Y]_t} \cdot \frac{V}{m}\right) \quad (1)$$

where V is the volume of suspension in L, m is the mass in g, and $[Y]_0$ and $[Y]_t$ are the initial and final molar concentrations of Y, respectively.

RESULTS. The sorption of Mn^{2+} on alumina increases with increasing pH, being maximum for pH > 9, whereas Sn^{2+} sorption on alumina is maximum for the entire range of pH evaluated and it only decreases at pH > 9 (Fig. 1). Mn^{2+} follows the trend of cation adsorption on metal oxides, which is favored because of electrostatic attraction of the negatively charged alumina surface and the cation.[3] Sn^{2+} is sorbed on the entire range of pH but the sorption mechanism is still to be determined as $Sn(OH)_2$ was not observed.
Once the solid pre-sorbed with X is dried, a solution containing Tc is added. Figure 2 shows K_{dTc} values when using alumina containing Sn pre-sorbed. They are one to two orders of magnitude higher than those by alumina with Mn pre-sorbed. This is due to the fact that the oxidation reaction of Mn^{2+} to MnO_2 is not as favored as the oxidation of Sn^{2+} to Sn^{4+}, thus a higher amount of Tc^{VII} remains in solution. However, at most of the evaluated pH values, the Tc sorption by Mn^{2+} pre-sorbed on alumina is enhanced compared to neat alumina, whose *Kd* maximum is 150 L/g.[4] This suggests that when Mn^{2+} is sorbed on alumina, its redox potential might be modified to favor the reduction of Tc^{VII} to Tc^{IV}. Nevertheless, this hypothetized redox potential modification is not sufficient to produce a quantitative Tc removal from solution, as it happens when alumina containing Sn pre-sorbed is used as sorbent.

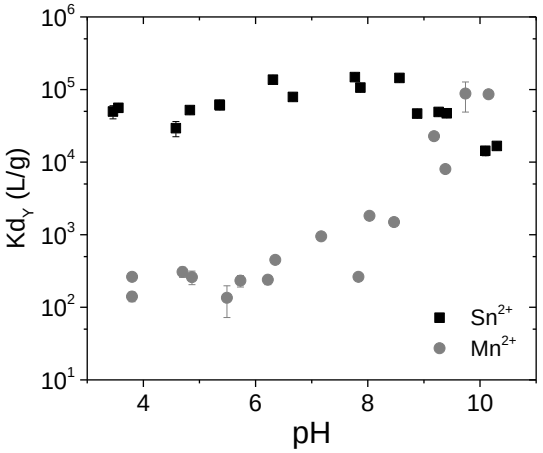

Fig. 1: Sorption of Y (Y = Sn^{2+} or Mn^{2+}) on alumina in H_2O as a function of pH.

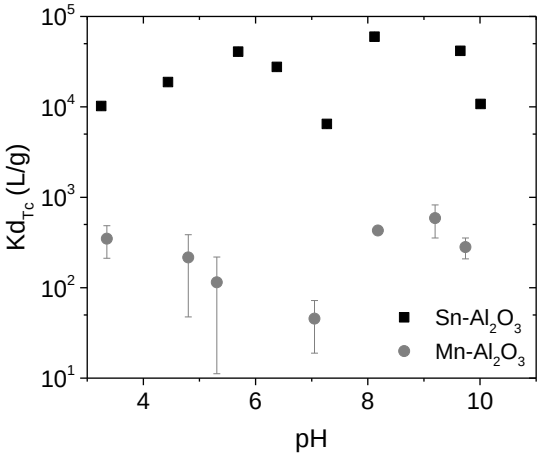

Fig. 2: Sorption of Tc promoted by Sn^{2+} or Mn^{2+} pre-sorbed on alumina in H_2O as a function of pH.

With respect to our recent study of alumina pre-sorbed with Fe^{2+},[4] the overall Tc heteroreduction in the presence of different reductants follows this order: $Sn^{2+} > Fe^{2+} > Mn^{2+}$. Further investigations are in progress to evaluate the advantages of using Sn as Tc heteroreductant instead of homoreductant.

ACKNOWLEDGEMENTS. This work was financed by the VESPA II project (02E11607B), funded by the German Federal Ministry of Economic Affairs and Energy (BMWi). We thank K. Schmeide for the Tc-glove box and S. Beutner for ICP-MS measurements.

[1] Owunwanne, A. *et al.* (1977) *J. Nucl. Med.* **18**, 822–826.
[2] Cui, D., Eriksen, T. E. (1996) *Environ. Sci. Technol*. **30**, 2259–2262.
[3] Mayordomo, N. *et al.* (2018) *Environ. Sci. Technol.* **52**, 581–588.
[4] Mayordomo, N. *et al.* (2020) *J. Hazard. Mater*. **388**, 122066.

New insights on the reductive immobilization of ^{99}Tc(VII) by iron sulfide

D. M. Rodríguez, N. Mayordomo, D. Schild,[1] V. Brendler, K. Müller, T. Stumpf

[1]Karlsruhe Institute of Technology (KIT), Institute for Nuclear Waste Disposal, Karlsruhe, Germany

The reductive immobilization of ^{99}Tc(VII) by pure pyrite and a synthetic mixture marcasite-pyrite 60:40 was studied by batch experiments, Raman microscopy and X-ray photoelectron spectroscopy (XPS). It was found that the presence of marcasite makes the retention slower and incomplete at pH 10 due to the change of redox active species with respect to pyrite: S^{2-} instead of Fe^{2+}.

Fe(II) minerals have shown a remarkable ability to immobilize ^{99}Tc(VII)O_4^-, a fission product of significant environmental concern due to its high solubility, by reducing it to Tc(IV).[1–3] Among them, ubiquitous pyrite (orthorhombic FeS_2) was identified as an excellent Tc scavenger in a broad range of pH.[4] However, even though there is strong evidence that polymorphism affects the retention of pollutants by minerals,[5, 6] no studies of the effect of marcasite (cubic FeS_2) of the Tc uptake by pyrite have been performed up to date.

EXPERIMENTAL. The pure pyrite was purchased from Alfa Aesar; the mixture marcasite-pyrite 60:40 (synthetic FeS_2) was synthetized following the procedure described by Hou *et al.*[7] Both solids were characterized by X-ray diffraction. The batch sorption experiments were carried out inside a glovebox (< 1 ppm O_2) where Tc was left in contact with aqueous suspensions of either pure pyrite or synthetic FeS_2 (1.3 g L^{-1}) under constant agitation. Experiments were performed as a function of pH, time, ionic strength and Tc concentration. After certain time the solids were separated by ultracentrifugation ($2.4 \times 10^5 \times g$ for 1 h) and 0.25 mL aliquots of the supernatant were analyzed by liquid scintillation counting to determine the percentage of Tc removed. Solids loaded with 1,000 ppm Tc at pH 6.0 and 10.0 were analyzed by XPS and Raman microscopy.

RESULTS. Figure 1 shows the pH effect on the technetium removal by pure pyrite and by the synthetic FeS_2 after 7 days in contact. While pyrite removes 100 % of Tc at pH ≥ 5.5, in the presence of marcasite complete uptake takes place at 6.0 < pH ≤ 9.0, being incomplete at pH 10.0. At pH ≤ 5.0, the Tc retention is incomplete in both solids due to the higher solubility of FeS_2 under acidic conditions.[8]

The kinetics of the Tc-uptake by pure pyrite and by the synthetic FeS_2 at pH 6.0 is presented in Fig. 2. For pure pyrite complete Tc removal is reached within one day, whereas marcasite slows down the process to one week.

Figure 3 shows the Fe 2p XPS spectra of the Tc loaded iron sulfides at pH 6.0 and 10.0. A peak around 711 eV demonstrates that at pH 6.0 both solids trigger the formation of Fe(III) after the reduction of Tc(VII). This new Fe(III) phase was characterized as hematite by Raman microscopy (not shown). At pH 10.0, the Fe 2p spectra show no formation of Fe(III) in the presence of marcasite, suggesting that it is not the reducing agent for Tc(VII). The analysis of the Tc loaded synthetic FeS_2 at pH 10.0 by Raman microscopy revealed the formation of sulfate minerals on its surface, revealing that at this pH the reduction of Tc(VII) is a result of the oxidation of S^{2-} instead of Fe^{2+}.

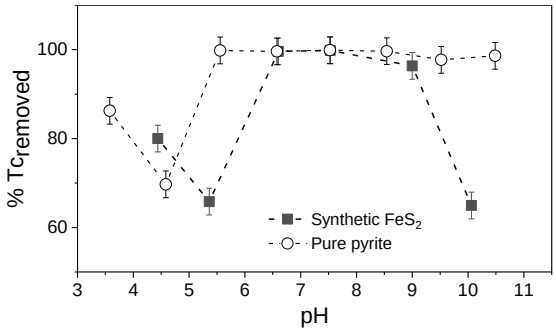

Fig. 1: pH effect on the Tc removal by pyrite and synthetic FeS_2 after 7 days.

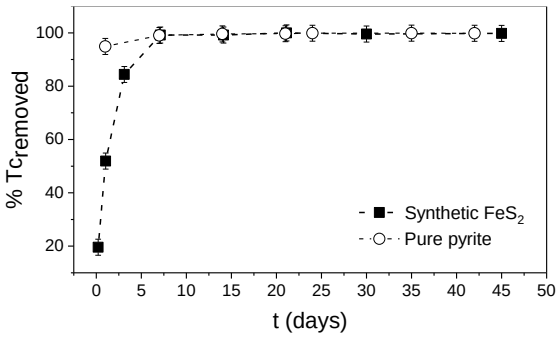

Fig. 2: Kinetics the Tc removal by pure pyrite and synthetic FeS_2 at pH 6.0.

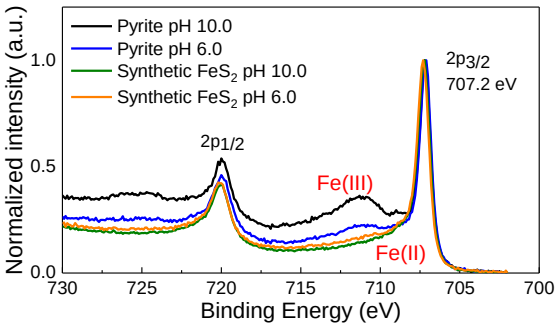

Fig. 3: Fe 2p XPS spectra of the Tc loaded iron sulfides. [Tc] = 1,000 ppm.

ACKNOWLEDGEMENTS. Funding from the German Federal Ministry of Economic Affairs and Energy (BMWi) is acknowledged (02E11607B).

[1] Wharton, M. J. *et al.* (2000) *Appl. Geochem.* **15**, 347–354.
[2] Kobayashi, T. *et al.* (2013) *Radiochim. Acta.* **101**, 323–332.
[3] Druteikiene, R. *et al.* (2014) *Appl. Radiat. Isot.* **89**, 85–94.
[4] Rodríguez, D. M. *et al.* (2020) *Environ. Sci. Technol.* **54**, 2678–2687.
[5] Baumer, T. *et al.* (2018) *J. Environ. Radioact.* **195**, 20–25.
[6] Khasanova, A. B. *et al.* (2007) *Radiochemistry* **49**, 419–425.
[7] Huo, L. *et al.* (2017) *Chemosphere* **174**, 456–465.
[8] Bonnissel-Gissinger, P. (1998) *Environ. Sci. Technol.* **32**, 2839–2845.

Heterogeneous sorption of radionuclides predicted by crystal surface nanoroughness

T. Yuan, S. Schymura, T. Bollermann, K. Molodtsov, P. Chekhonin, M. Schmidt, T. Stumpf, C. Fischer

Reactive transport modeling (RTM) is an essential tool for the prediction of contaminants' behavior in the bio- and geosphere. However, RTM of sorption reactions is constrained via two parameters, i. e., specific surface area (SSA) and specific site density (SSD). Their variability is responsible for heterogeneous sorption efficiency, not covered in current RTM approaches. Here, we study the spatially heterogeneous sorption behavior of Eu(III), as an analogue to trivalent actinides. We utilize polycrystalline calcite surfaces showing surface nanoroughness variability. We analyze the sorption efficiency as a function of surface nanoroughness. Based on experimental data from micro-focus time-resolved laser-induced luminescence spectroscopy (μTRLFS), vertical scanning interferometry (VSI), and electron back-scattering diffraction (EBSD), we re-parameterize a surface complexation model (SCM) based on nanotopographic data. Model validation of the quantitatively predicted spatial sorption heterogeneity suggests that retention reactions can be considerably controlled by nanotopographic surface features. Our study presents a way to implement heterogeneous surface reactivity into a predictive SCM for enhanced prediction of radionuclide retention.

EXPERIMENTAL. A polycrystalline marble sample surface was analyzed with EBSD to identify the crystallographic orientation of the crystal grains. The surface topography was then analyzed using VSI after a dissolution experiment. Subsequently, a batch europium sorption experiment was conducted by immersing the sample surface into a solution of 10^{-5} mol/L $Eu(NO_3)_3$ and 0.1 mol/L NaCl with a pH value of 8.5 for 24 hours. The sample was then rinsed with the background solution and dried. Spatially resolved information on the Eu(III) sorption capacity and the adsorbed species was gained using μTRLFS mapping with a spatial resolution of 20 μm.[1]

MODELING. The surface complexation model (SCM) was developed to describe Eu(III) adsorption on the calcite surface. Published site density and specific surface area (SSA) are 5 sites/nm² and 0.262 m²/g, respectively.[2] The chemical reactions were calculated using PHREEQC v3.5 with the Nagra/PSI Chemical Thermodynamic Database. The SCM results were validated using measured sorption efficiency data from the literature.[2]

RESULTS. Figure 1 shows an overview of the investigated calcite crystal surface maps including (a) the surface topography, (b) crystal orientations of the polycrystalline calcite material, and (c) normalized sorption capacity including selected spots where fluorescence lifetimes were collected. The luminescence intensity reveals a heterogeneous distribution of the Eu(III) sorption, even within single crystal faces, varying by a factor of around 10 between lowest and highest concentrations. Several grains show statistically significant differences in sorption capacity, however, no correlation between crystal orientation and sorption capacity is found. Therefore, other factors must be responsible for the variable surface sorption capacity observed by μTRLFS. We explored surface nanotopography, represented by surface nanoroughness (Sq), as a potential controlling factor of the surface energy distribution.[3] Based on analysis of the measured data from four different grains, a weak linear correlation

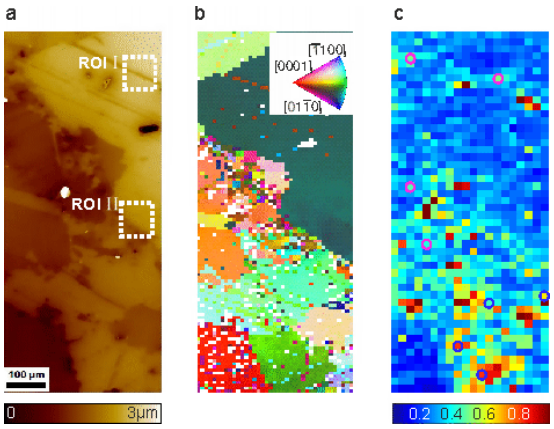

Fig. 1: Correlative microscopy of surface topography, field-of-view (FOV) size = 1 × 0.4 mm; ROIs I-II refer to two representative sub-regions for model validation (a). Crystal orientation mapping acquired by EBSD (b). Sorption capacity (normalized $F_1 + F_2$ μTRLFS peak sum). Spatial resolution: 20 × 20 μm (c).

($R^2 = 0.34$) between the calculated Sq values (FOV: 2.5 × 2.5 μm) and sorption capacity is identified. The quantitative relationship between the Eu sorption efficiency and specific surface area (SSA) by SCM allows us to quantitatively link SSA and Sq pixel by pixel by cross-referencing the experimental sorption capacity data and the model result. Therefore, we utilize this linear trend between SSA and Sq to parameterize a predictive SCM. A quantitative comparison of model results (Fig. 2a) with the measured data (Fig. 2b) in ROIs I and II shows good agreement within a 20 % discrepancy between model and experiment (Fig. 2c). In contrast to typical SCM approaches that employ a simple uniform SSA value, this modified SSA based on Sq analysis allows for the investigation of spatially resolved retention variability based on the variability of crystal surface energy.

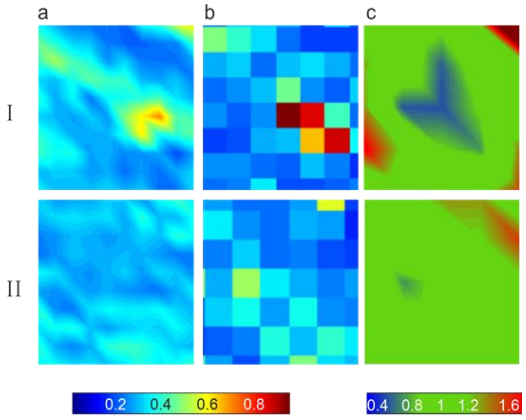

Fig. 2: SCM validations in ROIs I and II. SCM results of sorption efficiency, spatial resolution = 10 × 10 μm (a); normalized experimental results of sorption, spatial resolution = 20 × 20 μm (b); the ratio of model *vs.* experimental sorption efficiency (c).

ACKNOWLEDGEMENTS. We gratefully acknowledge funding by the German Federal Ministry of Education and Research (BMBF), grant 02NUK053B and the Helmholtz Association, grant SO-093 (iCross).

[1] Molodtsov, K. *et al.* (2019) *Sci Rep* **9**, 6287.
[2] Zavarin, M. *et al.* (2005) *Radiochim. Acta* **93**, 93–102.
[3] Fischer, C. *et al.* (2014) *Appl. Geochem.* **43**, 132–157.

PET imaging of actinide analogue transport and retention through fractured crystalline rock

S. Schymura, F. Jankovsky,[1] M. Zuna,[1] T. Frühwirt,[2] A. Mansel, K. Franke, J. Kulenkampff

[1]ÚJV Řež, a. s., Řež, Czech Republic; [2]TU Bergakademie Freiberg, Freiberg, Germany.

The migration of actinides determines the long-term safety of a final deposit of nuclear waste. This migration is influenced by mineralogical, topographical and hydrodynamic heterogeneities. To investigate the influence of flow heterogeneities at the core scale we performed Positron Emission Tomography (PET) imaging studies using Y-86 as a PET-traceable actinide analogue radiotracer.

EXPERIMENTAL. A gneiss drill core was procured from the Bukov Underground Laboratory in the Czech Republic. Two column samples were prepared by encasing parts of the core in epoxy resin. The two samples consisted of a natural fracture and an artificial fracture that was induced by a mechanical stress test. X-ray tomography (CT) images were taken to characterize the geometry of the fractures. First, for PET imaging, a conservative tracer experiment was performed using 10 mM [F-18]KF in aqueous 0.1 M NaCl at pH7.5. This was followed by a reactive experiment using 10^{-5} M [Y-86]Y$(NO_3)_3$ in aqueous 0.1 M NaCl at pH7.5. Y-86 and F-18 radiotracers (Tab. 1) were produced using the in-house cyclotron at Research Site Leipzig. For Y-86 a target of enriched $^{86}SrCO_3$ was proton irradiated to trigger the nuclear reaction Sr-86(p,n)Y-86. The target material was dissolved and the radiotracer was separated by ion chromatography using LN-resin. F-18 was produced from O-18 enriched water.

Tab. 1: Radiotracer properties.

Radiotracer	Halflife [h]	β^+ [%]
F-18	1.828	96.7
Y-86	14.7	33

RESULTS. The conservative PET imaging of the natural fracture showed a rather homogeneous flow.[1] However, upon repetition of the experiment a pronounced heterogeneity of the flow path was observed. Changes in the fracture between the experiments now lead to two diverging flow paths right after the entrance to the fracture. The flow was diverted around a middle section that was not accessible anymore. In the following reactive experiment using Y-86 most of the actinide analogue was deposited along one of the two divergent paths of the second F-18 experiment (Fig. 1). The bulk of the Yttrium is sorbed on the fracture surface and only 1 % is eluted. The distribution along the fracture can be fitted with a power law indicating an averaging of the influence of the mineralogical heterogeneity below the cm scale of the core.

For the artificial fracture, the F-18 experiment revealed a rather homogenous flow field, which nevertheless seems to be split in half due to a low-permeability surface topography feature in the fracture center right after the entrance. In the subsequent Y-86 transport experiment, it was observed that the bulk of the Yttrium got diverted to one side of the fracture taking only one of the divergent flow paths (Fig. 2). Furthermore, in the artificial fracture two distinct sorption hotspots could be observed that are related to mineralogical features. The mineralogical heterogeneity of the fracture surface is on a slightly higher scale than for the natural fracture, for which a levelling effect exists due to natural fracture filling material. In the artificial fracture, the influence of the mineralogical heterogeneity overlaps with the influence of the heterogeneous flow path.

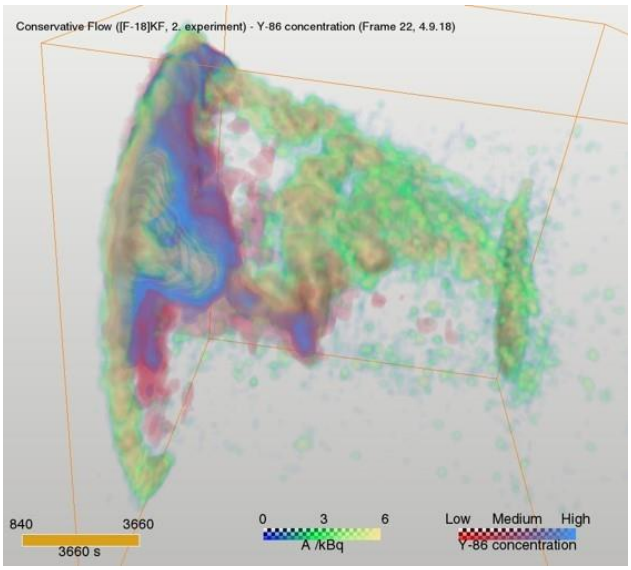

Fig. 1: Overlay of Y-86 sorption pattern on the gneiss fracture surface from PET (red-blue) and the conservative flow path measured with F-18 (blue-green-yellow). The Y-86 largely is deposited along one of the divergent flow paths seen in the F-18 experiment. The middle section of the fracture is not accessed by the flow.

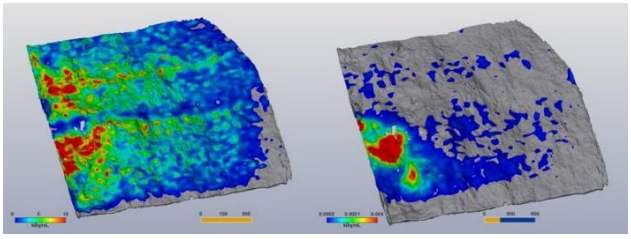

Fig. 2: Conservative flow path from PET process tomography (left) and Y-86 sorption pattern from PET (right). The conservative flow field is split in two by a central low-permeability feature. The Y-86 sorption pattern reveals a diversion of the flow to one side of the fracture with two distinct hotspots observable.

Our experiments show the impact on actinide migration by heterogeneous flow patterns. Future work will focus on the impact of fracture filling materials on the flow path and more detailed investigations into mineralogy and actinide speciation.

ACKNOWLEDGEMENTS. We acknowledge financial support by the Helmholtz-Association, grant PIE-0007 (CROSSING).

[1] Kulenkampff, J. *et al.* (2016) *Solid Earth.* **7**, 1217–1231.

Site-specific crystal surface reactivity

T. Bollermann, C. Fischer

The variability of crystal surface reactivity under identical chemical conditions is explained by significant intrinsic rate variability. This is quantified using rate maps of reacting surfaces and rate spectra as a statistical concept. We discuss the density and distribution of surface kink sites as the crucial parameter controlling the observed rate variability. For the first time, we present surface rate data that quantify simultaneously the rate contributions of specific surface portions of crystals, *i.e.*, facets, edges, and corners.[1] Resulting rate ranges could help improving the parametrization of reactive transport models at the pore scale.

Recent studies analyzed the rate variability and utilized rate maps and rate spectra as a means of quantifying multiple reaction rate portions.[2] Specifically, surface-sensitive methods with high spatial resolution, such as Atomic Force Microscopy (AFM), Vertical Scanning Interferometry (VSI), and confocal microscopy are used as complementary techniques for studying reacting single crystal surfaces. The results suggested the impact of crystallographic orientation, defect density, and exposure time on measured dissolution rates. Such investigations complement basic experimental and theoretical studies focusing on the reactivity of surface steps and pits. Surface kinks are discussed to be the major contributor to elevated surface rates. A comparison of surface portions with contrasting kink site densities (KSD) would inform quantitatively about specific rate ranges as a function of KSD (facets: low, edges: enhanced, corners: highest KSD).[1]

EXPERIMENTAL. We utilized a Sensofar Plu S neox microscope combining interferometer and confocal surface analysis techniques. For the rate data measurement, we analyzed the calcite crystal surface using two confocal objectives (150× and 20× magnification). The sample surface topography was analyzed before and after each dissolution period. Details about the dissolution experiment are available in literature.[1] Each measurement included a masked and a reacted surface portion. The measured datasets were processed with the software SPIP (version: 6.7.3; Image Metrology A/S, Hørsholm, Denmark). The velocity of height changes (dz/dt) equals the material flux at each point of the surface. Rate maps were calculated by dividing each dz/dt-value by the molar volume of calcite.

RESULTS. Figure 1 shows the topography of a calcite single crystal after five minutes of dissolution in a 2.2 mM Na_2CO_3 solution at pH 8.8, see background height map with amber-color scheme. The inset at the top of Fig. 1 illustrates the elevated dissolution rates at the crystal corner and edges, compared to facets. The analysis of rate data in the frequency domain (Fig. 2, left) shows a rate distribution covering about 2.5 orders of magnitude. The comparison to polycrystalline calcite dissolution rate data under identical chemical conditions illustrates the fundamental differences of the rate frequency distributions. Note the remarkably high rates at the corner of the single crystal, explained by the KSD scheme (Fig. 2, right side).

CONCLUSIONS. We categorized dissolution rate data based on kink site density, based on multiple literature data. The compilation suggests an explanation of the complex shape of multimodal rate spectra based on surface features and associated kink site densities. We suggest an application of this insight for the parametrization of pore scale models in reactive transport codes.

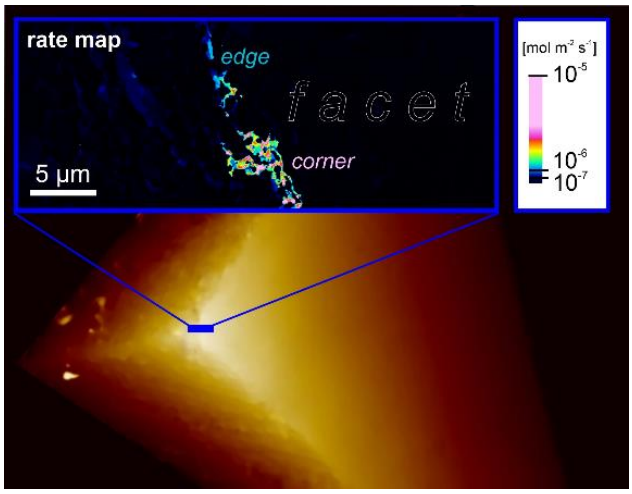

Fig. 1: Topography of a single calcite crystal with facets, edges and corner (background height map, amber-color scheme). Multiple measurements of the surface topography using interferometry microscopy are utilized to calculate a dissolution rate map of the specific surface building blocks (upper part).

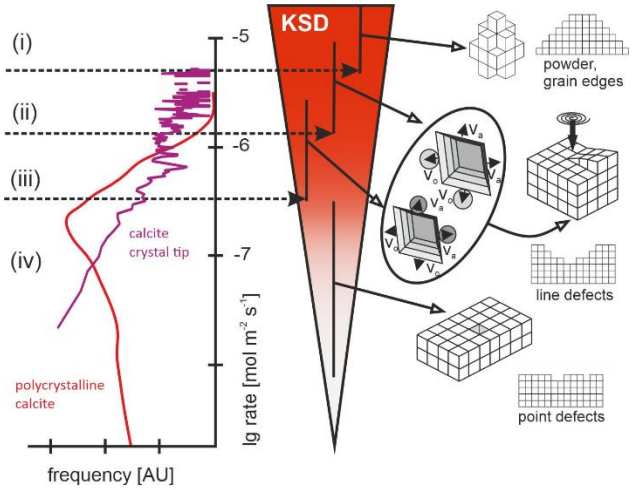

Fig. 2: Dissolution rate distribution of calcite single crystal (purple) *vs.* polycrystalline material (red) (left side). Schematic illustration of KSD increase (bottom-top) and explanation of rate increase, central part. Categories of KSDs (i–iv) represent simple endmember situations while measured rate spectra result from a complex superimposition of such endmembers. Right: Simplified mechanistic explanation of the KSD variability of crystal surfaces.

ACKNOWLEDGEMENT. We gratefully acknowledge funding by the German Federal Ministry of Education and Research (BMBF) (Grant 02NUK053B) and the Helmholtz Association (Grant SO-093).

[1] Bollermann, T. & Fischer, C. (2020) *Amer. J. Sci.* **320**, 53–71.
[2] Fischer, C. *et al.* (2012) *Geochim. Cosmochim. Acta* **98**, 177–185.

Effective diffusivity prediction of radionuclides in clay formations using an integrated upscaling workflow

T. Yuan, C. Fischer

Accurate estimation of radionuclides migration in the host rock using numerical tools plays a key role in the safety assessment of disposal concepts for nuclear waste. Current diffusive transport modeling applies a simplified parameterization of the effective diffusivity for simulating and predicting the radionuclides migration in the host rock such as the Opalinus clay (OPA). This prevents to model the heterogeneous diffusion behavior as indicated by the Positron Emission Tomography (GeoPET) measurements.[1] In this study, we propose an upscaling workflow that integrates nm- and µm-scale simulations based on synthetic multiscale digital rocks to predict the effective diffusivity of radionuclides in the OPA. The proposed numerical approach is validated with published experimental data confirming general applicability.[2] In this approach, the spatial variabilities of the pore network and compositional heterogeneities at the pore scale are now addressed and available for studying heterogeneous diffusion patterns compared to commonly assumed homogeneous behavior.

MODELING. The effective diffusivities of radionuclides are determined by digital rock physics. The respective synthetic digital rocks include two types of materials for studying diffusive transport. Clay-rich rock sections are the starting point, commonly referred to as the clay matrix, which contains sheet silicate crystals and pores at the nm-scale (Fig. 1a). At this scale, we consider the surface diffusion for the cations and anions transport within the diffuse layer (DL), and the surface electrostatic potential is calculated using the Donnan approach in PHREEQC v3.5. Second, we consider non-clay minerals, such as quartz grains and diagenetic calcite crystals, as non-porous components, thus including additional compositional complexity at the µm-scale (Fig. 1b). At each length scale, the diffusion-sorption equation is numerically solved by a previously developed numerical simulator.[3]

UPSCALING. The suggested upscaling workflow integrates nm- and µm-scale simulations, illustrated in Fig. 2. Detailed workflow steps include: (1) The diffusivity of each tracer in free water D_W and the geometrical model of clay matrix are used to determine the effective diffusivity D_e of the clay matrix at the nm scale. (2) D_e of clay matrix and geometrical model of microstructures of shales are used to determine the D_e of shale at the µm-scale. In this upscaling workflow, both small-scale information such as pore space and pore network geometry and larger-scale composition are considered.

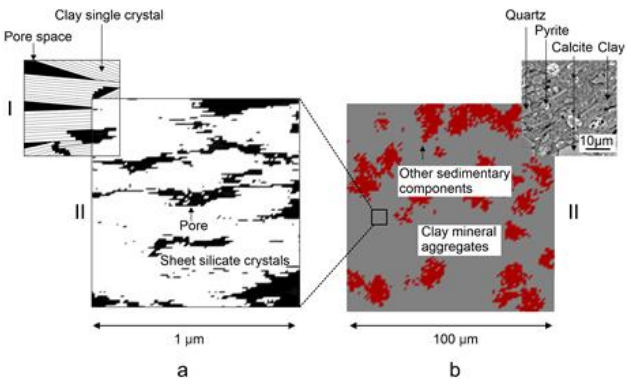

Fig. 1: Schematic representation (I) and digital rock model (II) of the partial rock structure built-up of sheet silicate crystals and pores (black). Black color represents pores and white color represents the clay crystals (a). (I) SEM image of the microstructure of OPA, indicating clay, quartz, calcite, and pyrite minerals. (II) Reconstructed digital rock with clay mineral aggregates (gray color) and other sedimentary components (red color) including quartz, calcite, and pyrite (b).

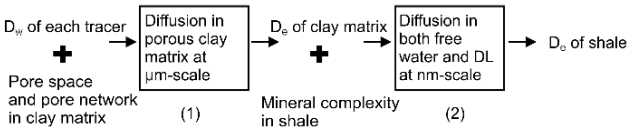

Fig. 2: Flow chart of the proposed upscaling workflow from the nm- to µm-scale. This includes diffusive flow in (1) porous clay matrix and (2) single laminae of varying composition.

RESULTS We determine the effective diffusivities of $^{22}Na^+$, HTO, and I^- in the shaly facies of OPA using workflow steps (1) and (2), as shown in Fig. 2. The synthetic digital rock of shale has a total porosity of 0.158 and is composed of 66 % clay minerals,[4] containing elongated pores.[5] The calculated mean values of effective diffusivities of $^{22}Na^+$, HTO, and I^- by the model and the experimentally measured values from literature are listed in Tab. 2. Good agreement between the diffusivity from the literature and our suggested upscaling workflow underscores the capability of predicting the diffusivity of the shales.[2] Due to the considerations of both small-scale information such as pore space and pore network as well as larger-scale compositional information in the geometrical models, our concept of upscaling allows us to model heterogeneous diffusivity caused by the spatial variability of pore networks in complex rocks as well as the compositional heterogeneities in shales. The suggested upscaling strategy is applicable to provide insight and input data to simulations at the core scale and above, thus contributing to enhanced predictability of radionuclide migration.

Tab. 1: Effective diffusion coefficients of $^{22}Na^+$, HTO, and I^- in shale from experimental data in the literature compared to the predicted mean values from the model results.[2]

Tracer	Diffusivity of shale (10^{-11} m²/s)	
	Experimental data[2]	Model results
$^{22}Na^+$	7.2–9.4	7.73
HTO	5.4–6.5	6.23
I^-	1.2–2.0	2.08

ACKNOWLEDGEMENT. We gratefully acknowledge funding by the German Federal Ministry of Education and Research (BMBF), grant 02NUK053B and the Helmholtz Association, grant SO-093 (iCross).

[1] Kulenkampff, J. *et al.* (2015) *Clay Miner.* **50**, 369–375.
[2] Leupin, O. X. *et al.* (2017) *Swiss J. Geosci.* **110**, 391–403.
[3] Yuan, T. *et al.* (2019) *water* **11**, 1957.
[4] Bossart, P. (2008) Report No.3., Swiss Geological Survey.
[5] Houben, M. E. (2013) *Appl. Clay Sci.* **71**, 82–97.

Combined µCT and MIP porosity measurements for identification of transport pathway distributions in salt rocks

J. Kulenkampff, T. Wilsnack[1]

[1]IBeWa – Ingenieurpartnerschat für Bergbau, Wasser und Deponiertechnik Wilsnack und Partner, Freiberg, Germany

Potential fluid transport pathways through rock material in close proximity to a barrier material by combining Mercury Intrusion Porosimetry (MIP) and Micro-Computed Tomography (µCT) on unconfined samples were analyzed. The MIP data generally suggest the occurrence of a small portion of tight percolation pathways of the bulk material. However, apparent low-pressure intrusion raises concern that additional conductive structures with a size around 0.1 mm could be present as well. These large structures could be attributed to the surface roughness of the samples by µCT data analysis. They are without consequences for the barrier function. In contrast, the largest detectable fracture structures of the bulk material are in the micrometer range and display low density contrast – either due to salt precipitates or residual brine.

Salt rocks are a prospective formation for hazardous and radioactive waste disposal owing to their extremely low permeability and their plasticity. Underground repositories require reliable technical barriers in close contact with the formation rock. Both elucidation of flow processes and assessment of injection concepts for technical improvements of the barrier are key issues.

EXPERIMENTAL. Small cubes with edge length of 20 mm were cut from salt rock drill cores by dry sawing. These samples were inspected with the Nikon XT-H-225 µCT-scanner (U = 190 kV, I = 90 µA, Filter: 0.5 mm Cu, voxel size: 12.4 µm).
Elaborate background corrections and filtering were conducted prior to segmentation of detectable fractures with low contrast, because the images were prone to background variations caused by the square sample shape. After top-hat segmentation (Fig. 1), the local void sizes were computed with the thickness map algorithm of the Avizo software (Fisher Scientific). The outer surface roughness was estimated as the thickness map of the rough sample volume and its smooth external envelope.
MIP was conducted with AutoPore V (Micromeritics), which features an extended low-pressure range, in order to quantify large pores up to D = 0.8 mm. The smallest detectable pore size is D = 3 nm, according to a maximum injection pressure of 400 MPa.

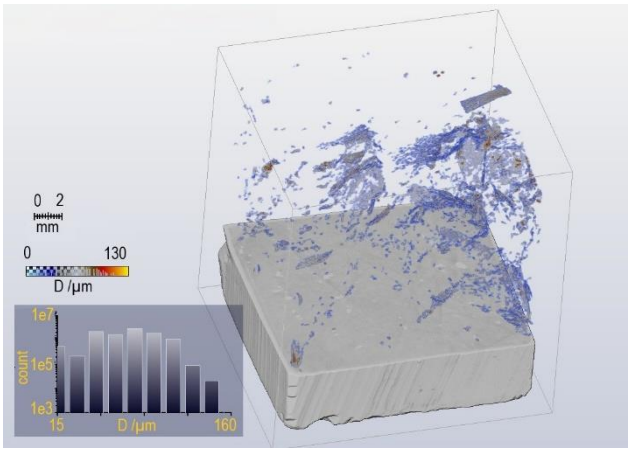

Fig. 1: µCT, showing saw-cut surface roughness (bottom); exposed thickness map of fracture system, color-coded (top); histogram of the thickness map (inset).

RESULTS. The MIP data show a considerable portion of almost millimeter-scaled voids that are suspected to provide potential flow pathways. Using µCT measurements, the existence of such pore structures is excluded. Instead, µCT suggests roughness of the sample surface as a source of potentially misleading MIP data interpretation (Fig. 2, negative range). However, the lack of a well-defined smooth reference surface limits the quantitative comparability of MIP and µCT with respect to large classes of the pore spectrum. We thus consider the size (D = 0.3 mm) of the largest pores detected by µCT as the maximum pore size existing in the bulk material.

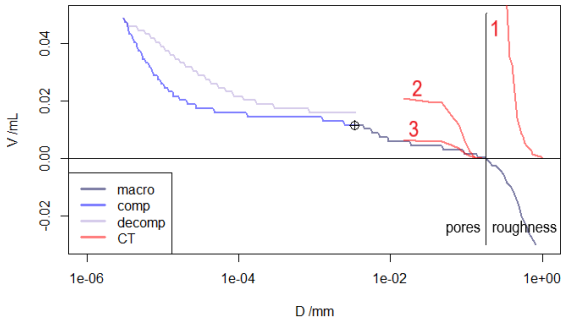

Fig. 2: Pore size distribution of a rock-salt sample. MIP in blueish colors (low pressure injection, high pressure injection, and decompression), µCT in reddish colors (1. surface roughness, 2. empty voids in the bulk volume, 3. voids with assumed porosity of 0.3). Negative MIP-volume values represent surface roughness, corrected by µCT.

In general, such voids in salt rock show the lowest density and are thus most probably air-filled. Interestingly, smaller voids show frequently considerably higher density compared to the larger ones. Most probably, such structures are not open, but contain portions of dense material. Consequently, these complex pore structures are considered as porous zones, either not detectable by MIP (solid fill, *e.g.*, brines) or correctly attributed to smaller pore classes (partly filled by microporous material, tentative porosity = 0.3, Fig. 2). Overall, the combined use of µCT and MIP provides critical insight into the complexity of pore size distributions.

ACKNOWLEDGEMENTS. The project Stroefun III is funded by the BMWi (02 E 11748). The MIP measurements were executed by PTA/Micromeritics Unterschleissheim.

PET transport experiments under confining pressure

J. Kulenkampff, S. Gruhne, D. Lösel

A new radiation-transparent vessel for the conduction of flow experiments under hydrostatic confining pressure particular suitable for Positron Emission Tomography (PET) and X-ray tomography (µCT) was designed. First promising results are presented.

It is common best practice in core analysis for reservoir evaluation to conduct flow experiments under hydrostatic confining pressure in a pressure vessel. With this procedure, *in situ* pressure conditions can be investigated. Second, an improved sealing between sample and containment is ensured, thus avoiding flow artifacts. Nevertheless, current process-tomographic experiments were lacking this vital feature. Commonly used steel pressure vessels cause strong scatter and attenuation of radiation and thus interfere with both tomographic methods, PET and µCT. To overcome these issues, we designed and successfully tested a plastic-material pressure vessel. This enables to conduct more realistic transport experiments. Additionally, this new setup allows for the analysis of reactive transport processes affecting shape and mechanical properties of the sample.

EXPERIMENTAL. The pressure vessel was lathed from polyoxymethylene copolymere (POM-C). It contains the mounted sample that is sealed with shrinking tube. (Fig. 1). The carrier medium for the confining pressure (p_c) is water, which can be pressurized with a pressure-controlled syringe pump or a gas pressure storage container (He). The thickness of the vessel wall is designed to withstand pressures up to 10 MPa, although the intended use is 2 MPa. The design of the sealing can be adapted to the sample size. The maximum diameter is limited to D = 120 mm, according to the maximum field-of-view of the scanners. The device has to fit entirely into the PET-scanner in order to include its scatter and attenuation effects into the image reconstruction process. Consequently, this limits the sample diameter to *ca.* 50 mm and the length to 100 mm.
Usually, our flow experiments are conducted with a slow constant flow rate and a driving pressure delimited to $p_d = P_c/2$, in order to avoid superficial flow and significant pore pressure effects. Within this pressure limit, the flow rate is adjusted to achieve a maximum flow velocity of *ca.* 60 mm/h. Although p_d can be reduced at will by decreasing the injection rate, a significant pressure gradient should be established to avoid too high sensibility to fluctuations.

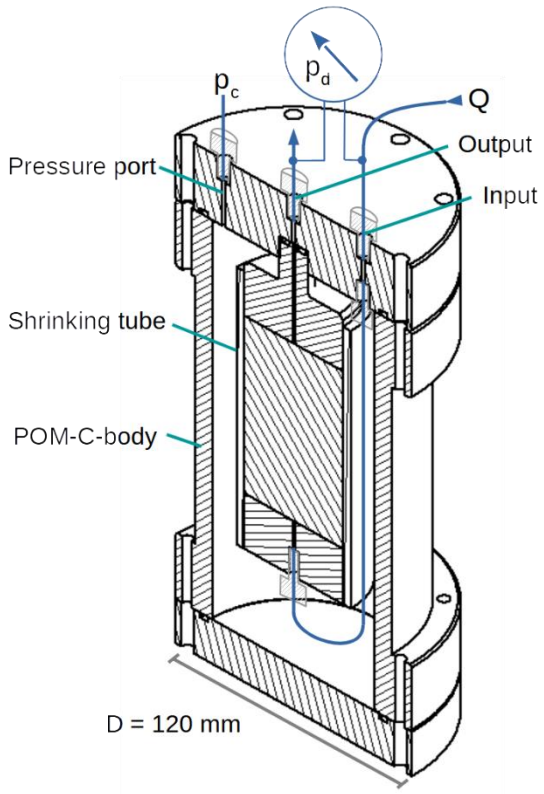

Fig. 1: Scheme of the radiation-transparent pressure vessel.

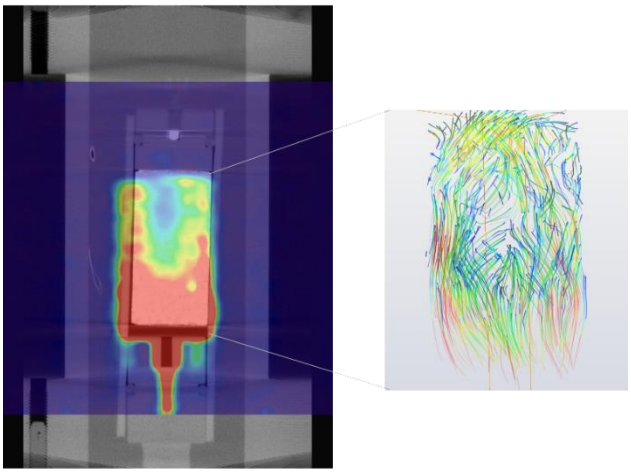

Fig. 2: First experiment on a Rotliegend sandstone sample in the new pressure vessel. Cross section of the PET-µCT overlay (µCT still without confining pressure) (left). Enlarged 3D-view of the flow vector field computed from the sequence of PET frames (right).

RESULTS. Test experiments on a Rotliegend sandstone sample with a diameter of 50 mm were performed successfully (Fig. 2). Another important result is the capability of the applied PET data correction algorithms of removing attenuation and scatter artefacts and obtaining fair image quality.
However, the first data analysis still shows increasing radial tracer concentration *versus* the sample surface (Fig. 2, left). The trough - shaped pattern indicates a disaggregated zone near the sample surface, but no superficial flow along a superficial fluid film. Additional experiments with varying confining pressure are planned, in order to study the flow behavior in such disaggregated zones.
In general, such pressure-dependent behavior of flow cells are usually not detectable without PET process tomography. Thus, we suggest PET measurements as the critical safeguard against misinterpretations of transport results collected by using pressure cells.

Production of ^{22}Na by the non-common nuclear reaction ^{nat}Mg(d,α) and purification of ^{22}Na for investigations with GeoPET

A. Mansel, T. Bollermann, J. Kulenkampff, K. Franke

A method for the production and purification of ^{22}Na ($T_{1/2}$ = 2.603 a, β^+ = 90.3 %), suitable for transport investigations in low-permeability systems, such as clay host rocks is introduced.

Opalinus clay is a possible host rock for nuclear waste repository systems. Currently, detailed studies are focusing on reactive transport properties of this complex geomaterial. GeoPET (Positron Emission Tomography optimized for geological samples) is an excellent method for the analysis of radionuclide transport and retention. Transport analysis requires a suitable non-reactive PET tracer, suitable for solutions mimicking the pore water chemistry of the Opalinus clay rock. Here, we present a method for the production and purification of ^{22}Na ($T_{1/2}$ = 2.603 a, β^+ = 90.3 %), suitable for transport investigations in low-permeability systems.

EXPERIMENTAL. *^{22}Na Opalinus water:* A magnesium foil (diameter: 11 mm; weight: 79 mg) was irradiated at the cyclotron Cyclone 18/9 (IBA RadioPharma Solutions, Belgium) with 9 MeV deuterons by using the nuclear reaction ^{nat}Mg(d,α)^{22}Na.[1] As depicted in Fig. 1, the magnesium foil was dissolved in 6 M HCl and the solution was evaporated to dryness. After dissolution in 0.1 M HCl the preconditioned cation exchanger Dowex 50W x 8 (0.1 M HCl) was used to fix both, magnesium and sodium on the column.[2] The ^{22}Na was eluted by 0.3 M HCl, while magnesium remains on the column. The fractions were measured by γ-spectrometry. After evaporation of the combined ^{22}Na-frations, the ^{22}Na was dissolved in saturated NaCl solution or Opalinus water, depending on the flow experiment. The column was regenerated by washing two times with 6 M HCl and preconditioned with 0.1 M HCl for the next separation.

Diffusion experiment with GeoPET/CT: Sample material was a drillcore of Opalinus clay (sandy facies, length: 95 mm, diameter: 67 mm) with centered axial borehole (diameter: 3 mm). The axial borehole was filled with synthetic Opalinus clay pore water, labelled with 0.55 MBq ^{22}Na$^+$. The GeoPET-image (Fig. 2) is the 9th from a suite of 32 frames (frame length: 30 min), acquired during a period of one month with a ClearPET scanner (Elysia-Raytest). The low resolution background μCT image was acquired with a Nikon XT-H-225 scanner for the purpose of PET attenuation and scatter correction.

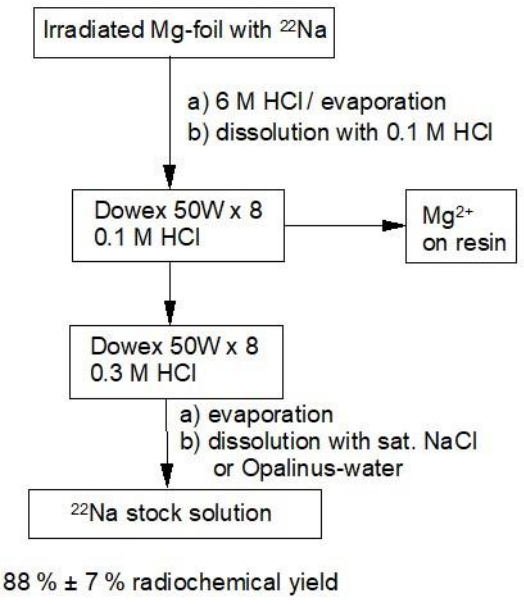

Fig. 1: Separation scheme for the purification of ^{22}Na from a deuteron irradiated ^{nat}Mg target.

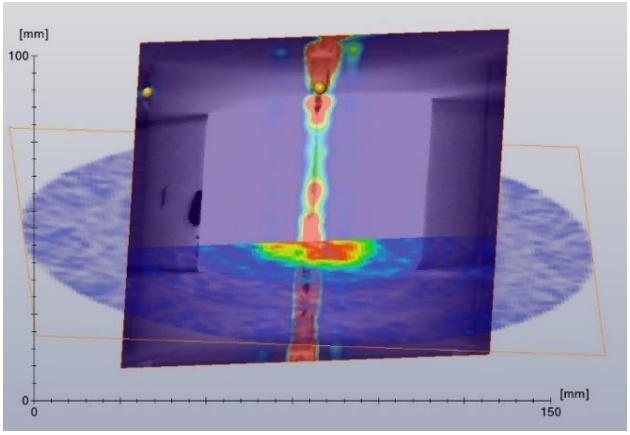

Fig. 2: Overlay picture of GeoPET and CT scans visualizing the diffusion of synthetic Opalinus water in an Opalinus drillcore.

RESULTS. The magnesium target material was separated completely; no visible residue remained after evaporation of the ^{22}Na fractions. The mean radiochemical separation yield was 88 ± 7 % for the stock solution. Using Opalinus water as stock solution no further sample manipulation is needed. The required chemical form of the tracer for the GeoPET studies with Opalinus clay could be precisely adjusted and is routinely provided for the GeoPET studies.

Fist applications were diffusion experiments with ^{22}Na Opalinus water in Opalinus clay. Due to its half-life of 2.603 a, ^{22}Na is an ideal PET tracer for such long-term diffusion studies. Figure 2 shows first results of diffusion experiments of the 0.5 mL sample within the water-saturated Opalinus clay drillcore using the combined GeoPET-CT approach. The overlay of diffusion patterns from GeoPET with the inhomogeneous fabric from μCT provides new insights into the heterogeneous diffusion process as the dominant transport process to be considered in performance assessment of the barrier function of clay rocks.

[1] Röhm, H. F. *et al.* (1969) *J. Inorg. Nucl. Chem.* **31**, 3345–3356.
[2] de Britto, F. *et al.* (1988) *J. Radioanal. Nucl. Chem. Lett.* **127**, 31–36.

First-time production of Nb-92m/95 at the cyclotron Cyclone 18/9 in Leipzig

K. Franke

The exit from nuclear energy implicates the dismantling of nuclear power plants in the near future. During this decommissioning, Nb-94 ($T_{1/2}$ = 112.03 × 10^4 a) has to be considered as a constituent of the radioactive waste in the dismantling process. This entails the need for suitable Nb-radiotracers to investigate experimentally the likely fate of Nb-94.

The half-life and decay mode suggest the isotope Nb-95 ($T_{1/2}$ = 34.991 d, E_γ = 765.80 keV/99.15 %) as promising candidate.[1] Nb-95 can be produced via a (d,x)-reaction with a Zr target with natural isotope abundance. The irradiation with 9 MeV deuterons results mainly in the generation of Y, Zr and Nb radionuclides.[2] Y and Zr radionuclides can be easily separated from Nb-95 during target processing. The relevant cross sections for the formation of the Nb isotopes suggest the formation of Nb-90, Nb-91m, Nb-92m, Nb-95, Nb-95m and Nb-96 (Fig. 1).

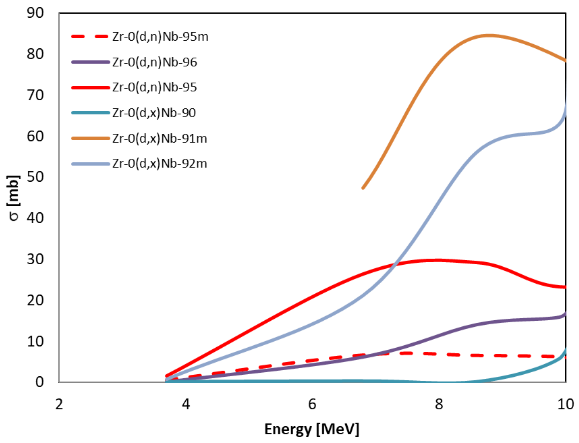

Fig. 1: Cross section for the formation of Nb isotopes Nb-90, Nb-91m, Nb-92m, Nb-95, Nb-95m and Nb-96 via Zr-nat(d,x) reaction.[2]

Most of the formed Nb isotopes can be neglected due to their half-life and their low γ-emission probability (Nb-90: $T_{1/2}$ = 14.6 h, Nb-91m: $T_{1/2}$ = 60.8 d, Nb-91: $T_{1/2}$ = 680 a, Nb-92: $T_{1/2}$ = 3.47 × 10^7 a and Nb-94: $T_{1/2}$ = 2.03 × 10^4 a). Only Nb-92m ($T_{1/2}$ = 10.15 d, E = 34.17 keV/99.15 %) has to be considered in the following experimental setup.[1] Luckily, Nb-92m and Nb-95 γ-emissions are easily distinguishable with common detection systems.

EXPERIMENTAL. *Cyclotron.* The cyclotron Cyclone 18/9 (IBA RadioPharma Solutions, Belgium) provides protons with an energy of 18 MeV and deuterons with an energy of 9 MeV. The maximal current on target is 100 µA for protons and 40 µA for deuterons.
Target station. Solid targets were irradiated at the Nirta® solid target system (IBA RadioPharma Solutions, Belgium) at port 3 of the cyclotron, mounted at a 2 m beam transfer line. The target is cooled with helium in front and water in the backside.
Windows. 12.5 µm Ti foil was used as vacuum window. No target entrance window was used for the target to avoid further degradation of deuteron energy. The Zr-foil was cooled directly with He.
Target capsule. The target was hold in a target capsule (Fig. 2.). It consists of an Al-backing and open Al-cover.

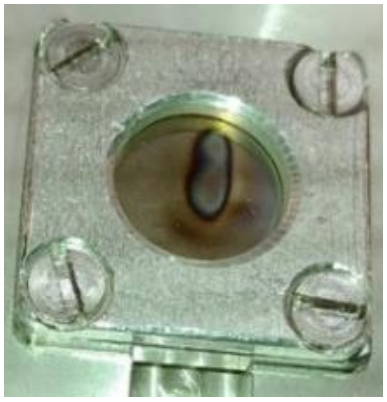

Fig. 2: Irradiated target capsule. Beam spot indicates non-ideal focused beam in horizontal alignment.

Target. A metallic Zr foil (Alfa Aesar, diameter: 12 mm, thickness: 127 µm) with natural isotopic composition was used as target material.
Irradiation. Irradiation was done with deuterons with an initial energy of 9 MeV and a current on target of 10 µA for 550 µAh.
γ-spectrometry. An HPGe-detector ORTEC GEM15180-P combined with signal processing module DSPEC 502 (ORTEC) was used for γ-spectrometry measurements.

RESULTS. The target capsule was opened 4 d after end of bombardment to allow short-lived radionuclides to decay. The target foil showed an oval burning mark (Fig. 2). Although this is not critical because of the low deuteron current and the high melting point of the Zr-foil further optimization of the beam focus is needed for a more homogeneous target irradiation. The irradiated Zr-foil was unloaded and transferred to γ-spectrometry. The spectrum confirms quantitatively the yield of Nb-92m (110 MBq), Nb-95 (27 MBq), Nb-95m (18 MBq) and Zr-95 (21 MBq) (Fig. 3). Subsequent chemical Zr/Nb separation combined with further decay of Nb-92m result in the required Nb-95. First applications at the Institute for Nuclear Waste Disposal, Karlsruhe Institute of Technology, Germany, include the investigation of the impact of isosaccharinic acid and chloride on the uptake of Nb(V) by cement (CEM I HCP).[3]

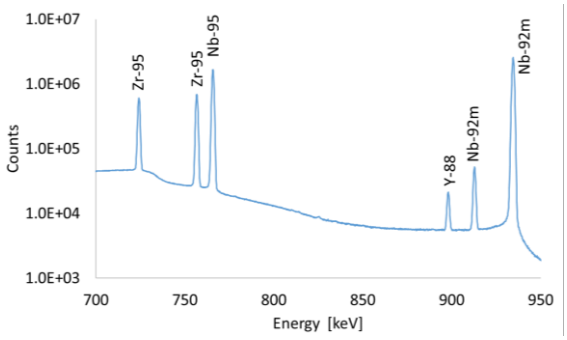

Fig. 3: Section of the γ-spectrum of the irradiated Zr foil. Prominent peaks of Y-88 (898.04 keV), Zr-95 (724.19 keV, 756.72 keV), Nb-92m (912.60 keV, 934.44 keV) and Nb-95 (765.80 keV).

[1] ENSDF database, available at http://www.nndc.bnl.gov/ensarchivals/.
[2] From EXFOR database available at http://www-nds.iaea.org/exfor/.
[3] Cevirim-Papaioannou, N. *et al.* (2021) NUWCEM-2021.

Metal dissociation from humic colloids: kinetics with time-dependent rate constants

H. Lippold, L. Zedek[1]

[1]Technical University of Liberec, Czech Republic

The mobility of radionuclides in aqueous subsurface environments is essentially governed by their interaction with humic or humic-like substances as colloidal constituents of Dissolved Organic Matter or high-molecular-weight organic components in clay. Dissociation is a slow kinetic process, which is even more impeded with increasing time of contact due to structural rearrangements. Based on results obtained in isotope exchange experiments, the convoluted time dependence of dissociation was fully described by integrating time-dependent rate "constants" to address the phenomenon of kinetics within kinetics.

Growing inertness of complexes with Natural Organic Matter was observed for a number of multivalent metals, such as Eu(III), Am(III), Th(IV) and U(VI).[1, 2] Based on thermodynamic constants, conventional transport models are, however, assuming steady local equilibria. To include kinetically hindered processes, their time dependence must be understood and parameterized. Solving the kinetic problem of convoluted reaction rates was the objective of this study.[3]

EXPERIMENTAL. The kinetic treatment refers to isotope exchange experiments performed with [^{160}Tb]Tb(III) and humic acid, delineated in Fig. 1.[4]

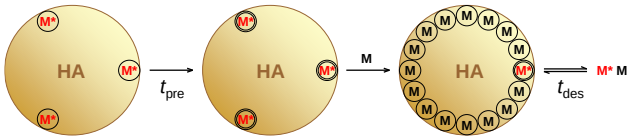

Fig. 1: Schematic representation of isotope exchange experiments starting from a low metal load of humic acid (HA) with the radioisotope (M*) for variable times of pre-equilibration (t_{pre}), followed by saturation with the stable isotope (M), which initiates partial desorption observed over variable times (t_{des}). Double circles indicate inertization.

RESULTS. As shown in Fig. 2, desorption of [^{160}Tb]Tb as a radiotracer (M*) was found to be very slow, and moreover, the rate was dependent on the time of pre-equilibration with humic acid prior to addition of the stable isotope ^{159}Tb (M).Thus, an inertization takes place. Each data series is in turn affected by this process, since it is also active during the slow liberation of [^{160}Tb]Tb.

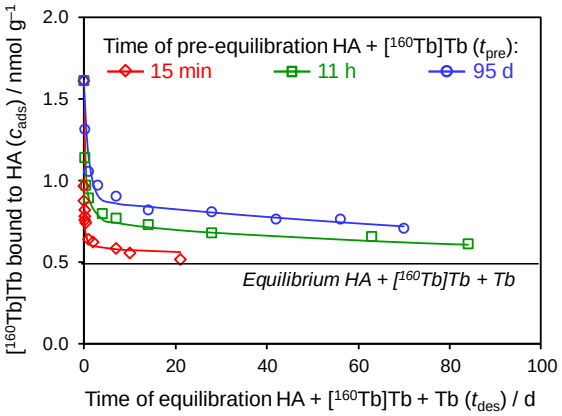

Fig. 2: Release of [^{160}Tb]Tb from humic acid (HA) initiated by saturation with non-radioactive Tb (pH 4.0, 0.5 g L^{-1} HA, 1 nM [^{160}Tb]Tb, 2 mM Tb, 0.1 M $NaClO_4$).

For an overall kinetic description of desorption superimposed by inertization, the first-order rate law for approach to equilibrium regarding the concentration of humic-bound [^{160}Tb]Tb (c_{ads}) was integrated including a time dependence of the rate constant k, given by an empirical function:

$$-\int_{c_{ads}^{ini}}^{c_{ads}} \frac{1}{c_{ads}-c_{ads}^{eq}}\, dc_{ads,1} = \int_{t_{des}=0}^{t_{des}} k(t)\, dt_{des} \qquad (1)$$

$$\text{with } k(t) = a\left(t_{pre}+t_{des}\right)^{b} + k_{\infty} \qquad (2)$$

The indices *ini* and *eq* refer to the initial and equilibrium state, respectively. The time t controlling k includes the pre-equilibration period. Beside the parameters a and b, an offset value k_∞ for infinite time was added because k does not necessarily decline to zero. With respect to the very fast desorption at the initial stage, the total amount of sites occupied by [^{160}Tb]Tb was split into a fast (index 1) and a slowly (index 2) desorbing part with the fractions x and (1–x), respectively. Integration yields:

$$c_{ads} = c_{ads}^{eq} + x\left(c_{ads}^{ini}-c_{ads}^{eq}\right)\exp\left\{\frac{a_1}{b_1-1}\left[\left(t_{pre}+t_{des}\right)^{1-b_1}-t_{pre}^{1-b_1}\right]\right\}$$
$$\exp\left(-k_{\infty,1}t_{des}\right)+(1-x)\left(c_{ads}^{ini}-c_{ads}^{eq}\right)$$
$$\exp\left\{\frac{a_2}{b_2-1}\left[\left(t_{pre}+t_{des}\right)^{1-b_2}-t_{pre}^{1-b_2}\right]\right\}\exp\left(-k_{\infty,2}t_{des}\right). \qquad (3)$$

With this equation, all time series can be well represented by one set of parameter values (line fits in Fig. 2), without assuming a metal transfer from fast sites to slow sites. The extracted time functions for k_1 und k_2 are shown in Fig. 3.

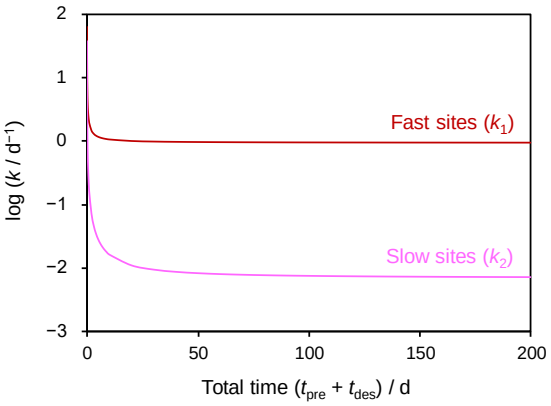

Fig. 3: Inertization process as reflected by decreasing rate constants.

CONCLUSIONS. This analysis, breaking the rules of classical kinetics, showed that the inertization process is limited in time and extent. Thus, for modeling speciation or migration in nearly stagnant systems on a long-time scale, thermodynamic concepts using equilibrium constants remain applicable. However, the kinetic effect must be considered in any attempt to predict organically bound metal fractions from the composition of aquatic systems (and *vice versa*) if conditions change relatively fast.

ACKNOWLEDGEMENT. This work was funded by the Federal Ministry for Economic Affairs and Energy (BMWi), support code 02E11415B.

[1] King, S. J. *et al.* (2001) *Phys. Chem. Chem. Phys.* **3**, 2080–2085.
[2] Geckeis, H. *et al.* (2002) *Environ. Sci. Technol.* **36**, 2946–2952.
[3] Lippold, H. *et al.* (2021) *Chemosphere*, submitted.
[4] Lippold, H. *et al.* (2017) *Geochim. Cosmochim. Acta* **197**, 62–70.

Stone–Wales defects cause high proton permeability and isotope selectivity of single-layer graphene

Y. An,[1,2] A. F. Oliveira,[2,3] T. Brumme,[1,3] A. Kuc,[2] T. Heine[2,3]

[1]Universität Leipzig, Wilhelm-Ostwald-Institute for Physical and Theoretical Chemistry, Leipzig, Germany; [2]HZDR, Campus Leipzig, Germany; [3]Technische Universität Dresden, Faculty of Chemistry and Food Chemistry, Chair of Theoretical Chemistry, Dresden, Germany

While the isotope-dependent hydrogen permeability of graphene membranes at ambient condition has been demonstrated,[1,2] the underlying mechanism has been controversially discussed during the past 5 years. The reported room-temperature proton-over-deuteron (H^+-over-D^+) selectivity is 10, much higher than in any competing method. Yet, it has not been understood how protons can penetrate through graphene membranes — proposed hypotheses include carbon vacancies and local hydrogenation. However, neither can explain both the high permeability and high selectivity of the atomically thin membranes. Here, it is confirmed that ideal graphene is quasi-impermeable to protons, yet the most common defect in sp^2 carbons, the topological Stone–Wales defect (5- and 7-membered rings formed from 6-membered rings), has a calculated penetration barrier below 1 eV and H^+-over-D^+ selectivity of 7 at room temperature and, thus, explains all experimental results on graphene membranes that are available to date. This is a topological defect and not a vacancy, thus, it would not be observed in typical experiments, *e.g.*, using a nanoballoon. The competing explanation, local hydrogenation, which also reduces the penetration barrier, but shows significantly lower isotope selectivity, is challenged.

In this work,[3] we calculated the flow of protons and their isotopes through graphene membranes and through the most common graphene defect sites to explain experimental results of graphene permeability and selectivity.[1,2] The models include, for comparison, pristine *h*BN and, as principal target material, graphene as pristine membrane, with the topological SW 55–77 defect (with two 5- and two 7-membered rings - 5MR and 7MR) and with a locally hydrogenated ring (Fig. 1). Note that SW 55-77 defect always appear as pairs of the two ring types, which is formed from by rotation of one C-C bond by 90°. The flow of protons (and their isotopes) was estimated including quantum tunneling via the Wentzel–Kramers–Brillouin (WKB) approximation.

EXPERIMENTAL. All structures were optimized using DFT, employing the PBE0 functional and 6–31+G(d,p) basis set. The D3-(BJ) correction of London dispersion interactions following the approach of Grimme was used as implemented in Gaussian 09 package. The transfer energy barriers (U_{max}) of a single proton going through different types of rings in the cluster and perpendicular to the flake plane were calculated using single point energies on the optimized cluster structures. Quantum tunneling was considered by applying the WKB approximation. See [3] for detailed methods description.

RESULTS. While we provide data for all three isotopes of hydrogen, including tritium for comparison, only the selectivity for the separation of H^+ and D^+ can be compared to the available experimental data and is, thus, the focus here. We show that the permeability of protons through perfect graphene is too low to generate appreciable particle flow, even though it would result in a very high selectivity (much higher than reported in the experiment). Local hydrogenation significantly lowers U_{max}, but also reduces significantly the isotope selectivity to values much lower (around 2) than those reported from the experiment. On the other hand, we argue that the topological, vacancy-free SW 55–77 defect, with U_{max} below 1 eV and H^+-over-D^+ (H^+/D^+) selectivity of about 7, matches well the experimental findings of about 10 by Lozada-Hidalgo *et al.*[2] The H^+ flow through the 7MR is 10^6 times larger than that through the 6MR, indicating that, even if the concentration of such a defect was as low as 1 ppm, it would still govern the transport process in the graphene flake (and yet neither be detectable in the Raman spectrum nor in the nanoballoon test). These findings indicate that increasing the concentration of 7MRs in vacancy-defect-free sp^2 carbon structures are a promising route for the design of hydrogen-isotope-separation and potentially proton-exchange membranes. It is worth noting that the experimentally detected H^+/D^+ selectivity of 10 was also obtained for *h*BN monolayers.[1,2] Since *h*BN has normally much less defects, we have calculated the energy barrier and selectivity using pristine model with 6MR. We again obtained H^+/D^+ selectivity of 7, in good agreement with the experiment. The summary of the finding of these studies is shown in Fig. 1.

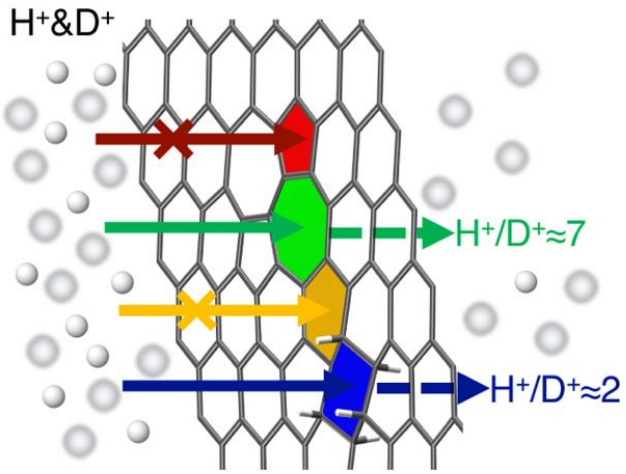

Fig. 1: Schematic representation and summary of proton (H^+) and deuteron (D^+) transfer and separation through graphene with different carbon ring sizes. The most plausible explanation of the high isotope selectivity is that seven-membered rings are present in the 2D membrane (green), as in the case of common SW 55–77 defects.

ACKNOWLEDGEMENTS. The authors acknowledge ZIH Dresden for computer time. Y. A. acknowledges China Scholarship Council. Y. A. and A. K. acknowledge Deutsche Forschungsgemeinschaft (DFG) GRK 2247/1 (QM3) for financial support. Open access funding enabled and organized by Projekt DEAL.

[1] Hu, S. *et al.* (2014) *Nature* **516**, 227.
[2] Lozada-Hidalgo, M. *et al.* (2016) *Science* **351**, 68.
[3] An, Y. *et al.* (2020) *Adv. Mater.* 2002442 – 1 – 6.

Size dependence of lattice parameter and electronic structure in CeO_2

D. Prieur, W. Bonani,[1] K. Popa,[1] O. Walter,[1] K. W. Kriegsman,[2] M. H. Engelhard,[3] X. Guo,[2] R. Eloirdi,[1] T. Gouder,[1] A. Beck,[4] T. Vitova,[4] A. C. Scheinost, K. O. Kvashnina, P. Martin[5]

[1]Joint Research Centre, European Commission, Karlsruhe, Germany; [2]Department of Chemistry and Alexandra Navrotsky Institute for Experimental Thermodynamics, Washington State University, Pullman, WA, U.S.A.; [3]Environmental Molecular Sciences Laboratory, Pacific Northwest National Lab, Richland, WA, U.S.A.; [4]Karlsruhe Institute of Technology (KIT), Institute for Nuclear Waste Disposal, Karlsruhe, Germany; [5]CEA, DEN, DMRC, SFMA, LCC, Bagnols-sur-Cèze, France.

Intrinsic properties of a compound, including electronic structure, crystallographic structure, optical and magnetic properties, define notably its chemical and physical behavior. In the case of nanomaterials, these fundamental properties depend on the occurrence of quantum mechanical size effects and on the considerable increase of the surface to bulk ratio. Here, we explore the size-dependence of both crystal and electronic properties of CeO_2 nanoparticles (NPs) with different sizes by state-of-the art spectroscopic techniques. X-Ray Diffraction (XRD), X-Ray Photoelectron Spectroscopy (XPS), and High-Energy-Resolution Fluorescence-Detected X-ray Absorption Near-Edge Structure (HERFD-XANES) demonstrate that the as-synthesized NPs crystallize in the fluorite structure and they are predominantly composed of Ce^{IV} ions. The strong dependence of the lattice parameter with the NPs size was attributed to the presence of adsorbed species at the NPs surface based on FTIR and TGA measurements.[1]

EXPERIMENTAL. Ceria nanoparticles samples were synthesized at JRC Karlsruhe by alkaline precipitation of cerium ammonium sulfate precursor followed by hydrothermal condensation in a pressurized autoclave at different temperatures. HERDF-XANES measurements were conducted at the CAT-ACT beamline (ACT station) of the synchrotron light source (KIT, Karlsruhe, Germany).

RESULTS. The oxidation state and electronic structure of Ce was assessed using Ce L_{III} edge HERFD-XANES (Fig. 1) and XPS. No characteristic band feature of Ce^{III} was found for samples across all crystallite sizes, indicating that only tetravalent cerium is present.

XRD and transmission electron microscopy data show that the as-synthesized CeO_2 NPs crystallize in the Fm−3m fluorite structure (space group 225). Depending on the experimental conditions (and particularly the annealing temperature), the average crystallite diameters vary from 2.0 ± 0.1 to 91 ± 12 nm.

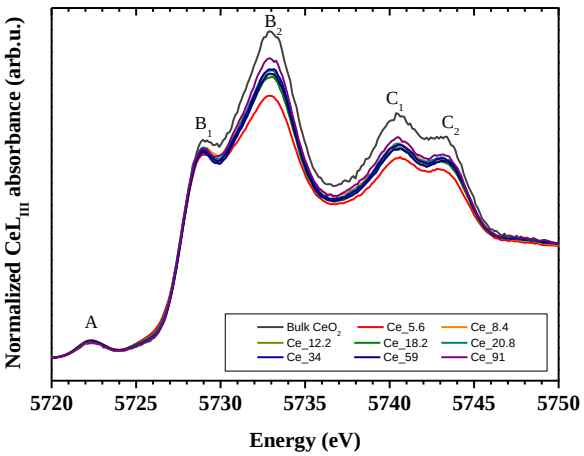

Fig. 1: Ce L_3 HERFD-XANES spectra of CeO_2 NPs with different sizes compared to bulk CeO_2 (> 100 nm).

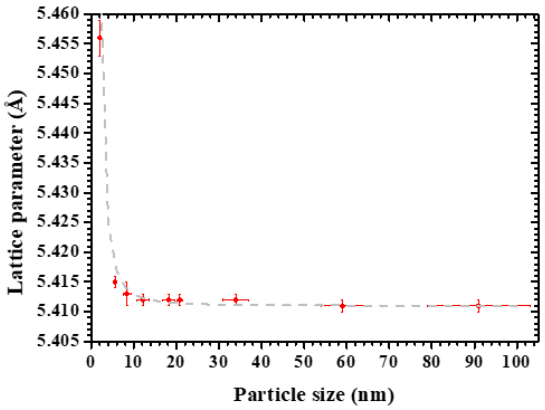

Fig. 2: Decrease of lattice parameter with the particle size.

Figure 2 presents the size dependence of the lattice parameters of the as-synthesized CeO_2 NPs. When the particle size changes from 2.0 to 91 nm, the unit cell value varies from 5.456 (3) to 5.411 (1) Å.

This lattice parameter variation as a function of the particle size has been ascribed to two mechanisms: either to the formation of oxygen vacancies in the smaller NPs, which leads to a change in the oxidation state of the constituting cation, or to the variation of the surface stress resulting from the difference of coordination between atoms on the surface and in the bulk.[2] This effect becomes more pronounced as the particle size reduces, *i. e.* as the contribution of the surface atoms to the structural characteristics increases. From our HERFD-XANES and XPS findings, the presence of Ce^{III} and hence of the oxygen vacancy, can be discarded, which means that the observed lattice expansion might then be only due to surface stress. To corroborate this assumption, the formation of species present at the NPs surface has been studied by FT-IR and TGA measurements. Indeed, our data confirms the presence of surface hydroxyl and carbonate groups that have a tensile effect on the crystalline lattice.

ACKNOWLEDGEMENTS. The authors acknowledge the KIT light source for provision of instruments at their beamlines and the Institute for Beam Physics and Technology (IBPT) for the operation of the storage ring, the Karlsruhe Research Accelerator (KARA).

[1] Prieur, D. *et al.* (2020) *Inorg. Chem.* **59**, 5760–5767.
[2] Diehm, P. M. *et al.* (2012) *Chemphyschem* **13**, 2443–2454.

Isotopic dual-radiolabeling of CeO_2 nanoparticles for uptake and dissolution studies

S. Schymura, I. Rybkin, T. Rijavec,[1] A. Mansel, A. Lapanje,[1] K. Franke, M. Strok[1]

[1] Jozef Stefan Institute, Ljubljana, Slovenia

Manufactured nanoparticles, such as CeO_2, give rise to novel risks when released into the environment. To assess these risks it is important to quantify the nanoparticle mass flows, as well as their speciation and the mechanisms of their transformation. The radiolabeling of nanoparticles can be a valuable tool allowing detection at very low concentrations, regardless of any complex backgrounds. We have developed an innovative dual-radiolabeling strategy for CeO_2 nanoparticles that will allow the tracking of these particles in uptake and dissolution studies with a sensitivity to dissolution effects.

The risks associated with manufactured nanoparticles (NPs) greatly depend on the transformation of said particles. Fast dissolving NPs can be treated as dissolved species while persistent NPs can be treated as particles. Slowly dissolving particles such as CeO_2 form a special case as transport and uptake can happen in particle form to deliver toxic ions *via* a Trojan horse effect. In particular for CeO_2, there are conflicting results on the role of dissolution effects in uptake by organisms.[1,2] Based on our previous efforts we developed an isotopic dual-radiolabeling strategy to shed light on uptake pathways of anthropogenic cerium in organisms (Fig. 1).

EXPERIMENTAL. CeO_2 nanoparticles were procured from the JRC Nanomaterial Repository and activated *via* neutron irradiation at the TRIGA Mark II nuclear reactor of the Jozef Stefan Institute (JSI). 30 mg of CeO_2 NPs were sealed in a quartz ampule and irradiated at a neutron flux of 1×10^{13} for 63 hours.[3]

Using the in-house IBA Cyclone 18/9 cyclotron at HZDR Research Site Leipzig Ce-139 radiotracer was produced by 10.9 MeV proton irradiation of a lanthanum metal foil at a current of 22 µA for about 23 hours yielding a current integral of 500 µAh. According to the reaction cross-section, the optimum proton energy was set by the design of the target using an 850 µm aluminum window.

The irradiated target was dissolved in conc. HNO_3 and the radiotracer was separated from the target material by extraction chromatography using UTEVA resin.

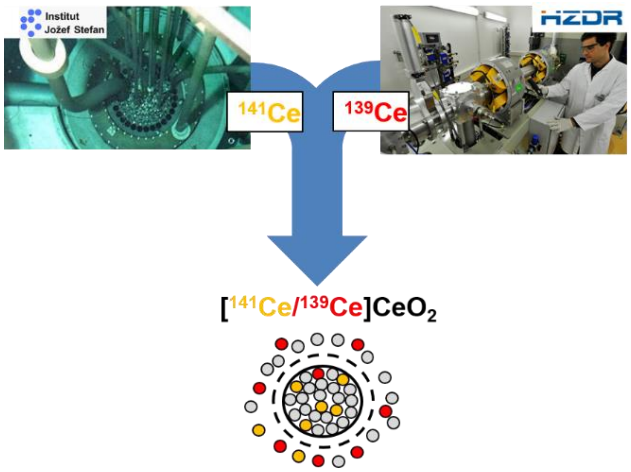

Fig. 1: Dual-radiolabelling strategy for manufactured CeO_2 NPs, illustrating the heterogeneous/isotopic distribution of the different radiotracers (particle volume vs. surface-near) in the nanoparticles and their release during dissolution.

For dual-radiolabeling the Ce-139 solution was added dropwise to the neutron activated [Ce-141]CeO_2 NPs followed by a 5 hours tempering step at 300 °C prompting in-diffusion of the Ce-139 into the NPs.

RESULTS. Irradiation of CeO_2 NPs with neutrons at the JSI nuclear reactor triggered the nuclear reaction Ce-140(n,γ)Ce-141, but also Ce-143 and Ce-139 were formed upon side reactions. Ce-143 was let decay, while Ce-139 was not expected to interfere with the further labeling strategy, since it was formed only two orders of magnitude less than Ce-141. Ce-139 was produced at the HZDR cyclotron with a yield of 0.1 MBq/µAh. The radiochemical yield of the tracer separation was 96 %.

The radiolabeling yield of the in-diffusion step was 99 % thereby successfully generating dual-labeled NPs of [Ce-139/Ce-141]CeO_2 (Tab. 1). The different radiolabels are distributed differently in the particles. While the Ce-141 is equally distributed within the particles, the Ce-139 is located mainly at the particle surface. Therefore, the different properties of the radioisotopes enable us to track dissolution processes *via* the Ce-141/Ce-139 ratio (Tab. 2).

Tab. 1: Characterization data and specific activities reached for radiolabelled CeO_2 NPs.

Particles	Size [nm]*	Specific Activity [MBq/mg]
CeO_2 NPs	221	–
[Ce-141]CeO_2 NPs	223	0.255 Ce-141
[Ce-139/Ce-141]CeO_2 NPs	219	0.272 Ce-139 0.107 Ce-141

*: as measured by DLS.

Tab. 2: Cerium radiotracer properties.

Radioisotope	Half-life [d]	γ-peak [keV]
Ce-139	137.64	168.86
Ce-141	32.51	145.44

ACKNOWLEDGEMENTS. We acknowledge financial support by the Helmholtz-Association, grant PIE-0007 (CROSSING).

[1] Schymura, S. *et al.* (2017) *Angew. Chem. Int. Ed.* **56**, 7411–7414.
[2] Zhang, P. *et al.* (2019) *Environ. Sci.: Nano* **6**, 60–67.
[3] Carbonne, S. *et al.* (2016) *Chemosphere* **162**, 16–22.

Uncertainty explorations in the context of nuclear waste management

S. Pospiech, V. Brendler

The EURAD joint program deals with various aspects of nuclear waste management, covering the whole range from waste packages to geotectonics. Its work package 10 (UMAN) is dedicated to the management of uncertainties potentially relevant to the safety of different radioactive waste management stages and programs. The task of the Institute of Resource Ecology (IRE) is to contribute to the development of general guidelines to identify, categorize and process uncertainties.

The IRE contributes within UMAN concerning identification, classification and quantification of numerical uncertainties that might be of relevance in the various stages of radioactive waste management (RWM). Main results are summarized in a EURAD report.[1] It provides definitions for frequently used terms, *e.g.* uncertainty in general, parameter uncertainty, uncertainty models, and aleatory *vs.* epistemic uncertainties. Sources used as input for this report were questionnaires, expert elicitation and literature survey. The following themes and stages of RWM were addressed:

1. National Program Management
2. Predisposal
3. Engineered Barrier System
4. Geoscience
5. Design and Optimization
6. Siting and Licensing
7. Safety Case

RESULTS. The consideration of urgency and potential benefit is the first step for a robust assessment of the priority for further investigation, established through expert judgement. It can be transferred into the following criteria:

- level of impact on safety,
- level of impact on decision-making process,
- time span till utilization within the RWM stages,
- priority for further investigation.

A categorization of uncertainties can be based on very different features and is in principle depending on the purpose of application. Typical categories are:

- epistemic (more information will reduce it) *vs.* aleatoric (intrinsic properties, no reduction possible) uncertainties,
- time step of occurrence within RWM,
- RWM system component affected,
- management option (reduce/mitigate/ignore),
- scale of application (generic, national, site-specific),
- type of heterogeneity with regard to space or time.

Two methodologies were applied for structuring uncertainties: fishbone diagrams and tables for uncertainty characteristics. Examples are given in Fig. 1 and Tab. 1.

Namely the fishbone diagrams are a flexible tool, regularly used to support the development of conceptual models required for uncertainty treatment. They can be used to combine and thus simplify uncertainty components, leading to model reduction. Also, they can carry information how the components are related to each other, *e.g.*, if they are additive or multiplicative and/or repeatable or repeatedly arising. This is an important step for the uncertainty quantification / approximation by probability density functions. Such diagrams promote structuring individual sources of uncertainties in different systems. Numerical uncertainties must be evaluated and transformed in a way that a respective model can make directly use of them. The three most often used mathematical approaches are deterministic/probability statistics, worst case analysis and fuzzy set theory.[2–4] Among the probability statistics, the two main branches are frequency statistics and Bayesian statistics.

Tab. 1: Disposal container uncertainty list applicable to high-level waste and spent nuclear fuel.

Component / process	Associated uncertainties	E/A*
Container corrosion (normal and specific aggressive conditions)	Interim storage times, container material composition & lifetime	E
Production of gases due to radiolysis and redox processes	Type and amount of gases produced, production rate	E
Leakages of gaseous compounds	Pressure build-up, release rates	E
Overall size requirement for a DGR**	Final volume of waste package per type of waste	E
Heat generation within a DGR	Interim storage times, inventory	E

*: (E)pistemic *vs.* (A)leatoric uncertainty type.
**: Deep Geological Repository.

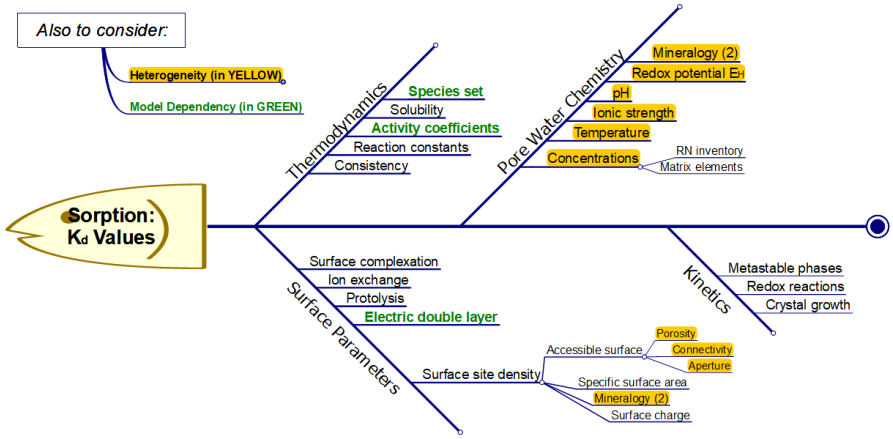

Fig. 1: Example for Fishbone (Ishikawa) diagram, highlighting the mutual relationship between uncertainties contributing to the overall uncertainty of distribution coefficients.

ACKNOWLEDGEMENTS. Financial support by the European Union through the EURAD program under grant 847593 is gratefully acknowledged.

[1] Brendler, V. *et al.* (2020) *Uncertainty identification, classification and quantification*, EURAD Report D10.3.
[2] Bárdossy, G. *et al.* (2004) *Evaluation of uncertainties and risks in geology: new mathematical approaches for their handling*. Springer, Berlin.
[3] Morgan, M. G. *et al.* (1990) *Uncertainty: a guide to dealing with uncertainty in quantitative risk and policy analysis.* Cambridge University Press, New York.
[4] Bandemer, H. *et al.* (1995) *Fuzzy sets, fuzzy logic, fuzzy methods: With applications.* Wiley, Chichester.

Implementation of the smart K_d-concept in the reactive transport code OpenGeoSys (OGS-6)

M. Stockmann, R. Lu,[1] V. Brendler

[1]Helmholtz Centre for Environmental Research – UFZ, Department of Environmental Informatics, Leipzig, Germany

Within the iCross project, the radionuclide transport through the far-field of a repository system is simulated with the transport code OpenGeoSys-6 (OGS).[1,2] The big challenge in large-scale reactive transport modelling is to find an acceptable way to integrate geochemistry at affordable cost and to balance between geochemical realism and computational efforts. As an effective alternative to a direct coupling of OGS-6 with PHREEQC,[3] the smart K_d-concept (www.smartkd-concept.de) has been implemented in OGS to consider variable geochemistry.[4,5]

METHODOLOGY. The fundamental strategy of the smart K_d-concept, a mechanistic approach mainly based on surface complexation models, is to compute *a priori* multidimensional look-up tables with distribution coefficients (referred to as smart K_d-values) for a wide range of important environmental input parameters, *e. g.* pH, ionic strength, concentration of competing cations and complexing ligands. Thereby, the "Component Additivity" approach is used to describe a natural system close to reality. This bottom-up approach is based on the principle that the sorption of contaminants can be determined from the competitive mineral-specific sorption of each dissolved species on all surfaces. For each transport step, a smart K_d-value valid for the actual geochemical conditions is interpolated from the pre-calculated look-up table and used for the transport simulations. The schematic workflow is shown in Fig. 1.

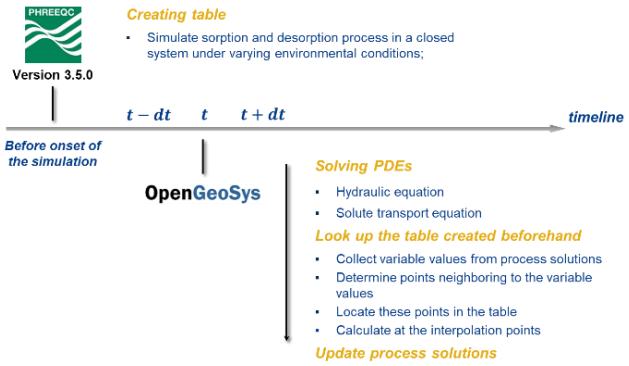

Fig. 1: Workflow of the look-up table approach in OGS-6.

MODEL SETUP. Based on a well-defined test case for a typical sedimentary rock system covering potential repository host rocks, namely salt and clay formations in Northern Germany,[5] a 2D transport model was developed. Thereby, a reduced set of chemical components was considered to keep the model simple and to reduce the computational effort. The transport of H^+, OH^-, Na^+, Cl^-, Ca^{2+}, dissolved inorganic carbon, and several radionuclides (RNs) was simulated through an initially saturated column of 20 m in length and 3 m in width (Fig. 2).

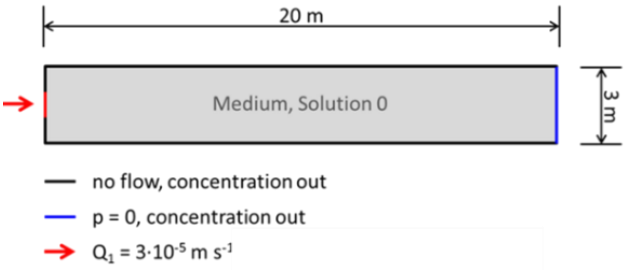

Fig. 2: Model domain with boundary conditions.

RESULTS. To validate the concept, we compared the results of the look-up table approach with the results of the direct coupling of OGS-6#PhreeqC3.5.0. The results show a good agreement between both approaches for all considered repository-relevant RNs (Cs, Ra, Ni, Am, Th, Np, U). Figure 3 shows the spatial distribution exemplarily for neptunium(V) - Np(5) after 500,000 s simulation time. Np(5) has the weakest sorption of all considered RNs with the peak maximum at a distance of 11 m from the inflow compared to the other radionuclides. The curves of both simulations lie nearly perfectly one upon another. This implies that the look-up table approach works well. We are able to reflect the RN-specific retardation effect. This real application case serves as a comprehensive proof-of-concept and as a benchmark for field-scale transport simulations.

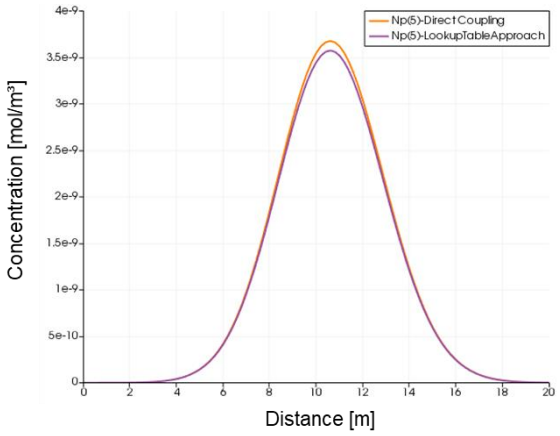

Fig. 3: Spatial distribution of neptunium after 500,000 s simulation time.

ACKNOWLEDGEMENTS. This project is funded by the German Federal Ministry of Education and Research (BMBF) (Grant 02NUK053B) and the Helmholtz Association (Grant SO-093).

[1] Jang, E. *et al.* (2018) *OpenGeoSys Tutorial III*, 103.
[2] Kolditz, O. *et al.* (2012) *Environ. Earth Sciences* **67**, 589–599.
[3] Stockmann, M. *et al.* (2019) *Report HZDR-110.*
[4] Stockmann, M. *et al.* (2017) *Chemosphere* **187**, 277–285.
[5] Noseck, U. *et al.* (2018) *Report GRS-500.*

Thermodynamic reference database THEREDA: 10. The cumulative 2020 data release and major developments

F. Bok, A. Richter, J. Sohr,[1] W. Voigt[1]

[1]TU Bergakademie Freiberg, Institute for Inorganic Chemistry, Freiberg, Germany

THEREDA[1,2] is a joined database project to assess potential radionuclide migration scenarios accurately and to make well-founded predictions about the long-term safety up to one million years. The number of elements for which data is provided as well as the upgrades in supported geochemical codes necessitated a change in release strategy. Another innovation is the comparison of experimental data and THEREDA calculations, through which users can assure themselves of the quality of the data offered.

THEREDA provides data for actinides, fission products as well as matrix and building materials using the Pitzer ion interaction model[3] for high saline solutions (ionic strength up to at least 7 molal) in the temperature range from 0 to 100 °C. In the fourth phase of the THEREDA project, the following relevant changes and new features have been introduced so far:

NEW RELEASE STRATEGY. In the earlier project phases, small, self-contained data packages on individual chemical systems were released. This should ensure data consistency and prevent cross-effects due to element combinations for which no validated data exists yet. This approach has become impracticable for updating purposes with increasing number of releases and supported geochemical codes. Therefore, all the released thermodynamic data and associated interaction parameters are now combined in one file per code. Furthermore, annual updates for the released data are intended. With the 2020 data release, THEREDA supports the codes ChemApp[4], GEMS[5], Geochemist's Workbench[6], PHREEQC[7] and ToughReact[8].

DATA RELEASE 2020. In the present THEREDA data release, data for actinides and their chemical analogues (Th, U, Np, Pu, Am, Cm & Nd), fission products (Se, Sr, Tc & Cs) and matrix elements (Na, K, Mg, Ca, Al, Si | Cl, SO_4, CO_3) are combined. Many updates as well as a polythermal selenium(IV/VI) data set have been included. Also, the current version of CEMDATA (18.1) was integrated for the calculation of cementitious phases.[9]

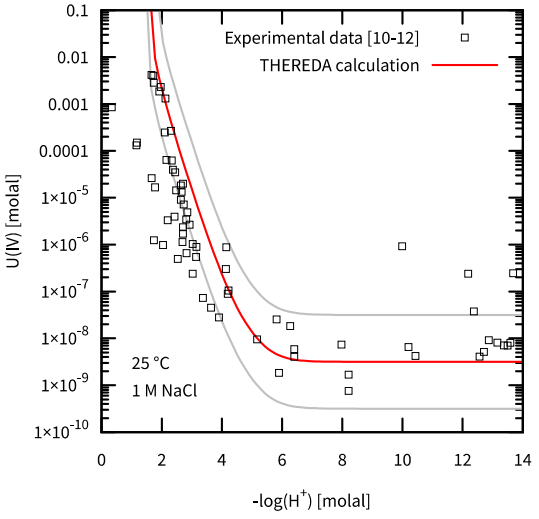

Fig. 1: Solubility of amorphous uranium(IV) hydroxide in 1 m NaCl solution at T = 25 °C. Symbols: experimental data,[10–12] Lines: calculation using THEREDA (red), uncertainty range from solubility constants error[13] (grey).

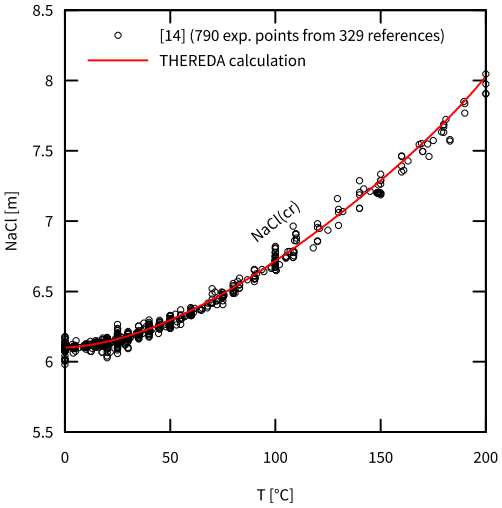

Fig. 2: Solubility of halite at T = 0–200 °C. Symbols: experimental data,[14] Line: calculation using THEREDA.

APPLICATION EXAMPLES. THEREDAs capabilities are now demonstrated using approx. 400 application case calculations, whose results were compared with experimental values published in literature. These demo calculations can be browsed on a new section of the website (thereda.de). Examples are shown in Figs. 1 and 2.

ACKNOWLEDGEMENTS. Knowing that database work of this kind can only be accomplished within a great team, the authors thank all members of the THEREDA team at GRS, KIT-INE, TUBAF and PSI-LES. THEREDA is funded by the Federal Company for Radioactive Waste Disposal (BGE) with the contract number 45181017.

[1] Altmaier, M. *et al.* (2008) *atw* **53**, 249–253.
[2] Moog, H.C. *et al.* (2015) *Appl. Geochem.* **55**, 72–84.
[3] Pitzer, K.S. (1991) *Activity Coefficients in Electrolyte Solutions*, 2nd Ed., CRC Press, Boca Raton.
[4] https://gtt-technologies.de/software/chemapp/
[5] http://gems.web.psi.ch/
[6] https://www.gwb.com/
[7] https://www.usgs.gov/software/phreeqc-version-3
[8] https://tough.lbl.gov/software/toughreact/
[9] Lothenbach, B. *et al.* (2019) *Cem. Concr. Res.* **115**, 472–506.
[10] Ryan, J. L., *et al.* (1983) *Polyhedron* **2**, 947–952.
[11] Rai, D. *et al.* (1997) *Radiochim. Acta* **79**, 239–247.
[12] Neck, V. *et al.* (2001) *Radiochim. Acta* **89**, 1–16.
[13] Grenthe, I. *et al.* (2020) *Second Update on the Chemical Thermodyamics of Uranium, Neptunium, Plutonium, Americium and Technetium*, OECD Nuclear Energy Agency, Boulogne-Billancourt.
[14] Krumgalz, B.S. (2017) *J. Phys. Chem. Ref. Data* **46**, 043101–1–16.

Biological Systems

Long-Lived Radionuclides in

BIOLOGICAL SYSTEMS

Proteomics confirms initiation of glutathione-mediated sequestration upon uranium exposure to tobacco (*Nicotiana tabacum*) BY-2 cells

W. A. John, N. Matschiavelli, D. Thieme,[1] W. Hoehenwarter,[1] S. Sachs

[1]Leibniz-Institut für Pflanzenbiochemie, Halle (Saale), Germany

Increases in glutathione (GSH) and enzymes involved in the removal of reactive oxygen species (ROS) are part of the cellular response to heavy metal stress. Proteomics was used to confirm that uranium in culture causes an increase in GSH metabolism in tobacco BY-2 cells even under culture conditions of phosphate deficiency.

Plants have adapted various ways of dealing with heavy metal stress. This is of particular importance for hyperaccumulator plants, which are able to grow in soils with potentially toxic abundances of heavy metals. Uranium as a heavy metal has a high potential to lead to the formation of ROS through Fenton reactions, which could cause irreparable cell damage.[1] Plant cells typically respond by increasing GSH reserves and producing antioxidative enzymes to help in metal chelation and ROS removal. Glu-Cys ligase is one of the enzymes responsible for the production of GSH and the enzyme GSH S-transferase facilitates the conjugation of GSH to xenobiotic substances for detoxification.[2] Superoxide dismutase, catalase and a variety of peroxidases are part of the enzyme repertoire involved in the inactivation of ROS. Previous research has exquisitely demonstrated the uranium-induced increase in GSH pools and ROS scavenging activity in *Brassica napus* using biochemical assays.[1] In this study, proteomics was used to contribute to a molecular process understanding of the interaction of uranium with plants by gauging the extent of the enzymatic response, using tobacco (*Nicotiana tabacum*) bright yellow 2 (BY-2) cells as a model for plant cells.

EXPERIMENTAL. BY-2 cells were grown in the dark in modified Murashige-Skoog (MS) medium (4.3 g/L basal salt, 200 mg/L KH_2PO_4, 30 g/L sucrose, 100 mg/L inositol, 1 mg/L thiamine and 200 µg/L 2,4D) for seven days.[3] 1.5 mL of this culture were sub-cultivated into three flasks of 30 mL regular MS medium and into six flasks of 30 mL phosphate deficient MS medium (MS-red; containing only 1.7 mg/L phosphate) and grown for three days. Into three of the flasks of MS-red medium, uranyl nitrate (20 µM) was added. All flasks were incubated for 24 h. 15 mL of each culture were gently centrifuged to remove the culture medium and the remaining pellet was washed with 15 mL of 50 mM MOPS buffer (pH 7.5). After another round of centrifugation, the cell pellet was resuspended in extraction buffer (50 mM MOPS, 2 mM dithiothreitol (DTT), 5 % polyvinyl polypyrrolindone and protease inhibitors) and lysed by grinding with a mortar and pestle in liquid nitrogen. The crude extract was spun down at 16,000 × *g* for 20 min at 4 °C and the sediment was discarded. Protein in the supernatant was subsequently quantified using a Pierce™ Bradford assay kit. 100 µg of the protein extract were centrifuged through cleaned 30 kDa Amicon® Ultra 0.5 mL filters and buffer exchange with 8 M Urea/50 mM Tris, reduction with 8 M Urea/50 mM Tris/100 mM DTT and alkylation with 8 M Urea/50 mM Tris/50 mM Iodoacetamide were all carried out inside the filters. A final buffer exchange step with 50 mM NH_4HCO_3 was performed prior to digestion with 0.5 µg of LysC enzyme and 2 µg of trypsin at 37 °C overnight. The resulting peptides were then centrifuged through the filters using extra NH_4HCO_3. The peptides were desalted using C18 STAGE-tips and subsequently resolved and analyzed by an EASY-nLC 1000 chromatography system coupled to an LTQ-Orbitrap Velos Pro mass spectrometer (Thermo Scientific). Protein and peptide identification were carried out as described elsewhere.[4]

Tab. 1: Logarithmic (base 2) fold changes of differential protein expression showing effects of uranium treatment and phosphate deficiency on BY-2 cells. Fold change of 1 indicates the treatment caused a doubling of protein compared to the control; −1 indicates that the protein quantity was half of the control; 0 means there was no difference in protein expression. Significance is denoted by $^{*}p < 0.05$, $^{**}p < 0.01$, $^{***}p < 0.001$.

Protein	Log_2 Fold Change	
	Uranium treatment	Phosphate deficiency
Glutathione S-transferase	0.82*	2.95***
Glutathione peroxidase	0.80*	1.17***
Glutamate-Cysteine ligase	−0.03	0.82*
Superoxide dismutase	0.08	1.29**
Catalase	0.07	0.67

RESULTS. The experimental conditions not only exposed the plant cells to uranium but also introduced conditions of phosphate (Pi) deficiency in order to avoid the formation of insoluble complexes of uranyl(VI) phosphate. It was apparent that Pi deficiency was already inducing stress, based on protein expression patterns (Tab. 1) and cell growth (not shown). All five proteins of interest were overexpressed with Pi deficiency, and all enzymes, except catalase, showed significant overexpression. This highlighted the importance of Pi to the culture and that three days of Pi deficient cultivation was sufficient to cause stress. Nevertheless, the presence of uranium elicited a specific response, whereby GSH S-transferase and GSH peroxidase were almost twofold overexpressed, suggesting the cells were sensitized to the presence of a foreign substance. GSH has been seen to form strong complexes with uranyl(VI) ions and other heavy metals.[5] Since Pi deficiency had already led to elevated GSH levels, it can be deduced that in this instance, energy is being expended to sequester cytosolic (and possibly organelle-bound) uranium with the help of GSH S-transferase, thereby reducing the propensity toward cellular damage *via* ROS. At present, further investigation is underway to determine how similar the cellular response would be with the absence of stress induced by Pi deficiency.

ACKNOWLEDGEMENTS. The authors thank Prof. P. Nick (Botanical Institute, KIT) for providing the first batch of BY-2 cells and J. Seibt for support with cell cultures. This work was funded by the Federal Ministry of Education and Research (contract number 02NUK051B).

[1] Viehweger, K. *et al.* (2011) *Biometals* **24**, 1194–1204.
[2] Forman, H. J. *et al.* (2009) *Mol. Aspects Med.* **30**, 1–12.
[3] Murashige, T. & Skoog, F. (1962) *Physiol. Plant* **15**, 473–497.
[4] Majovsky, P. *et al.* (2014) *J. Proteome Res.* **13**, 4246–4258.
[5] Frost, L. *et al.* (2011) *Proc. Radiochim. Acta* **1**, 357–362.

Do carotenoids quench uranium(VI) luminescence in TRLFS spectra of plant cells?

J. Jessat, M.-L. Bilke, S. Sachs

Previous Time-Resolved Laser-Induced Fluorescence Spectroscopic (TRLFS) studies on the interaction of U(VI) with the two plant cell systems *Brassica napus* (rapeseed/canola) and *Daucus carota* (carrot) showed that spectra of significantly lower quality had been obtained for the latter. Therefore, experiments on carotenoid extraction from the cells were carried out. It was shown that both organisms contain considerable amounts of carotenoids, however, these substances are not responsible for the observed luminescence quenching effects of U(VI).

Time-Resolved Laser-Induced Fluorescence Spectroscopy (TRFLS) is applied to study the interaction of U(VI) with plant cells and to elucidate the U(VI) speciation on/in the cells and in solution on a cellular and molecular level. TRLFS measurements with the two plant cell species *Brassica napus* (*B. napus)* and *Daucus carota* (*D. carota)* revealed that a significantly lower luminescence intensity could be observed in the *D. carota* system for U(VI) in the initial nutrient media, in supernatants after cell contact as well as in the biomass. Since the U(VI) concentrations in both systems were similar, these observations were attributed to the quenching of the U(VI) luminescence in the *D. carota* system. A possible explanation for these effects could be the occurrence of carotenoids in the plant cells. For uranyl(VI) compounds and all trans-β carotenoids, the absorption and emission spectra lie in a comparable wavelength range.[1–3] Thus, a significant reduction of the U(VI) luminescence can be expected when the absorption of excitation light by carotenoids present in the *D. carota* system occurs. The aim of this study was to extract carotenoids from *B. napus* and *D. carota* suspension cells and to examine the obtained carotenoid solution by UV-vis spectroscopy. Based on the findings, it was concluded whether the carotenoids contained in the cells could be responsible for the quenching effects in the *D. carota* system or not.

EXPERIMENTAL. *B. napus* cells were obtained as callus cell culture from DSMZ Braunschweig. *D. carota* callus cells were established as described by Sachs *et al*.[4] The cultivation of *B. napus* suspension cells was performed as described in the literature.[5] *D. carota* cells were cultivated in the same way, however, using medium B5C2[6] instead of medium R. Seven days after subcultivation, the suspension cells were separated from the culture media and frozen at −20 °C. The frozen cells were freeze-dried for three days (Alpha 1–4 LSC, Christ). Subsequently, the dried cells were crushed with a mortar and pestle while adding liquid nitrogen. The mortared cells were mixed in round bottom flasks with an acetone/petrol ether mixture (v/v = 1:1) with a solid/liquid ratio of 1 g/30 mL according to Yan *et al*.[7] The mixtures were heated to 42 °C in a water bath under reflux and stirring for 1 h (Fig. 1). After cooling the mixtures, the cell residues were separated by filtration and clear, bright yellow carotenoid solutions were obtained. The UV-vis measurement of the carotenoid solution was performed in quartz glass cuvettes (HELL117100F-10-40, Hellma Analytics) with a Silver-Nova spectrometer (Silver-Nova, StellarNet Inc.).

RESULTS. It was found that both systems, *B. napus* and *D. carota* cells, yield extracts that had a strong yellow coloration indicating the presence of carotenoids. The UV-vis measurement resulted in characteristic carotenoid spectra (Fig. 1) for the extracts of both organisms. According to this, it was concluded that both cell cultures contain similar carotenoids. An estimation of the carotenoid content based on the UV-vis measurement and the applied cell mass was possible and allowed the conclusion that both organisms also contain comparable amounts of carotenoids. Accordingly, it could be excluded that carotenoids are responsible for the observed quenching of the U(VI) luminescence in the *D. carota* system, since otherwise the quenching would also have to occur for *B. napus*, which was not the case. Therefore, the quenching effects must have a different reason. Most probably, small differences in the composition of the used cell culture media for both organisms, which still have to be elucidated, are responsible for the quenching effects.

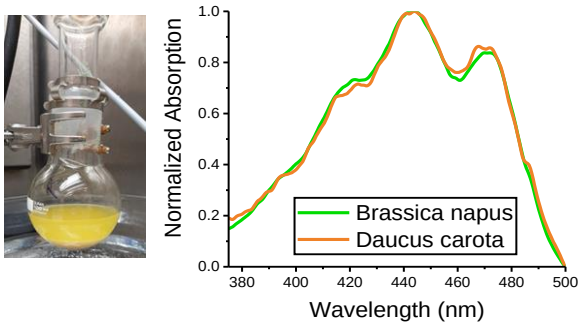

Fig. 1: Carotenoid extraction with *B. napus* suspension cells (left) and normalized absorption spectra of carotenoid extracts of *B. napus* and *D. carota* cells.

ACKNOWLEDGEMENTS. The authors thank J. Seibt and S. Heller for experimental support. This work was funded by the Federal Ministry of Education and Research under contract number 02NUK051B.

[1] Lee, J. *et al.* (2019) *Sci. Rep.* **9**, 3551.
[2] Meinrath, G. *et al.* (2000) *J. Alloys Compd.* **300–301**, 107–112.
[3] Drobot, B. *et al.* (2014) *Chem. Sci.* **6**, 964–972.
[4] Sachs, S. *et al.* (2020) *Report HZDR-110*, p. 238.
[5] Sachs, S. *et al.* (2017) *Environ. Sci. Technol.* **51**, 10843–10849.
[6] https://www.dsmz.de/fileadmin/Bereiche/PlantCellLines/Dateien/B5C2.pdf (last viewed: 11/17/2020).
[7] Yan, F. *et al.* (2015) *J. Food Qual.* **38**, 377–386.

Interactions of *Desulfosporosinus hippei* DSM8344 with Eu(III)

M. Puhlmann, S. Hilpmann, H. Moll, T. Stumpf, A. Cherkouk

Different *Desulfosporosinus* species were detected in bentonite and clay formations, which are suitable as barriers for nuclear waste disposal. Therefore, *Desulfosporosinus hippei* DSM8344^T was selected as a good representative to investigate its interactions with europium as a function of time. Time-resolved laser-induced fluorescence spectroscopy (TRLFS) revealed the presence of two Eu(III) species associated with the cells.[1]

Microorganisms, which are common in bentonite or clay formations, can potentially impact the retardation or mobility of radionuclides.[2] Diverse *Desulfosporosinus* species were verified to be present in bentonite,[3] a potential geotechnical barrier material, and clay formations, a potential host rock for nuclear waste repository. *Desulfosporosinus hippei* DSM8344^T a mesophilic sulfate-reducing bacterium was selected to study its interactions with europium which is a non-radioactive analog for trivalent actinides, *e.g.* curium and americium.

EXPERIMENTAL. *D. hippei* DSM8344^T was purchased from the Leibniz Institute DSMZ-German Collection of Microorganisms and Cell Cultures (DSMZ, Braunschweig, Germany) and cultivated in DSM641 medium as already described.[1] Europium bioassociation in batch systems was performed in a synthetic Opalinus Clay porewater solution (pH~5) with 10 mM sodium lactate and 50 or 100 µM Eu(III) as europium chloride.[4] The Eu(III) concentration in the supernatant after incubation for different times was measured with inductively coupled plasma mass spectrometry (ICP-MS). Eu(III) was used as molecular probe to investigate its speciation on cells and in supernatants using luminescence spectroscopy (TRLFS). Therefore, supernatants, as well as washed and resuspended cells, were investigated separately in a quartz glass cuvette at room temperature as described earlier.[5]

RESULTS. The association of Eu(III) on *D. hippei* DSM8344^T cells was investigated at 50 µM and 100 µM Eu(III) as a function of incubation time. The initial concentration of Eu(III) decreased only slightly under these conditions (data not shown). Approximately 17 % and 13 % of the Eu(III) was associated with the biomass at 50 µM and 100 µM Eu(III), respectively. During the incubation of up to 48 h an agglomeration of the cells was observed. The batch experiments could be done only with a relatively low amount of biomass. This might be one reason for the small effect observed in relation to the amount of bioassociated Eu(III).

Figure 1 summarizes the luminescence data measured for the Eu(III)-*D. hippei* system in the presence of 100 µM Eu(III). The spectrum of the blank (red graph in Fig. 1) is characterized by a strong increase of the $^7F_2$-transition in comparison with the Eu^{3+}-ion (black graph in Fig. 1). The $^7F_2$-transition is sensitive to changes of the chemical environment of the luminescent Eu(III).[6] The luminescence decay follows a mono-exponential law with an average lifetime of 132 ± 5 µs (N_{H_2O} = 7.5). This value is longer compared with the Eu^{3+}-ion (110 µs, N_{H_2O} = 9.0). Both information confirm a strong complexation of Eu(III) by inorganic components of the synthetic Opalinus Clay porewater at pH ~5.

The spectra showed no changes for Eu(III) present in the supernatants as a function of the incubation time. Hence, Fig. 1 presents the averaged data (olive graph in Fig. 1). The spectroscopic findings of Eu(III) in the supernatants in terms of

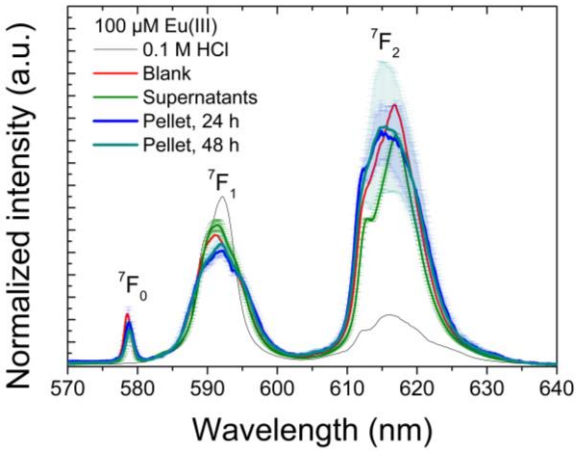

Fig. 1: Eu(III)-luminescence spectra measured after incubation of the *Desulfosporosinus hippei* DSM8344^T cells in synthetic Opalinus Clay porewater (pH ~ 5) and 100 µM Eu(III).

intensity of the $^7F_2$-transition and the luminescence decay behavior were similar to the values of the blanks. A change in the luminescence behavior in the supernatants could be attributed to a release of metabolites or lyzed cells. In the present case the amount of cells was probably too small for the observation of measurable effects.

The shape of the spectra of the cell-bound Eu(III) (blue and dark cyan graphs in Fig. 1) differs from the blank and supernatant. The appearance of the symmetry-forbidden $^7F_0$-transition in combination with the intensity increase of the $^7F_2$-transition points to a different Eu(III) coordination environment as found in Eu^{3+}, supernatant, and blank. In contrast, a bi-exponential luminescence decay was measured: 61 ± 27 µs and 367 ± 191 µs (N_{H_2O} = 2.3). The short lifetime is even shorter than the value of the Eu^{3+}-ion. Additional ligand-specific quench processes other than from OH^--ligands could explain this finding.[7] The long lifetime is a measure for significant changes in the first Eu(III) coordination sphere due to interactions with bacterial surface functionalities. In conclusion, the findings indicate a biosorption or bioaccumulation of Eu(III) by the cells in combination with a Eu(III) speciation change.

ACKNOWLEDGEMENTS. We acknowledge funding by the BMBF (Grant 02NUK053B) and HGF (Grant SO-093).

[1] Puhlmann, M. (2020) Master thesis, University of Applied Sciences Dresden, and references therein.
[2] Lloyd, J. R. & Macaskie, L. (2002) in: *Interactions of microorganisms with radionuclides. Radioactivity in the environment.* p. 313–342, Elsevier.
[3] Matschiavelli, N. *et al.* (2019) *Environ. Sci. Technol.* **53**, 10514–10524.
[4] Wersin, P. *et al.* (2011) *Appl. Geochem.* **26**, 931–953.
[5] Bader, M. *et al.* (2019) *Environ. Sci. Pollut. Res.* **26**, 9352–9364.
[6] Binnemans, K. (2015) *Coord. Chem. Rev.* **295**, 1–45.
[7] Kuke, S. *et al.* (2010) *Spectrochim. Acta Part A* **75**, 1333–1340.

Influence of fetal bovine serum and citrate on Eu speciation in cell culture medium

A. Heller,[1,2] F. Bok, A. Barkleit

[1]Professorship of Molecular Cell Physiology and Endocrinology, TU Dresden, Germany; [2]Central Radionuclide Laboratory, TU Dresden, Germany

The solubility and speciation of Eu in cell culture media with different contents of fetal bovine serum (FBS) and citrate were investigated by mass spectrometry (ICP-MS) and luminescence spectroscopy (TRLFS).[1,2] Results demonstrate that FBS is the key factor affecting Eu solubility and speciation, while citrate has no significant effect in the presence of FBS. Eu speciation is dominated by (a) soluble protein complexe(s) in FBS containing medium. In FBS free medium, insoluble Eu complexes with inorganic anions, mostly carbonate and phosphate, dominate. Up to now, thermodynamic modeling of the Eu speciation largely diverges from experimental results.

The knowledge of the lanthanides' speciation in cell culture media is crucial for the elucidation of the chemical affinities of these metals to the prevailing biomolecules and the resulting biological effects.

EXPERIMENTAL. Four different cell culture media, *i.e.* standard medium with 10 % FBS (st), serum-reduced medium with 1 % FBS (sr), serum-free medium (sf), and st-medium with 0.1 mM citrate (st-cit), were incubated with 10^{-5} or 10^{-3} M Eu. Eu solubility was derived from ICP-MS measurements of the medium supernatants after sterile filtration. TRLFS spectra in cell free culture media were recorded at room temperature after 24 and 48 h incubation time. The theoretical Eu speciation in each medium was calculated with thermodynamic modeling using current data.

RESULTS. After 24 h, Eu is completely soluble up to 1 mM in medium containing 10 % FBS (Fig. 1). Lowering the FBS content leads to significant decrease in Eu solubility indicating that proteins of FBS stabilize Eu in solution, thus making it bioavailable for cells. Identical results were obtained after incubation for 48 h. Citrate seems to have no additional effect on Eu solubility.

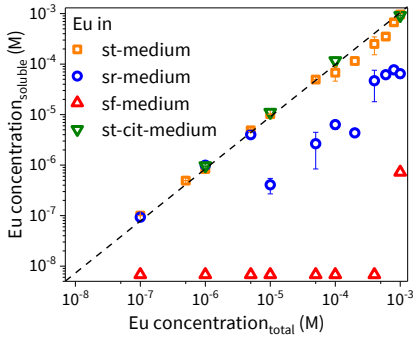

Fig. 1: Solubility of Eu in different cell culture media after incubation for 24 h. The dotted line equals 100 % solubility.

At 10^{-3} M Eu, visible precipitation occurs in sr- and sf-medium. Analysis of the settled deposits revealed elemental ratios of Eu:P ~ 1:1, indicating the formation of insoluble Eu-phosphate, and Eu:Ca ~ 1:0.2. TOC measurements indicate that also inorganic carbonate is contained in the deposits from both cell culture media, whereas the content of organic carbon is significantly higher in deposits from sr-medium. The latter points to organic ligands like proteins to be present in deposits from sr-medium, too.

In general, TRLFS spectra recorded after 24 and 48 h incubation time are very similar and indicate the coexistence of two Eu species in all four cell culture media (Fig. 2). In medium with 10 % FBS, the long lifetimes suggest the presence of only one or none water molecule left in the Eu^{3+} complexation shell. Hence, the complexation of Eu by (a) protein(s) from FBS can be assumed which concurs with solubility results. Citrate addition has no significant effect on TRLFS spectra indicating the same speciation in st- and st-cit-media. In FBS deficient media, especially at 10^{-3} M Eu, TRLFS spectra demonstrate the predominant complexation of Eu by (a) protein(s) as long as some FBS is present. However, also Eu complexes with phosphate, carbonate, and organic ligand(s) occur. This becomes obvious in the supernatant of sf-medium by completely different steady-state spectra and a significantly shorter luminescence lifetime (see Fig. 2C and D). In summary, we propose four different Eu species in dependence on the composition of the cell culture medium: Eu bound to (*i*) protein(s), (*ii*) phosphate, (*iii*) carbonate, and (*iv*) organic low molecular weight ligand(s).

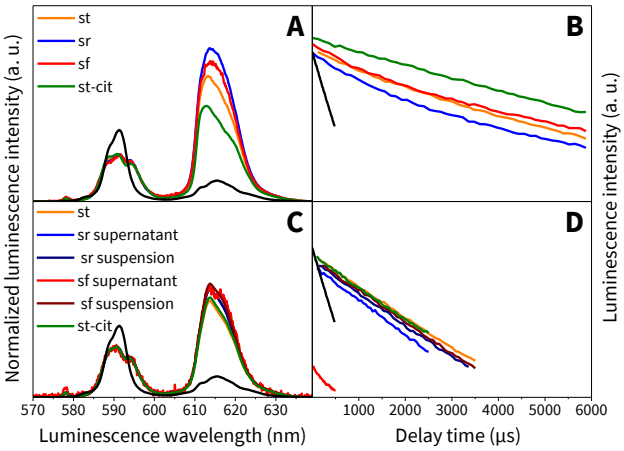

Fig. 2: Steady-state spectra (A, C) and luminescence decay curves (B, D) of 10^{-5} (A, B) and 10^{-3} M Eu (C, D) in different cell culture media after incubation for 24 h. Data for the Eu^{3+} aquo ion is given in black.

Independent from the medium composition, calculated Eu speciation diagrams are very similar and predict a predominant carbonate and, to some extent, phosphate complexation, whereas organic constituents are predicted to be negligible. The main reason for this discrepancy with our experimental results is most probably the lack of thermodynamic data for Eu complexes with proteins and other organic ligands as well as the variable and largely unknown composition of FBS. Hence, there is an urgent need to extend the current thermodynamic data sets of Eu complexes with organic ligands and proteins, to improve thermodynamic modeling for speciation predictions in complex biological fluids.

ACKNOWLEDGEMENTS. This work was funded by the Deutsche Forschungsgemeinschaft (HE 7054/2-1).

[1] Heller, A. *et al.* (2019) *Ecotox. Environ. Safe.* **173**, 469–481.
[2] Heller, A. *et al.* (2021) *Toxicology*, submitted.

Lanthanide–dependent methanol dehydrogenase studied by computational chemistry

S. Tsushima

Molecular dynamics (MD) simulations were employed to rationalize enzymatic activities of methanol dehydrogenase (MDH) carrying different lanthanides.[1]

Lanthanides were long believed to have no biological function until a catalytic role of La^{3+} ion for MDH was discovered.[2] This fact expanded the importance of Ln^{3+} ions in biochemistry and in bacterial metabolism. Moreover, it was revealed that bacteria growth depends significantly on the size of lanthanide and that the activity of MDH decreases as the size of Ln^{3+} ion decreases. This fact has significant impact to chemical engineering and could possibly provide a breakthrough in Ln^{3+} separation.[3–5] Here, MD simulations were employed to study the active sites of Ln^{3+}–MDH.

CALCULATION. MD simulations were performed using AMBER 15. Protonation state of the protein was adjusted to model pH 7.4. Na^+ ions were added to make the system electrostatically neutral. TIP3P waters were added with minimum water thickness of 6 Å. 1 ns preconditioning run was performed after which 50 ns MD run was performed in a periodic boundary condition in NPT ensemble at 320 K. For each M^{n+}–MDH, 50 ns MD simulation was performed, from which only the last 30 ns MD trajectory was used for statistical sampling.

RESULTS. MD simulations were performed on M^{n+}–MDH from strain SoIV (XoxF–type) for M^{n+} = La^{3+}, Eu^{3+}, Yb^{3+} and also that isolated from *Methylorubrum extorquens* AM1 (MxaF–type) for M^{n+} = Ca^{2+}, Eu^{3+}. Initial structure of the protein including cation and cofactor was taken from the crystal structure. Three carboxylic groups of PQQ were deprotonated. In all M^{n+}–MDH carrying different metals, the residues associated with the metal centers are identical, namely Glu^{172}, Asn^{256}, Asp^{299}, and Asp^{301}. These metal–binding residues are also identical to those in the crystal structure of Eu^{3+}–MDH. Among different Ln^{3+}–MDH (La^{3+}, Eu^{3+}, Yb^{3+}), all metal–binding residues are in the same binding modes except for Glu^{172} which switches from bidentate to unidentate in going from lighter (La, Eu) to heavier (Yb) lanthanide (Fig. 1). In addition, coordination of PQQ to Ln^{3+} switches from chelate binding mode involving pyridine nitrogen to unidentate fashion with single dangling carboxylic oxygen in going from lighter (La, Eu) to heavier (Yb) lanthanide. To fill the remaining coordination site around Ln center, maximum of one water is attached to the metal. There are discreet differences in the residues associated to PQQ amongst La^{3+}–, Eu^{3+}–, and Yb^{3+}–MHD. In Eu^{3+}–MHD, PQQ interacts with (besides Eu^{3+}) Trp^{238} (through π–π stacking), Cys^{104}–Cys^{105} (to disulfide bond), and Arg^{326} (through H–bond), whereas no interaction with disulfide bond is found in La^{3+}–MDH and no interaction with Arg^{326}/Trp^{238} in Yb^{3+}–MDH.
Basically, as it shifts from lighter to heavier lanthanides, lanthanide contraction triggers closer contact between Ln with protein or with PQQ, favoring unidentate coordination. Coordination mode of PQQ to Ln^{3+} has critical importance to the activity of Ln^{3+}–MDH because nucleophilic attack of methanol oxygen on PQQ occurs on its carbonyl oxygens. Upon switching of the Ln–to–PQQ binding from chelate binding to unidentate, carbonyl oxygens become loosely associated to the metal. Thereby PQQ exhibits less tendency towards reduction when associated with heavier lanthanides. The difference between the active sites of La^{3+}– and

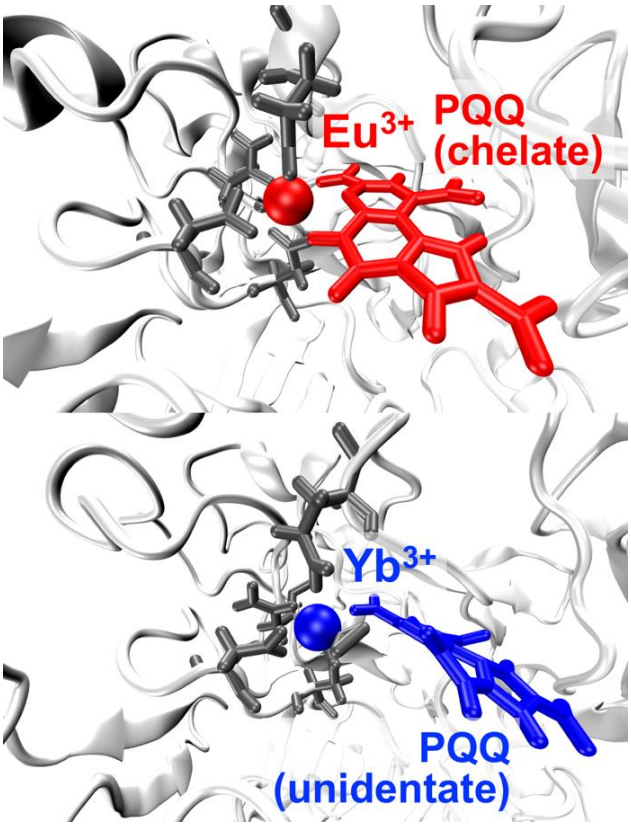

Fig. 1: Representative structures in the vicinities of the active sites of Eu^{3+}–(upper) and Yb^{3+}–bound MDH. Ln^{3+} ions and PQQ molecules are highlighted with red and blue.

Eu^{3+}–MDH is overall minor and the largest difference is that there is additional water coordinated to the metal in the case of the La^{3+}–MDH. It is unclear at this moment if and how additional water coordination correlates to the observed higher activity of La^{3+}–MDH. It is possible that solvent–accessibility of the metal in La^{3+}–MDH stimulates facile contact between PQQ and MeOH and eventually leads to the higher activity of La^{3+}–MDH.

ACKNOWLEDGEMENTS. All MD calculations were performed on the supercomputer at Dresden University of Technology.

[1] Tsushima, S. (2019) *Phys. Chem. Chem. Phys.* **21**, 21979–21983.
[2] Hibi, Y. *et al.* (2011) *J. Biosci. Bioeng.* **111**, 547–549.
[3] Daumann, L. (2019) *Angew. Chem., Int. Ed.* **58**, 12795–12802.
[4] Christoserdova, L. (2019) *Mol. Microbiol.* **111**, 1127–1131.
[5] Skovran, E., Martinez-Gomez, N. C. (2015) *Science* **348**, 862–863.

Interactions of *Brassica napus* callus cells with Eu(III) and U(VI)

H. Moll, W. A. John, S. Sachs

Experiments using *Brassica napus* callus cells grown *in vitro* in the presence of Eu(III) or U(VI) showed that *B. napus* cells were able to bioassociate both potentially toxic metals (PTM). Most of the Eu(III) and U(VI) was found to be enriched in the cell wall fraction. Under high metal stress (200 µM), cells responded with reduced cell vitality and growth. Speciation analyses using both metals as luminescence probes confirmed that *B. napus* callus cells provided multiple-binding environments for Eu(III) and U(VI).[1]

The accumulation of radionuclides, such as U(VI), and other potentially toxic metals (PTM), such as Eu(III), into plants, and, thus, into the food chain, represents a potential pathway for human exposure. Hence, studies exploring the interaction of PTMs with plants at the cellular and molecular level are necessary. Accordingly, our study was designed to determine the tolerance of canola (*B. napus*) callus cells to U(VI) and Eu(III) at two different metal concentrations. The effects of both PTMs on cell growth and vitality, as well as on the total phenolic content of the cells, were studied. Furthermore, this investigation also focused on the speciation of bioassociated U(VI) and Eu(III) and their distribution in various fractions of *B. napus* cells, since *B. napus* is known to be able to accumulate PTMs in higher quantities than many other species.[2]

EXPERIMENTAL. *Brassica napus* callus cells (DSMZ PC-1113) were grown on a solid medium R with a reduced phosphate concentration spiked with 20 or 200 µM $UO_2(NO_3)_2$ or 30 or 200 µM $EuCl_3$ (99.999 %, Aldrich, Taufkirchen, Germany) for about 6 weeks. All details concerning cell cultivation, vitality measurements, estimation of phenolic compounds, statistical analyses, cell fractionation, and laser-induced luminescence spectroscopy experiments can be found in literature.[1]

RESULTS. *Brassica napus* cells had a strong capacity to bioassociate both PTMs, 628 nmol Eu/$g_{fresh\ cells}$ and 995 nmol U/$g_{fresh\ cells}$ in the presence of 200 µM Eu(III) and U(VI), respectively. Most of the Eu(III) and U(VI) ions were bound on the cell wall fraction. This finding indicates that the cell wall might serve as an effective protective barrier of metabolically active cells against the threat of PTMs. In particular, under high Eu(III)/U(VI) stress, both metals were found in the cytosol fraction indicating an uptake of Eu(III)/U(VI) into the cells. Moreover, this study confirmed that cell growth was reduced in combination with a decrease in cell vitality (cf. Fig. 1). The total cellular phenolic content, which was expected to increase due to PTM stress, was similar for cells that were exposed to 30 or 200 µM Eu(III), 200 µM U(VI), as well as for our controls. Only a slight tendency for a slightly higher phenolic content was found for cells grown in the presence of 20 µM U(VI).

The appearance of the symmetry-forbidden $^7F_0$ peak in the luminescence emission spectra of Eu(III) bound to *B. napus* cells points to the formation of Eu(III) complexes. The occurrence of a bi-exponential luminescence decay confirmed the existence of two Eu(III) coordination environments. The strong intensity of the $^7F_2$ peak, as a measure of changes in the Eu(III) speciation, indicates the formation of strong Eu(III) complexes. Further analysis of the Eu(III) coordination environment revealed strong inner-sphere Eu(III) species, possibly with organic phosphate and carboxyl groups provided by the *B. napus* cells. From this we conclude, that *B. napus* cells show multiple-binding environments for Eu^{3+}. Due to the bioassociation of U(VI) onto *B. napus* cells, we observed a significant bathochromic shift of the U(VI) emission bands of the plant cell species compared to the spectra of the reference solution (U(VI) in 0.154 M $NaNO_3$) (cf. Fig. 1). Further, by comparing our findings with model compounds and other biological systems, there is a clear argument to be made for the predominant binding of U(VI) by organic and/or inorganic phosphate groups of the plant biomass.

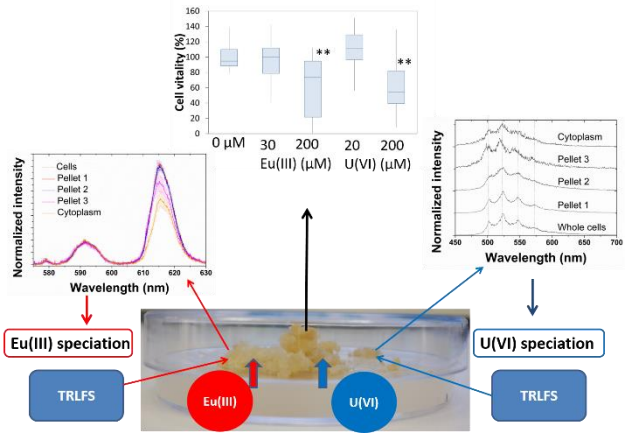

Fig. 1: Schematic overview of our study. TRLFS: Time-Resolved Laser-Induced Fluorescence Spectroscopy.

In conclusion, *B. napus* cells are able to accumulate and tolerate PTMs like Eu(III) and U(VI). As a result, these metals have the potential to enter the food chain and may become a severe health risk for humans. The results of this study were obtained through a combination of biological, biochemical, and spectroscopic methods. Hence, this integrative approach will contribute to an enhanced understanding of the interaction processes between actinides/lanthanides and plants at the molecular level, which is important for modeling the transfer of these elements in the environment.

ACKNOWLEDGEMENTS. This work was partly funded by BMBF under contract number 02NUK051B.

[1] Moll, H. *et al.* (2020) *Environ. Sci. Pollut. Res.* **27**, 32048–32061.
[2] Laurette, F. *et al.* (2012) *Environ. Exp. Bot.* **77**, 87–95.

Evidence of uranium immobilization by *Magnetospirillum magneticum* AMB-1 under ambient conditions

J. Ramtke, R. Hübner,[1] S. Kluge, E. Krawczyk-Bärsch

[1]Institute of Ion Beam Physics and Materials Research, HZDR, Dresden, Germany

The α-proteobacterium *Magnetospirillum magneticum* AMB-1 is known as a motile, magnetotactic, gram-negative bacterium. It is facultative anaerobe and usually found in oxic-anoxic transition zones. In kinetic batch experiments at pH 6.5, cells of *Magnetospirillum magneticum* AMB-1 were contacted with 0.01, 0.05, and 0.1 mM U(VI) for 24 h. The results show that the cells are able to remove most of the U from the solution during the first hours of incubation, independently on the initial U concentration. For TEM-based studies, the cells were contacted with 0.1 mM U(VI) for 24 h. Element distribution analysis reveal that U is bound predominantly in the outer membrane of the cells.

EXPERIMENTAL. 100 mL of a cell suspension of *Magnetospirillum magneticum* AMB-1 were grown in 200 mL flasks in 1.5 mM MagMin medium, modified by CEA Cardarache with the addition of iron malate (1:2,000) and vitamin elixir (1:2,000).[1] The flasks were kept at 30 °C on a rotary shaker at 80 rpm. An inoculation of the bacteria was carried out every 2–3 days. For each U kinetic batch experiment, 8 flasks were taken, each with an OD_{600nm} of 0.3–0.4, and washed twice with sterilized tap water with a pH adjusted to 6.5. The final OD_{600nm} in each experiment was 1.66 ± 0.04 which corresponds to 76.28 ± 0.66 mg dry biomass. The washed cells were suspended in a 200 mL flask with 100 mL sterilized tap water (pH 6.5), and a 0.1 M stock solution of $UO_2(NO_3)_2$ was added to a final concentration of 0.01, 0.05, and 0.1 mM, respectively. The cell suspensions were incubated at 30 °C and 80 rpm on a rotary shaker. After distinct times, 1 mL samples were taken to determine the residual U concentration in the supernatant by inductively coupled plasma mass spectrometry (ICP-MS) measurements. For transmission electron microscopy (TEM) studies, cells of *Magnetospirillum magneticum* AMB-1 previously contacted for 24 h with $UO_2(NO)_3$ solution (0.1 mM, pH 6.5) under sterile conditions, were recovered by centri-fugation (5500 rpm, 10 min). The supernatant was removed, and the cell pellet was washed twice with sterile tap water (pH 6.5). Subsequently, the pellet was fixed at 1 % (vol/vol) glutardialdehyde from 25 % (vol/vol) stock solution. Further preparation was performed at the Center of Regenerative Therapies (TU Dresden). About 100-nm-thick sections of the samples were analyzed by TEM and spectrum imaging analysis based on energy-dispersive X-ray spectroscopy (EDXS) for element distribution determination.

RESULTS. The results show a substantial removal of U by *Magnetospirillum magneticum* AMB-1 cells during the first hours of incubation with emphasis on the first hour, where even 39.55 %, 63.71 %, and 77.51 % of U was removed from the suspensions with an initial U concentration of 0.01, 0.05, and 0.1 mM U, respectively (Fig. 1). Furthermore, the U removal capacity of *Magnetospirillum magneticum* AMB-1 cells at 0.01, 0.05, and 0.1 mM U after 24 hours was determined to be 0.87, 12.54 and 30.17 mg U/g DBM, which correspond to 29.94 %, 85.99 % and 95.51 %, respectively. TEM imaging of *Magnetospirillum magneticum* AMB-1 cells contacted with 0.1 mM U for 24 h (Fig. 2, left) shows an area of high mass-absorption contrast that can be interpreted as a detaching

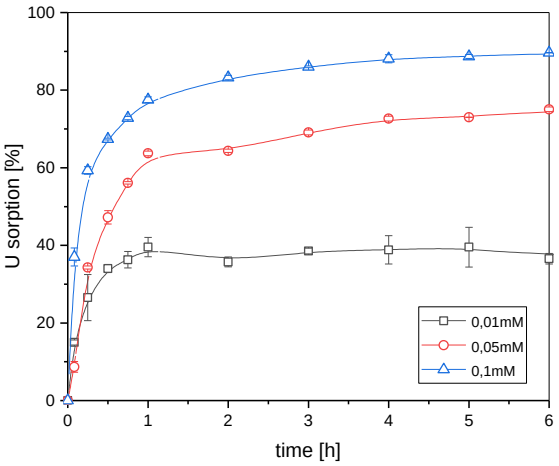

Fig. 1: Comparison of U sorption by *Magnetospirillum magneticum* AMB-1 during the first 6 h of incubation using initial uranium concentrations of 0.01, 0.05, and 0.1 mM under aerobic conditions at pH 6.5.

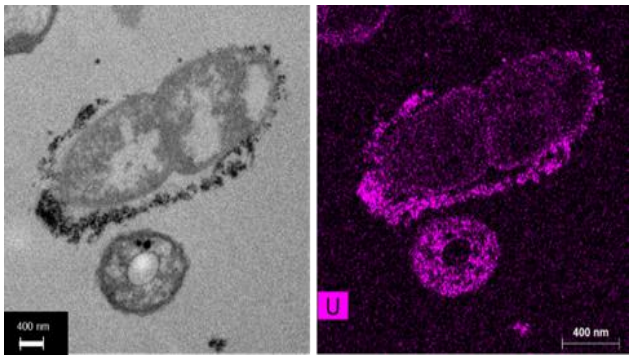

Fig. 2: TEM image (left) and EDXS-based U element distribution analysis (right) of *Magnetospirillum magneticum* AMB-1 cells. Initial U concentration: 0.1 mM, 24 h incubation.

cell membrane. Element distribution analysis (Fig. 2, right) performed for this bacterium clearly indicates that U is entirely present in this cell membrane. The fast immobilization of U by *Magnetospirillum magneticum* AMB-1 in the membrane within the first hours can be interpreted as a passive process. Live-dead staining experiments performed with Syto®9 and Propidiumiodide show that the cells are mostly alive during the batch sorption experiments. Consequently, we conclude that living cells of *Magnetospirillum magneticum* AMB-1 are responsible for the immobilization of U by passive biosorption during the first hours of incubation.

ACKNOWLEDGEMENTS. The authors are grateful to D. Faivre and S. Prévéral (CEA Cardarache, France) for providing the strain of *Magnetospirillum magneticum* AMB-1. We would like to thank S. Beutner (HZDR, Germany) for ICP-MS measurements. The use of the HZDR Ion Beam Center TEM facilities is gratefully acknowledged.

[1] Komeili, A. *et al.* (2004) *Proc. Natl. Acad. Sci. U.S.A.* **101**, 3839–3844.

Microbially influenced corrosion of cast iron in different types of bentonite: microscopic investigation

V. Sushko, M. Dressler, N. Matschiavelli, A. Schierz, T. Stumpf, A. Cherkouk

Cast iron is used as a potential container material for radioactive waste in a deep geologic repository (DGR) concept. Therefore, mesocosms containing different types of bentonite, cast iron coupons and a synthetic Opalinus Clay porewater solution were setup. After an incubation of 271 days, the surface damage associated with the corrosion was characterized by Scanning Electron Microscopy with Energy Dispersive X-ray (SEM-EDX) analysis to verify the impact of indigenous microorganisms on the corrosion process in the various bentonites. The results showed that selecting the appropriate bentonite for a DGR with the goal to control the microbial activity and thus corrosion of cast iron is a crucial step.

EXPERIMENTAL. The experimental mesocosm-setup was described elsewhere.[1] For the current setup three different bentonites were used: B25, Calcigel® and MX-80. Aliquots of bentonites (15 g) were dispersed into glass bottles together with 30 mL of synthetic Opalinus Clay porewater solution and GGG40 cast iron plates. Also, some of the mesocosms were supplemented with 5 mM sodium lactate and hydrogen (to 0.5 bar of total pressure) to stimulate microbial activity. The mesocosms were incubated for 271 days at 30 °C.
The mesocosm material was split after the incubation time and subjected to various analyses. First, metal coupons were removed and washed with deionized water, a portion of the slurry was used for DNA extraction, and the remainder was centrifuged. The filtrated supernatant was subjected to geochemical analysis to determine the concentration of various metals, sulfate, lactate, acetate and pyruvate (ICP-MS, IC, HPLC). To evaluate the changes in surface morphology and identify the corrosion components, metal coupon surfaces were examined by scanning electron microscopy coupled with energy-dispersive X-ray spectroscopy (SEM-EDX).

RESULTS. The presence of black precipitates was visible for the mesocosms containing Calcigel with lactate as substrate and for all the substrate-containing samples with MX-80. The geochemical analysis of these two bentonites showed a decrease in the sulfate concentration, which could be the electron acceptor for the respiration of sulfate-reducing bacteria (SRB). The strongest effect appeared in MX-80 bentonites.
With the exception of the B25 sample without a substrate, SEM data showed significant surface damage for all samples. Furthermore, two types of crystalline structures were found, covering to some degree the surface area of the coupons. One of these structures was iron and/or calcium carbonate, which was present in all the samples based on EDX (Fig. 1) and Raman spectroscopy (data not shown).
Iron carbonate in this case is most likely the product of the CO_2-corrosion. It forms a protective layer which reduces the rate of corrosion. It has been argued that the formation of this kind of protective iron carbonate films decreases the corrosion rate by blocking the surface of the metal rather than reducing the diffusion of the corrosive material.[2]
Iron sulfide was found on the surface of cast iron coupons incubated in B25 mesocosms supplemented with hydrogen, in MX-80 mesocosms with no substrate and with hydrogen (Fig. 2), and in Calcigel mesocosms without any substrate.

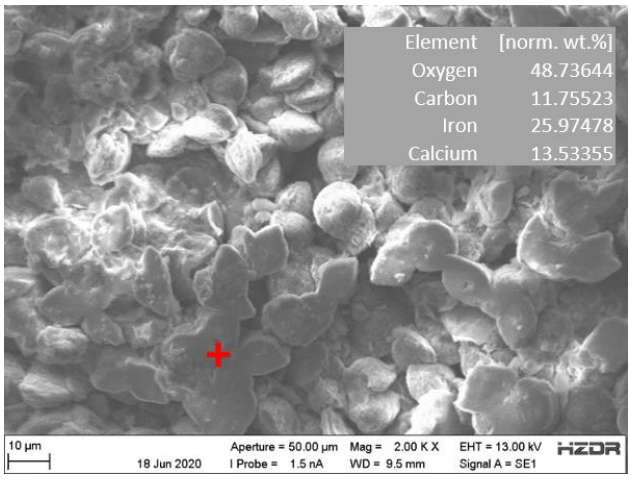

Fig. 1: SEM-micrograph and selected EDX-analysis of the surface of GGG40 coupon incubated with Calcigel and 5 mM lactate in synthetic Opalinus Clay porewater solution. The square inset shows the EDX result of the marked position.

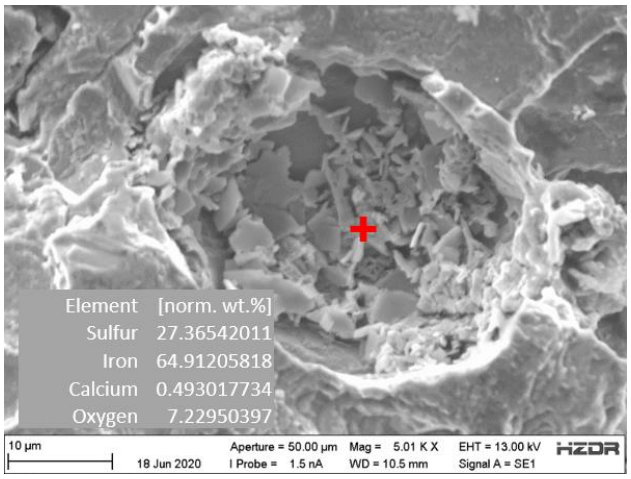

Fig. 2: SEM-micrograph and selected EDX-analysis of the surface of GGG40 coupon incubated with MX-80 in synthetic Opalinus Clay porewater solution and hydrogen as a substrate. The square inset shows the EDX result of the marked position.

Iron sulfides can occur as part of a mixture of anaerobically corroded iron found in mineral and organic deposits. But iron sulfides are also characteristic products of SRB-induced corrosion.[3] So, the presence of such products could be an indication for SRB activity. The analysis of the microbial communities is still ongoing. But a different microbial community structure was observed by intergenic spacer analysis (RISA) depending on the conditions applied and used bentonite (data not shown). So, different bentonites show different reactivity and a distinct microbial community. Therefore, the selection of the bentonite seems to have a big influence on the integrity of the container material and, thus, on the safe long-term storage of nuclear waste.

ACKNOWLEDGEMENT. We acknowledge funding by the BMBF (Grant 02NUK053B) and HGF (Grant SO-093).

[1] Matschiavelli, N. *et al.* (2019) *Environ. Sci. Technol.* **53**, 10514–10524.
[2] Nešić, S. *et al.* (2003) *Corros. Sci.* **59**, 616–628.
[3] Enning, D. *et al.* (2020) *Appl. Environ. Microbiol.* **80**, 1226–1236.

Corrosion at the bentonite-cast iron interface under high-salt conditions with H_2

V. Sushko, T. Neubert, M. Löffler,[1] B. Rellinghaus,[1] A. Schierz, A. Cherkouk, N. Matschiavelli

[1]Dresden Center for Nanoanalysis (DCN), Center for Advancing Electronics Dresden (cfaed), TU Dresden, Dresden, Germany

The metal canister that contains the high-level radioactive waste (HLW) in a deep geological repository (DGR) should act as an effective shielding against external disturbances like the influx of pore water through the bentonite barrier. In order to study the resistance of ductile iron against corrosive conditions in a DGR located in saline clay rock formations, microcosms were set up. First results indicate the formation of deep pits that expand into the metal, leading to a high porosity of the protective metal barrier.

Corrosion is the destructive attack of a metal by its reaction with the environment.[1] The safe retention of HLW in a DGR is realized by applying a multi barrier system where the metal canister is in direct contact to the bentonite barrier, which acts as buffering and sealing material when clay or granite serves as host rock. Cast iron offers excellent machinability combined with good impact resistance which makes it a suitable canister material.[2] When selecting clay rock in the northern parts of Germany as final disposal site, saline pore water can enter the DGR. Anaerobic corrosion can take place at the interface between bentonite and cast iron, subsequently leading to the generation of H_2 that can promote microbial activity.[3]
In order to study the influence of saline pore water and H_2 on the corrosion process of cast iron as well as on the microbial community structure, microcosms were set up.

EXPERIMENTAL. Microcosms were set up as described previously[2] with the additional application of three ductile iron plates (cast iron type GGG40; L × W × H: 10 × 10 × 5 mm) in each microcosm. For simulating saline pore water, diluted cap-rock solution (CAP) was used.[4] The microcosms were incubated for 30 days at 37 °C. Sampling was performed as described.[3] After opening the flasks, cast iron plates were taken out with sterile plastic forcipes and stored under anaerobic conditions until further analytics. Surface analyses were performed by low-voltage Scanning Electron Microscopy (SEM) and local cross-sections were prepared using a 30 keV Ga+ Focused Ion Beam (FIB) and subsequently analyzed with SEM in a FEI Helios Nanolab 660. Extraction of DNA and sequencing was performed as described elsewhere.[3]

RESULTS AND DISCUSSION. The influx of naturally formed saline pore water into the DGR is a crucial issue for the long-term stability of the cast iron canister harboring the HLW. Usually, corrosion of ductile iron in soils is decelerated, but it has been shown that chloride ions participate in corrosion reactions.[5] Higher chloride ion concentrations lead to higher corrosion rates, larger pit depths and suppress the initial decreasing of corrosion rates.[5]
The CAP solution applied contains 14 wt.-% of NaCl and is therefore much higher concentrated compared to previous experiments that dealt with cast iron corrosion in solutions ranging between 1 wt.-% and 3.5 wt.-% NaCl.[5, 6] Indeed, the analysis of the cast iron surfaces reveals a more perforated surface compared to cast iron plates that were incubated in bentonite microcosms containing Opalinus Clay pore water (OPA) and H_2 (data not shown). The observed pits are very deep and "grow" into the metal surface, even beneath an intact surface (Fig. 1).

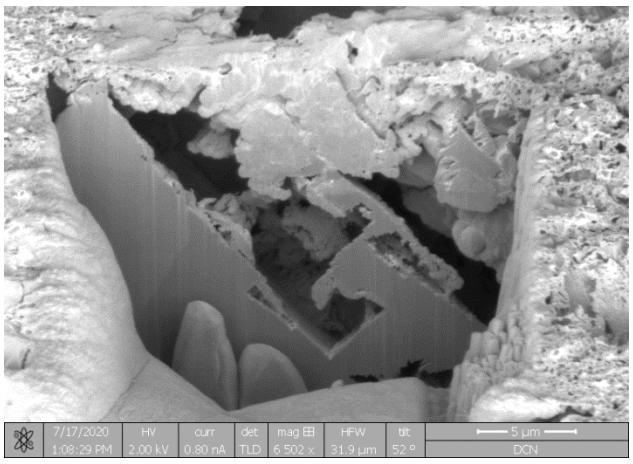

Fig. 1: FIB-SEM cross-section through an incubated cast iron surface. The respective cast iron plate was incubated for 30 days at 37 °C in anaerobic bentonite microcosms containing CAP rock solution and H_2. The cross-section is part of a sequence of cross-sections that allows viewing the 3D-shape of the sub-surface voids.

At first glance, the results of this work argue against an application of the cast iron as a technical barrier for a DGR. However, it has been shown, that Ni-alloyed cast iron is more corrosion resistant than unalloyed.[6] Thus, testing different cast iron alloys might identify more suitable metals. Furthermore, a longer exposure time may thicken the rust layers, thereby retarding corrosion conversely.[5] Indeed, Raman spectroscopy and SEM-EDX analyses of the here analyzed plates, revealed the presence of siderite ($FeCO_3$, data not shown), which could potentially form a passivating film on the cast iron surface.
In former experiments, dealing with the microbial influence on corrosion of cast iron, sulfate reducing bacteria (SRB) have been detected.[7] Additionally, it has been shown that the bentonite applied here harbors SRB, which are active in OPA-containing microcosms supplemented with H_2.[3] The microbial diversity analysis is still ongoing and might reveal a distinct role of detected microbial genera during the corrosion processes.

ACKNOWLEDGEMENTS. We thank S. Kaufhold (BGR, Hannover, Germany) for providing B25 Bavarian bentonite. Cast iron plates (type GGG40) were provided by the GRS gGmbH (Braunschweig, Germany). This work was partially funded by the BMBF (Grant 02NUK053B) and HGF (Grant SO-093). The FIB/SEM investigation was conducted in the Dresden Center for Nanoanalysis (DCN) at the Center for Advancing Electronics Dresden (cfaed), TU Dresden.

[1] McCafferty, E. (2010) *Introduction to Corrosion Science*, Springer Science+Business Media, LLC, 233 Spring Street, New York, U.S.A.
[2] Patel R. *et al.* (2012) *Nagra Technical Report*, NTB 12–06.
[3] Matschiavelli, N. *et al.* (2019) *Environ. Sci. Technol.* **53.** 10514–10524.
[4] Meleshyn, A. (2015), *Report GRS-A-3844*.
[5] Song, Y. (2017) *Sci Rep* **7**, 6865.
[6] Hsu, C.-H., Chen, M.-L. (2010) *Corrosion Science* **52**, 2945–2949.
[7] Necib, S. *et al.* (2017) *Corros. Eng. Sci. Technol.* **52**, 127–130.

When the biofilm on materials is needed: biofilm formation after electrostatically attachment of films of living bacterial cells

D. Deev,[1] I. Rybkin, T. Rijavec,[1] A. Lapanje[1]

[1]Department of Environmental Sciences, Jožef Stefan Institute, Ljubljana, Slovenia

The modification of the surfaces of cells or material by polyelectrolytes (PEs) allows the deposition of bacterial cells, biofilm forming and non-forming ones, in order to construct artificial biofilms with prolonged stability, causing the selective pressure on further colonization of environmentally occurring bacteria.

Bacterial attachment is crucial in many biotechnological applications. However, biofilms have deteriorative effects on materials. That is why the current strategies to manage biofilms are focused on biofilm inhibition. Knowing that biofilm formation is an inevitable process, instead of biofilm prevention, we propose to manage its microbial composition by formation of biofilms with beneficial microbes. Using an artificial biofilm prepared with the potentially probiotic strain of *Bacillus* sp., we were able to reduce the attachment and completely inhibit the growth of *E. coli* cells on the surface of the *Bacillus*-based artificially induced biofilm.

EXPERIMENTAL. Different bacterial strains were selected based on their intrinsic physiological properties. The strains were used for (*i*) testing the toxicity of the modified PEs, (*ii*) observing the effect of PE deposition on the formation and stability of biofilms and (*iii)* proving the concept of the protective nature of artificial biofilms. In preliminary experiments polyethyleneimine (PEI) demonstrated toxicity when exposed to bacterial cells. Consequently, it was tested if reducing the number of amino groups in the PE molecule would decrease its toxicity. We used acetic anhydride to acetylate PEI. Further, we tested the efficiency of biofilm formation for biofilm-forming and non-forming bacteria, coated with acetylated and non-acetylated PEI, incubating cells upside down over 48 hours. To observe how the artificial biofilm of *Bacillus* 25.2.M inhibited the attachment of a potentially pathogenic bacterium we firstly deposited acetylated PEI coated *Bacillus* 25.2.M on the glass surface and secondly *E. coli* on the top of *Bacillus* 25.2.M and left to incubate.

RESULTS. As acetylated PEI allowed to manipulate the cell surface charge without being toxic to the cell, we determined how the electrostatic deposition of cells to the glass surface enabled both the biofilm forming and non-forming bacteria to occupy the freshly exposed surfaces (Fig. 1). In contrast to the controls, where almost all the cells of the biofilm forming bacteria were detached after 48 hours, surface modifications by PEs resulted in 4.66 times larger occupied surface areas. Furthermore, the occupied surface areas were 26.02 times larger for the non-biofilm-forming strains. To test the effects of the artificial biofilm in an in vitro system containing two different bacterial species, we constructed the biofilm with *Bacillus* 25.2.M, a potential oral probiotic strain, and deposited the cells of *E. coli* over its surface (Fig. 2). In the presence of the artificial biofilm the cell number of *E. coli* TOP10 - emGFP was constant over time and no significant growth was observed within the 24 hours exposure period. Here, we have demonstrated a new solution which does not prevent the inevitable establishment of the biofilm, but carefully manages its development by attachment of live bacteria. The modification of PEs widens the repertoire of strains that can be used in the purification systems used for drinking and waste water treatment, and consequently the proposed approach can be applied to different surfaces in a variety of industries such as biotechnology, medical and other sectors, where prevention and control of biologically induced corrosion is important.

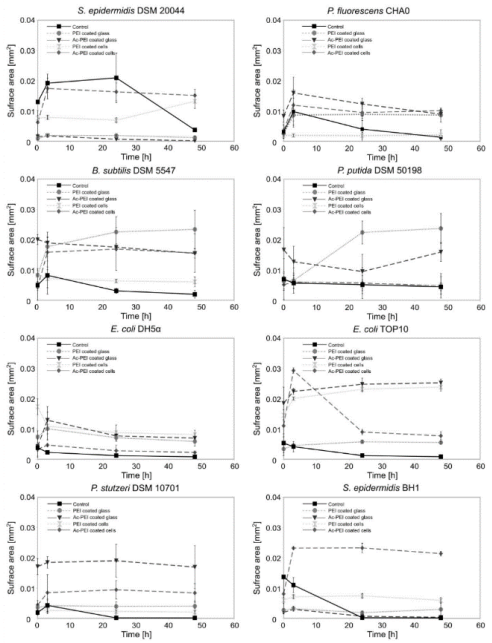

Fig. 1: The modification of the cell's surface charge or the charge of the material surface affects the number of cells that attach onto the surface and the following growth of the biofilm. The surface area covered by cells was examined for 8 different bacterial strains, biofilm forming or biofilm non-forming, over a 50 h period.

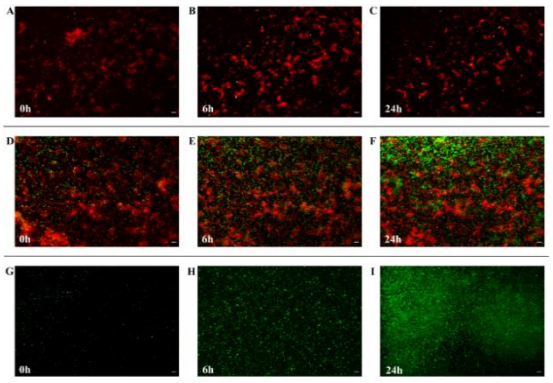

Fig. 2: The colonization and growth of potentially pathogenic *E. coli* are inhibited by the artificial biofilm made from the probiotic candidate strain *Bacillus* sp. 25.2.M. The number of attached cells of *E. coli* TOP10 emGFP, expressing the green fluorescent protein (gfp) (green), was determined at 0, 6 and 24 hours of cultivation when the artificial biofilm was made from the antimicrobial-producing *Bacillus* sp. 25.2.M, being deposited onto the glass surface (A–C) or from *E. coli* TOP10 (red) not producing gfp (positive control) (D–F), or no pre-applied biofilm on the surface (negative control) (G–I). Scale bar equals 10 µm.

ACKNOWLEDGEMENTS. The research was performed at Jožef Stefan Institute in collaboration with HZDR. We acknowledge financial support by the Helmholtz-Association, grant PIE-0007 (CROSSING).

The lab lysimeter – an application for biogeochemical research with radionuclides

A. Günther, J. Raff

This report summarizes technical details and application of a lab lysimeter, which was developed and built by ecoTech Umwelt-Meßsysteme GmbH, Bonn, Germany, for a research project according to our requirements.[1] The goal of the project is the identification of the underlying processes determining the migration behavior of radionuclides in a complex environment composed of soil, organic matter, microorganisms, and plants.

TECHNOLOGY. Lysimeters are measuring devices for water and material balance parameters and are used for the investigation of the interaction and accordingly mass transport between atmosphere, different organisms (such as plants, fungi, animals), soil and water in environmental research.
Our lab lysimeter consists of a cylinder made of polypropylene, which consists of an upper transparent and a lower nontransparent part. The total height is 105 cm and the diameter is 30 cm (Fig. 1).

Fig. 1: Lab lysimeter system in the control area of the institute.

A sprinkling head equipped with light emitting diodes controls the water content of the soil matrix and the illumination during the growing of plants and fungi with an adjustable intensity in the range of 3,000 to 12,000 Lumen (Fig. 2). Furthermore, it is possible to connect up to 54 redox electrodes, pH electrodes, and suction candles arranged in 9 levels about each other at a distance of 5 cm between each level. Thus, 6 sensors can be installed at every level. Additionally, different tensiometers can be used for the determination of the soil water or soil moisture.
In the lower part of the lysimeter a suction bottom consisting of 7 segments and connected to a bottle system allows the collection of seepage water (Fig. 3). The controlling, data registration modules and a data transfer technology are integral parts of the lab lysimeter system.

Fig. 2: Lighting and sprinkling unit.

Fig. 3: Sevenfold segmented suction bottom (left) and bottle system (right).

APPLICATION. The main attention of the scientific work with the lysimeter is paid on the decent investigation of the interactions of radionuclides and metals with components of the soil and of the soil solutions. Furthermore, information on the horizontal and vertical distribution of the heavy metals in soils and their uptake by organisms under near natural conditions can be gained from the experiments.
With respect to the soil, measurements determining soil parameters and their change upon gradual adding of selected heavy metals and radionuclides as well as complexing organic agents will be carried out. Here, the focus is on the sorption of the metal ions onto the soil particles, the determination of the corresponding metal speciation, and the examination of the immobilization effects of the chelating agents on the radionuclides. The studies to the metal- and radionuclide behavior in soils and other porous materials will be connected with the performance of flow analyses, determination of flow paths and the hydrodynamics regarding the assessment of groundwater contamination by heavy metals.
Considering biological aspects, the influence of plants, fungi, and bacteria on the migration behavior and transport of metals and radionuclides in soils will be studied. The characterization of radionuclide uptake by the organisms at well-defined soil conditions is feasible, for instance by monitoring the biome composition using molecular biological methods.
In analogy to performed batch experiments, the aim is to obtain information on radionuclide and metal speciation in the biomass cultivated in the lysimeter at molecular level using various spectroscopic and microscopic methods.
The outcome of the experiments with the lab lysimeter system is crucial for the transferability of data gained from small-scale experiments to larger scales and or the modeling of the radionuclide's behavior in the environment.

[1] https://www.ecotech.de.

Liquid light guide technology augments use of small economical detectors in liquid scintillation counting

S. Stalke, R. Steudtner, K. Grossmann[1]

[1]VKTA – Strahlenschutz, Analytik & Entsorgung Rossendorf e.V., Dresden, Germany

In pursuit of smaller and more economic detectors in liquid scintillation counting (LSC), silicon photomultipliers (SiPM) seem to be promising candidates, as they are robust, can be produced in a small size, at low costs and require much lower operating voltages than conventional photomultiplier tubes.[1] Here, we show that, for small scale SiPM detectors, liquid light guide (LLG) technology will enhance the collection efficiency for the scintillating light, giving rise to the analysis of sub-mL LSC samples or samples with low activity.

EXPERIMENTAL. 0.3 mL of ^{14}C citric acid dissolved in ultima gold (~100 Bq/mL) was measured in fluoro-ethylene-propylene (FEP) polymer hosing and in Eppendorf microvials made of polypropylene (PP). The scintillating pulses were detected with a 3 × 3 mm SiPM detector,[2] attached to a printed circuit board with stabilized 30 V power supply. The SiPM is an avalanche photodiode in Geiger mode and was operated 5 V above its breakdown voltage. The produced voltage pulses were amplified by a pre-amplifier to give ~60 ns voltage pulses of up to 500 mV. In the results shown, analog digital conversion (ADC) and mean pulse voltage analysis were performed by a 2.5 GHz oscilloscope with 8 bit resolution. Pulse width was measured additionally to act as a quality monitoring quantity, *i.e.* only pulses with widths between 40 and 150 ns were used for analysis. Due to the slow process of oscilloscope data acquisition and analysis (~5 s per pulse) counting time was usually several hours. Hereby, low energy scintillation pulses were discriminated by setting the trigger level of the oscilloscope as well as setting the vertical voltage resolution. For all measurements, both quantities were selected to be well above the amplitude of the dark current pulses coming from the SiPM (< 10 mV). Typically, the selected range for the detected voltage pulses was between 50–450 mV and the trigger level was at 20 mV. The mean data of the pulses collected was then converted to a histogram and normalized with respect to counting time using Origin™.

RESULTS. The enhancement of collecting scintillation light using FEP hosing is shown in Fig. 1. Herein, ^{14}C is used as the radioactive source, which has been dissolved in the scintillator and inserted into the FEP hosing. Due to the high differences in refractive indices between FEP (1.34) and the scintillator (1.59) the system is highly LLG active. Therefore, a nearly tenfold increase in collection efficiency is observed compared to conventional, only slightly LLG active polypropylene tubes (refractive index ~1.48) with additional diffuse reflector.

In order to further test the sensitivity of the rudimentary liquid scintillation counter mentioned above, measurements were also performed with blank scintillation cocktail in FEP hosing with and without lead shielding and by having a radioactive source (plate of uranium glass) nearby.

The results are shown in Fig. 2. It can be seen that the uranium plate as well as the different environment are clearly recognized by the apparatus. Due to the small size of the SiPM, this could give rise to pen sized ionizing radiation monitoring devices.

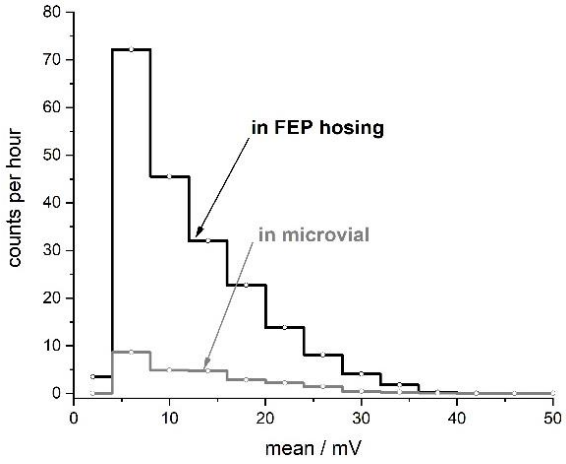

Fig. 1: Mean histogram of ^{14}C citric acid in Ultima Gold with lead shielding in FEP hosing and in PP microvial with reflector.

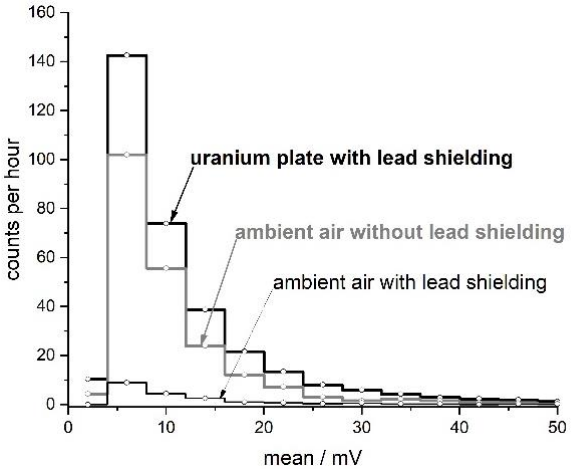

Fig. 2: Mean histogram of blank Ultima Gold in FEP hosing in different environments.

OUTLOOK. Currently, we are testing different ADC options, having 8 bit/2.5 GHz, 10 bit/2.5 GHz and 14 bit/125 MHz specifications. Especially for the latter case, a pulse shaper was also implemented in the setup. Additionally, two different multichannel analyzers are available, which allow hardware pulse analysis as well as automated histogram formation. By hardware pulse analysis, pulses can be captured at a much higher rate, which will shorten the measurement time. The automated histogram formation, on the other hand, will reduce the time for data analysis.

ACKNOWLEDGEMENTS. The project is kindly funded by Forschungszentrum Jülich (100455901) in the scope of WIPANO. B. Bauer and S. Bartel are gratefully acknowledged for providing the lead shielding and for fruitful discussions.

[1] Piatek, S. (2018) *Webinar Hamamatsu.*
[2] KETEK GmbH (2020) SiPM application note KETEK.

Nuclear Reactor

SAFETY RESEARCH

The dominant mechanisms for the formation of solute clusters in steels exposed to irradiation

F. Bergner

Until recently, there was much debate about the dominant mechanisms of the formation of solute atom clusters in low-Cu reactor pressure vessel steels exposed to neutron irradiation. The crucial role of solute segregation to TEM-invisible irradiation-induced dislocation loops has now been uncovered by atomistic simulations supported by nm-scale experimental evidence.

Fast neutrons give rise to displacement cascades in reactor pressure vessel (RPV) steels. As a direct result, a high number of point defects is produced, namely essentially equal amounts of vacancies and self-interstitial atoms. At reactor-ambient temperatures, both vacancies and interstitials migrate in the body-centered cubic Fe lattice of low-alloy RPV steels. Interstitials migrate faster. Under continued irradiation they reach a quasi-steady state concentration at the μs time scale. For vacancies the quasi-steady state is reached at the ms to s time scale. The long-term evolution of the microstructure covers the following processes:

- recombination of a vacancy and an interstitial,
- clustering of vacancies to form three-dimensional sub-nm voids,
- clustering of interstitials to form two-dimensional dislocation loops.
- Loss of vacancies and interstitials in microstructural sinks such as dislocations and grain boundaries.
- Binding of point defects with solute atoms to form complexes often also capable of migrating in the lattice.

Given this background, a huge variety of possible mechanisms for the rearrangement of solute atoms as well as the formation of solute clusters and stable precipitates is theoretically possible. The question is, which mechanism(s) is (are) dominant in RPV steels exposed to reactor neutron irradiation.

For Cu-rich first- and second-generation RPV steels, the answer was already anticipated in the 1980s.[1] The dominant mechanism was essentially confirmed and worked out in more detail in the decades that followed. It was found that the increased vacancy concentration gives rise to irradiation-enhanced Cu diffusion resulting in the formation of coherent Cu-rich vacancy-containing precipitates. At longer time scales, alloying elements such as Mn and Ni do contribute as well.

For low-Cu second- and third-generation RPV steels, the problem turned out to be more puzzling. The same is true for Cu-rich RPV steels irradiated at such high fluences that the remaining matrix-Cu already went below the solubility limit. Collaborative international efforts including multiscale modelling and complementary nm-scale experimental approaches[2] recently allowed the dominant mechanisms of cluster formation to be uncovered as described in brief below:

(1) Interstitials cluster together to form dislocation loops. In pure Fe (but not in RPV steels), these loops grow to TEM-visible sizes.

(2) The sub-nm sized loops are mobile in one dimension. Upon loop migration, they encounter solute atoms which bind to the loops and immobilize them. The loops are now essentially unable to grow further.

(3) Solute atom migration via vacancy or interstitial drag gives rise to an enrichment of loops with solute atoms. Such segregated loops are often observed by means of atom probe tomography (APT), see Fig. 1 for an example.[3]

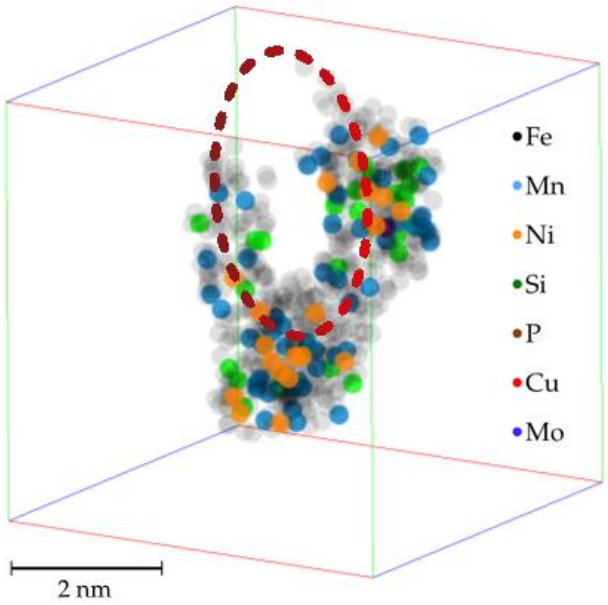

Fig. 1: Segregated half-toroid shaped loop reconstructed from an APT measurement on a neutron-irradiated low-Cu A533B-type RPV model steel.[3] The probable position of the original dislocation loop was superposed to the as-measured APT map.

(4) Upon further segregation, the loops lose their toroidal shape to become three-dimensional solute clusters or even stable precipitates as evidenced by APT and small-angle neutron scattering (SANS).

The mechanisms described above in (1)–(4) and the mechanism outlined before for Cu-rich steels may operate in parallel, and, if this is the case, influence one another. It is important to note that the segregated-loop mechanism of cluster formation is essentially irradiation-induced as opposed to irradiation-enhanced, that means it would not operate under thermal conditions.

Evidence for the multistep process was derived from object-kinetic Monte-Carlo simulations built upon a carefully parameterized model. The simulation results were compared with experimental results obtained for the mean size, number density, volume fraction and composition of clusters that formed in numerous neutron-irradiated RPV steels.[2]

Another interesting point is the time scale at which the vacancy-Cu-based mechanism and the segregated-loop mechanism operate. There is experimental evidence indicating that the former process is effectively faster. On the other hand, once the impurity Cu in excess of the solubility limit is consumed, no or relatively few new clusters will form via this mechanism. In contrast, the segregated-loop mechanism is mainly based on solute atoms of alloying elements such as Mn, Ni and Si, which are available in RPV steels practically without limit to form Mn-Ni-Si-enriched clusters. A consequence of these competing mechanisms is a relatively wide variability of the functional dependence of the total cluster volume fraction on neutron fluence.

ACKNOWLEDGEMENTS. This work received funding from the EC within the project SOTERIA under grant agreement number 661913.

[1] Odette, G. R. (1983) *Scripta Metall.* **17**, 1183–1188.
[2] Castin, N. *et al.* (2020) *Mater. Today Energy* **17**, 100472.
[3] Wagner, A. (2017) PhD Thesis, Martin-Luther Universität Halle-Wittenberg, Germany.

Use of the small punch test for the estimation of ductile-to-brittle transition temperature shift of irradiated steels

E. Altstadt, F. Bergner, M. Houska

The correlation between ductile-to-brittle transition temperatures (DBTTs) obtained from the small punch test technique and from the standard Charpy impact test is investigated. Tests at different temperatures were performed on various steels including materials from original reactor pressure vessels in the unirradiated, neutron irradiated and annealed condition. It is demonstrated that the small punch test is a reliable and effective supportive means for the estimation of the irradiation-induced shift of the ductile-to-brittle transition temperature.

The small punch (SP) test has been recognized as a possible replacement of the Charpy impact test in cases of insufficient amounts of material available for the fabrication of the necessary number of Charpy samples. As a screening procedure, the SP test is intended to provide estimations of the material properties with small amounts of material, allowing an evaluation of ageing mechanisms such as irradiation-induced hardening and embrittlement.[1, 2] The shift of the DBTT is a key element of reactor pressure vessel (RPV) embrittlement surveillance. It is therefore interesting to evaluate whether the DBTT shift can be reliably measured by means of the SP test. As for the SP-test-based estimation of the DBTT, T_{SP}, the following simple correlation is used:

$$T_{SP}[K] = \alpha \cdot T_{CVN}[K] \quad (1)$$

where T_{CVN} is the DBTT from the Charpy impact test using standard specimens 10 × 10 × 55 mm with a 2 mm V-notch (so-called CVN specimens). The factor of proportionality α depends on SP geometry, the material class, the fitting procedure for T_{SP}, and the criterion for the definition of T_{CVN} (*e.g.*, T_{41J}, T_{47J}, T_{68J}, $T_{50\%US}$).

EXPERIMENTAL. A number of seven different steels were investigated. These materials include bainitic RPV steels, base metals as well as weld metals. The experimental program covers different irradiation conditions, namely unirradiated (u), neutron irradiated (i) and neutron irradiated and annealed (ia). CVN specimens were tested according to the standard ISO 148-1. The test temperature range was from −25 to 225 °C for the irradiated steels and from −150 to 150 °C for the unirradiated steels. The impact energy W_t was calculated as integral of the force-deflection curve $F(s)$. SP specimens of 10 × 10 × 0.54 mm were manufactured from tested or unused Charpy-sized SE(B) specimens. In total, more than 500 SP tests were performed. The test temperatures were in the range from −172 to +100 °C for the irradiated materials and from −194 to +100 °C for the unirradiated materials. For each test, the force-displacement curve $F(v)$ was recorded and the small punch energy E_{SP} was calculated as integral of $F(v)$ up to maximum force F_m. The normalized small punch energy was obtained by $E_n = E_{SP}/F_m$. The DBTTs of the Charpy impact and small punch test series were determined by means of a tanh-fit of the energies W_t and E_n as function of the test temperature. T_{47J} is the temperature at which the tanh-fit of W_t takes the value of 47 J, while T_{SP} corresponds to the inflection point of the tanh-fit of E_n.

RESULTS. Figure 1 shows the correlation between T_{SP} and T_{CVN} (T_{47J}). The coefficient of determination is $R^2 = 0.986$.

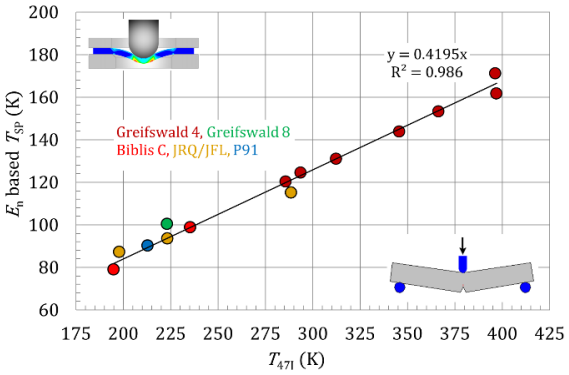

Fig. 1: Correlation between E_n based T_{SP} (tanh-fit) and T_{47J}.

Considering that seven different steels are involved, the correlation Eq. (1) works surprisingly well. The application of the T_{SP}–T_{47J} correlation to the core weld of the RPV of NPP Greifswald 4 is shown in Fig. 2. For the as-irradiated condition, a characteristic through-thickness dependence of T_{47J} is observed in the Charpy impact test, which exhibits a pronounced minimum close to the welding root. This is nicely reproduced with the SP-based T_{SP} for the as-irradiated condition. The recovery of mechanical properties due to the annealing treatment is clearly indicated by significantly lower DBTTs (Fig. 2). Again, the Charpy- and SP-based values of T_{47J} give a coherent picture. In the annealed condition, there is no significant difference between the DBTT for the welding root and the filling layers. This is in contrast to the as-irradiated condition. At a first glance, the particular through-thickness behavior seems to be unexpected, as the neutron fluence is decreasing from the inner surface to the outer surface. However, this finding is well in line with the through-thickness variation of the concentration of Cu, which is the most important promoter of irradiation-induced embrittlement. Indeed, the Cu concentration was reported to be lowest in the welding root.[3]

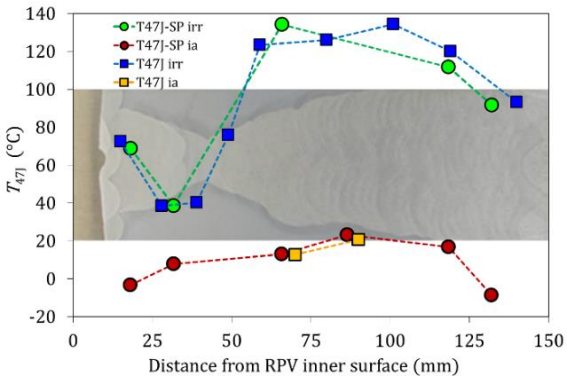

Fig. 2: DBTT T_{47J} obtained from Charpy impact tests and from SP test, recalculated with Eq. (1), as a function of position in the core welding seam of the RPV of Greifswald unit 4 (material 10KhMFT); as-irradiated (irr) and annealed (ia) conditions; the background picture shows the structure of the weld.

[1] Misawa, T. *et al.* (1987) *J. Nucl. Mater.* **150**, 194–202.
[2] Altstadt, E. *et al.* (2016) *J. Nucl. Mater.* **472**, 186–195.
[3] Viehrig, H. W. *et al.* (2015) *J. Nucl. Mater.* **456**, 334–343.

Microstructural characterization of inhomogeneity in 9Cr ODS EUROFER steel

P. Chekhonin, A. Das, E. Altstadt, F. Bergner, C. Kaden

Inhomogeneous regions of an oxide dispersion strengthened (ODS) steel were investigated. It was demonstrated that optical microscopy alone is insufficient to identify these inhomogeneous regions as residual ferrite and advanced techniques based on electron microscopy as well as site-specific nanoindentation are required.

Given their enhanced resistance against creep and high-temperature strength, ODS steels are interesting candidate materials for cladding tubes in Gen-IV nuclear fission reactors and blankets for fusion reactors. The presence of residual α-ferrite, the phase which remains untransformed during austenitization, was often reported in 9 wt.-% Cr ODS steels. Typically, residual ferrite is identified as bright, smooth and somewhat elongated region (bright stripe) against a dark matrix under optical microscopy (OM). Recently, there was confusion regarding similarly looking bright regions that are attributed to the absence of nanoparticles.
The present investigation focuses on electron microscopy to clarify this issue in the case of the air-cooled EU batch of ODS EUROFER.

EXPERIMENTAL. Samples of ODS EUROFER have been analyzed by means of OM, nanoindentation, scanning electron microscopy (SEM), electron backscatter diffraction (EBSD) and scanning transmission electron microscopy (STEM). Focused ion beam (FIB) preparation was used to select specific sample areas for subsequent TEM analysis.

RESULTS. Optical microscopy on etched samples indicates the occasional presence of bright stripes. Their volume fraction is estimated to be approximately 4 %. SEM investigations demonstrate a lower carbide density (Fig. 1) inside bright stripes, while EBSD mappings confirm a body centered cubic steel phase and indicate a larger grain size. Nanoindentation experiments prove that the bright stripe region is softer in comparison to the matrix. Applying the FIB technique a thin lamella was extracted containing both, a bright stripe region as well as the adjoining matrix (Figs. 2a and 2b). STEM investigations reveal the absence of nanoparticles inside the bright stripe (Fig. 2c), while many nanoparticles are recognizable inside the matrix (Fig. 2d). Furthermore, STEM indicates a significantly lower dislocation density of approximately an order of magnitude, thus, qualitatively as well as quantitatively explaining the lower yield strength in the bright stripes.[1]

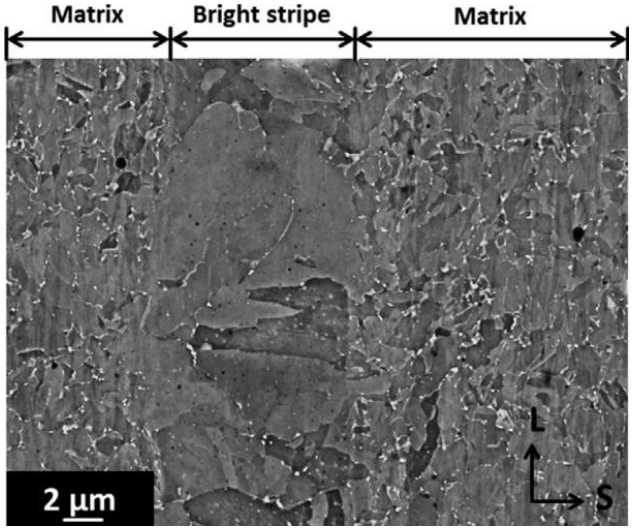

Fig. 1: Backscatter electron contrast micrograph with a bright region and adjoining matrix regions. The carbides appear as bright spots.

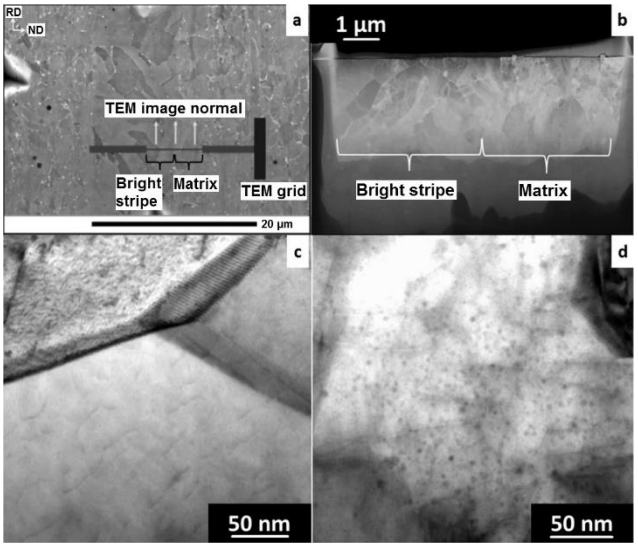

Fig. 2: SEM micrograph showing the FIB lamella taken out from the EU batch of ODS EUROFER including areas from a bright stripe and the adjoining matrix region(a). STEM bright field image of the lamella including both the regions (b). STEM bright field image from the bright stripe region (c), and from the matrix region (d).

These results present clear evidence that in this ODS steel the bright stripes cannot be residual ferrite or retained austenite. Instead, these bright stripes are most probably formed due to improper mechanical alloying (MA) resulting in the absence of nanoparticles in certain regions. This gives rise to higher grain boundary mobility, larger grain size and lower number density of grain boundary carbides, which finally is believed to result in the distinct etching behavior as observed by optical microscopy. An extension of the MA period during manufacturing should lead to a homogenous microstructure, eliminating particle-free regions which are not expected to contribute to the creep resistance and high temperature strength of ODS steels.
Finally, it should be pointed out that these inhomogeneities do not only affect the yield strength, but additionally lead to a reduced fracture toughness, particularly at temperatures at and below room temperature,[2] in comparison to differently produced ODS steels that exhibit more homogeneous MA. More details on the presented investigation including an advanced discussion can be found in reference [1].

ACKNOWLEDGEMENTS. This work contributes to the Joint Programme on Nuclear Materials (JPNM) within the European Energy Research Alliance (EERA). The authors would like to thank M. Rossner for metallographic preparations, A. Kunz for the FIB preparation and W. Webersinke for nanoindentation measurements.

[1] Das, A. *et al.* (2020) *J. Nucl. Mater.* **533**, 152083.
[2] Das, A. *et al.* (2020) *J. Nucl. Mater.* **542**, 152464.

Microstructure and fracture toughness characterization of three 9Cr ODS EUROFER steels with different thermo-mechanical treatments

A. Das, P. Chekhonin, E. Altstadt, D. McClintock,[1] F. Bergner, C. Kaden, R. Lindau[2]

[1]Oak Ridge National Laboratory, Oak Ridge, TN, U.S.A.; [2] Karlsruhe Institute of Technology (KIT), Institute of Applied Materials, Karlsruhe, Germany

Ferritic martensitic oxide dispersion strengthened (ODS) steels are promising structural materials for future Gen-IV nuclear fission and fusion reactors. The dependence of fracture toughness on microstructure was investigated. For this, three 9Cr ODS EUROFER steels manufactured through different thermo-mechanical processing routes were compared using fracture mechanics testing and microstructural characterization. It was found that variations in thermomechanical treatments can produce significant differences in microstructure and fracture toughness behavior of ferritic martensitic ODS steels.

Systematic development of reduced activation ferritic-martensitic (RAFM) ODS steels as structural material for nuclear applications in Europe resulted in ODS EUROFER, which can withstand operating temperatures up to 650 °C and exhibits high-temperature creep strength and resistance towards irradiation induced effects due to the oxide particles dispersed in the microstructure. ODS EUROFER batches were manufactured via different thermo-mechanical routes and hence developed slight variations in microstructure. The fracture toughness of a material is directly related to the microstructure, and is an extremely important parameter affecting the loading capacity, machinability and formability. Therefore, it becomes important to study the impact of variation in microstructure on the fracture toughness of 9Cr ODS EUROFER steels.

EXPERIMENTAL. The nominal composition of ODS EUROFER is (wt.-%) 8.9 Cr, 1.1 W, 0.2 V, 0.14 Ta, 0.42 Mn, 0.06 Si, 0.11 C, 0.3 Y_2O_3 and Fe for the balance. The production route of all the three ODS EUROFER batches involved mechanical alloying followed by hot isostatic pressing, hot-rolling at 1150 °C followed by austenitization at 1100 °C for 30 min. Hereafter, slightly different heat treatments were followed as indicated in Tab. 1. Tempering was then performed for all the materials at 750 °C for two hours.

Tab. 1: Heat treatments of the three ODS EUROFER batches.

Batch Name	Heat Treatments	Ref.
ODS_WQ_450	water quenching to 450 °C	[1, 2]
ODS_WQ_RT	water quenching to RT	[1, 3–5]
ODS_AC_RT	air cooling to RT	[6]

Microstructure characterization of the bulk was performed using OM, SEM, EBSD and TEM. Quasi-static fracture toughness testing was performed at −100 °C to 600 °C using sub-sized compact tension 0.25T C(T) specimens. The fracture surfaces were characterized using SEM.

RESULTS. After austenitization, ODS_WQ_450 was water quenched to 450 °C, which is above the martensite start temperature. Hence, its microstructure consists only of coarse globular ferrite grains. ODS_WQ_RT and ODS_AC_RT exhibited martensitic microstructure with ODS_WQ_RT containing residual α-ferrite phases which are harder than the matrix. ODS_WQ_450 contained larger sub-micron particles enriched with Cr, W, C and O while smaller particles were observed in the other two materials.

At low temperatures (−100 °C and RT), ODS_WQ_RT exhibits higher fracture toughness and more stable fracture behavior as compared to ODS_AC_RT (Fig. 1) due to higher amount of secondary cracking which may be explained by the mismatch of mechanical properties between the elongated hard residual ferrite phases and the soft tempered martensite matrix. At these temperatures, ODS_WQ_450 exhibits the lowest fracture toughness because it contained the largest sub-micron particles. No information about the occurrence of secondary cracks on the fracture surfaces could be obtained from literature.[2]

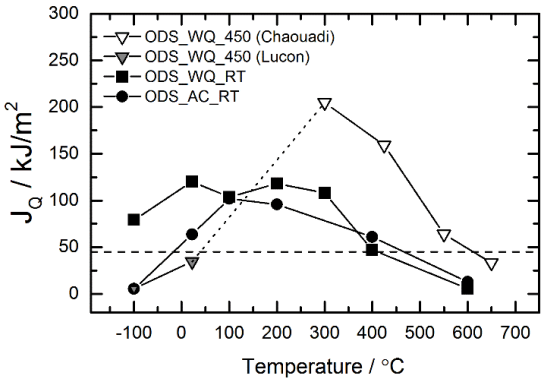

Fig. 1: Fracture toughness comparison over a wide temperature range for ODS_AC_RT and ODS_WQ_RT along with ODS_WQ_450.[2] For ODS_WQ_450, the results for −100 °C and 22 °C are taken from Lucon et al. (grey symbols).[1] The dashed line indicates the acceptable fracture toughness value of J_Q = 45 kJ/m² (K_{JQ} = 100 MPa√m).[5]

At temperatures between 100 °C and 500 °C, ODS_WQ_RT and ODS_AC_RT exhibit more or less similar fracture toughness as the matrix ductility of these two materials is similar. On the other hand, ODS_WQ_450 exhibits the highest fracture toughness which can be explained by its higher matrix ductility.

At temperatures above 500 °C, reduced fracture toughness values for ODS_WQ_RT and ODS_AC_RT were observed due to a shift from transgranular ductile to intergranular fracture. On the other hand, ODS_WQ_450 still exhibited higher fracture toughness as its coarse-grained microstructure behaved better against intergranular fracture.

ACKNOWLEDGEMENTS. The authors thank Dr. R. Chaouadi for providing ODS_WQ_450. We thank W. Webersinke, M. Houska, M. Rossner, A. Kunz and the Ion Beam Center for their support.

[1] Lucon, E. (2006) SCK. CEN Open Rep. BLG-1024.
[2] Chaouadi, R. *et al.* (2010) *J. Nucl. Mater.* **403**, 15–18.
[3] Klimiankou, M. *et al.* (2007) *J. Nucl. Mater.* **367–370**, Part A, 173–178.
[4] McClintock, D. *et al.* (2009) *J. Nucl. Mater.* **392**, 353–359.
[5] Byun, T. S. *et al.* (2017) *J. Nucl. Mater.* **484**, 157–167.
[6] Lindau, R. (2018), private communication.

Relationships between primary radiation damage, irradiation-induced microstructure and hardening of ion-irradiated Fe-Cr and ODS Fe-Cr alloys

K. Vogel, C. Kaden, P. Chekhonin, F. Bergner

Ion irradiations are a powerful tool for investigating radiation effects like radiation hardening. However, the extraction of radiation hardening as a function of displacement damage from the nanoindentation (NI) response of ion-irradiated materials is a challenge. In this study, we analyzed the microstructure and the NI response for two ion-irradiated Fe-Cr alloys. Cross-sectional Transmission Electron Microscopy (TEM) indicated the appearance of irradiation-induced dislocation loops but no other types of visible microstructural changes. NI indicated maxima of radiation hardening as a function of contact depth. Links between the depth-resolved primary radiation damage, the observed depth-dependent characteristics of the loops and the measured hardening are considered.

The irradiation with MeV ions gives rise to a depth-dependent displacement of atoms from their lattice sites, a deposition of injected ions at interstitial sites of the crystal lattice and a formation of irradiation-induced defect clusters such as dislocation loops. The consequence of these effects is a degradation of the mechanical properties in terms of embrittlement and hardening. One of the long-term goals of ion-irradiation studies is the extraction of radiation hardening as a function of displacement damage. In our study, the effect of 5 MeV Fe-ion irradiation of Fe-Cr alloys on microstructure and hardening is addressed. Empirical models are applied to link primary radiation damage with the irradiated microstructure and the microstructure with irradiation hardening.[1]

EXPERIMENTAL. The materials studied are an Fe-Cr model alloy (8.4 wt.-% Cr) and an oxide dispersion strengthened (ODS) Fe-Cr (9.1 wt.-% Cr) alloy. The ion irradiations were performed with the 3 MV tandetron accelerator of the Ion Beam Center at HZDR. Fe^{2+} ions of 5 MeV energy were implanted at a temperature of 300 °C. The depth profiles of displacements per atom (dpa) and injected interstitials per atom (ipa) were calculated using the binary collision code SRIM-2013.00. The microstructure was studied by cross-sectional TEM using a FEI Talos F200X microscope. Irradiation-induced dislocation loops were imaged under various diffraction conditions. Depth profiles of loop number density and size were obtained by counting and sizing the loops in TEM bright-field images. The sample thickness was estimated by means of convergent beam electron diffraction. NI hardness was measured using a Universal Nanomechanical Tester (UNAT, ASMEC GmbH). Hardness *vs.* depth plots were calculated from about 30 indentation tests by averaging.

RESULTS. For both materials, the TEM images indicate the appearance of irradiation-induced dislocation loops as the one and only type of visible microstructural changes. Figure 1a displays a TEM bright-field overview image of the ion-irradiated ODS FeCr sample. A defect-rich band aligned parallel to the specimen surface is visible in the depth range from 1.2 to 1.6 µm, which is close to the peak positions in the dpa- and ipa-profiles (not displayed here). The band contains a large number of dislocation loops appearing as black dots under two-beam kinematical bright-field conditions and as white dots under weak-beam dark- field conditions as shown in Figs. 1b and 1c. The depth-dependent number

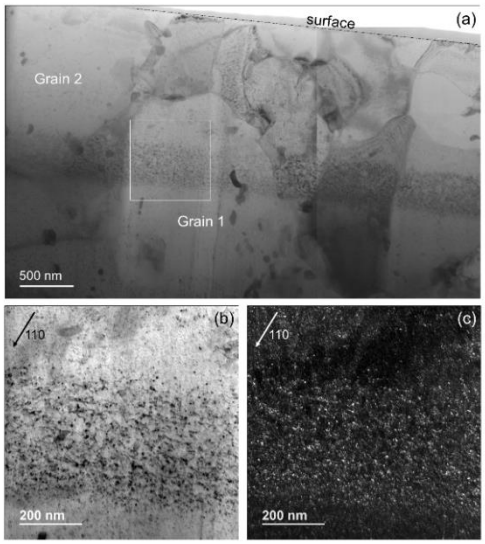

Fig. 1: TEM images of ion-irradiated ODS FeCr. Overview (a), two-beam kinematical bright-field (b) and weak-beam dark-field image (c) of the area marked in (a).

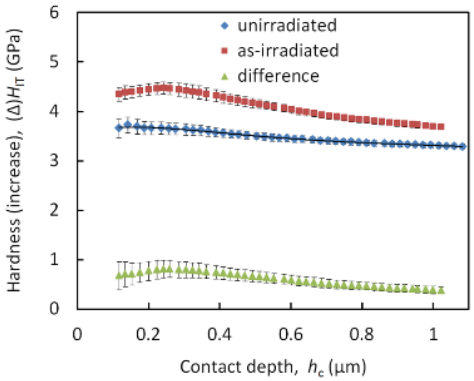

Fig. 2: Indentation hardness measured for the unirradiated and irradiated state of ODS FeCr.

density of dislocation loops determined from the TEM images was decomposed into fractions arising from displacement damage and injected interstitials (see ref. [1] for details). The latter fraction corresponds to 2 % of the total injected interstitials for ODS FeCr.

For both materials, a maximum of the irradiation-induced hardness increase as a function of contact depth was found as demonstrated in Fig. 2 for ODS FeCr. This observation is rationalized by a combination of the dispersed barrier hardening model and the half-sphere approximation of the indentation plastic zone, with the amount of the predicted hardening depending on the selected superposition rule of the contributions from pre-existing and irradiation-induced barriers for dislocation glide.

ACKNOWLEDGEMENTS. This work received funding by the EU within the projects MATISSE and M4F. The irradiations were carried out at the Ion Beam Center at HZDR. We would like to thank M. Roßner for the surface preparation and A. Kunz for the TEM sample preparation.

[1] Vogel, K. *et al.* (2020) *Nucl. Mater. Energy* **24**, 100759.

Vacancy-solute clustering in Fe-Cr alloys after neutron irradiation

A. Ulbricht, M. J. Konstantinovic[1]

[1]SCK CEN, Mol, Belgium

Vacancy-solute clustering in neutron irradiated Fe-Cr alloys with various concentrations of Cr and minor solutes (Ni, Si and P) were studied by using positron annihilation spectroscopy (PAS) and small-angle neutron scattering (SANS). The results indicate the existence and formation of vacancy-CrNiSiP clusters that play a detrimental role in irradiation hardening. In Fe9Cr alloys with significantly reduced concentration of minor solute elements, the main defects are vacancy clusters with a cluster size up to 10 vacancies. A high concentration of α'-precipitates was observed in Fe14Cr(NiSiP). However, both vacancy clusters and α'-precipitates provide significantly less impact to hardening in comparison to vacancy-CrNiSiP clusters.

High Cr ferritic/martensitic (F/M) steels are candidate structural materials for the construction of key components in future reactors, since they offer better radiation resistance in comparison to austenitic steels. In order to provide a solid interpretation of the mechanical properties and to verify the association between solutes and point-defects, a thorough microstructure examination is needed. The defect characterization by PAS and SANS shows that vacancy-CrNiSiP clusters are formed and are dominant in irradiation hardening.

EXPERIMENTAL. The investigated materials are listed in Tab. 1. The composition of materials, the performed neutron irradiation up to 0.11 displacements per atom (dpa) and detailed descriptions of the PAS and SANS experiments are given in [1] and references therein. The A-ratio is defined as the ratio of total and nuclear irradiation-induced scattering. It is a one-parameter signature of the cluster composition.

Tab. 1: FeCr model alloys, volume fraction *c*, and *A*-ratio of irradiation-induced nano-features derived by SANS and changes of Vickers hardness ΔHV10 after irradiation (0.11 dpa).

Material	*c* (vol.-%)	*A*-ratio	ΔHV10
Fe9Cr F/M	0.13 ± 0.01	2.20 ± 0.2	27 ± 3
Fe9Cr	0.15 ± 0.01	1.45 ± 0.1	22 ± 3
Fe9CrNiSiP	0.29 ± 0.01	1.90 ± 0.15	72 ± 3
Fe5CrNiSiP	0.13 ± 0.01	3.50 ± 0.5	68 ± 4
Fe14CrNiSiP	1.75 ± 0.05	2.15 ± 0.15	94 ± 7

RESULTS. All irradiated materials exhibit an increase of the S-parameter and a decrease of the W-parameter in the PAS experiment, indicating that positrons are trapped and annihilate at vacancy-rich complexes induced by neutron irradiation. Fe9Cr ferrite has the strongest enhancement in the low momentum region of all materials. In the high momentum region, the smallest difference with respect to the reference Fe sample was observed for Fe9Cr F/M alloy. The coincidence Doppler broadening spectra of all other alloys fall in between these two extreme cases (Fig. 1).

The size distribution of irradiation-induced clusters determined by SANS are shown in Fig 2. An average radius of about 1 nm was estimated for all alloys containing minor solutes. The *A*-ratio (Tab. 1) observed for ferritic pure Fe9Cr indicates that the majority of irradiation-induced scatterers are vacancy clusters (theoretical value 1.4). The higher *A*-ratios of the other alloys indicate a dominant contribution

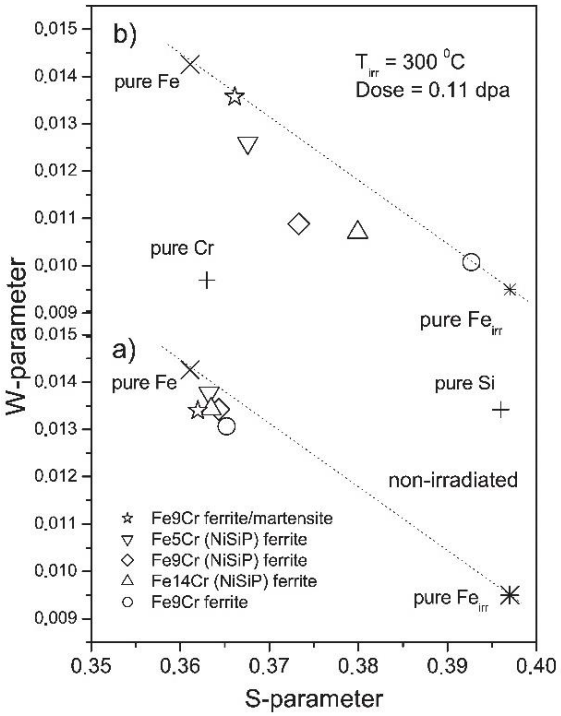

Fig. 1: PAS results: S *vs.* W parameter. Non-irradiated condition (a), neutron irradiated FeCr alloys (b).

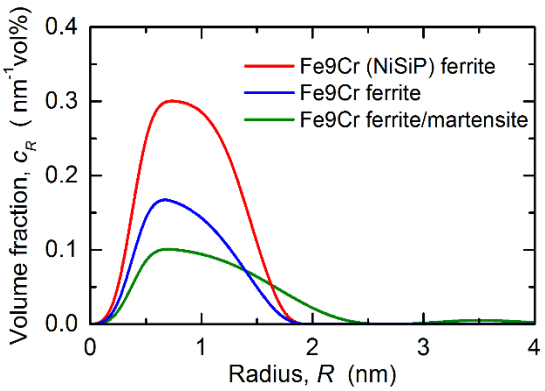

Fig. 2: SANS results: size distribution of irradiation-induced nano-features in different Fe9Cr alloys after the same neutron irradiation up to 0.11 dpa.

of solute clusters. It is worth to note that an *A*-ratio of 2.05 is expected for Cr-rich α'-phase particles, as observed in Fe14CrNiSiP. Moreover, the high-volume fraction in Fe14CrNiSiP provides additional argument for the presence of Cr-rich α'-phase particles in this alloy.

ACKNOWLEDGEMENTS. This work received funding by the EU within the project MATISSE. The SANS experiment was performed at LLB Saclay. Access is gratefully acknowledged.

[1] Konstantinovic, M. J. *et al.* (2020) *J. Nucl. Mater.* **540**, 152341.

Characterization of the porous network structure of concrete

Q. I. Roode-Gutzmer, J. Kulenkampff

The porosity and specific surface area of a small intact core of concrete (~0.2 g) was characterized non-destructively by micro-computed tomography (µ-CT), N_2/BET and destructively by Mercury Intrusion Porosimetry (MIP).

Biological shielding concrete that has been subjected to neutron radiation is prone to degradation *via* the alkali silica reaction.[1] This has two implications: loss of mechanical strength (which impacts service life), and a change in the porous structure and reactive surface in terms of the sorption characteristics and transport of radionuclides (either occurring *in situ via* neutron activation or *ex situ* due to contamination of leaked reactor cooling water). The objective of this work is to investigate the characterization of pore structure on intact specimens of concrete (as small as possible) so that reactive transport processes can be directly correlated.

EXPERIMENTAL. Non-radioactive concrete (*ca.* 48 years old) from the dome section of a reactor pressure vessel forming the base of the reactor was acquired during the dismantling of a decommissioned nuclear power plant, Stade, Niedersachsen, Germany. A diamond-coated core driller (dry; 200 rpm) was used to remove a small core (Ø = ~5 mm; L = 2 mm; 0.17 g) from a larger drill core (Ø = 73.6 mm; L = 150.7 mm) that remained intact and without any visible cracks after being subjected to a standard test (EN 13412:2006-11) for modulus of elasticity under compression (21.7 GPa). This small core was analyzed non-destructively by µ-CT and Scanning Electron Microscopy (SEM) (sample surface: rough, uncoated), then dried at 100 °C overnight prior to an N_2/BET measurement in triplicate. MIP was subsequently conducted on the small intact core in accordance with ISO 1509-1. µ-CT scans were acquired on the large and small drill cores using a Nikon XT H225 employing a tungsten target. A SEM image was obtained using a JEOL JSM-F100. The Pascal 140 and 440 Series from Thermo Electron Cooperation were used to conduct MIP. Specific surface area determined by N_2/BET was performed using a Thermo Scientific Surfer Analyzer.

RESULTS. The results are summarized in Figs. 1 and 2. It is clear that the methods of MIP and µ-CT yield pore-size information on different scales with a small overlap in the region 4–75 µm. The specific surface area calculated using the cylinder and plate model from the MIP results is 9.94 m²/g, whereas N_2/BET yields a value of 6.07 m²/g (s. d. = 0.54). A higher value for MIP is due both to the ink-bottle effect (large pores with narrow throats)—smaller pores are overestimated at the expense of larger pores—and to fracking. The hysteresis of the mercury intrusion and extrusion curves suggests needle-like pores.[2] The initial constant volume with decreasing pressure and the fact that 51.5 % of the mercury remains in the sample after extrusion is indicative of ink-bottle pores, as well as non-equilibrium compression and decompression conditions. Larger cores (*i. e.* ~1 g) revealed similar pore features in their differential pore-size distribution curves, but cores <0.1 g displayed erroneous results. While MIP yields information on the connectivity of the transport pores, the specimen is unfortunately unusable for further reactive transport experiments.

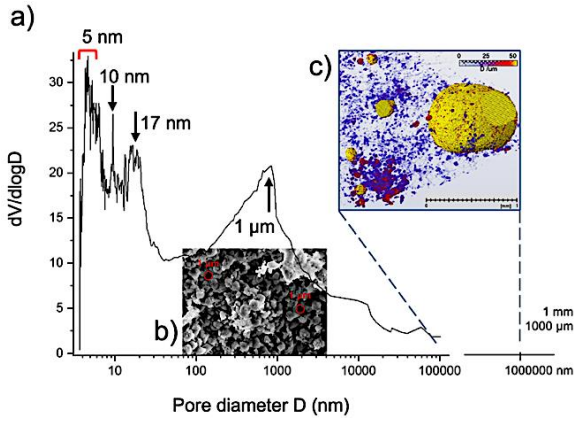

Fig. 1: Differential volume pore-size distribution curve (a) of a small intact core of concrete determined by mercury intrusion porosimetry illustrating on the logarithmic scale gel pore features (5–17 nm) and capillary pores of ~1 µm, which can clearly be seen in the SEM image of the cement matrix (b) and a thickness map (c) of a sub-volume of the small concrete core obtained from µ-CT portraying air voids (yellow) in millimeter range, and micropores of ~40 µm (red) and ~20 µm (blue).

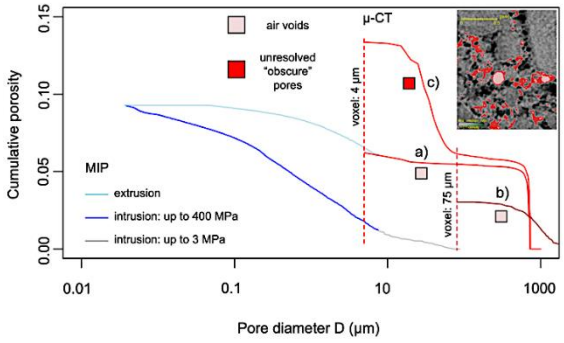

Fig. 2: Accumulated porosity *vs.* pore-size on the logarithmic scale determined by MIP and µ-CT. True air voids and pores are calculated with background greyscale values (inset: pink) for a sub-volume of the real small core (with voxel size 4 µm) (a) and a digitally extracted volume from the big drill core including the small core as sub-volume (with voxel-size 75 µm) (b). Between the cement matrix and immediately adjacent to the aggregate exists a greyscale that is neither air nor grain (inset: red).[3] This greyscale is not well resolved and could suggest obscure pores, possibly in a network of unresolved needles. This volume fraction is illustrated for the real small core (c).

ACKNOWLEDGEMENTS. A. Willomitzer (TU Dresden) is gratefully appreciated for carrying out the MIP measurements. This work is supported within the funding framework of FORKA, German Federal Ministry of Research and Education (WERREBA project: Grant Number 15S9412).

[1] Roode-Gutzmer, Q. I. *et al.* (2020) this report, p. 76.
[2] Zgrablich, G. *et al.* (1991) *Langmuir* **7**, 779–785.
[3] Kulenkampff, J. *et al.* (2020) this report, p. 41.

Volume expansion of quartz aggregate in ion-irradiated concrete

Q. I. Roode-Gutzmer, S. Schymura, H. Lippold

Quartz aggregate in concrete irradiated by Si-ions with a fluence of 5×10^{14} ions/cm² at 300 keV exhibited an out-of-plane expansion of ~80 nm.

Quartz is the primary mineral component of most concretes and exhibits the highest neutron radiation-induced volume expansion (*i.e.* 17.8 %) of all minerals yet examined.[1] The volume expansion is due to structural relaxation that occurs when a critical concentration of defects (E′ centers) has been produced by the interaction of the radiation imparted to the crystal lattice.[2] The mechanism of this amorphization process appears to be indifferent to the type of radiation (*i.e.* neutrons, electrons, ions, and photons, *e.g.* gamma). The chemical durability of concrete is largely dependent on the reactivity of the silicate aggregates to alkaline pore water, which ultimately results in the alkali-silica-reaction. The rate-determining step for the dissolution of quartz is associated with $Q^4 \rightarrow Q^3$, which is considerably slower relative to the subsequent dissolution steps $Q^n \rightarrow Q^{n-1}$, where the Q^n nomenclature represents the Si-tetrahedron with n being the number of Si-atoms the tetrahedron is bound to.[3] As quartz amorphizes due to radiation, the concentration of Q^3 species increases. The ultimate goal of this work is to examine how radiation-induced changes in quartz effects dissolution behavior in alkaline media and to resolve (spatially and temporally) the influences of grain boundaries, defects, crystal strain, and Q^3 content. In this paper we examine the volume change of quartz.

EXPERIMENTAL. Non-radioactive concrete (*ca.* 48 years old) from the dome section of a reactor pressure vessel forming the base of the reactor was acquired during the dismantling of a decommissioned nuclear power plant, Stade, Niedersachsen, Germany. Two slices (*ca.* 5 mm thick) of concrete from a drill core were obtained using a diamond-coated and water-cooled circular saw. Four polished sections with a diameter of 3 cm were prepared by vacuum impregnation using a two-component epoxy-based resin (Araldite 2020). The samples were ground smooth using SiC paste with a final diamond polish (3 µm). Mineralogical composition of the aggregates was identified *in situ* by µ-Raman spectroscopy (HORIBA Jobin Yvon LabRAM Aramis Vis) using an excitation wavelength of 532 nm. Aluminium foil was placed on each polished section so as to respectively protect and expose parts of the aggregate to radiation. Si-ion irradiation with a fluence of 5×10^{14} ions/cm² at 300 keV was conducted under vacuum at room temperature without cooling. Some sputtering could be observed on the samples after irradiation. Depth profiles of the irradiated samples were examined by Vertical Scanning Interferometry (VSI) and Confocal Microscopy using an S Neox 3D Optical Profiler (Sensofar Metrology).

RESULTS. The minerals making up the aggregate were clearly identified by µ-Raman spectroscopy to be α-quartz and potassium feldspar (microcline: $KAlSi_3O_8$), the latter always intergrown with quartz. The results are illustrated in Fig. 1. The most significant depth profile change observed in the sample is the ablation of the epoxy resin (−600 nm). The volume change in quartz is observed as an increase in height of 80 nm. Taking into account an ion-penetration depth of 429 nm (estimated in the Kinchin-Pease calculation by SRIM)[4] for pure quartz, the volume expansion amounts to

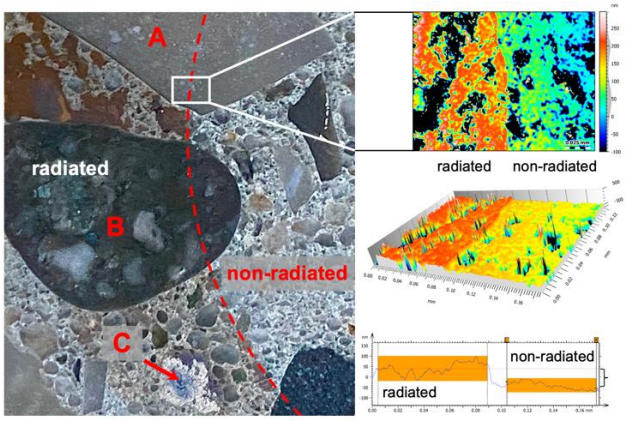

Fig. 1: Image showing radiated area (epoxy resin tarnished brown) left of the red dashed line and non-radiated area (epoxy resin clear) right of the dashed red line. Area of interest (AOI) in the white square depicting the boundary between radiated and non-radiated regions on large quartz aggregate. A = quartz (SiO_2), B = feldspar (microcline: $KAlSi_3O_8$), C = sputtering from Si-ion irradiation. VSI of AOI indicating depth profile, exhibiting +80 nm on quartz, −600 nm on epoxy resin, and unspecified on feldspar.

15.7 %. No observable difference in average height between radiated and non-radiated areas on the black aggregate containing feldspar could be ascertained. Aggregates containing feldspar were generally found to display a rougher surface than aggregates containing only quartz. The maximum volume expansion observed for potassium feldspar has been reported to be 7.7 %.[1] Considering the same extent of radiation damage as observed for the quartz aggregate in this work, and a calculated ion-penetration depth for $KAlSi_3O_8$ (estimated by SRIM) of 604 nm, a height increase in microcline of ~41 nm is expected. The troughs that the rougher surface of microcline exhibits could accommodate the expansion laterally in the plane, which decreases the expected out-of-plane expansion to ~3.4 nm, which is close to the resolution for VSI (1–2 nm). In addition, curvature of granular surfaces deflects light, which inhibits VSI measurements. Finer surface polishing of the specimen is therefore required in order to accurately observe radiation-induced volume expansion of microcline.

ACKNOWLEDGEMENTS. Ion-beam irradiation of samples were performed by Dr. S. Akhmadaliev at the Ion Beam Centre (IBC) at HZDR. This work is supported within the funding framework of FORKA, German Federal Ministry of Research and Education (WERREBA project: Grant Number 15S9412).

[1] Le Pape, Y. *et al.* (2018) *J. Adv. Concr. Tech.* **16**, 191–209.
[2] Douillard, L. *et al.* (1996) *Nucl. Instrum. Methods Phys. Res.* **B107**, 212–217.
[3] Crundwell, F. *et al.* (2014) *Hydrometallurgy* **149**, 265–275.
[4] Ziegler, M. D. *et al.* (2010) *Nucl. Instrum. Methods Phys. Res.* **B268**, 1818–1823.

Microscopic characterization of un-irradiated and irradiated steel shielding material of a nuclear power plant

G. Yassin, A. Barkleit, V. Brendler

Nuclear power plants (NPPs) have been considered an important energy source in Europe over a long time. However, in Germany the government decided that NPPs must terminate their operation end of 2022 at the latest, due to their possible threats on humans and the environment. The question arises, how much the long term irradiation of an NPP poses safety risks, in particular, in the reactor pressure vessel (RPV), which is the main shielding barrier of the radioactive fuel. For this purpose, the microstructural features, the composition, and the radioactive inventory of the steel shielding material in the RPV are investigated.

Figure 1 shows a photograph of a dismantled RPV of the decommissioned VVER prototype reactor from Greifswald NPP.[1] The region next to the reactor core in the RPV is normally the part exposed to the highest neutron fluencies.[2] Its steel mainly consists of both base metal and weld metal, which needs to be investigated in understanding the irradiation impact on the RPVs. Here, blocks of base metal and weld metal were taken from Greifswald NPP unit 8 RPV. It was produced by ŠKODA steel works in former Czechoslovakia by the end of 1970s, however it never went into normal operation mode.[3]

EXPERIMENTAL. Specimens were extracted from the inner core of the RPV and cut into segments. These were neutron irradiated in JRC-Petten laboratories for a period of time 271 days, which mimics the long-term irradiation process. Analysis followed of both un-irradiated and irradiated samples, which were sliced into 10×10×1 mm sections and underwent a polishing process. Optical emission spectroscopy (OES) measurements on the un-irradiated samples provided the chemical composition of the alloying elements, which are sensitive to the neutron irradiation. Furthermore, surface analysis based on scanning electron microscopy/energy dispersive X-ray spectroscopy (SEM/EDX) of both un-irradiated and irradiated samples revealed microstructural features related to their composition and irradiation conditions.

RESULTS. Table 1 contains accurate mass measurements of the alloying material within the RPV shielding steel samples based on OES experiments. Results from the SEM/EDX measurements are shown in Fig. 2, they document an increase of the dark cluster size after the irradiation process and a distribution of white precipitates. Based on the EDX analysis, our results revealed the presence of manganese(II) sulfide (MnS) inclusions within the dark clusters, and the presence of molybdenum in the white distributed precipitates. Such a phenomenon can be explained as the long term irradiation on the steel shielding material may give rise to enhanced diffusion and rearrangement of the solute atoms in the Fe lattice. This consequently leads to the formation of clusters and segregation of the atom particles.

ACKNOWLEDGEMENTS. This work is funded by the German Federal Ministry of Education and Research (BMBF) under contract number 15S9412. The authors gratefully thank J. Konheiser for his valuable collaboration in the project, and M. Houska for preparing the samples of interest.

Fig. 1: RPV of the decommissioned Greifswald NPP.[1]

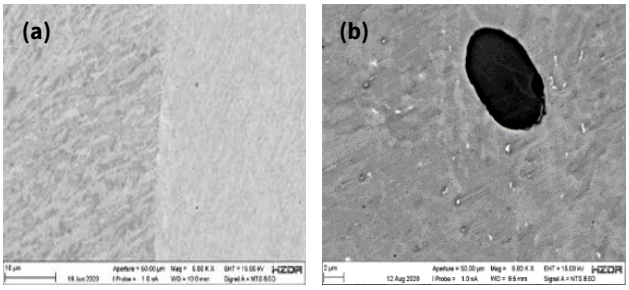

Fig. 2: SEM measurements of the base metals from the RPV showing their bainitic ferrite microstructural features of un-irradiated (a) and irradiated (b) steel shielding samples. The latter reveals the presence of high surface area of dark clusters containing MnS inclusions, and the distribution of white precipitates of Molybdenum.

Tab. 1: Mass concentration (%) of the chemical composition identified in the base metal of shielding steel samples in the RPV by OES.

	C	Si	Mn	Cr	Ni
%	0.15	0.26	0.47	2.87	0.07
SD*	0.006	0.003	0.003	0.01	0.0006
	V	Mo	Cu	Fe	
%	0.29	0.72	0.048	95	
SD*	0.002	0.008	0.0002	0.007	

*: denotes the standard deviation.

[1] Viehrig, H.-W. *et al.* (2018) *Report HZDR-088*.
[2] Christien, F. *et al.* (2004) *Journal of Nuclear Materials* **324**, 90–96.
[3] IAEA, *Nuclear Energy Reactors in the World* (2014) International Atomic Energy Agency, Vienna.

Neutron fluence calculations and validation based on metal foils placed inside a German PWR

R. Rachamin, J. Konheiser, A. Barkleit

In 2011, the German Atomic Energy Act was amended to phase out nuclear energy for the commercial production of electricity. As a result, all German nuclear power plants (NPPs) will have been shut down by the end of 2022. In order to dismantle the NPPs in a safe, economical, and timely manner, decommissioning studies have to be performed. The planning and implementation of a decommissioning strategy for an NPP require knowledge of the neutron activation and contamination levels, which have emerged during its operation. The extent and levels of activation in an NPP depend on the neutron fluence distribution within the NPP components. The neutron fluence is, therefore, one of the most fundamental and important parameter in the decommissioning studies. Hence, it should be as accurately estimated as possible. In this study, a 3D detailed Monte-Carlo (MC) model of a German PWR was developed to calculate the neutron fluence characteristics within the reactor components. The neutron fluence prediction capability of the developed model was validated based on activation measurement of several monitors composed of thin metal foils placed along the ex-core instrumentation channel. A very good agreement was obtained between the calculations and the measurements.

REACTOR MODEL AND MC CALCULATIONS. The German PWR was simulated using the Monte-Carlo code MCNP (version 6.2).[1] The reactor was modeled in detail based on original technical drawings. The model extends from the reactor core through the reactor pressure vessel (RPV) and its internals into the ex-vessel components including the thermal insulation and the interior and exterior biological shields. A schematic view of the model is shown in Fig. 1. The model was used to calculate the neutron fluence characteristics (spectrum and distribution) of the reactor. In addition, experiments were carried out in two reactors for the validation purpose of the model. For this, the activation of several metal isotopes were calculated at 10 points inside the ex-core instrumentation channel located in the interior biological shield (Fig. 1). The results were then compared with the activation measurements of monitors composed of thin metal foils placed in these locations.

EXPERIMENTAL MEASUREMENTS. Several activation monitors connected with a steel cable were placed inside the ex-core instrumentation channel of an active reactor (parallel to the reactor core). Each monitor was composed of an aluminum box filled with thin metal foils: Ti, Fe, Ni, Cu, Zn, In, and Sn. The metal foils have a thickness of 0.1 mm and a size of 5 × 5 mm to 10 × 10 mm or 10 mm diameter. The monitors were irradiated in the reactor for about 6 months. After recovery, the neutron activation products were analyzed by gamma spectroscopy using coaxial high purity germanium (HPGe) detector (GMX, 30 % efficiency, Ortec-Ametek, Inc.).

CALCULATIONS *VS.* MEASUREMENTS. The activation was calculated for each metal foil, and the obtained result was compared with the corresponding measured value. Because the exact position of the monitors inside the channel is not known, the calculations were performed for 3 possible locations of the monitors: close to the outer wall of the channel (C1 - Out), in the middle of the channel (C2 - Mid.), and close to the inner wall of the channel (C3 - In). The activation

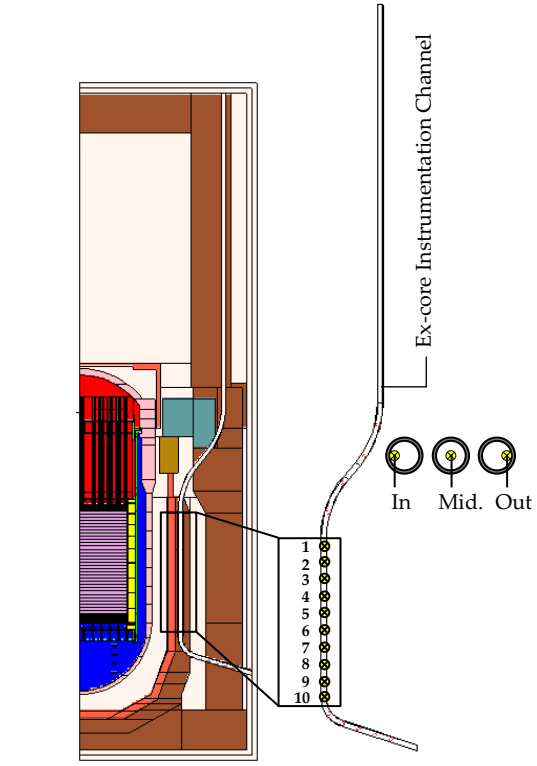

Fig. 1: 3D MCNP model of a German PWR.

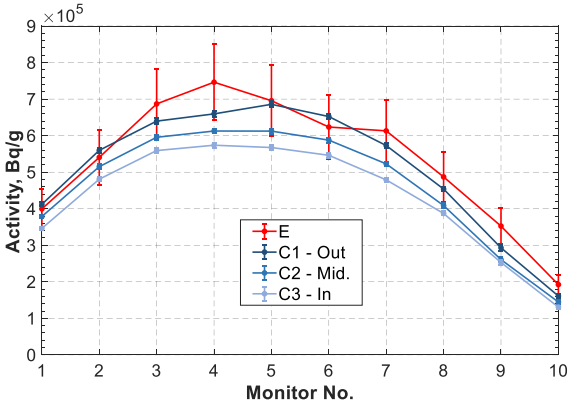

Fig. 2: Activation calculations *vs.* measurements for ^{113}In (n,ɣ) ^{114m}In.

calculations *vs.* measurements for ^{113}In (n,ɣ) ^{114m}In are shown in Fig. 2. As can be seen, the results of the calculations agreed very well with the measurement values. The same observation was obtained for all of the examined metal foils activation reaction.

ACKNOWLEDGEMENTS. This work is funded by the Federal Ministry of Education and Research (BMBF) under contract number 15S9409A and supported by PreussenElektra GmbH.

[1] Goorley, T. *et al.* (2012) *Nucl. Technol.* **180**, 298–315.

Coupled thermal hydraulic and neutronic simulations of the ESFR-SMART core

E. Nikitin, E. Fridman

The in-house reactor dynamics code DYN3D[1] was used to perform coupled core thermal hydraulic (TH) and neutronic simulations of the European Sodium Fast Reactor core in the framework of the Horizon 2020 ESFR-SMART project, hereinafter referred to as the ESFR-SMART core. The consideration of burn-up dependence of the fuel stoichiometry and porosity was found to be critical for fuel temperature calculations. As compared to stand-alone mode calculations, the effect of the coupling was evaluated by comparing radial distributions of power, average fuel temperature and coolant heat-up. Lastly, the safety relevant global reactivity coefficients were evaluated in coupled simulations.

REFERENCE CORE DESCRIPTION. The ESFR-SMART core is a large 3,600 MWth oxide core containing 216 inner core and 288 outer core fuel subassemblies (S/As), 31 corium discharge tubes, and 24 control and 12 dedicated shutdown devices. The active core is surrounded by three types of reflector layers with a total of 268 S/As. At 293 K, the S/A pitch size is 20,985 cm, and the height of the inner and outer active cores are 75 cm and 95 cm, respectively. In this study, the core was modeled at End of Equilibrium Cycle (EOEC) with nominal power, 668 K core inlet temperature and a total coolant flowrate of 18,705 kg/s. The burn-up distribution was obtained with the Serpent code in six batches per zone,[2] separately for fissile and fertile axial regions. The full specification is available in the project deliverables.[3]

NEUTRONICS. In stand-alone neutronic calculations, a uniform fuel temperature of 1,500 K and coolant density of 0.837 g/cm³ was assumed. In coupled calculations, the spatial distribution of these two parameters was provided by the TH module of DYN3D. The applied homogenized few-group cross sections, generated with Serpent, were parametrized by fuel temperature and coolant density.

THERMAL HYDRAULICS. In stand-alone TH calculations, the power distribution was provided from the stand-alone neutronic results of DYN3D. In coupled calculations, the power distribution was calculated by the code. According to the recommendation of the project's fuel performance and gap conductance task group,[4] the following new correlations were added to the TH module for proper simulation of the fuel rod thermal conductance in mixed oxide sodium cooled fast reactor fuels:

- Philipponneau correlation for thermal conductivity,[5]
- burn-up dependent fuel stoichiometry,
- burn-up dependent fuel porosity,
- burn-up and linear heat rate dependent gap conductance.

FUEL ROD TEMPERATURES. Typically in system analyses, fixed values of fuel stoichiometry (x) and porosity (p) are used, *e. g.*, $x = 0.02$ and $p = 0.045$ for fresh fuel. Such simplification of disregarding burn-up (bu) dependence leads to an opposite tendency of fuel conductivity with increasing burn-up (Fig. 1). It was found that applying fresh fuel stoichiometry and porosity in the ESFR-SMART core will result a significantly lower average fuel temperature (by about 80 K) within S/As with a low-burn-up of 23.21 MWd/kg. Furthermore, in the core center, between S/As with low-burn-up and high-burn-up such as 112.42 MWd/kg, the difference in fuel temperature changes drastically (swings from −10 K to +120 K) when considering burn-up dependence in x and p.

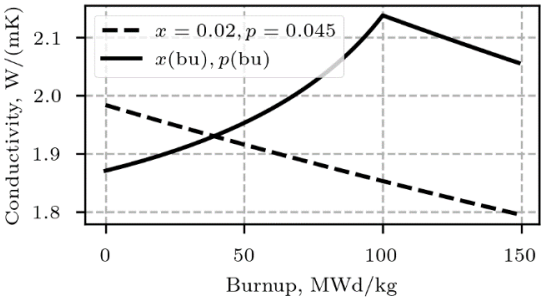

Fig. 1: Difference in fuel thermal conductivity at 1,500 K. Fixed *vs.* parametrized fuel stoichiometry and porosity.

COUPLED RESULTS. The spatial distributions of power, fuel temperature and coolant heat-up obtained in coupled simulation were compared against the stand-alone mode calculation, as seen in Fig. 2. It can be concluded that taking into account the TH feedbacks with a non-uniform temperature field can deviate the power distribution up to 0.8 % (Fig. 2a). Consequently, this will affect the average fuel temperature and coolant heat-up in S/As up to about 7 K and 2 K (Fig. 2b–c), respectively.

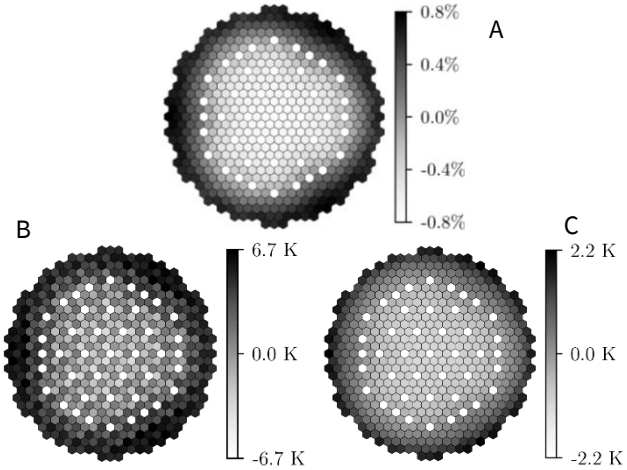

Fig. 2: Differences in radial distributions of selected quantities between coupled *vs.* stand-alone modes. Power (A), fuel temperature (B), and coolant heat-up (C).

Finally, by using the coupled model, the following global reactivity coefficients were obtained at nominal core state:

- $k = -0.59$ pcm per 1 K change of the inlet temperature,
- $g = -0.30$ pcm per 1 K change of the core heat-up,
- $h = -3.21$ pcm per 1 % change of reactor power.

These negative values indicate a high level of ESFR-SMART core self-protection and safety.

[1] Rohde, U. *et al.* (2016) *Prog. Nucl. Energy.* **89**, 170–190.
[2] Leppänen, J. *et al.* (2015) *Ann. Nucl. Energy* **82**, 142–150.
[3] Rineiski, A. *et al.* (2018) Deliverable D1.1.2, ESFR-SMART project.
[4] Lavarenne, J. *et al.* (2020) Deliverable D1.2.3, ESFR-SMART project.
[5] Philipponneau, Y. (1992) *J. Nucl. Mater.* **188**, 194–197.

Validation of a CFD simulation against a ROCOM mixing experiment

A. Grahn, E. Diaz Pescador, S. Kliem, F. Schäfer, T. Höhne[1]

[1]Institute of Fluiddynamics, HZDR, Dresden, Germany

The CFD simulation of a boron dilution scenario is compared with experimental results obtained at the ROCOM test facility. The main features of the scenario are asymmetric, transient mass flow conditions in the affected loops 1 and 2 of a KONVOI-type reactor vessel and reduced density of the underborated coolant slugs fed into the reactor trough the cold legs of both loops.

Boron is a neutron absorber. In pressurized water reactors, it is added as boric acid to the primary loop coolant at varying concentrations over the fuel cycle in order to remove excess reactivity from the reactor core. Under normal conditions with forced circulation, boric acid is homogeneously dissolved in the coolant inventory. In the aftermath of a small break loss of coolant accident (SB LOCA), decay heat is removed from the core by coolant evaporation. Subsequent condensation in the steam generator leads to the formation of underborated liquid coolant that accumulates in the loop seals of the primary circuit. After refilling and restart of natural circulation (NC), slugs of underborated coolant reach the reactor core and give rise to re-criticality and power insertion. Boron dilution was identified as a key issue of PWR safety. Its analysis is part of the design and of the licensing and oversight procedures. Nevertheless, the underlying physical process – single phase natural circulation flow with liquid mixing – is a challenging task for numerical analysis.

EXPERIMENTAL. The ROCOM (ROssendorf COolant Mixing) test facility, formerly located at Helmholtz-Zentrum Dresden-Rossendorf (HZDR), was a 1:5 acrylic glass mock-up of the German four-loop pressurized water reactor KONVOI (Siemens KWU) including the primary coolant circuit. The E2.3 experiment serves as the validation base for the CFD study, its measurement data are publicly available.[1,2] It models asymmetric flow conditions with an ethanol-water mixture representing underborated slugs which arrive at different and time-dependent mass flow rates through vessel inlets of loops 1 and 2; loops 3 and 4 remain unaffected from underboration and mass flow changes. Mixing is measured by means of wire-mesh sensors based on local electrical conductivity.

NUMERICAL STUDY. The mixing process was simulated with the CFD software ANSYS CFX. The computational geometry is shown in Fig. 1. The highlighted sections of loops 1 and 2 hold the entire volume of underborated coolant at the start of transient calculation. Measured and simulated boron distributions in the inlet cross sections indicate that slug and regular coolant are layered one on top of the other (Fig. 2). After opening the valves, the initially vertical concentration front is tipping over because of the different densities of the fluids. In the top half of the pipe, the lighter, underborated slug is moving towards the pressure vessel. Coolant mixing in the downcomer region is shown in Fig. 3. Simulated and experimental distributions resemble each other, presenting similar vortex-like flow structures. In the core inlet plane, underboration dominates the peripheral coolant channels of the upper and lower left quadrants, where loops 1 and 2 are located (Fig. 4). A band of underboration across the central part can be observed, creating two zones of channels with little underboration. The shown distributions suggest that three-dimensional CFD is able to properly simulate buoyancy-driven fluid mixing in the different parts of a pressure vessel.

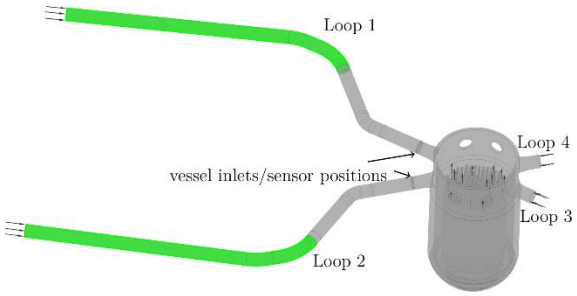

Fig. 1: Computational domain.

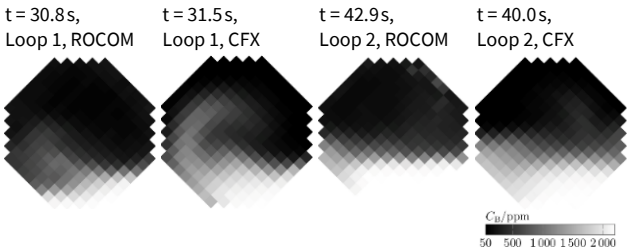

Fig. 2: Experimental and simulated boron distributions at inlet sensor positions at the time of minimum area-averaged concentration.

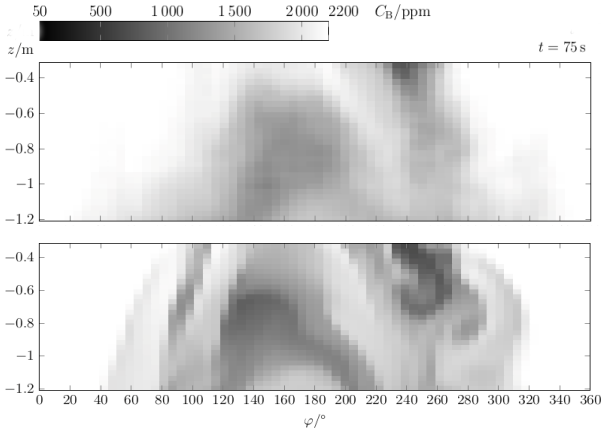

Fig. 3: Experimental (top) and simulated boron distributions in the unwrapped downcomer.

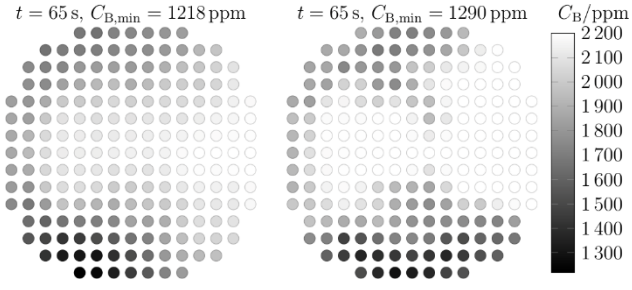

Fig. 4: Boron distributions in the core inlet plane.

[1] Diaz Pescador, E. *et al.* (2020) *Nucl. Eng. Design.* **367**, 110775.
[2] Kliem, S. (2020) URL: https://doi. org/10.14278/rodare.528.

Validation of McSAFE simulation tools

Y. Bilodid, S. Kliem, A. Gommlich

One of main goals of the EU Horizon 2020 McSAFE project was the development of a high-fidelity multiphysics tool combining Monte Carlo neutron transport, subchannel thermalhydraulics and fuel-performance analysis. The final stage of this work was validations *versus* nuclear power plant measurement data. A full-core pin-by-pin depletion of the first operating cycle of a Pre-Konvoi PWR plant was simulated. The critical boron concentration and a set of pin-level neutron flux profiles were compared against measurements with very good agreement.

In the framework of the EU Horizon 2020 McSAFE project, the continuous-energy Monte Carlo code Serpent 2 has been coupled to SUBCHANFLOW (SCF), a subchannel thermal-hydraulics code, and TRANSURANUS (TU), a fuel-performance code (Fig. 1).[1–4] The purpose of this three-code coupling is to perform highly detailed depletion simulations combining high-fidelity neutronics with pin-by-pin thermal-hydraulic and thermomechanic analysis. This methodology allows for the direct calculation of burnup-dependent local safety parameters at pin level for Light Water Reactor (LWR) designs, which is one of the main objectives of the project.

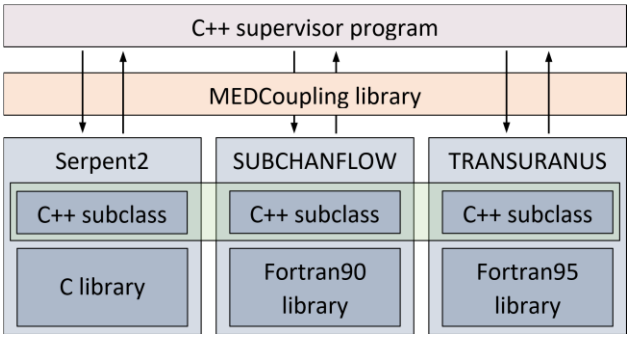

Fig. 1: Software design.

Each code is implemented as a C++ solver class derived from a common base class, defining a standard coupling interface and masking the internal calculation methods, data structures and programming languages. Feedback data is handled through fields defined in unstructured meshes using the MEDCoupling open-source library, which facilitates the data exchange and the code-to-code interpolations. The actual coupling scheme is implemented in a C++ supervisor program using object-oriented features. This methodology is particularly useful for this three-code coupling, since it increases the maintainability and reusability of the code with respect to traditional approaches such as master-slave coupling.

VALIDATION. The validation of Serpent-SCF-TU pin-level burnup capabilities were validated on data from a German Pre-Konvoi PWR Nuclear Power Plant (NPP). For the beginning of the first cycle of operation, numerical results are compared with measured critical boron concentration and neutron flux profiles. To assess the impact of the fuel solution method, the results obtained performing the thermomechanic analysis in TU, *i. e.* with the three-code coupling, are compared with the ones using Serpent-SCF without TU, solving the fuel behavior in SCF with a simplified approach.

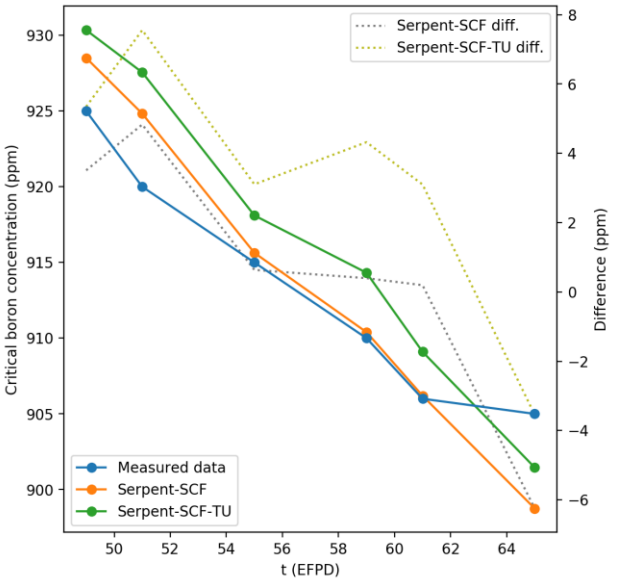

Fig. 2: Critical boron concentration.

RESULTS. The calculated and measured critical boron concentration is shown in Fig. 2. The RMS difference between the results and the experimental data is 3.5 and 4.8 ppm for Serpent-SCF and Serpent-SCF-TU respectively. The deviations with the measurements are well below the acceptability criterion for this type of calculation, which is usually of the order of 50 ppm, and within the typical uncertainties due to specifications and nuclear data. Moreover, the differences between results with and without TU, which are lower than 3 ppm for the whole range, are not significant. These results serve to verify the calculation of global parameters like reactivity, which involve the burnup simulation with equilibrium xenon and the critical boron iteration.

Pin-level neutron flux profiles obtained with Serpent are compared with aeroball measurements and the results are consistent with the experimental data within their statistical uncertainty. These results demonstrate the accuracy of the simulation tool, both in terms of global behavior and of local pin-level parameters.

The fuel solution method has shown minor effect on the neutronics for the amount of burnup considered in this work. The advantage of using TU should be clearer at higher burnup due to phenomena such as the corrosion layer and the behavior of the high-burnup structure, and therefore the current work should be extended to higher depletion.

ACKNOWLEDGEMENTS. This work has been funded from the McSAFE project which is receiving funding from the Euratom research and training program 2014-2018 under grant agreement No 755097.

[1] Leppänen, J. *et al.* (2015) *Ann. Nucl. Energy* **82**, 142–150.
[2] Imke, U. *et al.* (2012) *Sci. Technol. Nucl. Install.* **2012**, ID 465059.
[3] Van Uffelen, P. *et al.* (2008) *J. Nucl. Mater.* **383**, 137–143.
[4] Garcia, M. *et al.* (2020) *Ann. Nucl. Energy* **139**, 107213.

Assessment of ATHLET heat transfer models by comparison to steam condensation experiments performed at the COSMEA test rig

M. Jobst

Steam condensation experiments performed at the HZDR COSMEA test rig are modelled with the system code ATHLET and numerical results are compared to experimental data. With the default Dittus-Boelter correlation applied in ATHLET, the code under-predicts the experimental data significantly. Alternative correlations were applied considering the increased heat transfer on secondary side due to swirl elements.

Future nuclear power plant designs, such as the boiling water reactor KERENA, will be based on passive safety system for decay heat removal which are independent from electrical power. For safety assessment of nuclear power plants, system codes such as AC² ATHLET or RELAP are applied. These codes have been qualified and validated for active thermal-hydraulic circuits, but there is still further work necessary to validate them for passive decay heat removal systems. In order to obtain experimental data for such code validation, the COSMEA (COndenSation test rig for flow Morphology and hEAt transfer studies) has been implemented to the TOPFLOW test facility at HZDR.[1]

EXPERIMENTAL SET-UP. The COSMEA test rig is a slightly inclined tube-in-tube condenser. Its inner condenser tube is made of stainless steel with 43.1 mm inner diameter, 2.6 mm wall thickness and 2,992 mm length.[1] Saturated steam at specified inlet quality is injected at different flow rates and the condensation mass flow rate is measured. The inner tube is cooled by the coaxially arranged outer tube. Experiments have been performed for different steam pressures from 5 to 65 bar.[1]

NUMERICAL MODEL. An ATHLET model of COSMEA has been set up, which includes primary and secondary side of the condenser tube, and thus the major heat transfer processes of the experiment are included: steam condensation on the inside of the tube, heat conduction and convective heat transfer on the outside of the tube. Figure 1 shows the nodalization scheme of the model with axial division of the condensation tube into 100 nodes (control volumes). The Dobson-Chato condensation model is applied on the primary side, the convective heat transfer on the secondary side is calculated according to the Dittus-Boelter correlation.[2]

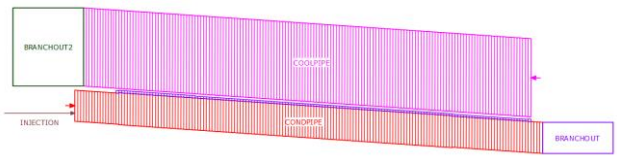

Fig. 1: Nodalization scheme of the COSMEA ATHLET model.

RESULTS. A total of 28 COSMEA tests from the 2018 measurement campaign[1] with different boundary conditions were calculated with ATHLET, from which 17 have been selected for discussion in this paper. Figure 2 shows the calculated condensation mass flow rates (solid lines) for different primary pressures and averaged steam volume flows. The comparison to experimental data (dashed lines) reveals, that ATHLET under-predicts the condensation rates (up to 15 %). In the experiments carried out in 2018, five swirl elements were attached to the secondary side in order to achieve the

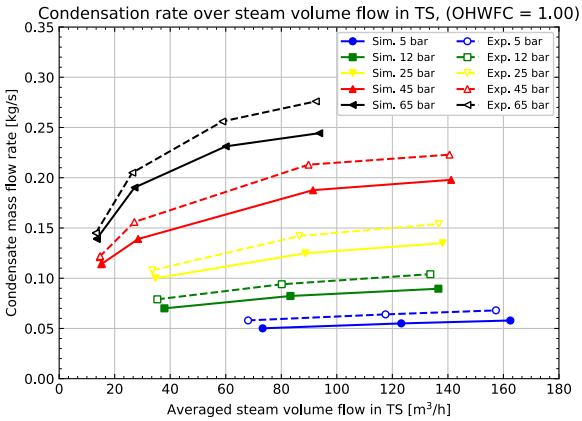

Fig. 2: Condensation mass flow rate depending on steam pressure and averaged steam volume flow in the test section (TS). Heat transfer on secondary side is calculated by Dittus-Boelter correlation.

best possible mixing and a high and uniform heat transfer. By definition, the Dittus-Boelter correlation cannot describe this increase in the heat transfer coefficient. Therefore, the literature was searched for suitable correlations. The swirl elements deflect the flow by about 30°, and this angle decreases with increasing distance from the swirl element. The correlations after Cavazzuti and Corticelli describe both the decrease of the swirl angle and the dependence of the Nusselt number on the swirl angle.[3] Thus, an average increase of the heat transfer coefficient compared to the Dittus-Boelter correlation of 40 % was determined. This factor can be accounted for the ATHLET input data set and a much better agreement with the measurement results was obtained after recalculation (Fig. 3).

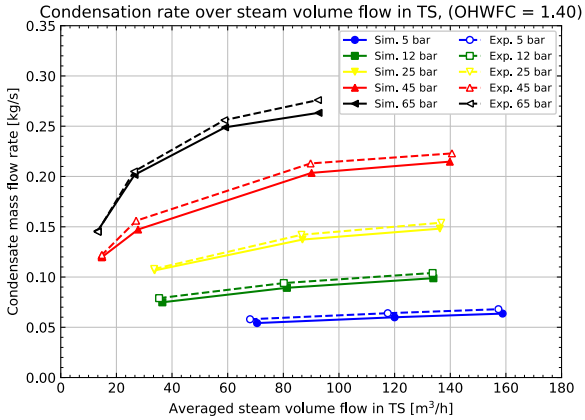

Fig. 3: Condensation mass flow rate depending on steam pressure and averaged steam volume flow in the test section. Improved heat transfer on secondary side due to swirl elements is taken into account by application of factor OHWFC = 1.40.

ACKNOWLEDGEMENTS. The author expresses his gratitude to the colleagues of Institute of Fluid Dynamics for providing the test facility description and experimental data. This work was funded by the German Federal Ministry of Economic Affairs and Energy (BMBF) with the grant number 02NUK041B on the basis of a decision by the German Bundestag. The responsibility for the content of this publication lies with the author.

[1] Bieberle, A. *et al.* (2020) *Nucl. Eng. Des.* **361**, 110553.
[2] ATHLET 3.2 documentation „Models and methods".
[3] Cavazzuti, M. *et al.* (2017) *Appl. Therm. Eng.* **120**, 517–529.

Investigations on the multiscale and multi-physics dynamic behavior of German PWRs during reactivity accidents

E. Diaz Pescador,[1] F. Schäfer, Y. Bilodid, S. Kliem

[1]Technische Universität Dresden, Dresden, Germany

Despite the high degree of maturity reached by system codes in nuclear safety research, the accurate simulation of complex accident sequences, such as reactivity accidents still presents several gaps. The main uncertainties arise from the correct modelling of asymmetries in the reactor coolant system (RCS) together with local thermohydraulic phenomena in the vessel and reactivity feedback effects in the core. The accurate representation of such phenomena requires a combined multi-physics and multiscale approach. This is investigated with ATHLET-DYN3D, exploiting the 3-D Neutron Kinetics of DYN3D together with the 3-D features of ATHLET 3D-Module.

The present project is enclosed in the KEK (*Kompetenzerhalt in der Kerntechnik*) initiative, which fosters the preservation of the competence on safety-related problems in nuclear technology in Germany. The main goal is the development and application of new and improved reactor models for the investigation of the early in-vessel phase of hypothetical core melt scenarios with an eventual asymmetric cold-water injection into the RCS. The development of advanced reactor configurations in ATHLET to enhance the simulation of large 3-D effects in vessel and piping, together with multi-physics calculations by ATHLET-DYN3D fosters a more realistic simulation of complex accident sequences. Investigation on the effectiveness of the implementation of bleed and feed procedures is also foreseen in the project.[1] The investigation is applied to generic German PWRs of Konvoi type.

VALIDATION OF ATHLET 3D-MODULE. During the project, the 3D-Module of ATHLET has been validated for the simulation of coolant mixing under buoyancy-driven flow conditions based on the experiments E2.3,[2] T1.1 and T2.1[3] conducted at the ROCOM test facility. With this aim, an ATHLET model of ROCOM has been developed and additional sensitivity runs have been performed based on the spatial resolution as well as verification of boron transport models. The results from the validation exercises have been successful and have demonstrated the ability of ATHLET to simulate coolant mixing during boron dilution and overcooling conditions.[4]

ACCIDENT ANALYSES. Two postulated reactivity accident scenarios have been selected in the project, one consisting of a main steam line break (MSLB) with double-guillotine break in steam generator 1 and a small-break loss of coolant accident (SBLOCA) with inherent boron dilution. The break in the SBLOCA is located in cold leg 1 and accounts for 44 cm². The analysis of the SBLOCA sequence is divided into two different parts, one focusing on the study of inherent boron dilution, whereas second part models a simultaneous loss of AC power meant to investigate the plant dynamic response during the implementation of bleed and feed procedures to prevent core meltdown. An ATHLET model of a Generic PWR of Konvoi type has been developed for the analyses with 1-D and 3-D vessel topologies, meant for comparison of the results between both.

RESULTS AND DISCUSSION. The results from the MSLB study show that even with conservative boundary conditions, in none of the runs a power surge takes place in the core. The negative reactivity from the control rods exceeds the positive reactivity by the Doppler and moderator density feedback effects. The results with the traditional 1-D vessel model show a temperature difference of about 40 K with respect to the validated 3-D approach, which in turn leads to higher reactivity insertion by the Doppler. Regarding the study of SBLOCA with inherent boron dilution, some important insights are:

- Large accumulation of condensate in U-tubes and loop seals (up to 30,000 kg) under failure of safety systems together with high thermal loads in steam generators.
- Counter-current flow limitation (CCFL) and flooding limit exceeded in hot legs and U-Tubes.
- Very effective mixing of condensate with water from the safety systems in the loop seals and cold legs.
- Increase in the boron concentration in the core along with evaporation. Acts as a safety inherent mechanism.

On the other hand, implementation of bleed and feed procedures show grace times of 1 h and 2 h during primary and secondary side depressurization, respectively. Feeding the secondary and primary sides with an external pump has proven to be a very efficient mechanism to ensure long-term core cooling and prevent core meltdown, being secondary feeding the preferred option.

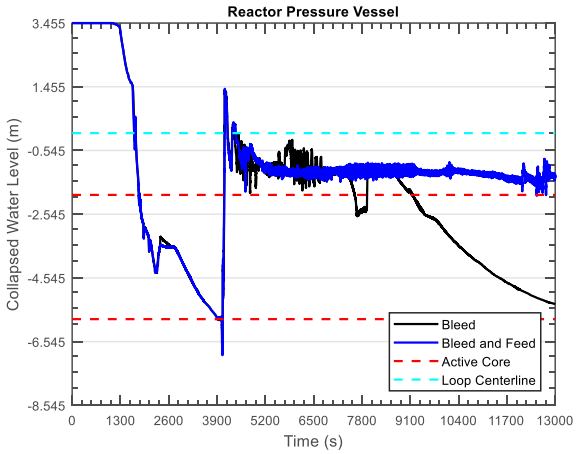

Fig. 1: Vessel water level during secondary bleed and feed.

ACKNOWLEDGEMENTS. This project is funded by the German Federal Ministry for Economic Affairs and Energy (BMWi) with grant number 1501540.

[1] Roth-Seefrid, H. *et al.* (1994) *Nucl. Eng. Des.* **148**, 133–150.
[2] Kliem, S. *et al.* (2006) Institute Report FZD\FWS\2006\03.
[3] Kliem, S. *et al.* (2012) Institute Report HZDR\FWO\2012\03.
[4] Diaz Pescador, E. *et al.* (2020) *Nucl. Eng. Des.* **367**, 110776.

Extension of ATHLET/DYN3D to SFRs: Verification against DYN3D on the Phénix reactor core

V. A. Di Nora

The ATHLET/DYN3D code is currently under extension for being applied to the analysis of entire sodium-cooled fast reactors (SFRs) systems. In this regard, modifications have been implemented on the code-system and then tested. This work provides an overview of the verification tests executed on the Phénix reactor core and the related outcomes obtained.

INTRODUCTION AND MOTIVATION. The DYN3D code is a three-dimensional neutron kinetic (NK) solver equipped with built-in thermal-hydraulic (TH) and fuel rod behavior modules.[1] The code has been currently extended to the safety analysis of SFRs cores. The extension includes a newly implemented thermal-mechanical (TM) module that accounts for radial diagrid and axial fuel thermal expansions.[2] The upgraded DYN3D was validated against the IAEA benchmark devoted to the Phénix natural circulation (NC) test.[3, 4] To further broaden the applicability of the code to safety analyses of whole SFR systems, DYN3D should be coupled with a TH code able to model the liquid sodium as a coolant. The TH code ATHLET was chosen for the purpose. A previous coupled ATHLET/DYN3D version was already developed and validated for LWRs.[5] However, the application of the code system to SFRs has required the update and extension of the existing code coupling routines.
Preliminarily to the application onto whole SFR plants, the modified code version has to be tested. The prediction capabilities of the new ATHLET/DYN3D and DYN3D standalone are expected to be equivalent or comparable. The current research aims to verify such an expectation through the benchmark of the codes conducted at the core level of the Phénix SFR.

TEST DESCRIPTION AND METHODOLOGY. The Phénix reactor was a small-size SFR prototype with a MOX-loaded kernel subdivided into inner and outer core fissile regions, radial blanket, and peripheral reflector. On the occasion of the reactor shut-down, in 2009, several experiments were conducted, including the NC test. For such an experiment, the reactor was stabilized at a power level of 120 MWth. The test was then initiated by manually inducing the steam generators' dry out, originating thus a loss of heat sink scenario. Details on core geometry, material compositions, and system perturbations are available from the benchmark specifications. The verification is conducted by:

- Considering as references the static and transient DYN3D solutions of the NC test, respectively found at time zero and along the first 458 seconds of the test.
- Developing an ATHLET/DYN3D model of the Phénix NC test, equivalent to the existing DYN3D model, and comparing the related calculations results against the references. For the static analysis, the study compares the region-wise temperature distributions of fuel, cladding, and sodium. Evolutions of power, reactivity components, and the average temperatures of fissile and fertile channels are then benchmarked for the transient analysis.

RESULTS. Table 1 summarizes the results of the verification under static conditions. The fuel, clad and sodium temperature distributions are in good agreement with each other with errors below 1.5 %. The best agreement is found for the sodium (Na) distribution which maximum error was 0.2 %. Figure 1 shows the comparison of transient solutions against the reference. Figures 1a) and b) show the evolutions of power and reactivity components, namely, Doppler, Sodium density (Na-ϱ), clad-driven fuel axial expansion, and radial diagrid expansion. The curves are in good agreement and basically overlap. Figure 1c) shows the temperature evolutions of fuel, clad, and sodium averaged within the inner and outer core regions. Similarly, Fig. 1d) presents the average temperature trends of the blanket materials. Even in this case, the curves are very close to each other.

Tab. 1: Phénix static comparison ATHLET/DYN3D against DYN3D: RMS error on temperature distributions.

Material	Inner core	Outer core	Blanket
Fuel	0.59	0.65	0.63
Clad	1.31	1.20	0.61
Na	0.16	0.14	0.08

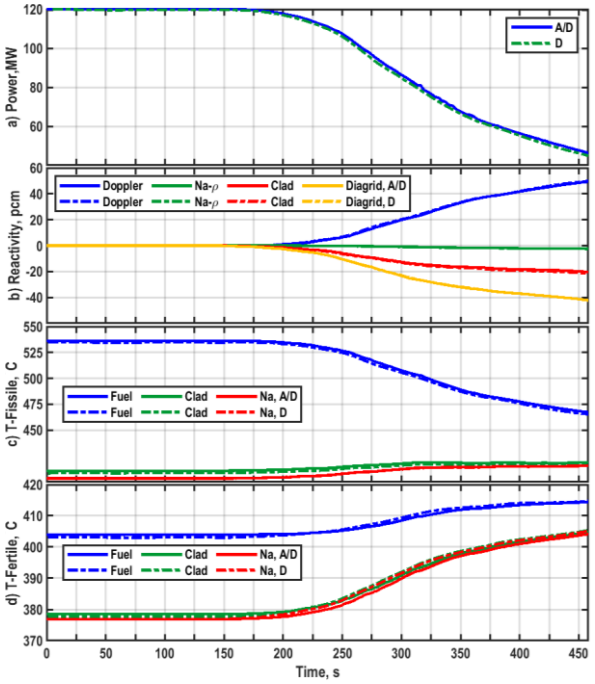

Fig. 1: Phénix transient comparison evolutions of power, reactivity, and temperatures of core materials.

CONCLUSIONS. The current benchmark activity performed at the Phénix core level demonstrates that either using ATHLET/DYN3D or DYN3D-standalone, practically equivalent results are obtained. Consistent and close temperature distributions were found under static conditions, and excellent agreements were observed on the transient evolutions of power, reactivity, and temperatures of core materials. Such findings lay the foundations for applying ATHLET/DYN3D to the analyses of the entire Phénix primary system.

[1] Rohde, U. *et al.* (2016) *Prog. Nucl. Energy* **89**, 170–190.
[2] Nikitin, E. *et al.* (2018) *Ann. Nucl. Energy* **119**, 382–389.
[3] Nikitin, E. *et al.* (2018) *Ann. Nucl. Energy* **119**, 390–395.
[4] IAEA, (2013) IAEA-TECDOC-1703, Vienna, Austria.
[5] Kozmenkov, Y. *et al.* (2015) *Ann. Nucl. Energy* **84**, 153–165.

New developments of the Monte Carlo code TRAMO and their validations on experiments of Russian VVER-1000 reactor equipment

S. Baier,[1] J. Konheiser, P. Borodkin[2]

[1]Technische Universität Dresden, Dresden, Germany; [2]Scientific and Engineering Centre for Nuclear and Radiation Safety, Moscow, Russia

The Russian Partner SEC NRS (Scientific and Engineering Centre for Nuclear Radiation Safety) is very much interested in using TRAMO as an independent computer code for validation and verification of activity and shielding studies at Russian nuclear power plants. For this purpose, TRAMO and its auxiliary programs have been further developed in such a way that the Russian partner is now in principle able to perform independent calculations. This paper gives a brief overview of these development steps.

TRAMO[1] is a Monte Carlo code for three-dimensional geometries developed at the Helmholtz-Zentrum Dresden-Rossendorf and was optimized especially for structures of a nuclear power plant. It can be used to calculate neutron and gamma fluences in the reactor pressure vessel and its internals. In principle, however, other geometries are also conceivable. The possibility of obtaining results with sufficient statistical accuracy in a reasonable time is ensured by various optimization methods. These include variance reducing methods such as weight window, Russian roulette and implicit capture as well as source biasing. The heart of the optimization, however, is the auxiliary program TRAWEI,[1] which generates spatial and energy-dependent weight factors precisely matched to the geometry. For a calculation with TRAMO, additional input variables are necessary. In detail, these are the source distribution, which is supplemented by a pin distribution if necessary, and various cross-section data based on common nuclear databases such as ENDF-B/VII or JENDL-4.0.[2, 3]

Within the framework of the scientific-technical cooperation between Germany and Russia in the field of the peaceful use of nuclear energy on the basis of an agreement of 1987, there is a long-standing and intensive cooperation with the Russian partner, which is reflected in many joint projects. In the current project, TRAMO has to be further developed and improved in such a way that it is possible for the Russian partner to carry out fluence calculations on its own, since Russian nuclear safety regulations require calculations with an independent code.[4, 5] For this purpose, a number of necessary steps have been agreed upon.

First of all, the TRAMO code itself was transferred into a modern Fortran and contemporary programming structures, so that on the one hand the readability was increased and on the other hand the possibility of further model development (also by externals) was given at all. Furthermore, the Russian partner sent us all material compositions of relevant VVER-440 and VVER-1000 reactors, so that an extensive database with cross section data and scattering matrices in two energy group structures was generated. A detailed geometry model was provided for one reference case each of a VVER-440 (Kola-3) and VVER-1000 (Rovno-3). Various material samples (monitors) are located at the outside surface of the reactor pressure vessel, which can be used to experimentally determine the neutron fluence within a cycle. On their basis, we developed a generalized TRAMO input model with special focus on the regions of the monitors. For each horizontal and vertical set of monitors, TRAWEI was used to generate corresponding weight data sets, and TRAMO was used to generate source biasing data by activating and deactivating specific source regions.

To make it easier for the Russian partner to handle the code and the numerous helper programs, a shell script was developed. It regulates the whole process of a TRAMO calculation including input and output steps and includes in detail the selection of the reactor type, the orientation of the monitors, the positions of them (height and angle), the energy group structure and a selection of a 60° sector of the VVER reactor. In addition, global settings such as reactor power can still be specified in a simplified input file. The script reads and generates an appropriate base input file, selects the correct weight data sets, source biasing data and effective cross sections, and converts the source and pin data distribution to TRAMO format. Then, the actual calculation is performed and a detailed and a reduced output file are written. With the help of a data evaluation program, the fluences at the monitor positions are interpolated if necessary and converted into measurable quantities such as reaction rates. The entire software package, including the necessary data and a manual for the use and explanation of the input variables, was handed over to the Russian partner for independent use.

To verify the correct implementation of the new input models, the existing models of the reference cases mentioned above were adjusted and recalculated. The fluence values were found to be largely in agreement. Thereupon, the VVER-1000 model was adapted to the Kalinin-4 nuclear power plant. The active zone of the core is slightly larger than at Rovno, otherwise the design is almost identical. One horizontal and one vertical arrangement of monitors each was entered into the model according to the specifications of the Russian partner, and corresponding calculations were performed. The fluences agree well with those of Rovno-3. The deviations amount to a maximum of 10 %. The comparison with the experimentally obtained data will be performed by the Russian partner and is expected soon.

An outline for a follow-up project has been submitted and has successfully passed the preliminary review. Within this, the TRAMO package is to be turned into a holistic tool for reactor dosimetry and activity calculations. Besides the model development by introducing elliptical bodies, TRAWEI shall be integrated directly into TRAMO, so that the user can determine whether weight data sets shall be calculated or whether they are already available, the possibility for parallelization (and thus for a considerable increase in computing speed) shall be created and a graphical input tool shall facilitate the handling by users.

ACKNOWLEDGEMENTS. This project is funded by the German Federal Ministry of Economic Affairs and Energy, Grant No. 1501531

[1] Barz, H.-U., Konheiser, J. (1998) *Report FZR-245*.
[2] Chadwick M.B. *et al.* (2006) *Nuclear Data Sheets* **107**, 2931–3060.
[3] Shibata, K. *et al.* (2011) J. *Nucl. Sci. Technol.* **48**, 1–30.
[4] Baier, S. *et al.* (2017) *Proceedings of ISRD-16*, May 07–12, 2017, Santa Fe, U.S.A.
[5] The List of Basic Legal Statements and Regulatory Standards used by Gosatomnadzor of Russia for State Regulation of Safety in the Field of Use of Atomic Energy. P-01–01–2011, Rostechnadzor, Moscow, Russia, 2011 (in Russian).

Development of a generally usable weight window generator using the TRAWEI code

P. Yadav, R. Rachamin, J. Konheiser, S. Baier[1]

[1]Technische Universität Dresden, Dresden, Germany

Nuclear decommissioning is currently one of the most important activities of the nuclear industry. The optimal planning of the decommissioning requires good estimations of the neutron activation distribution in the structural materials of the nuclear power plant. These estimations are associated with deep penetration problems, which can be solved using Monte-Carlo (MC) codes such as the MCNP. In Monte-Carlo codes, a large number of simulated particles with corresponding long computational times are usually needed to obtain statistically reliable results in volumes far away from the source. Therefore, variance reduction techniques are required to achieve highly accurate results in a reasonable computation time. Weight window is one of the most widely used variance reduction techniques for MC deep penetration problem calculations. However, in complicated shielding calculations, the estimation of optimal weight window parameters is quite challenging. The present work is aimed to develop an optimal weight window generator program based on Recursive Monte-Carlo (RMC) method, which is to be tested in neutron fluence calculations in a German Pressurized Water Reactor (PWR) decommissioning study.

The MCNP code has a build-in weight-window parameters generator.[1] In complicated shielding calculations the generator outputs zero weight windows. Several approaches have been suggested and applied to solve this problem and achieve more meaningful (non-zero) weight window parameters, such as the MAGIC method,[2] Density method, and Distributed method. However, those approaches are not straightforward and require iterative calculations. Therefore, the present work aims to develop an optimal and direct zone-weights parameters generator based on Recursive Monte-Carlo (RMC) method. The development is based on the TRAWEI code.[3] The developed generator will output space- and energy-dependent mesh-based zone weights, which can directly be used with the MCNP code.

THE RECURSIVE MONTE CARLO METHOD. The RMC method is specifically applied for deep-penetration problems, such as in the case of decommissioning of nuclear power plants.[4] The method is used to calculate the importance functions of a focus region, *i.e.*, the probabilities that a neutron from one cell will reach the result region, using already generated results from the neighborhood cells and lower energy groups. At this point, the influence on the target zone is known, and the value calculated up to this point is weighted accordingly. Based on the results already obtained, the influence functions of the next cells are successively determined. The Monte-Carlo play of a particle can be interrupted when it crosses a cell with known influence. From this point on, the influence on the target zone is known and can be used for the calculation. By skillfully sequencing the cell calculations, the calculation can be accelerated. The same procedure is used for the down scattering of neutrons, starting with the lowest energy group and continuing with the next higher one. The already existing results can then be used for down scattering. The weights are estimated by taking the reciprocal values of the importance function. This procedure ensures that for each volume element (cell), a weight value is determined and no iteration is necessary.

THE TRAWEI CODE. The TRAWEI code was developed at Helmholtz-Zentrum Dresden-Rossendorf (HZDR) to calculate cell weights, which can be used in the TRAMO code. The TRAMO and TRAWEI codes are 3D multi-group Monte-Carlo codes applicable for typical reactor geometries.[3] The codes were specially developed for solving particle transport problems in the field of reactor dosimetry and shielding calculations. They use various nuclear data files (ENDF/B-VII, JEFF3.3, own data supply). TRAWEI is an RMC code that is responsible for generating the weights. The weights can be used directly in TRAMO. Currently, an external weight transfer program is developed to transfer the TRAWEI weights also for MCNP calculations. A schematic view of the development structure is shown in Fig. 1.

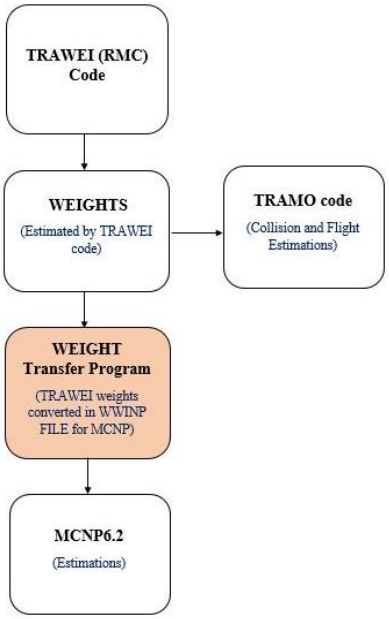

Fig. 1: Utilization of TRAWEI weights for Monte Carlo calculations.

ONGOING DEVELOPMENT. The developed weight window generator program will be used together with the MCNP code for German PWRs decommissioning studies. Several realistic geometries have been prepared to validate the accuracy of the developed program. The preparation of the TRAWEI code has been completed and the development of the transfer programs has been initiated. First test calculations have been carried out. They will be evaluated by comparison with existing weight window generators, *e.g.*, MCNP's weight-window generators.

ACKNOWLEDGEMENTS. This work is funded by the Federal Ministry of Education and Research (BMBF) under contract number 15S9409A.

[1] Goorley, T. *et al.* (2012) *Nucl. Technol.* **180**, 298–315.
[2] Pan, Q. & Wang, K. (2019) *Ann. Nucl. Energy* **128**, 171–180.
[3] Barz, H.-U. & Konheiser, J. (1998) *Report FZR-245.*
[4] Goldstein, M. & Greenspan, E. (1980) *Report No. ORNL/RSIC—44.*

- Articles (peer-reviewed)
- Editorial Work
- Further Contributions
- Patent
- Oral Presentations
- Theses

ARTICLES (PEER-REVIEWED)

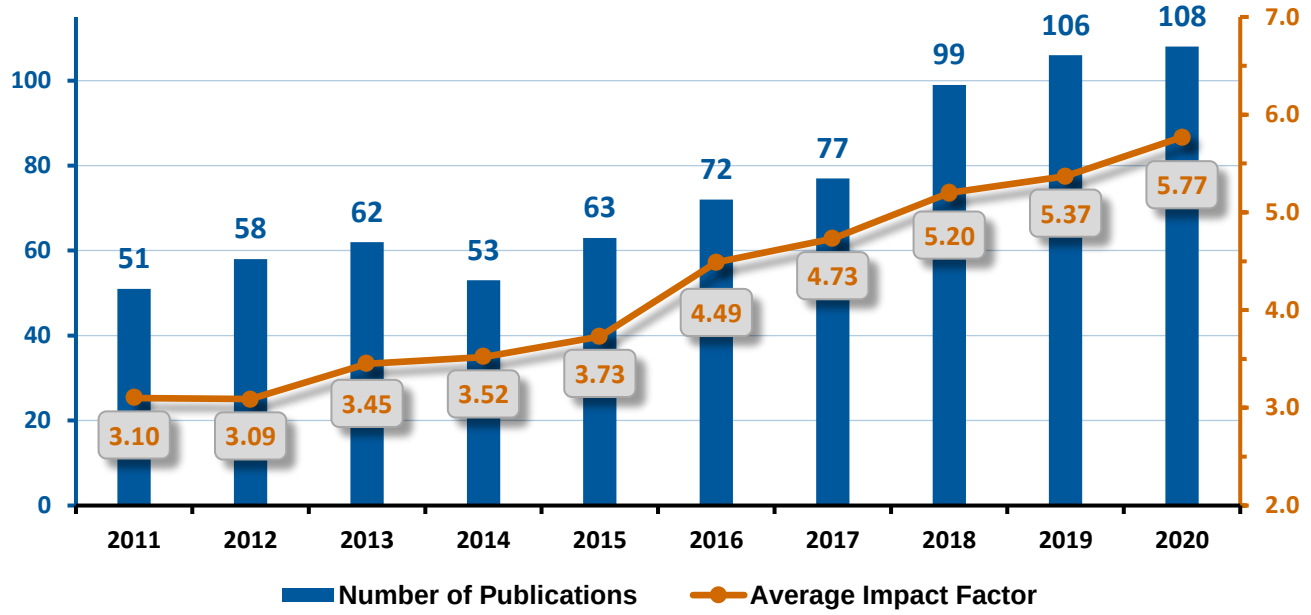

Statistics on the publication activity of the Institute of Resource Ecology (IRE) within the last 10 years. The diagram considers peer-reviewed articles that were published under primary responsibility of the institute. Note that the given impact factors based on data from 2019. The annual update might change the statistics retrospectively.
The following compilation provides 113 peer-reviewed articles published in 2020 representing any contribution of members of the Institute of Resource Ecology.

Ahmed, S. S.; Hippmann, S.; Roode-Gutzmer, Q. I.; Fröhlich, P.; Bertau, M.
Alginite rock as effective demulsifier to separate water from various crude oil emulsions
Colloids and Surfaces A: Physicochemical and Engineering Aspects 611, 125830 (2020).

An, Y.; Faria Oliveira, A.; Brumme, T.; Kuc, A. B.; Heine, T.
Stone-Wales defects cause high proton permeability and isotope selectivity of single-layer graphene
Advanced Materials 32, 2002442 (2020).

Arcudia, J.; Kempt, R.; Eduardo Cifuentes-Quintal, M.; Heine, T.; Merino, G.
Blue Phosphorene Bilayer Is a Two-Dimensional Metal and an Unambiguous Classification Scheme for Buckled Hexagonal Bilayers
Physical Review Letters 125, 196401 (2020).

Bacic, V.; Heine, T.; Kuc, A. B.
Analytical Approach to Phonon Calculations in the SCC-DFTB Framework
Journal of Chemical Physics 153, 144109 (2020).

Bahmani, M.; Faghihnasiri, M.; Lorke, M.; Kuc, A. B.; Frauenheim, T.
Electronic Properties of Defective MoS_2 Monolayers Subject to Mechanical Deformations: A First-Principles Approach
Physica Status Solidi (B) 257, 1900541 (2020).

Batra, K.; Zahn, S.; Heine, T.
Benchmark of Simplified Time-Dependent Density Functional Theory for UV–Vis Spectral Properties of Porphyrinoids
Advanced Theory and Simulations 3, 1900192 (2020).

Bauters, S.; Scheinost, A. C.; Schmeide, K.; Weiß, S.; Dardenne, K.; Rothe, J.; Mayordomo Herranz, N.; Steudtner, R.; Stumpf, T.; Abram, U.; Butorin, S.; Kvashnina, K. O.
Signatures of Technetium Oxidation States: A New Approach
Chemical Communications 56, 9608–9611 (2020).

Belskaya, O. B.; Zaikovskii, V. I.; Gulyaeva, T. I.; Talsi, V. P.; Trubina, S. V.; Kvashnina, K. O.; Nizovskii, A. I.; Kalinkin, A. V.; Bukhtiyarov, V. I.; A. Likholobov, V.
The effect of Pd(II) chloride complexes anchoring on the formation and properties of $Pd/MgAlO_x$ catalysts
Journal of Catalysis 392, 108–118 (2020).

Berardi, S.; Kesavan, J. K.; Amidani, L.; Meloni, E. M.; Marelli, M.; Boscherini, F.; Caramori, S.; Pasquini, L.
Better Together: Ilmenite/Hematite Junctions for Photoelectrochemical Water Oxidation
ACS Applied Materials and Interfaces 12, 47435–47446 (2020).

Bergner, F.; Hernandez-Mayoral, M.; Heintze, C.; Konstantinovic, M. J.; Malerba, L.; Pareige, C.
TEM observation of loops decorating dislocations and resulting source hardening of neutron-irradiated Fe-Cr alloys
Metals 10, 147 (2020).

Bilodid, Y.; Fridman, E.; Lötsch, T.
X2 VVER-1000 benchmark revision: fresh HZP core state and the reference Monte Carlo solution
Annals of Nuclear Energy 144, 107558 (2020).

Bollermann, T.; Fischer, C.
Temporal evolution of dissolution kinetics of polycrystalline calcite
American Journal of Science 320, 53–71 (2020).

Bonato, L.; Virot, M.; Dumas, T.; Mesbah, A.; Dalodière, E.; Dieste Blanco, O.; Wiss, T.; Le Goff, X.; Odorico, M.; Prieur, D.; Roßberg, A.; Venault, L.; Dacheux, N.; Moisy, P.; Nikitenko, S. I.
Probing the Local Structure of Nanoscaled Actinide Oxides: A Comparison between PuO_2 and ThO_2 Nanoparticles Rules out PuO_{2+x} Hypothesis
Nanoscale Advances 2, 214–224 (2020).

Boulanger, N.; Kuzenkova, A. S.; Iakunkov, A.; Romanchuk, A. Y.; Trigub, A. L.; Egorov, A. V.; Bauters, S.; Amidani, L.; Retegan, M.; Kvashnina, K. O.; Kalmykov, S. N.; Talyzin, A. V.
Enhanced Sorption of Radionuclides by Defect-Rich Graphene Oxide
ACS Applied Materials and Interfaces 12, 45122–45135 (2020).

Cametti, G.; Scheinost, A. C.; Churakov, S. V.
Structural Evolution of Ag-LEV Zeolite upon Heating: an in situ Single-Crystal X-ray Diffraction (SC-XRD) and X-ray Absorption Spectroscopy (XAS) Study
ACS Omega 5, 31774–33178 (2020).

Castin, N.; Bonny, G.; Bakaev, A.; Bergner, F.; Domain, C.; Hyde, J. M.; Messina, L.; Radiguet, B.; Riddle, N.; Malerba, L.
The dominating mechanisms for the formation of solute-rich clusters in steels under irradiation
Materials Today Energy 17, 100472 (2020).

Chaudhari, T.; Mallampudi, N.; Bansal, D.; Mohapatra, D.; Tandon, V.
Protecting-Group-Directed Diastereo- and Enantioselective Approach to Substituted Chiral Tetrahydropyrroloquinolines
European Jounal of Organic Chemistry 18, 2771–2780 (2020).

Das, A.; Chekhonin, P.; Altstadt, E.; Bergner, F.; Heintze, C.; Lindau, R.
Microstructural characterization of inhomogeneity in 9Cr ODS EUROFER steel
Journal of Nuclear Materials 533, 152083 (2020).

Das, A.; Chekhonin, P.; Altstadt, E.; McClintock, D.; Bergner, F.; Heintze, C.; Lindau, R.
Microstructure and fracture toughness characterization of three 9Cr ODS EUROFER steels with different thermo-mechanical treatments
Journal of Nuclear Materials 542, 152464 (2020).

Demnitz, M.; Hilpmann, S.; Lösch, H.; Bok, F.; Steudtner, R.; Patzschke, M.; Stumpf, T.; Huittinen, N. M.
Temperature-dependent luminescence spectroscopic investigations of U(VI) complexation with the halides F^- and Cl^-
Dalton Transactions 49, 7109–7122 (2020).

Diaz Pescador, E.; Grahn, A.; Kliem, S.; Schäfer, F.; Höhne, T.
Advanced modelling of complex boron dilution transients in PWRs – Validation of ATHLET 3D-Module against the experiment ROCOM E2.3
Nuclear Engineering and Design 367, 110776 (2020).

Eibl, M.; Shaw, S.; Prieur, D.; Roßberg, A.; Wilding, M. C.; Hennig, C.; Morris, K.; Rothe, J.; Stumpf, T.; Huittinen, N. M.
Understanding the local structure of Eu^{3+} and Y^{3+} stabilized zirconia – Insights from luminescence and X–ray absorption spectroscopic investigations
Journal of Materials Science 55, 10095–10120 (2020).

Epifano, E.; Prieur, D.; Martin, P. M.; Guéneau, C.; Dardenne, K.; Rothe, J.; Vitova, T.; Wiss, T.; Dieste, O.; Konings, R. J. M.; Manara, D.
Melting behaviour of uranium-americium mixed oxides under different atmospheres
The Journal of Chemical Thermodynamics 140, 105896 (2020).

Epifano, E.; Vauchy, R.; Lebreton, R.; Lauwerier, F.; Joly, A.; Scheinost, A.; Guéneau, C.; Valot, C.; Martin, P. M.
On the O-rich domain of the U-Am-O phase diagram
Journal of Nuclear Materials 531, 151986 151986 (2020).

Estevenon, P.; Kaczmarek, T.; Rafiuddin, M. R.; Welcomme, E.; Szenknect, S.; Mesbah, A.; Moisy, P.; Poinssot, C.; Dacheux, N.
Soft hydrothermal synthesis of hafnon, $HfSiO_4$
Crystal Growth & Design 20, 1820–1828 (2020).

Fichter, S.; Kaufmann, S.; Kaden, P.; Brunner, T. S.; Stumpf, T.; Roesky, P. W.; März, J.
Enantiomerically pure Tetravalent Neptunium Amidinates: Synthesis and Characterization
Chemistry - A European Journal 26, 8867–8870 (2020).

Fischer, C.; Arvidson, R. S.
Preface of a special issue of the American Journal of Science
American Journal of Science 320, 3–6 (2020).

Fischer, S.; Krause, T.; Lederer, F.; Merroun, M. L.; Shevchenko, A.; Hübner, R.; Stumpf, T.; Jordan, N.; Jain, R.
***Bacillus safensis* JG-B5T affects the fate of selenium by extracellular production of colloidally less stable nanoparticles**
Journal of Hazardous Materials 384, 121146 (2020).

Fridman, E.; Álvarez-Velarde, F.; Romojaro-Otero, P.; Tsige-Tamirat, H.; Jiménez-Carrascosa, A.; García-Herranz, N.; Bernard, F.; Gregg, R.; Krepel, J.; Massara, S.; Poumerouly, S.; Girardi, E.; Mikityuk, K.
Neutronic analysis of the European Sodium Fast Reactor: Part I - fresh core results
Journal of Nuclear Engineering and Radiation Science (2020).

Fridman, E.; Álvarez-Velarde, F.; Romojaro-Otero, P.; Tsige-Tamirat, H.; Jiménez-Carrascosa, A.; García-Herranz, N.; Bernard, F.; Gregg, R.; Krepel, J.; Massara, S.; Poumerouly, S.; Girardi, E.; Mikityuk, K.
Neutronic analysis of the European Sodium Fast Reactor: Part II - burnup results
Journal of Nuclear Engineering and Radiation Science (2020).

Fridman, E.; Huo, X.
Dynamic simulation of the CEFR control rod drop experiments with the Monte Carlo code Serpent
Annals of Nuclear Energy 148, 107707 (2020).

Fridman, E.; Valtavirta, V.; Aufiero, M.
Nuclear Data Sensitivity and Uncertainty Analysis of Critical VENUS-F Cores with the Serpent Monte Carlo Code
Annals of Nuclear Energy 138, 107196 (2020).

Garcia, M.; Tuominen, R.; Gommlich, A.; Ferraro, D.; Valtavirta, V.; Imke, U.; van Uffelen, P.; Mercatali, L.; Sanchez, V.; Leppänen, J.; Kliem, S.
A Serpent2-SUBCHANFLOW-TRANSURANUS coupling for pin-by-pin depletion calculations in Light Water Reactors
Annals of Nuclear Energy 139, 107213 (2020).

Gerber, E.; Romanchuk, A.; Pidchenko, I.; Amidani, L.; Roßberg, A.; Hennig, C.; Vaughan, G.; Trigub, A.; Egorova, T.; Bauters, S.; Plakhova, T.; Hunault, M.; Weiß, S.; Butorin, S.; Scheinost, A. C.; Kalmykov, S.; Kvashnina, K. O.
The missing pieces of the PuO_2 nanoparticles puzzle
Nanoscale 12, 18039–18048 (2020).

Ghosh, S.; Nakada, A.; Springer, M.; Kawaguchi, T.; Suzuki, K.; Kaji, H.; Baburin, I.; Kuc, A. B.; Heine, T.; Suzuki, H.; Abe, R.; Seki, S.
Identification of Prime Factors to Maximize the Photocatalytic Hydrogen Evolution of Covalent Organic Frameworks
Journal of the American Chemical Society 142, 9752–9762 (2020).

Griebsch, A.; Matschiavelli, N.; Lewandowska, S.; Schmidtke, K.
Presence of *Bradyrhizobium sp.* under continental conditions in Central Europe
Agriculture 10, 446 (2020).

Gu, B.; Chekhonin, P.; Schaarschuch, R.; Oertel, C. G.; Xin, S. W.; Ma, C.L.; Zhou, L.; Gan, W. M.; Skrotzki, W.
Microstructure, texture and hardness of a metastable β-titanium alloy after bar-rolling and annealing
Journal of Alloys and Compounds 825, 154082 (2020).

Heidsiek, M.; Butscher, C.; Blum, P.; Fischer, C.
Small-scale diagenetic facies heterogeneity controls porosity and permeability pattern in reservoir sandstones
Environmental Earth Sciences 79, 425 (2020).

Henfling, S.; Kempt, R.; Klose, J.; Kuc, A. B.; Kersting, B.; Krautscheid, H.
The dithiol-dithione tautomerism of 2,3-pyrazinedithiol in the synthesis of copper and silver coordination compounds
Inorganic Chemistry (2020).

Hennig, T.; Stockmann, M.; Kühn, M.
Simulation of diffusive uranium transport and sorption processes in the Opalinus Clay
Applied Geochemistry 123, 104777 (2020).

Herzog, S. D.; Kvashnina, K.; Persson, P.; Kritzberg, E.
Organic Iron Complexes Enhance Iron Transport Capacity along Estuarine Salinity Gradients
Biogeosciences 17, 331–344 (2020).

Hieckmann, E.; Mühle, U.; Chekhonin, P.; Zschech, E.; Gambino, J.
Investigations of internal stresses in high-voltage devices with deep trenches
Journal of Vacuum Science & Technology B 38, 064004 (2020).

Höhne, T.; Kliem, S.
Detailed Simulation of the Nominal Flow and Temperature Conditions in a Pre-Konvoi PWR Using Coupled CFD and Neutron Kinetics
Fluids 5, 161 (2020).

Höllriegl, V.; Barkleit, A.; Spielmann, V.; Li, W. B.
Measurement, model prediction and uncertainty quantification of plasma clearance of cerium citrate in humans
Radiation and Environmental Biophysics 59, 121–130 (2020).

Inoue, T.; Kazama, H.; Tsushima, S.; Takao, K.
Essential Role of Heterocyclic Structure of N-Alkylated 2-Pyrrolidone Derivatives for Recycling Uranium from Spent Nuclear Fuels
Bulletin of the Chemical Society of Japan 93, 846–853 (2020).

Jäschke, A.; Stumpf, T.; Aliabadi, A.; Büchner, B.; Kataev, V.; Hahn, T.; Kortus, J.; Kersting, B.
Tetranuclear Lanthanide Complexes Supported by Hydroxyquinoline-Calix[4]arene-Ligands: Synthesis, Structure, and Magnetic Properties of $[Ln_4(H_3L)_2(\mu\text{-}OH)_2(NO_3)_4]$ (Ln = Tb, Dy, Yb) and $[Dy_2(H_4L)_2(NO_3)](NO_3)$
European Journal of Inorganic Chemistry 2020, 4203–4214 (2020).

Jing, Y.; Heine, T.
Making 2D topological polymers a reality
Nature Materials 19, 823–824 (2020).

Joos, J.; van der Heggen, D.; Martin, L.; Amidani, L.; Smet, P.; Barandiarán, Z.; Seijo, L.
Broadband Infrared LEDs based on Europium-To-Terbium Charge Transfer Luminescence
Nature Communications 11, 3647 (2020).

Joos, J. J.; Korthout, K.; Amidani, L.; Glatzel, P.; Poelman, D.; Smet, P. F.
Identification of Dy^{3+} /Dy^{2+} as electron trap in persistent phosphors
Physical Review Letters 125, 033001 (2020).

Kahl, W. A.; Yuan, T.; Bollermann, T.; Bach, W.; Fischer, C.
Crystal surface reactivity analysis using a combined approach of X-ray micro-computed tomography and vertical scanning interferometry
American Journal of Science 320, 27–52 (2020).

Karimzadeh, L.; Lippold, H.; Stockmann, M.; Fischer, C.
Effect of DTPA on europium sorption onto quartz – Batch sorption experiments and surface complexation modeling
Chemosphere 239, 124771 (2020).

Kempt, R.; Kuc, A. B.; Heine, T.
Two-Dimensional Noble-Metal Dichalcogenides and Phosphochalcogenides
Angewandte Chemie - International Edition (2020).

Kéri, A.; Dähn, R.; Marques Fernandes, M.; Scheinost, A. C.; Krack, M.; Churakov, S. V.
Iron adsorption on clays inferred from atomistic simulations and XAS spectroscopy
Environmental Science and Technology 54, 11886–11893 (2020).

Kiani, M.; Du, N.; Vogel, M.; Raff, J.; Hübner, U.; Skorupa, I.; Bürger, D.; Schulz, S. E.; Schmidt, O. G.; Blaschke, D.; Schmidt, H.
Disturbing-free determination of yeast concentration in DI water and in glucose using impedance biochips
Biosensors 10, 7 (2020).

Kieffer, J.; Vals, V.; Blanc, N.; Hennig, C.
New tools for calibrating diffraction setups
Journal of Synchrotron Radiation 27, 558–566 (2020).

Kloditz, R.; Fichter, S.; Kaufmann, S.; Brunner, T. S.; Kaden, P.; Patzschke, M.; Stumpf, T.; Roesky, P. W.; Schmidt, M.; März, J.
Series of Tetravalent Actinide Amidinates: Structure Determination and Bonding Analysis
Inorganic Chemistry 59, 15670–15680 (2020).

Knaus, J.; Sommer, M.; Duchstein, P.; Gumeniuk, R.; Akselrud, L. G.; Sturm, S.; Auffermann, G. D.; Hennig, C.; Zahn, D.; Hulliger, J.; Sturm, E. V.
Polar structure formation in solid solution of strontium substituted fluorapatite-gelatin composites: from structural and morphogenetic aspects to pyroelectric properties
Chemistry of Materials 32, 8619–8632 (2020).

Konheiser, J.; Mueller, S. E.; Seidl, M.
Study of the influence of water gaps between fuel assemblies on the activation of an aeroball measurement system (AMS)
Annals of Nuclear Energy 136, 107005 (2020).

Konstantinovic, M. J.; Ulbricht, A.; Brodziansky, T.; Castina, N.; Malerba, L.
Vacancy-solute clustering in Fe-Cr alloys after neutron irradiation
Journal of Nuclear Materials 540, 152341 (2020).

Kowalski, P. M.; Lange, S.; Deissmann, G.; Sun, M.; Kvashnina, K. O.; Baker, R.; Kegler, P.; Murphy, G.; Bosbach, D.
Modeling of Nuclear Waste Forms: State-of-the-Art and Perspectives
MRS Advances 5, 213–222 (2020).

Kozmenkov, Y.; Jobst, M.; Kliem, S.; Kosowski, K.; Schäfer, F.; Wilhelm, P.
The efficiency of sequential accident management measures for a German PWR under prolonged SBO conditions
Nuclear Engineering and Design 363, 110663 (2020).

Krawczyk-Bärsch, E.; Scheinost, A. C.; Roßberg, A.; Müller, K.; Lehrich, J.; Bok, F.; Hallbeck, L.; Schmeide, K.
Uranium and neptunium retention mechanisms in *Gallionella ferruginea* / ferrihydrite systems for remediation purposes
Environmental Science and Pollution Research, DOI: 10.1007/s11356-020-09563-w (2020).

Kretzschmar, J.; Strobel, A.; Haubitz, T.; Drobot, B.; Steudtner, R.; Barkleit, A.; Brendler, V.; Stumpf, T.
Uranium(VI) Complexes of Glutathione Disulfide Forming in Aqueous Solution
Inorganic Chemistry 59, 4244–4254 (2020).

Kretzschmar, J.; Tsushima, S.; Drobot, B.; Steudtner, R.; Schmeide, K.; Stumpf, T.
Trimeric uranyl(VI)–citrate forms Na^{+}, Ca^{2+}, and La^{3+} sandwich complexes in aqueous solution
Chemical Communications 56, 13133–13136 (2020).

Kuc, A. B.; Springer, M.; Batra, K.; Juarez-Mosqueda, R.; Wöll, C.; Heine, T.
Proximity effect in crystalline framework materials: stacking-induced functionality in MOFs and COFs
Advanced Functional Materials 30, 1908004 (2020).

Kupka, N.; Kaden, P.; Jantschke, A.; Schach, E.; Rudolph, M.
Acidified water glass in the selective flotation of scheelite from calcite, part II: species in solution and related mechanism of the depressant
Physicochemical Problems of Mineral Processing 56, 797–817 (2020).

Kuzenkova, A.; Romanchuk, A.; Trigub, A.; Maslakov, K.; Egorov, A.; Amidani, L.; Kittrelle, C.; Kvashnina, K. O.; Toure, J.; Talyzin, A.; Kalmykov, S.
New insights into the mechanism of graphene oxide and radionuclide interaction through vacancy defects
Carbon 158, 291–302 (2020).

Lange, T.; Schneider, P.; Schymura, S.; Franke, K.
The fate of anthropogenic nanoparticles, $nTiO_2$ and $nCeO_2$, in waste water treatment
Water 12, 2509 (2020).

Leinders, G.; Bes, R.; Kvashnina, K. O.; Verwerft, M.
Local Structure in U(IV) and U(V) Environments: The Case of U_3O_7
Inorganic Chemistry 59, 4576–4587 (2020).

Liu, J.; Wei, X.; Zhou, Y.; Tsang, D. C. W.; Bao, Z.; Yin, M.; Lippold, H.; Yuan, W.; Wang, J.; Feng, Y.; Chen, D.
Thallium contamination, health risk assessment and source apportionment in common vegetables
Science of the Total Environment 703, 135547 (2020).

Liu, J.; Zhou, Y.; She, J.; Tsang, D. C. W.; Lippold, H.; Wang, J.; Jiang, Y.; Wei, X.; Yuan, W.; Luo, X.; Zhai, S.; Song, L.
Quantitative isotopic fingerprinting of thallium associated with potentially toxic elements (PTEs) in fluvial sediment cores with multiple anthropogenic sources
Environmental Pollution 266, 115252 (2020).

Lösch, H.; Raiwa, M.; Jordan, N.; Steppert, M.; Steudtner, R.; Stumpf, T.; Huittinen, N. M.
Temperature–dependent luminescence spectroscopic and mass spectrometric investigations of U(VI) complexation with aqueous silicates in the acidic pH–range
Environment International 135, 105425 (2020).

Maiwald, M. M.; Müller, K.; Heim, K.; Trumm, M.; Fröhlich, D. R.; Banik, N. L.; Rothe, J.; Dardenne, K.; Skerencak-Frech, A.; Panak, P. J.
Determination of thermodynamic functions and structural parameters of NpO_2^+ lactate complexes
New Journal of Chemistry 44, 17033–17046 (2020).

Mandal, K.; Bansal, D.; Kumar, Y.; Khan, R.; Shukla, J.; Mukhopadhyay, P.
Halogen Bonded Assemblies of Arylene-imides and -diimides: Insight from Electronic, Structural and Computational studies
Chemistry - A European Journal 26, 10607–10619 (2020).

Martin, A.; Hassan-Loni, Y.; Fichtner, A.; Péron, O.; David, K.; Chardon, P.; Larrue, S.; Gourgiotis, A.; Sachs, S.; Arnold, T.; Grambow, B.; Stumpf, T.; Montavon, G.
An integrated approach combining soil profile, records and tree ring analysis to identify the origin of environmental contamination in a former uranium mine (Rophin, France)
Science of the Total Environment 747, 141295 (2020).

Mayordomo Herranz, N.; Rodriguez Hernandez, D. M.; Schild, D.; Molodtsov, K.; Johnstone, E. V.; Hübner, R.; Shams Aldin Azzam, S.; Brendler, V.; Müller, K.
Technetium retention by gamma alumina nanoparticles and the effect of sorbed Fe^{2+}
Journal of Hazardous Materials 833, 122066 (2020).

Meza, A.; Macía, E.; García-Junceda, A.; Antonio Díaz, L.; Chekhonin, P.; Altstadt, E.; Serrano, M.; Eugenia Rabanal, M.; Campos, M.
Development of New 14 Cr ODS Steels by Using New Oxides Formers and B as an Inhibitor of the Grain Growth
Metals 10, 1344 (2020).

Moll, H.; Lehmann, F.; Raff, J.
Interaction of curium(III) with surface-layer proteins from *Lysinibacillus sphaericus* JG-A12
Colloids and Surfaces B: Biointerfaces 190, 110950 (2020).

Moll, H.; Sachs, S.; Geipel, G.
Plant cell (*Brassica napus*) response to europium(III) and uranium(VI) exposure
Environmental Science and Pollution Research 27, 32048–32061 (2020).

Monico, L.; Cotte, M.; Vanmeert, F.; Amidani, L.; Janssens, K.; Nuyts, G.; Garrevoet, J.; Falkenberg, G.; Glatzel, P.; Romani, A.; Miliani, C.
Damages induced by synchrotron radiation-based X-ray microanalysis in chrome yellow paints and related Cr-compounds: assessment, quantification and mitigation strategies
Analytical Chemistry 92, 14164–14173 (2020).

Pan, Z.; Bártová, B.; Lagrange, T.; Shen, T.; Tileli, V.; Butorin, S.; Hyatt, N. C.; Stennett, M. C.; Kvashnina, K. O.; Bernier-Latmani, R.
Nanoscale mechanism of UO_2 formation through uranium reduction by magnetite
Nature Communications 11, 4001 (2020).

Pelli Cresi, J.; Znaiguia, R.; Carlà, F.; Isern, H.; Benedetti, F.; Gasperi, G.; Amidani, L.; Valeri, S.; Boscherini, F.; Luches, P.
Structure of Reduced Cerium Oxide Ultrathin films on Pt(111): Local Atomic Environment and Long-range Order
Advanced Materials Interfaces 7, 2000737 (2020).

Penkov, S.; Raghuraman, B. K.; Erkut, C.; Oertel, J.; Galli, R.; Ackerman, E. J. M.; Vorkel, D.; Verbavatz, J. M.; Koch, E.; Fahmy, K.; Shevchenko, A.; Kurzchalia, T. V.
A metabolic switch regulates the transition between growth and diapause in C. elegans
BMC Biology 18, 31 (2020).

Pidchenko, I.; Bauters, S.; Sinenko, I.; Hempel, S.; Amidani, L.; Detollenaere, D.; Vinze, L.; Banerjee, D.; Silfhouth, R.; Kalmykov, S.; Göttlicher, J.; Baker, R. J.; Kvashnina, K. O.
A multi-technique study of altered granitic rock from the Krunkelbach Valley uranium deposit, Southern Germany
RSC Advances 10, 25529–25539 (2020).

Pidchenko, I.; März, J.; Hunault, M. O. J. Y.; Bauters, S.; Butorin, S. M.; Kvashnina, K. O.
Synthesis, Structural, and Electronic Properties of $K_2Pu^{VI}O_2(CO_3)_{3(cr)}$: An Environmentally Relevant Plutonium Carbonate Complex
Inorganic Chemistry 59, 11889–11893 (2020).

Prieur, D.; Bonani, W.; Popa, K.; Walter, O.; Kriegsman, K.; Engelhard, M.; Guo, X.; Eloirdi, R.; Gouder, T.; Beck, A.; Vitova, T.; Scheinost, A. C.; Kvashnina, K. O.; Martin, P.
Size Dependence of Lattice Parameter and Electronic Structure in CeO_2 Nanoparticles
Inorganic Chemistry 59, 5760–5767 (2020).

Qiu, C.; Chen, W.; Schmidt, M.; Majs, F.; Douglas, T. A.; Trainor, T. P.
Selective Adsorption of Pb(II) on an Annealed Hematite ($1\bar{1}02$) Surface: Evidence from Crystal Truncation Rod X-ray Diffraction and Density Functional Theory
Environmental Science & Technology 54, 6651–6660 (2020).

Rachamin, R.; Hampel, U.
Feasibility assessment of using external neutron and gamma radiation measurements for monitoring the state of fuel assemblies in dry storage casks
Annals of Nuclear Energy 135, 106975 (2020).

Radoske, T.; Kloditz, R.; Fichter, S.; März, J.; Kaden, P.; Patzschke, M.; Schmidt, M.; Stumpf, T.; Walter, O.; Ikeda, A.
Systematic comparison of the structure of homoleptic tetradentate N_2O_2-type Schiff base complexes of tetravalent f-elements (M(IV) = Ce, Th, U, Np, and Pu) in solid state and in solution
Dalton Transactions 49, 17559–17570 (2020).

Radoske, T.; März, J.; Patzschke, M.; Kaden, P.; Walter, O.; Schmidt, M.; Stumpf, T.
Bonding Trends in Tetravalent Th–Pu Monosalen Complexes
Chemistry - A European Journal 26, 16853–16859 (2020).

Robba, A.; Barchasza, C.; Bučar, K.; Petric, M.; Žitnik, M.; Kvashnina, K.; Vaughan, G. B. M.; Bouchet, R.; Alloin, F.; Kavčič, M.
Fingerprinting mean composition of lithium polysulfide standard solutions by applying high energy resolution fluorescence detected X-ray Absorption Spectroscopy
The Journal of Physical Chemistry Letters 11, 5446–5450 (2020).

Rodriguez Hernandez, D. M.; Mayordomo Herranz, N.; Scheinost, A. C.; Schild, D.; Brendler, V.; Müller, K.; Stumpf, T.
New insights into ^{99}Tc(VII) removal by pyrite: A spectroscopic approach
Environmental Science & Technology 54, 2678–2687 (2020).

Ruiz-Fresneda, M. A.; Lopez Fernandez, M.; Martinez-Moreno, M. F.; Cherkouk, A.; Ju-Nam, Y.; Ojeda, J. J.; Moll, H.; Merroun, M. L.
Molecular binding of Eu^{III}/Cm^{III} by *Stenotrophomonas bentonitica* and its impact on the safety of future geodisposal of radioactive waste
Environmental Science & Technology 54, 15180–15190 (2020).

Ruiz-Moreno, A.; Hähner, P.; Kurpaska, L.; Jagielski, J.; Spätig, P.; Trebala, M.; Hannula, S. P.; Merino, S.; de Diego, G.; Namburi, H.; Libera, O.; Terentyev, D.; Khvan, T.; Heintze, C.; Jennett, C.
Round robin into best practices for the determination of indentation size effects
Nanomaterials 10, 130 (2020).

Sarotto, M.; Firpo, G.; Kochetkov, A.; Krása, A.; Fridman, E.; Cetnar, J.; Domanska, G.
Neutronic analyses of the FREYA experiments in support of the ALFRED LFR core design and licensing
Journal of Nuclear Engineering and Radiation Science 6, 011402 (2020).

Scheibe, B.; März, J.; Schmidt, M.; Stumpf, T.; Kraus, F.
Synthesis and crystal structures of transition metal(II) fluoridometallate(IV) hydrates of neptunium and plutonium: $A^{II}M^{IV}F_6{\cdot}3H_2O$ (A^{II} = Mn, Zn; M^{IV} = Np, Pu)
European Journal of Inorganic Chemistry 23, 2279–2284 (2020).

Scheibe, B.; Patzschke, M.; März, J.; Conrad, M.; Kraus, F.
A Molecular Octafluoridoneptunate(IV) anion in $(NH_4)_4[NpF_8]$ and Theoretical Investigations of the $[MF_8]^{4-}$ System (M = Th - Bk)
European Journal of Inorganic Chemistry 39, 3753–3759 (2020).

Shah, V.; van Dommelen, J. A. W.; Altstadt, E.; Das, A.; Geers, M. G. D.
Brittle-ductile transition temperature of recrystallized tungsten following exposure to fusion relevant cyclic high heat load
Journal of Nuclear Materials 541, 152416 (2020).

Springer, M.; Liu, T. J.; Kuc, A. B.; Heine, T.
Topological Two-Dimensional Polymers
Chemical Society Reviews 49, 2007–2019 (2020).

Sprinzl, D.; Krysl, V.; Mikolas, P.; Zavorka, J.; Timr, J.; Bilodid, Y.; Temesvari, E.; Pos, I.; Kalinin, Y.; Shcherenko, A.; Aleshin, S.; Bahadir, T.
"Full-Core" VVER-1000 calculation benchmark
Kerntechnik 85, 231–244 (2020).

Takao, K.; März, J.; Matsuoka, M.; Mashita, T.; Kazama, H.; Tsushima, S.
Crystallization of colourless hexanitratoneptunate(IV) with anhydrous H^+ countercations trapped into hydrogen bond polymer with diamide linkers
RSC Advances 10, 6082–6087 (2020).

Tamain, C.; Bonato, L.; Aupiais, J.; Dumas, T.; Guillaumont, D.; Barkleit, A.; Berthon, C.; Solari, P. L.; Ikeda-Ohno, A.; Guilbaud, P.; Moisy, P.
Role of the hydroxo group in the coordination of citric acid toward trivalent americium
European Journal of Inorganic Chemistry, 1331–1344 (2020).

Traxler, L.; Wollenberg, A.; Steinhauser, G.; Chyzhevskyi, I.; Dubchak, S.; Großmann, S.; Günther, A.; Gupta, D. K.; Iwannek, K. H.; Kirieiev, S.; Lehmann, F.; Schulz, W.; Walther, C.; Raff, J.; Kothe, E.
Survival of the basidiomycete *Schizophyllum* commune in soil under hostile environmental conditions in the Chernobyl Exclusion Zone
Journal of Hazardous Materials 403, 124002 (2020).

Trigub, A. L.; Trofimov, N. D.; Tagirov, B. R.; Nickolsky, M. S.; Kvashnina, K. O.
Probing the local atomic structure of In and Cu in sphalerite by XAS spectroscopy enhanced by reverse Monte-Carlo algorithm
Minerals 10, 841 (2020).

Trindade Pedrosa, E.; Fischer, C.; Morales, L. F.; Rohlfs, R. D.; Lüttge, A.
Influence of chemical zoning on sandstone calcite cement dissolution: The case of manganese and iron
Chemical Geology 559, 119952 (2020).

Trofimov, N. D.; Trigub, A. L.; Tagirov, B. R.; Filimonova, O. N.; Evstigneeva, P. V.; Chareev, D. A.; Kvashnina, K. O.; Nickolsky, M. S.
The state of trace elements (In, Cu, Ag) in sphalerite studied by X-ray absorption spectroscopy of synthetic minerals
Minerals 10, 640 (2020).

Vivas, J.; De-Castro, D.; Altstadt, E.; Houska, M.; San-Martin, D.; Capdevila, C.
Design and high temperature behavior of novel heat resistant steels strengthened by high density of stable nanoprecipitates
Materials Science and Engineering A 739, 139799 (2020).

Vogel, K.; Heintze, C.; Chekhonin, P.; Akhmadaliev, S.; Altstadt, E.; Bergner, F.
Relationships between depth-resolved primary radiation damage, irradiation-induced nanostructure and nanoindentation response of ion-irradiated Fe-Cr and ODS Fe-Cr alloys
Nuclear Materials and Energy 24, 100759 (2020).

Wasserbäch, W.; Skrotzki, W.; Chekhonin, P.
Strengthening of ODS silver wires
Materialia 12, 100818 (2020).

Wulf, T.; Heine, T.
Small Crown-Ether Complexes as Molecular Models for Dihydrogen Adsorption in Undercoordinated Extraframework Cations in Zeolites
Journal of Physical Chemistry C 124, 9409–9415 (2020).

Wyżga, P.; Carrillo-Cabrera, W.; Akselrud, L.; Veremchuk, I.; Wagler, J.; Hennig, C.; Tsirlin, A.; Leithe-Jasper, A.; Kroke, E.; Gumeniuk, R.
Crystal structure, phase transition and properties of indium(III) sulfide
Dalton Transactions 49, 15903–15913 (2020).

Wyżga, P.; Veremchuk, I.; Bobnar, M.; Hennig, C.; Leithe-Jasper, A.; Gumeniuk, R.
Ternary MIn$_2$S$_4$ (M = Mn, Fe, Co, Ni) thiospinels - crystal structure and thermoelectric properties
Zeitschrift für Anorganische und Allgemeine Chemie 646, 1091–1098 (2020).

Yuan, L.; Zheng, B.; Kunstmann, J.; Brumme, T.; Kuc, A. B.; Ma, C.; Deng, S.; Blach, D.; Pan, A.; Huang, L.
Twist-angle-dependent interlayer exciton diffusion in WS_2–WSe_2 heterobilayers
Nature Materials 19, 617–623 (2020).

○ Editorial Work

Fischer, C.; Arvidson, R. S. (Eds.)
Special issue of the American Journal of Science – Andreas Lüttge Special Issue: Part II
Yale University, New Haven, CT, U.S.A. (2020).

Lloyd, J.; Cherkouk, A. (Eds.)
The Microbiology of Nuclear Waste Disposal
Elsevier, Amsterdam, The Netherlands (2020).

Stockmann, M.; Brendler, V.
How to integrate geochemistry at affordable costs into reactive transport for large-scale systems
Wissenschaftlich-Technische Berichte / Helmholtz-Zentrum Dresden-Rossendorf; HZDR-111 (2020).

Further Contributions

Davies, U.; Margulis, M.; Shwageraus, E.; Fridman, E.; Garcia-Herranz, N.; Jimenez-Carrascosa, A.; Cabellos, O.; Gregg, R.
Evaluation of the ESFR End of Cycle State and Detailed Spatial Distributions of Reactivity Coefficients
PHYSOR 2020, Cambridge, United Kingdom (2020).

Lopez Fernandez, M.; Matschiavelli, N.; Merroun, M. L.
Bentonite Geomicrobiology
in: The Microbiology of Nuclear Waste Disposal, Elsevier, Amsterdam, The Netherlands (2020).

Mijnendonckx, K.; Monsieurs, P.; Cerna, K.; Hlavackova, V.; Steinova, J.; Burzan, N.; Bernier-Latmani, R.; Boothman, C.; Miettinen, H.; Kluge, S.; Matschiavelli, N.; Cherkouk, A.; Jroundi, F.; Larbi Merroun, M.; Engel, K.; Neufeld, J. D.; Leys, N.
Molecular techniques for understanding microbial abundance and activity in clay barriers used for geodisposal
in: The Microbiology of Nuclear Waste Disposal, Elsevier, Amsterdam, The Netherlands (2020).

Rydlewicz, W.; Fridman, E.; Shwageraus, E.
Modelling ASTRID-Like Sodium-Cooled Fast Reactor with Serpent DYN3D Code Sequence
PHYSOR 2020, Cambridge, United Kingdom (2020).

Swanson, J. S.; Bader, M.; Cherkouk, A.
Potential microbial influence on the performance of subsurface, salt-based nuclear waste repositories
in: The Microbiology of Nuclear Waste Disposal, Elsevier, Amsterdam, The Netherlands (2020).

Villanueva, W.; Filippov, A.; Jules, S.; Lim, K.; Jobst, M.; Bouydo, A. M.; Qais, S.; Wang, H.; Fichot, F.; Bechta, S.
Thermo-mechanical modelling of reactor pressure vessel during core melt invessel retention
International Seminar "In-vessel retention: outcomes of IVMR project", Juan-les-Pins, France (2020).

Patent

Gutzmer, J.; Kutschke, S.; Pollmann, K.; Raff, J.
Device and method for obtaining 2- and 3-valent metal ions from primary and secondary materials with the aid of microbial metabolites
EP 3 084 022 B1; November 18, 2020.

Oral Presentations

Bergner, F.
Diffraction techniques in nuclear materials
European School on Nuclear Material Science, November 09–13, 2020, online (2020).

Bergner, F.
Nanoindentation testing and TEM observations of irradiated F/M alloys
ONLINE M4F Plenary Project Meeting, June 16–17, 2020, online (2020).

Brinkmann, H.; Neumann, J.; Britz, S.; Brendler, V.; Stumpf, T.; Schmidt, M.
Sorption of trivalent actinides (Cm, Am) and their rare earth analogues (Lu, Y, Eu, Nd, La) onto orthoclase: Batch experiments, Time-Resolved Laser Fluorescence Spectroscopy (TRLFS) and Surface Complexation Modeling (SCM)
EGU General Assembly 2020, May 04–08, 2020, Vienna, Austria (2020).

Chekhonin, P.
ENTENTE WP2 Task 2.4: Data Collection
ENTENTE Kickoff Meeting, September 09–10, 2020, Dresden, Germany (2020).

Chekhonin, P.
ENTENTE WP3 Task 3.2: Task 3.2: Microstructural Examinations in RPV Steels and Model Alloys
ENTENTE Kickoff Meeting, September 09–10, 2020, Dresden, Germany (2020).

Chekhonin, P.; Bergner, F.
Reconstruction of austenite grain boundaries in bainitic reactor pressure vessel steels by EBSD
AK-Treffen Mikrostrukturcharakterisierung im REM, October 22, 2020, Freiberg, Germany (2020).

Eibl, M.; Shaw, S.; Hennig, C.; Prieur, D.; Wilding, M.C.; Morris, K.; Stumpf, T.; Huittinen, N.
Trivalent Lanthanide and Actinide Incorporation into Zirconium(IV) oxide – Spectroscopic Investigations of Defect Fluorite Structures
Joint Polish-German Crystallographic Meeting 2020, February 24 – 27, 2020, Wrocław, Poland (2020).

Hennig, C.; Schmidt, M.; Ikeda-Ohno, A.; Radoske, T.; Feig, M.; Findeisen, S.; Claußner, J.; Exner, J.; Naudet, D.; Baumann, N.; Scheinost, A.C.
Two new diffractometers at BM20/ESRF for single crystal, powder and surface diffraction
Joint Polish-German Crystallographic Meeting 2020, February 24–27, 2020, Wroclaw, Poland (2020).

Huittinen, N.; Scheinost, A.C.; Ji, Y.; Kowalski, P.M.; Arinicheva, Y.; Neumeier, S.
Curium incorporation in rhabdophane solid solutions ($La_{1-x}Gd_xPO_4 \cdot 0.67H_2O$)
Joint Polish-German Crystallographic Meeting 2020, February 24 – 27, 2020, Wrocław, Poland (2020).

John, W.; Matschiavelli, N.; Thieme, D.; Hoehenwarter, W.; Sachs, S.
Elucidating the mechanism of uranium uptake and processing in tobacco BY-2 cells
Biometals 2020, July 05–09, 2020, Villard de Lans, France (2020).

Kelly, N.; Sanchez Loredo, M.G.; Dupal, O.; Chekhonin, P.; Ebert, D.; Möckel, R.; O'Toole, N.; Reuter, M.
Rückgewinnung von Vanadium aus alkalischen Laugungslösungen unter der Synthese von Nanopartikeln
Jahrestreffen der ProcessNet-Fachgruppen Fluidverfahrenstechnik, Adsorption und Extraktion, February 26–28, 2020, Berchtesgaden, Germany (2020).

Kloditz, R.; Radoske, T.; Patzschke, M.; Stumpf, T.
Multiconfigurational calculations of ground state and excited states of tetravalent uranium complexes
Theory Frontiers in Actinide Sciences, February 02–05, 2020, Santa Fe, U.S.A. (2020).
XIIIth Workshop on Modern Methods in Quantum Chemistry, March 02–05, 2020, Mariapfarr, Austria (2020).

Marques Fernandes, M.; Baeyens, B.; Daehn, R.; Scheinost, A.C.; Churakov, S.V.
Fate of contaminants from repositories for radioactive waste based in clay-rock?
18th Swiss Geoscience Meeting, November 06–07, 2020, Zurich, Switzerland (2020).

Matschiavelli, N.; Dressler, M.; Neubert, T.; Kluge, S.; Schierz, A.; Cherkouk, A.
The role of microorganisms in the bentonite barrier of high-level radioactive waste repositories
EGU General Assembly 2020, May 04–08, 2020, Dresden, Germany (2020).

Matschiavelli, N.; Dressler, M.; Neubert, T.; Kluge, S.; Schierz, A.; Cherkouk, A.
Why should we care about microorganisms in the bentonite back fill material for the storage of high-level radioactive waste in deep geological repositories?
6th Joint Conference of DGHM & VAAM, March 08–11, 2020, Leipzig, Germany (2020).

Mayordomo, N.
Radiochemistry and the radioactive nuclear waste management
Lectures about chemistry (Lecciones de química), February 06, 2020, Alcalá de Henares, Spain (2020).

Raff, J.; Cherkouk, A.; Matschiavelli, N.; Sushko, V.; Dressler, M.
Ideen zur Untersuchung der MIC Beständigkeit von vorgealterten Materialien
DECHEMA/GfKORR Fachgruppensitzung „Mikrobielle Materialzerstörung und Materialschutz", October 27, 2020, online, Germany (2020).

Scheinost, A.C.
Interfacial redox reactions, X-ray absorption spectroscopy, and how they can contribute to the safety of radioactive-waste repositories
GFZ Talk, September 17, 2020, Postdam, Germany (2020).
&
Azeotrope Chemistry Seminar at National Institute of Technology (NIT) Rourkela, November 25, 2020, Rourkela, India (2020).

Schymura, S.; Hildebrand, H.; Neugebauer, M.; Lange, T.; Schneider, P.; Franke, K.
Assessing nanoparticle release from waste water treatment using radiolabeled nanoparticles
Nanosafe 2020, November 16–20, 2020, Grenoble, France (2020).

Stockmann, M.; Noseck, U.; Britz, S.; Flügge, J.; Becker, D.A.; Brendler, V.
Smart Kd-concept as efficient approach to improve geochemistry in reactive transport modelling
International Workshop on "How to integrate geochemistry at affordable costs into reactive transport for large-scale systems", February 05–07, 2020, Dresden, Germany (2020).

Ulbricht, A.
STRUctural MATerials research for safe Long Term Operation of LWR NPPs (STRUMAT-LTO) Work Package 3: Synergetic effects of Ni, Mn and Si on RPV embrittlement at high fluences
STRUMAT-LTO Kick-off Meeting, September 07–08, 2020, online (2020).

Yuan, T.
Numerical modeling and simulation of reactive flow and transport processes in subsurface formations
Numerical simulation of subsurface flow, September 25, 2020, Beijing, China (2020).

Yuan, T.; Kulenkampff, J.; Bollermann, T.; Fischer, C.
Radionuclide transport and retention at the core scale identified by GeoPET analysis and reactive transport modeling
InterPore 2020, August 31–September 04, 2020, Qing Dao, China (2020).

THESES

(Technische Universität Dresden, 2020, except where noted)

DOCTORAL THESES

Brinkmann, H.
Spektroskopische Untersuchungen zur Wechselwirkung zwischen Uranyl(VI) und den Cellulose-Abbauprodukten α-Isosaccharinsäure und Acetat

Eibl, M.
Actinide Interaction with Zr-bearing Phases: Spectroscopic Investigations of An^{3+} Sorption and Incorporation Reactions with Zirconia

Fichter, S.
Synthesis and Characterization of Tri- and Tetravalent Actinide Amidinates

Iric, K.
Assembly of DNA-encapsulated lipid bilayers and their application to studies of GPCRs

Lehmann, S.
Uran unter reduzierenden Bedingungen – Spektroskopische und thermodynamische Charakterisierung der wässrigen Speziation

Melix, P.
Flexible Metalic-Organic Frameworks, On Intra- and Intermolecular Interactions

Molodtsov, K.
Speziation von Eu(III) an heterogenen Oberflächen mithilfe von orts- und zeitaufgelöster Laserfluoreszenzspektroskopie (μTRLFS)

Philipp, T.
U(VI) retention by Ca-bentonite and clay minerals at (hyper)alkaline conditions

Wolter, J.-M.
Stability of U(VI) and Cm(III) doped calcium (alumino)silicate hydrate phases at high ionic strengths

MASTER THESES

Kliemann, J.
Untersuchungen der mikrobiellen Diversität in Salzgestein und Wechselwirkung halophiler Isolate mit Europium

Schabernack, J.
Europium Adsorption on the (001) Muscovite Face: A Kinetic Monte Carlo Study

Diploma Thesis

Füssel, T.
Die Wirkung von sorbierten redoxaktiven Spezies auf Aluminiumoxid-Nanopartikeln bei der Immobilisierung von Technetium

Bachelor Thesis

Gerlach, L.-M.
Mikrokalorimetrische Messungen zur kinetischen Analyse einer statischen Kultur von Lactococcus lactis

Lückel, B.
Untersuchung der Endozytose als Aufnahmeprozess von Uran(VI) in Tabak BY-2-Zellen

Neubert, T.
Untersuchung des mikrobiellen Einflusses auf Kupfer- und GGG40-Grenzflächen im Bentonit unter halophilen Bedingungen

- WORKSHOP
- SEMINARS
- TEACHING ACTIVITIES

❍ International Workshop on "How to integrate geochemistry at affordable costs into reactive transport for large-scale systems"

HZDR, Germany, February 05–07, 2020

Experts from fields of reactive transport modelling (RTM), statistics, computational numerics, thermodynamics, radiochemistry or geosciences were brought together to discuss RTM on large scales, namely time (up to one million of years) and space (dozens of kilometers). Full-fledged incorporation of basic, geochemical processes, *e. g.* sorption, precipitation, or redox reactions, will thus demand inacceptable long computing times.

As an effective way to integrate geochemistry at affordable costs into RTM, different numerical concepts (*e. g.* multidimensional look-up tables, surrogate functions, machine learning, utilization of uncertainty and sensitivity analysis etc.) already exist and were extensively discussed throughout the workshop.

In total, 40 scientists from 28 research institutes and 8 countries followed the invitation of the organizers, Dr. Madlen Stockmann and Prof. Vinzenz Brendler, HZDR, and presented their research in keynote and regular lectures and during poster session. A tour on the radiochemical laboratories of the IRE had been offered.

Based on the intensive discussions and very positive feedback on the workshop, a continuation is intended to bundle and strengthen the respective research activities and stipulate the international network that started to form during the conference days.

The main topics of the workshop were:

- Introduction and discussion of existing geochemical concepts in reactive transport modelling to describe sorption and related retardation processes of contaminants on a variety of sediments and rocks.
- Focusing on large-scale natural systems as experienced, *e.g.* in nuclear waste disposal, carbon capture & storage, environmental remediation, or geothermal applications.
- Integration of the discussed approaches into current paradigms in Thermo-Hydraulic-Mechanic-Chemical (THMC) models and long-term safety assessments at affordable costs.
- Promotion of the exchange of scientific knowledge and practical experience between the workshop participants.

List of keynote speakers:

Allan Leal
ETH Zurich, Switzerland

Haibing Shao
Helmholtz Centre for Environmental Research – UFZ Leipzig, Germany

Carl I. Steefel
Lawrence Berkeley National Laboratory, Berkely, U.S.A.

Paolo Trinchero
Amphos21, Spain

For more information please visit:
www.hzdr.de/smartkd

ACKNOWLEDGEMENTS. The organizers would like to thank the HZDR administration for their kind support and the German Federal Ministry for Economic Affairs and Energy (BMWi) for the partial funding under contract No. 02E 11668B.

Seminars (Talks of Visitors)

Majzlan, Jurai
Friedrich-Schiller-Universität Jena, Germany
What controls the solubility of arsenic and antimony at old mining sites?
February 4, 2020

Qin, Guam
Department of Petroleum Engineering, University of Houston, U.S.A.
Multi-scale and multi-physics numerial simulation of fluid transport processes in porous media
March 23, 2020

Albrecht-Schmitt, Thomas
Department of Chemistry and Biochemistry, Florida State University, Tallahassee, U.S.A.
Chemistry Beyond Plutonium: How Relativity Alters Electronic Structure in Heavy Elements
June 30, 2020

Fränzle, Stefan
Professur für Umweltbiotechnologie, TU Dresden, Germany
Chritin: Going a long way from Nuclear Fuel Recycling, towards Mining, Applications in Fuel Cells and environmental Trace Element Monitoring – and maybe back
December 3, 2020

Teaching Activities

(Winter term: WT; summer term: ST)

Lectures

Bok, F.
Friedrich-Schiller-Universität, Jena
ST 2020
Geochemische Modellierung mit Geochemist's Workbench®

Brendler, V.
Dresden University of Applied Sciences,
ST 2020
Radiochemistry

Fahmy, K.
Technische Universität Dresden,
WT 2019/2020
Molecular Biophysic: Concepts and Methods
ST 2020
Biological thermodynamics

Fischer, C.
Universität Bremen,
ST 2020
Diagenese

Universität Leipzig
WT 2020/2021
Moderne Methoden in der Materialwissenschaft

Heine, T.
Technische Universität Dresden,
WT 2019/2020
Quantenchemie
WT 2019/2020, WT 2020/2021
PC II (Theorie der Chemischen Bindung)
PC III (Einführung in die Computerchemie)
WT 2020/2021
Theoretische Chemie
Computational Spectroscopy
Quantum Chemistry

Yonsei University Seoul, Korea
ST 2020
Artificial Intelligence and Machine Learning

Huittinen, N.
Technische Universität Dresden,
ST 2020
Radioecology

Kuc, A. B.
Universität Leipzig,
WT 2019/2020, WT 2020/2021
Computational Chemistry of Solids

Lippold, H.
Universität Leipzig,
ST 2020
Radioanalytik
Entstehung und Eigenschaften ionisierender Strahlung
WT 2019/2020, WT 2020/2021
Radiochemische Analysenmethoden

Raff, J.
Dresden University of Applied Sciences, WT 2019/2020, WT 2020/2021
Mikrobiologie

Technische Universität Dresden, WT 2019/2020, WT 2020/2021
Mikrobielle Laugung

Schmidt, M.
Technische Universität Dresden, ST 2020
Chemistry of the *f*-elements

Schymura, S.
Universität Leipzig WT 2019/2020, WT 2020/2021
Radioanalytik

Stumpf, T.
Technische Universität Dresden, WT 2019/2020, WT 2020/2021
Radiochemistry

Courses

- The laboratory course "Radiochemistry" was provided from August 24–September 04, 2020, as a part of a module of the chemistry master degree program at the Technische Universität Dresden.

Advisers:

Acker, M.	Kretzschmar, J.
Brinkmann, H.	Mayordomo, N.
Demnitz, M.	Neumann, J.
Eibl, M.	Nucke, L.
Fichter, S.	Patzschke, M.
Hilpmann, S.	Rodriguez Hernandez, D. M.
Huittinen, N.	Roode-Gutzmer, Q. I.
Jessat, I.	Sachs, S.
Jessat, J.	Schmidt, M.
John, W.	Subramanian, M.
Jordan, N.	Sushko, V.
Kaden, P.	Taut, S.
Kloditz, R.	Weiss, S.
Köhler, L.	Yassin, G.

- The IRE provided the experiment "Alpha spectrometric isotope dilution analysis of uranium" of the laboratory course "Instrumental Analysis" held by the Institute for Analytical Chemistry, Technische Universität Dresden.

Advisers:

WT 2019/2020	
Hilpmann, S	Roode-Gutzmer, Q. I.
Köhler, L	Weiss, S.
Neumann, J.	

- Biophysics course of the Dresden-International-Graduate School.

Advisers:

WT 2019/2020 & WT 2020/2021		
Fahmy, K.	Oertel, J.	Philipp, J.

- Courses and seminars were held referring to the following lectures:

Fahmy, K.
Technische Universität Dresden, WT 2019/2020, WT 2020/2021
Biophysics course of the Dresden-International-Graduate School

Faria Oliveira, A.
Technische Universität Dresden, WT 2020/2021
Spektroskopie mit dem Computer

Kuc, A. B.
Universität Leipzig, WT 2020/2021
Spektroskopie (PC)
WT 2020/2021
Computational Chemistry for Solids

Springer, M.
Technische Universität Dresden, WT 2020/2021
Theorie der chemischen Bindung

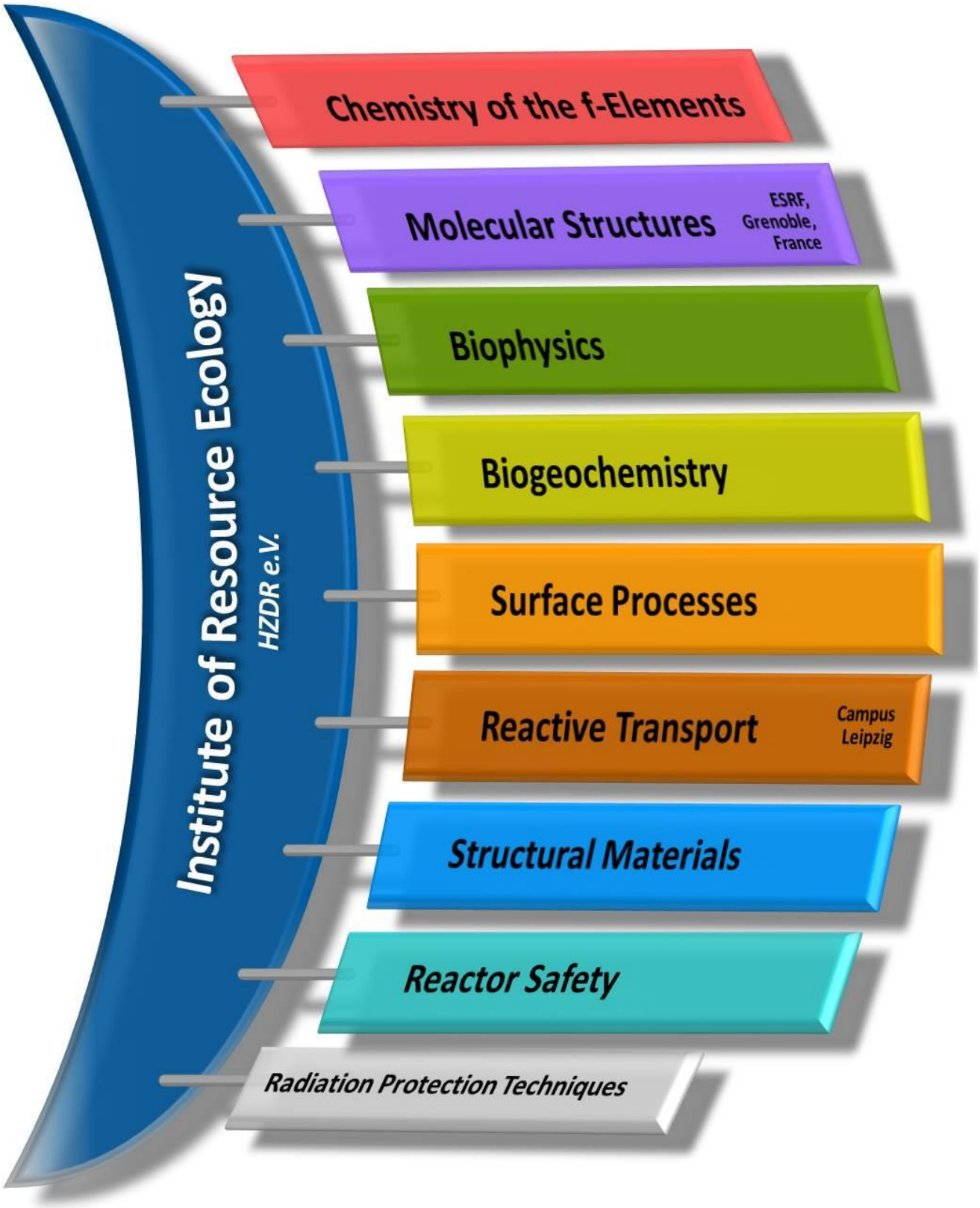
Institute of Resource Ecology
HZDR e.V.
Chemistry of the f-Elements
Molecular Structures
ESRF, Grenoble, France
Biophysics
Biogeochemistry
Surface Processes
Reactive Transport
Campus Leipzig
Structural Materials
Reactor Safety
Radiation Protection Techniques

HEAD OF INSTITUTE: Prof. Dr. Thorsten Stumpf

ADMINISTRATION:
Office Dresden: Gorzitze, Jana; Theuner, Bettina; Kovacs, Jenny; Kurde, Kerstin; Rott, Sonja
Office Leipzig: Gerstner, Katrin; Meinken, Roswitha

PROJECT COORDINATION:
Dr. Arnold, Thuro

RADIATION PROTECTION:
Bachmann, Stefanie; Dräger, Eric; Eisold, Silke; Falkenberg, Dirk; Henke, Steffen; Jimenez Hernandez, Susana; Nebe, Kathrin; Rumpel, Annette
Sysad (IT): Berndt, Ronny

BIOGEOCHEMISTRY

DR. RAFF, JOHANNES

Bertheau, Rahel
Dr. Drobot, Björn
Flemming, Katrin
Dr. Günther, Alix
Heller, Sylvia
Jessat, Jenny*
Dr. John, Warren*
Dr. Krawczyk-Bärsch, Evelyn
Dr. Mandal, Poulami
Dr. Moll, Henry
Dr. Sachs, Susanne
Seibt, Jana
Dr. Stalke, Sebastian
Dr. Steudtner, Robin
Wollenberg, Anne*

BIOPHYSICS

PROF. DR. FAHMY, KARIM

Dornbusch, Daniel*
Dr. Kielar, Charlotte
Nucke, Lisa*
Dr. Oertel, Jana
Philipp, Jenny
Dr. Sayed, Ahmed M. T.
Prof. Dr. Tsushima, Satoru
Subramanian, Madhumalar*

CHEMISTRY OF THE F-ELEMENTS

PD DR. SCHMIDT, MORITZ

Dr. Bezzina, James P.
Dr. Kaden, Peter
Kloditz, Roger*
Neumann, Julia*
Dr. Patzschke, Michael
Dr. Taylor, Corey

METALLORGANIC ACTINIDE CHEMISTRY
Dr. März, Juliane
Dr. Bansal, Deepak
Dr. Fichter, Sebastian
Köhler, Luisa*
Radoske, Thomas*

MOLECULAR STRUCTURES — ESRF, Grenoble

DR. HABIL. SCHEINOST, ANDREAS C.

Dr. Baumann, Nils
Dr. Estevanon, Paul
Exner, Jörg
Dr. De Bona, Emanuele
Dr. Faria Oliveira, Augusto
Dr. Hennig, Christoph
Dr. Prieur, Damien
Dr. Rossberg, André
Zimmermann, Thomas

ERC GRANT: Dr. Kvashnina, Kristina O.

Dr. Amidani, Lucia
Dr. Bauters, Stephen
Galenzew, Jurij
Naudet, Damien

SURFACE PROCESSES

PROF. DR. BRENDLER, VINZENZ **DR. MÜLLER, KATHARINA**

CODES & DATA BASES
Dr. Abbasova, Dinara
Dr. Bok, Frank
Dr. Brinkmann, Hannes
Butscher, Daniel*
Friedrich, Sebastian*
Dr. Kretzschmar, Jérôme
Dr. Richter, Anke
Dr. Schmeide, Katja
Shams Aldin Azzam, Salim
Dr. Stockmann, Madlen
Zechel, Susanne

MICRO-/SPECTROSCOPY
Demnitz, Maximilian*
Dietze, Alexandra
Goldbach, Dominik
Jessat, Isabelle*
Dr. Jordan, Norbert
Lösch, Henry*
Dr. Mayordomo Herranz, Natalia
Müller, Christa
Neubert, Heidrun
Rodriguez Hernandez, Diana M.*
Dr. Schierz, Ariette
Weiss, Stephan

ANALYTICS
Dr. Foerstendorf, Harald
Beutner, Sabrina
Chlupka, Aline
Eckardt, Carola
Gürtler, Sylvia
Heim, Karsten

INCORPORATION INTO SOLID PHASES
Dr. Huittinen, Nina
Dr. Barkleit, Astrid
Dr. Eibl, Manuel
Roode-Gutzmer, Quirina
Dr. Yassin, Ghada

REACTIVE TRANSPORT — Campus Leipzig

PD DR. FISCHER, CORNELIUS

Bollermann, Till*
Cardenas, Maria*
Dr. Franke, Karsten
Gruhne, Stefan
Dr. Kulenkampff, Johannes
Dr. Lippold, Holger
Lösel, Dagmar
Dr. Mansel, Alexander
Schabernack, Jonas*
Schößler, Claudia
Dr. Yuan, Tao

NANOSAFETY
Dr. Schymura, Stefan
Rybkin, Iaroslav*
Uygan, Su*

PROF. DR. HEINE, THOMAS, Chair Theor. Chem. TU Dresden / PD DR. KUC, AGNIESZKA BEATA

Jha, Gautam*
Lurz, Christian*
Ramzan, Muhammad Sufyan*
Springer, Maximilian*
Wulf, Toshiki*

STRUCTURAL MATERIALS

DR. ALTSTADT, EBERHARD / DR. KADEN, CORNELIA

Dr. Bergner, Frank
Dr. Chekhonin, Paul
Dr. Das, Aniruddh
Houska, Mario
Dr. Kapoor, Garima
Pietzsch, Jens
Reinke, Vanessa
Richter, Tony
Roßner, Michaela
Skorupa, Ulrich
Dr. Ulbricht, Andreas
Dr. Vogel, Karin
Webersinke, Wolfgang
Welz, Tilo

REACTOR SAFETY

DR. KLIEM, SÖREN

Dr. Bilodid, Yurii
Diaz, Pescador Eduard*
Dr. Fridman, Emil
Gommlich, André
Dr. Grahn, Alexander
Jobst, Matthias
Konheiser, Jörg
Dr. Nikitin, Evgeny
Di Nora, Vincenzo Anthonio*
Dr. Pönitz, Erik
Dr. Rachamin, Reuven
Dr. Schäfer, Frank
Yadav, Pratibha*

*: Ph.D. student (as of 2020/12/31)

GUEST SCIENTISTS

Baier, Silvio	*Technische Universität Dresden, Germany*
Bilodid, Yevgen	*Scientific-technical Centre for Nuclear and Radiation Safety of the Ukraine, Kiew, Ukraine*
Brumme, Thomas	*Technische Universität Dresden, Germany*
Das, Aniruddh	*Technische Universität Dresden, Germany*
Formánek, Petr	*Leibniz-Institut für Polymerforschung Dresden e.V., Germany*
Heller, Anne	*Technische Universität Dresden, Germany*
Ieremenko, Maksym	*Scientific-technical Centre for Nuclear and Radiation Safety of the Ukraine, Kiew, Ukraine*
Lyu, Kai	*Stipendiat Chinese Science Council*
Malcomson, Thomas	*Lancaster University, Lancaster, United Kingdom*
Reinke, Vanessa	*Technische Universität Dresden, Germany*
Sittel, Thomas	*Karlsruhe Institute of Technology, Institute for Nuclear Waste Diposal, Karlsruhe, Germnany*
Vogel, Manja	*HZDR Innovation GmbH*

CO-FUNDED PH.D. STUDENTS

An, Yun	*University of Leipzig, Germany / China Scholarship Council, Beijing, China*
Böhm, Wendelin	*Technische Universität Dresden, Germany*
He, Yihua	*Subatech, Nantes, France*
Li, Huanjian	*School of Earth Sciences & Resources China University of Geosciences, Wuhan, China*
Jha, Gautam	*Technische Universität Dresden, Germany*
Melix, Patrick	*Technische Universität Dresden, Germany*
Newman Portela, Antonio	*Department of Microbiology, University Granada, Spain*
Wöhner, Kevin	*Universität Leipzig, Germany*

MASTER/DIPLOMA/BACHELOR

Bilke, Marie-Louise	Füssel, Tobias	Klotzsche, Max	Puhlmann, Michael
Claus, Gerda	Gerlach, Lisa-Marie	Kühn, Luise	Padberg, Gero
Fankhänel, Tobias	Kliemann, Jonas	Lückel, Benita	

GRADUATE ASSISTANTS, STUDENT ASSISTANTS, TRAINEES

Asteriadis, Adam	Huang, Yun-Hsuan	Limberger, Heidi	Reichmayr, Fanny
Blei, Magdalena K.	Klähn, Lukas	Michak, Marvin	Ramtke, Justus
Dressler, Magdalena	Lessing, Jessica	Mphirime, Doreen	Schabernack, Jonas
Dullies, Paul	Lessing, Richard	Näder, Adrian	Urbank, Christian
Hädinger, Pauline	Kola, Naga Suresh	Opitz, Lucas	Waurick, Lukas

ACKNOWLEDGEMENTS

The Institute of Resource Ecology is one of the eight institutes of the Helmholtz-Zentrum Dresden–Rossendorf e.V. (HZDR). As registered, non-profit institution, the HZDR is supported by the authorities of the Federal Government and the Free State of Saxony. In addition to the basic funding, the financial support of the projects listed below by the given organizations and companies is greatfully acknowledged.

FUNDING ORGANIZATION / COMPANY	PROJECT TITLE	CONTRACT NO. (if applicable)
Commission of the European Communities (EU)	CONCERT – European Joint Programme for the Integration of Radiation Protection Research	*H2020-662287*
	ENTENTE – European Database for Multiscale Modelling of Radiation Damage	*H2020-900018*
	ESFR-SMART – European SFR – Safety Measures Assessment and Research Tools	*H2020-754501*
	EURAD – European Joint Programme on Radioactive Waste Management CORI, DONUT, FUTURE T2 + T3, SFC, UMAN, KMSoK	*H2020-847593*
	FRACTESUS – Fracture mechanics testing of irradiated RPV steels by means of sub-sized specimens	*H2020-900014*
	INSIDER – Improved Nuclear Slte characterization for waste minimization in DD operations under constrained EnviRonment	*H2020-755554*
	M4F – Multiscale Modeling for Fusion and Fission Materials	*H2020-755039*
	McSAFE – High-Performance Monte Carlo Methods for Safety Demonstration– From Proof of Concept to realistic Safety Analysis and Industry-like Applications	*H2020-755097*
	McSAFER – High-Performance Advanced Methods and Experimental Investigations for the Safety Evaluation of Generic Small Modular Reactors	*H2020-945063*
	R2CA: Reduction of Radiological Consequences of Design Basis and Design Extendion Accidents	*H2020-847656*
	RadoNorm – Towards effective radiation protection based on improved scientific evidence and social considerations – focus on radon and NORM + RadoNorm Open Call Grant	*H2020-900009*
	STRUMAT-LTO – STRUctural MATerials research for safe Long Term Operation of LWR NPPs	*H2020-945272*
	SurfBio – Innovation hub for surface and colloid biology research	*H2020-952379*
	TOP – ERC Starting Grant - Towards the Bottom of the Periodic Table	*H2020-759696*
Bundesministerium für Wirtschaft und Energie (BMWi) & Bundesministerium für Bildung und Forschung (BMBF)	EMPRADO – Entwicklung einer Methode zur Pre-Aktivitäts- und Dosisleistungsberechnung von reaktornahen Bauteilen auf Basis von Neutronenfluenzverteilungen Berechnung der Neutronenfluenzverteilung in reaktornahen Bauteilen und deren Validierung an Experimenten als Basis der Aktivitätsrechnungen	*15S9409A*
	f-Char – Spektroskopische Charakterisierung von f-Element-Komplexen mit soft donor-Liganden	*02NUK059B*
	FENABIUM – Struktur-Wirkungsbeziehungen zwischen f-Elementen und organischen Ligandsystemen mit Naturstoff-basierten Bindungsfunktionen in Hinblick auf eine mögliche Mobilisierung in der Umwelt	*02NUK046B*
	GRaZ – Geochemische Radionuklidrückhaltung an Zementalterationsphasen	*02E11415B*
	GRaZ II – Geochemische Radionuklidrückhaltung an Zementalterationsphasen	*02E11860B*
	iCross – Integrität von Endlagersystemen für radioaktive Abfälle – Skalenübergreifendes Systemverständnis	*02NUK053B*

FUNDING ORGANIZATION / COMPANY	PROJECT TITLE	CONTRACT NO. (if applicable)
	KRIMI – Kinetik der Radionuklidimmobilisierung	*02NUK056C*
	MgO-S3 – Spritzbeton für Streckenverschlüsse für HAW-Endlager im Steinsalz	*02E11769B*
	PANAS – Untersuchungen zu passiven Nachzerfallswärme-Abfuhrsystemen; Teilprojekt B: Untersuchungen zu Kondensationsprozessen im Notkondensator und numerische Simulation einer passiven Wärmeabfuhrkette	*02NUK041B*
	RADEKOR – Speziation und Transfer von Radionukliden im Menschen unter besonderer Berücksichtigung von Dekorporationsmitteln	*02NUK057A*
	ResKin_Move – Geschwindigkeitsfeld-Analyse mit Positronen-Emmissions-Tomografie (PET): Parametrisierung und Validierung von Transportmodellen (Plug-Skala)	*03G0900A*
	SMILE – Smart-K_d in der Langzeitsicherheitsanalyse – Anwendungen	*02E11668B*
	STROEFUN III – Strömungstechnischer Funktionsnachweis für Verschlussbauwerke und flüssigkeitsgestützte Abdichtung des Kontaktbereiches Phase III: Vertiefung Kenntnisstand Kontaktbereich & Injektionsmittel, in situ-Versuche	*02E11748B*
	TRANS-LARA – Transport- und Transferverhalten langlebiger Radionuklide entlang der kausalen Kette Grundwasser-Boden-Oberfläche-Pflanze unter Berücksichtigung langfristiger klimatischer Veränderungen	*02NUK051B*
	TransForm – Transnationale Forschungsinfrastruktur und multidisziplinäre akadamische Nachwuchsförderung	*01DT20004*
	VESPA II – Verhalten langlebiger Spalt- und Aktivierungsprodukte im Nahfeld eines Endlagers und Möglichkeiten ihrer Rückhaltung	*02E11607B*
	WERREBA – Wege zum effizienten Rückbau von Reaktorkomponenten und Betonabschirmung: Berechnung des Aktivitätsinventars und deren Validierung an Bohrkernen sowie Mobilitätsuntersuchungen von Radionukliden	*15S9412*
DAAD	DAAD PPP Frankreich 2020–2021 – Programm des projektbezogenen Personenaustausches mit Frankreich 2020–2021	*57512305*
DFG	DFG-Programmpauschalen ab 2014 – Verwaltung von 25 % der ab 2014 zu den DFG-Projekten bewilligten Programpauschalen	
	DNA-Struktur Molekulare Mechanismen der Interaktion chaotroper Salze mit natürlichen und künstlichen DNA-Strukturen	*FA 248/8-1*
	SFB 1415 – Sonderforschungsbereich 1415 „Chemie der synthetischen zweidimensionalen Materialien“	*SFB 1415/1 2020*
EnBW Kernkraft GmbH	NanoExperte – Gutachten Nachweis von Nanomaterialien	*P97417*
Helmholtz-Gemeinschaft Deutscher Forschungs-zentren e.V. (HGF)	CROSSING – Crossing borders and scales – an interdisciplinary approach	*PIE-0007*
	Extract	
	Exzellenznetzwerk-Phase 3 "Physics of Life – The Dynamic Organization of Living Matter"	*ExNet-0029-Phase2-3*
	NUSAFE / iCross – Integrität von Endlagersystemen für radioaktive Abfälle – Skalenübergreifendes Systemverständnis	*SO-093*
HTW	Altstahl – Bruchmechanische Prüfung im Rahmen eines Forschungsprojektes der HTW	

FUNDING ORGANIZATION / COMPANY	PROJECT TITLE	CONTRACT NO. (if applicable)
PT Jülich	Ultrasens (WIPANO) – Ultrasensiver spektraler Sensor zur indirekten Messung ionisierender Strahlung	*03THWSN004*
TÜV NORD	Prüfung geologischer Fragen	*M.ASS.06.015.01.F70*
TÜV SÜD	Gemischte Reaktorkerne: Sicherheitstechnische Analysen für gemischte Reaktorkerne sowie zur Rekritikalität bei einem schweren Kernschmelzunfall für WWER-1000-Reaktoren (AP12)	*3617R01520*
	TÜV VVER 1200 code 1 – Support and consulting services	
	WWER AP03	*500603389*
UJV Rez, a.s.	DYN3D für UJV Wartung 2019/2020	

INDEX OF AUTHORS

AUTHOR	PAGE
Abram, U.	26
Acker, M.	17
Altstadt, E.	70, 71, 72
Amidani, L.	13, 14, 24
An, Y.	46
Baier, S.	85, 86
Baldinozzi, G.	15
Balice, L.	15
Bansal, D.	20
Barkleit, A.	58, 77, 78
Bauters, S.	13, 26
Beck, A.	24, 47
Bergner, F.	69, 70, 71, 72, 73
Bilke, M.-L.	56
Bilodid, Y.	81, 83
Bok, F.	32, 51, 58
Bollermann, T.	37, 39, 43
Bonani, W.	47
Borodkin, P.	85
Brendler, V.	32, 36, 49, 50, 77
Brinkmann, H.	32
Britz, S.	32
Brumme, T.	46
Butorin, S. M.	13, 24, 26
Causse, J.	23
Chekhonin, P.	37, 71, 72, 73
Cherkouk, A.	57, 62, 63
Cognini, L.	15
Cologna, M.	15
Dacheux, N.	23
Dardenne, K.	26
Das, A.	71, 72
De Bona, E.	15
Deev, D.	64
Demnitz, M.	31
Di Nora, V. A.	84
Diaz Pescador, E.	80, 83
Dressler, M.	62
Drobot, B.	16, 27
Egorova, T.	13
Eloirdi, R.	47
Eng, P.	34
Engelhard, M. H.	47
Estevenon, P.	23
Fichter, S.	18, 22
Fischer, C.	37, 39, 40
Foerstendorf, H.	17, 27, 28, 33
Franke, K.	38, 43, 44, 48
Fridman, E.	79
Frühwirt, T.	38
Füssel, T.	35

AUTHOR	PAGE
Galanzew, J.	24
Gerber, E.	13, 14
Gommlich, A.	81
Gouder, T.	47
Grahn, A.	80
Grossmann, K.	66
Günther, A.	65
Guo, X.	47
Heine, T.	46
Heller, A.	58
Hennig, C.	13
Hilpmann, S.	57
Hoehenwarter, W.	55
Höhne, T.	80
Holzhäuser, M.	15
Houska, M.	70
Hübner, R.	61
Huittinen, N.	17, 28
Hunault, M. O. J. Y.	13
Ikeda-Ohno, A.	24
Jankovsky, F.	38
Jessat, I.	33
Jessat, J.	56
Jobst, M.	82
John, W. A.	55, 60
Jordan, N.	33
Kaden, C.	71, 72, 73
Kaden, P.	20
Kalmykov, S. N.	13, 14
Kliem, S.	80, 81, 83
Kloditz, R.	22
Kluge, S.	61
Köhler, L.	21
Konheiser, J.	78, 85, 86
Konstantinovic, M. J.	74
Krawczyk-Bärsch, E.	61
Kretzschmar, J.	16
Kriegsman, K. W.	47
Kuc, A.	46
Kulenkampff, J.	38, 41, 42, 43, 75
Kvashnina, K. O.	13, 14, 24, 26, 47
Lapanje, A.	48, 64
Lindau, R.	72
Lippold, H.	45, 76
Löffler, M.	63
Lu, R.	50
Lützenkirchen, J.	32

AUTHOR	PAGE
Mansel, A.	38, 43, 48
Martin, P.	47
März, J.	18, 19, 21, 22, 24
Matschiavelli, N.	55, 62, 63
Mayordomo, N.	26, 35, 36
McClintock, D.	72
Mesbah, A.	23
Moisy, P.	23
Moll, H.	57, 60
Molodtsov, K.	31, 37
Müller, K.	31, 35, 36
Neubert, T.	63
Neumann, J.	32, 34
Nikitin, E.	79
Oliveira, A. F.	46
Patzschke, M.	19, 20, 22
Pidchenko, I.	13
Plakhova, T. V.	13, 14
Poinssot, C.	23
Popa, K.	15, 47
Pospiech, S.	49
Prieur, D.	15, 47
Puhlmann, M.	57
Qiu, C.	34
Rachamin, R.	78, 86
Radoske, T.	19
Raff, J.	65
Ramtke, J.	61
Rellinghaus, B.	63
Richter, A.	51
Rijavec, T.	48, 64
Rodríguez, D. M.	35, 36
Romanchuk, A. Y.	13, 14
Roode-Gutzmer, Q. I.	75, 76
Rossberg, A.	13, 25, 27
Rothe, J.	26
Rybkin, I.	48, 64
Sachs, S.	55, 56, 60
Schäfer, F.	80, 83
Scheinost, A. C.	13, 26, 47
Schierz, A.	31, 62, 63
Schild, D.	24, 36
Schmeide, K.	16, 26
Schmidt, M.	19, 20, 22, 31, 32, 34, 37
Schymura, S.	31, 37, 38, 48, 76
Shams Aldin Azzam, S.	17, 28
Skanthakumar, S.	34
Soderholm, L.	34
Sohr, J.	51
Stalke, S.	66
Steudtner, R.	16, 26, 27, 66
Stockmann, M.	32, 50
Strok, M.	48
Stumpf, T.	16, 19, 21, 26, 32, 34, 36, 37, 57, 62
Sushko, V.	62, 63
Szenknect, S.	23
Ta, S.	17
Taube, F.	17
Thieme, D.	55
Trigub, A.	13
Tsushima, S.	16, 59
Ulbricht, A.	74
Vaughan, G. B. M.	13, 14
Vitova, T.	24, 47
Vogel, K.	73
Vogel, M.	27
Voigt, W.	51
Walter, O.	15, 47
Weiss, S.	13, 14, 17, 24, 26, 28
Welcomme, E.	23
Wilsnack, T.	41
Wiss, T.	15
Yadav, P.	86
Yassin, G.	77
Yuan, T.	37, 40
Zedek, L.	45
Zuna, M.	38

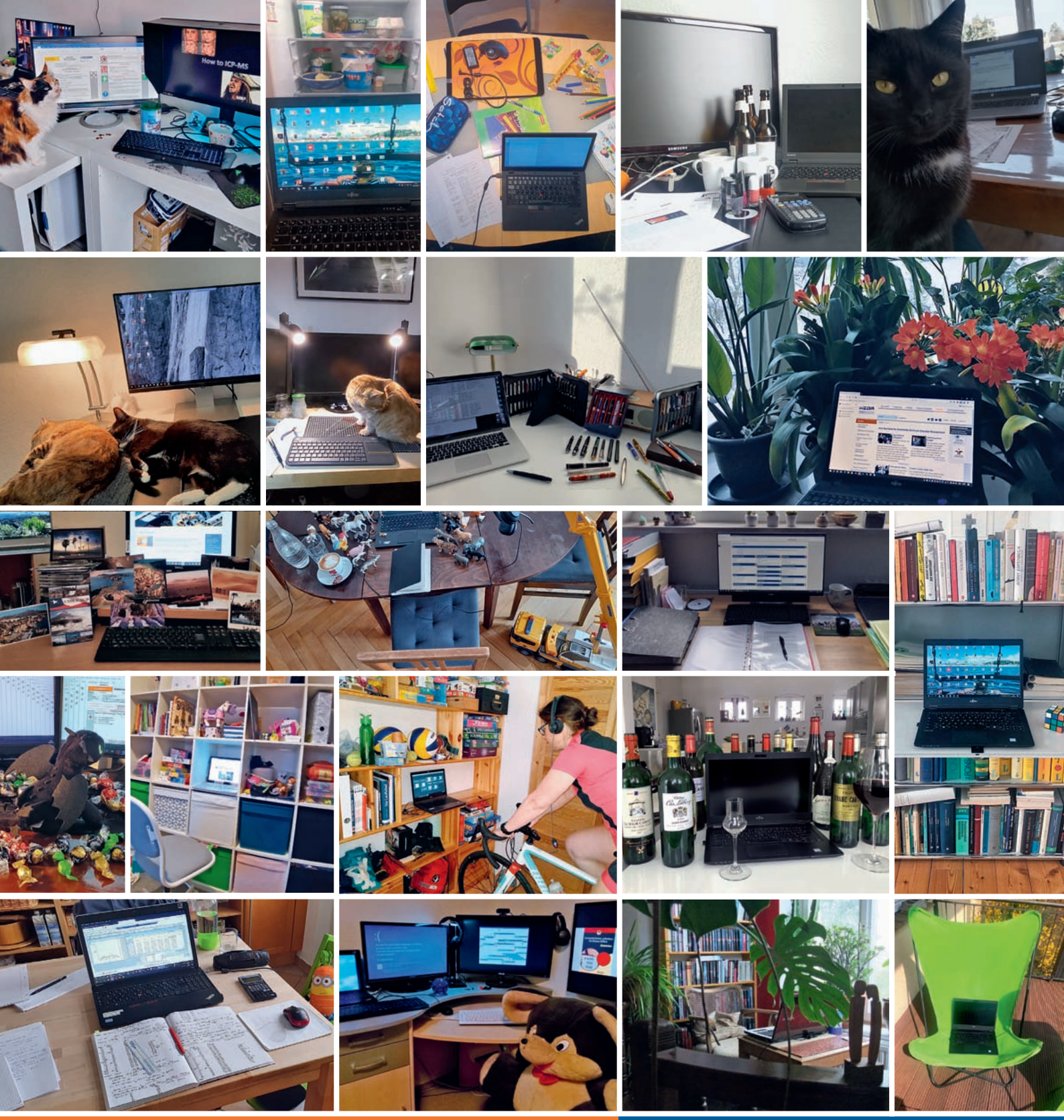

HZDR
HELMHOLTZ ZENTRUM
DRESDEN ROSSENDORF

Institute of Resource Ecology
Bautzner Landstrasse 400
01328 Dresden/Germany
Phone +49 351 260-3210
Fax +49 351 260-3553
Email contact.resourceecology@hzdr.de
http://www.hzdr.de

Member of the Helmholtz Association